

RESPONSE OF FIRE EXPOSED CONCRETE BRIDGE GIRDERS

By

Augusto Masiero Gil

A DISSERTATION

Submitted to
Michigan State University
in partial fulfillment of the requirements
for the degree of

Civil Engineering – Doctor of Philosophy

2024

ABSTRACT

Fire represents a significant hazard to bridges, often resulting in damage or collapse of structural members. Typically, bridge fires result from crashes or overturns of vehicles carrying large amounts of flammable materials near bridges. These fires have become a growing concern over the last decade due to increasing urbanization and transportation of hazardous materials. Characterized by the rapid onset of very high temperatures (above 1000°C), these fires significantly affect the stability and integrity of structural members. Despite these risks, current bridge codes and standards do not specify any fire safety features in the design and construction of bridges, leaving critical transportation infrastructure vulnerable to fire hazard.

While there has been some research in recent years on the fire response of steel and composite bridges, there have been limited studies on the fire problem in concrete bridges. Further, prestressed concrete girders, designed with slender cross-sections to reduce self-weight and span longer distances, can experience faster degradation during fire exposure due to rapid temperature propagation within the girder cross-section. Although conventional concrete members have good fire response properties, newer concrete types such as High-Strength Concrete (HSC) and Ultra-High Performance Concrete (UHPC) experience faster degradation of mechanical properties at elevated temperatures and are also more susceptible to fire-induced spalling.

To address some of the identified knowledge gaps, experimental and numerical studies on the fire response of concrete bridge girders have been carried out. As part of the experimental work, pore pressure measurements in concrete at elevated temperatures were conducted to evaluate the mechanisms that lead to fire-induced spalling in concrete. Also, shear strength tests were carried out to assess the degradation of shear strength with temperature in UHPC. Complementing the experimental studies, a comprehensive finite element-based numerical model was developed

to trace the response of concrete bridge girders under fire conditions. The model accounts for varying fire scenarios, loading conditions, and temperature-dependent thermal and mechanical properties of steel and concrete, and was validated with data from fire tests. To develop typical bridge fire scenarios, fire dynamics simulations were carried out and incorporated into the model.

A set of parametric studies were undertaken to evaluate the effect of critical parameters on the fire response of concrete bridge girders. Results demonstrate that smaller concrete sections present lower fire resistance due to their lower thermal mass, and that I-shaped concrete girders are susceptible to shear failure from the high temperatures in their webs. Other design parameters, such as span length and concrete strength, also significantly affect the fire performance of concrete bridges. In addition, fire simulations have shown that bridge fires present high severity and are influenced by the bridge geometrical features. Based on these findings, recommendations to improve the fire design of bridge girders have been proposed. For conventional concrete bridge girders, increasing cross-sectional size and limiting exposure of the web near the supports to the high temperatures can improve fire performance. Spalling can be reduced in UHPC members through addition of polypropylene fibers. Additionally, parameters for assessing the fire resistance of bridge girders, such as failure criteria and a bridge fire curve that accounts for the thermal gradient along the girder length were proposed. The developed numerical tool is also applied to analyze the fire-induced collapse of the I-95 overpass in Philadelphia on June 11, 2023.

Keywords: Concrete bridges, Fire safety, Bridge girders, Ultra-high performance concrete

*To my beloved wife, Patricia,
for all her love and support.*

ACKNOWLEDGMENTS

I would like to express my sincere gratitude to my advisor, Dr. Venkatesh Kodur, for his invaluable support, guidance, and encouragement during my studies. I am truly thankful for the opportunity of working with him and gaining invaluable learning experiences under his guidance. I also would like to thank my TA supervisor, Dr. Jenahvive Morgan, for all her support during the 10 semesters that I was a TA for EGR100, as well as for the engineers in the Bridges Load Rating Unit at the Wisconsin Department of Transportation during my 2023 summer internship.

I would like to express my appreciation to Dr. Nizar Lajnef, Dr. Qingxu Jin, and Dr. Patton Allison for serving in my Ph.D. committee and for their constructive comments and words of encouragement. I also would like to express my sincere gratitude to Dr. Srishti Banerji for her support and guidance, especially with fabrication of specimens and pore pressure measurements. Also, I am thankful to Dr. Roberto Felicetti, Politecnico di Milano, Italy, for providing the sintered metal heads. In addition, I would like to thank Mr. Brian Gietzel for his assistance during the experimental work, especially with the fabrication of the shear strength test apparatus.

I also would like to express my gratitude to sponsors and partners who made the development of this research possible. I am thankful for Precast/Prestressed Concrete Institute (PCI) for providing financial support, Pennsylvania Department of Transportation (PennDOT) for sharing the design plans of the I-95 overpass in Philadelphia, and Thunderhead Engineering for sharing a license to PyroSim. I am also thankful to Michigan State University for providing the resources for my professional growth, especially to Dr. Katy Colbry and Sandy Christlieb for their kindness and support in several opportunities. Additionally, I would like to thank all the CEE department administrative staff for their assistance in several occasions over the last five years, especially to Dr. Peter Savolainen, Laura Post, Shelly Harbenski, and Bailey Weber.

I would like to thank my peers Dr. Ankit Agrawal, Dr. Pratik Bhatt, Dr. Puneet Kumar, Dr. Roya Solhmirzaei, Dr. Srishti Banerji, Dr. Svetha Venkatachari, Ankush Jha, Manish Sah, and Tejeswar Rayala for their help in several moments. In addition, I would like to thank my colleagues in the department Dr. Brijen Miyani, Behlul Kula, Dr. Celso Santos, Dr. Ceren Aydin, Christiana Kiesling, Feyza Bulduk, Jeonga Kang, Mehdi Bulduk, Dr. Haluk Sinan Coban, Dr. Wasif Naqvi, and Yazmin Dasgar, and others, for their friendship and support. I also would like to express my appreciation to my mentors and colleagues from Unisinos University, especially Dr. Bernardo Tutikian, Dr. Roberto Christ, Dr. Fernanda Pacheco, and Dr. Bruno Fernandes, for introducing me to academia and always providing opportunities for my professional growth and improvement throughout my journey.

Finally, I am deeply grateful for my whole family and friends in Brazil for understanding my absence during this time and for always welcoming me back in their lives. My deepest gratitude goes to my parents Maxi and Raul, and my brother Leonardo for their unconditional love and support, as well as to my lovely wife Patricia, for being compassionately by my side at each step of this journey. I also would like to thank Patricia's family, especially Miriam and Sandro, for their support and for taking such good care of Clinker during our absence. I would not have gotten to this point without you. Amo vocês!

TABLE OF CONTENTS

1. INTRODUCTION	1
2. STATE-OF-THE-ART REVIEW.....	17
3. EXPERIMENTAL STUDIES.....	67
4. NUMERICAL STUDIES	101
5. MODEL APPLICABILITY	129
6. PARAMETRIC STUDIES	150
7. DESIGN RECOMMENDATIONS	182
8. CONCLUSIONS.....	205
REFERENCES	214
APPENDIX A – TEMPERATURE-DEPENDENT MATERIAL MODELS.....	234
APPENDIX B – MESH SENSITIVITY ANALYSIS.....	241
APPENDIX C – FIRE DYNAMICS SIMULATIONS RESULTS.....	245
APPENDIX D – THERMO-STRUCTURAL ANALYSIS RESULTS	250
APPENDIX E – FIRE LOAD CALCULATION	256
APPENDIX F – PUBLICATIONS	258

1. INTRODUCTION

1.1. General

Bridges are an essential part of a nation's infrastructure system, allowing the transportation of vehicles, people, and commodities across communities and regions. They overcome geographical barriers and allow uninterrupted flow of traffic through intersections, facilitating people movement, efficient trade, and integration. Bridges are also very important from a social perspective, as they facilitate the movement of vital resources and foster accessibility to education, healthcare, and opportunities. Interruptions in bridge operations can lead to significant traffic disruptions and result in economic and social consequences. Given their vital importance, bridges must be designed to withstand various hazards for extended service life, with minimal interruptions due to maintenance, repair, and replacements works [1–4].

A fundamental factor in ensuring the long-term functionality and safe operation of bridge structures is their durability [5]. The ability of structures to withstand a wide range of natural hazards without compromising its structural integrity is achieved through proper material selection, adequate construction techniques, and thoughtful maintenance practices [6,7]. By prioritizing durability in the design, engineers must take into consideration all the environmental hazards a bridge might be exposed to during their service life. This includes possible fire exposure, considered one of the most severe hazardous situations that a structural member can experience [8]. A key consideration in overcoming fire hazard in bridges is providing adequate fire resistance to the main structural members. Fire resistance represents the period of time during which a member can withstand the effects of high temperatures while maintaining structural integrity and stability [9]. However, current bridge design codes and standards do not present specific fire resistance requirements for bridge structures to sustain the effects of bridge fires [10].

The development of standards and regulations that outline the design and maintenance of bridge structures usually results from learnings and impacts of previous incidents. One of the most notorious bridge collapses in the United States happened in 1947 at the Silver Bridge, connecting Ohio and West Virginia [11]. The collapse resulted from an instantaneous fracture of a single eye-bar due to fatigue and led to the creation of the National Bridge Inspection Program (NBIP), which mandates regular inspections of bridges [12]. Regulations advanced as other bridge collapses occurred, including the case of Mianus River Bridge in 1983 and Schoharie Creek Bridge in 1987, which led to more rigorous inspection procedures for fracture critical members and structures susceptible to scour [13]. Recently, the collapses of critical bridge structures due to fire incidents, as seen with the cases of an I-85 overpass in Atlanta in 2017 and an I-95 overpass in Philadelphia in 2023, have highlighted the importance of accounting for fire hazard in bridge structures [14,15].

The formulation of fire protection measures relies on the type of structural material being used, since different materials exhibit distinct behaviors under fire conditions. Prestressed concrete bridges are the most popular structural system used in bridges nowadays. Of the more than 610,000 highway bridges in the United States, approximately 160,000 are prestressed concrete bridges [16]. Since its first application in 1950 at the Walnut Lane Bridge in Philadelphia, prestressed concrete has quickly become the primary construction method for new bridges in the United States [17]. The popularity of prestressed concrete in bridge construction relies on its higher durability and reduced maintenance costs, especially when compared to steel [18]. With new types of concrete continually being developed and integrated into the design of bridges, there is the need to ensure that these structures can withstand the effects of high temperatures generated during severe fires. The development of more resilient infrastructure, capable of resisting and recovering fire events, is also important for sustainability reasons.

In recent years, the field of bridge engineering has witnessed several advancements that are changing the design, construction, and maintenance of bridge structures. The integration of superior materials, such as high strength concrete (HSC) and ultra-high performance concrete (UHPC), as well as high strength steels and fiber reinforced polymers (FRP), has significantly enhanced the durability and load-bearing capacity of bridges, allowing longer service life and reduced maintenance costs [19–21]. Moreover, the utilization of sophisticated sensors and monitoring systems allow for structural health monitoring to detect potential issues and deterioration in real time [22,23]. Computational tools, powered by machine learning (ML) and artificial intelligence (AI), can be employed to optimize bridge designs for improved performance [24,25]. These collective advancements are redefining the design and maintenance of modern infrastructure and generating new possibilities for increasing resiliency to various hazards, including thermal exposure from fire incidents.

1.2. Fire Hazard in Bridges

Bridge structures can be exposed to fires resulting from different causes. Most commonly these fires happen due to crashes or overturn of vehicles carrying significant amounts of fuel in the vicinity of bridges, which are characterized by intense burning and onset of very high temperatures in the early stages of fire exposure. However, bridge fires can also arise as a secondary event, following an earthquake or a blast, or due to other causes, such as wild fires in remote areas or vandalism, as seen in the fires at I-85 in Atlanta and at I-10 in Los Angeles [14,26]. The involvement of gasoline-based fuel and open-air burning conditions makes fires on bridges more severe than in buildings [27,28]. Yet, the probability of a fire breakout in a bridge is low and for this reason bridges are not designed with any specific fire safety features.

The low risk of bridges to fire hazard is based on two common assumptions. First, bridges are typically open spaces that people can easily escape, not presenting a high risk for life safety. Secondly, heat and smoke are dissipated into the environment (open air burning), so structural members are unlikely to experience high temperatures as they would in a built environment [8]. While these assumptions hold true in some cases, the increasing number of fire incidents in recent years with substantial property damage and monetary losses have shown that bridge fires still pose a significant hazard [29]. A survey conducted by the New York Department of Transportation [30] analyzed the cause of bridge collapses of 52 bridges in 18 states. Results of the survey demonstrated that the probability of collapse during a fire was three times higher than during an earthquake, which was attributed to the fact that fire is not considered in the design of bridges, while earthquakes are considered.

Fire incidents in the vicinity of bridges are becoming more common in recent years. This has been attributed to the increase in ground transportation of hazardous materials, including chemicals and other flammable materials, as well as increasing urbanization, which raises the risk of accidents involving trucks and tankers around bridges [8,31,32]. Table 1.1 summarizes major fire incidents in concrete bridges over the past 20 years in the United States. Peris-Sayol et al. [29] conducted a detailed analysis of the causes and associated damage levels in 154 bridge fire incidents around the world between 1997 to 2015, considering different structural materials. Through a statistical analysis, the authors showed that tankers carrying gasoline in the vicinity of a bridge are responsible for most fires and that these types of fires are more likely to induce damage or collapse of the bridge. Furthermore, it was found that concrete bridges can experience a significant level of damage, and that bridges made with I-shaped girders are more prone to experience damage, requiring more repair after a fire incident.

Table 1.1: Major fires in concrete bridges in the last decades in the United States

Bridge location / Reference	Date	Structural characteristics	Cause of fire and extent of damage
Puyallup River Tacoma, WA [33]	Dec., 2002	Prestressed concrete bridge girders ($f'c = 48$ MPa) with a span of 44.8 m span. Bridge pier and decks were also made with concrete ($f'c = 34.5$ MPa).	A railroad tanker collision resulted in burning of 113.5 m ³ of methanol for 1 hour. Spalling and change of concrete color was observed in the concrete piers, but deflections or misalignments were not observed.
State Road Washington, OR [34]	Nov., 2004	Precast concrete bridge girders with a span of 11.4 m and voided slabs with a depth of 457 mm.	A car abandoned beneath the bridge was set on fire. Temperature on concrete surface was estimated to be around 300°C. Spalling occurred in area of 610 mm with a depth of 76 mm. It did not result in loss of capacity nor large deflections.
Norwalk River Ridgefield, CT [34]	Jul., 2005	Precast prestressed concrete box girders and cast-in-place concrete slab with a length of 24.4 m.	A tanker with 30.3 m ³ of gasoline jack-knifed during an accident and spilled its content over the bridge, resulting in a huge fire. Large amounts of spalling occurred, and the slab needed to be replaced, while the girders did not experience loss of capacity.
Belle Isle Bridge Oklahoma City, OK [34]	Jan., 2006	Precast prestressed I-shaped girders and cast-in-place concrete slab	A truck crashed into the ground near the ramp of the bridge, resulting in a fire. There was no significant structural damage, only cosmetic damage and slight deformation of concrete girders.
Bill Williams River Parker, AZ [34]	Jul., 2006	Prestressed concrete girders with span of 23.2 m and cast-in-place concrete slab	A tanker carrying 28.7 m ³ of diesel fuel overturned and spilled the fuel that resulted in a large fire. There were large spalled regions, but a small loss of capacity identified.
State Road 386 Nashville, TN [34]	Jun., 2007	Concrete hollow box-girder	A collision between a fuel tanker and a truck beneath the bridge. The incident resulted in minor structural damage.
I-5 Tunnel Exit Santa Clara, CA [34]	Oct., 2007	Tunnel exit was composed of concrete box girders supported on top of concrete strutted abutments	A truck exiting a 167 m-long truck-bypass tunnel lost control, overturned, and resulted in a massive fire in the tunnel exit. The fire resulted in five deaths and damaged one-sixth of the total superstructure.
Interstate 85 Atlanta, GE [8]	Mar., 2017	Precast prestressed I-shaped girders with span of 28 m and cast-in-place concrete slab	Plastic conduits stored under the bridge for a renovation project were set on fire. The huge fire resulted in spalling of concrete and collapse of one deck. The other five decks needed to be replaced due to severe damage.
Interstate 70 Indianapolis, IN [35]	Feb., 2020	Precast prestressed I-shaped girders and concrete slab	A fuel tanker carrying 15 m ³ of jet fuel overturned and resulted in a fire that burned for 40 minutes. The fire resulted in spalling at certain points but caused no major structural damage.
Interstate 10 Los Angeles, CA [36]	Nov., 2023	Prestressed box girders strengthened with steel beams near supports	The arson quickly spread over the mile-long elevated section due to the big number of wooden pallets and vehicles stored there. More than 100 columns were damaged, nine or 10 of them severely. Several spalled areas on the columns and deck. Strengthening and repairs were needed to reopen the section.

According to the National Fire Protection Association [37], there were more than 174,000 highway vehicle fires in the United States in 2021 with a total estimated monetary loss of \$1.55 billion. A single fire incident can result in large traffic disruptions and have a significant economic impact to a community. For instance, the structural damage caused by the fire resulting from overturn of a tanker at the I-80/880 Interchange in Oakland, California in 2007 took 26 days to be repaired at an estimated cost of \$ 9 million [38]. This is in addition to huge indirect monetary losses resulting from the closure of the highway and impacts to local economic activities, which can be much more expensive than the costs of repair and reconstruction of the bridge itself [39]. The fire incident that occurred at Interstate 85 in Atlanta, Georgia in 2017 resulted in collapse of one of the bridge spans, which cost \$15 million to be reconstructed. Delays to over 250,000 vehicles that used the bridge daily resulted in an increase of up to 20% in the unit cost per mile for shipping items [26]. Similarly, a recent incident at an I-95 overpass in Philadelphia, Pennsylvania impacted 160,000 vehicles daily and took months to be completed [40,41]. Even though these incidents represented low risk for life, they led to significant economic losses and have impacted local communities. Detours create severe congestion on the surrounding traffic network and have large economic implications, and the accelerated repair or replacement of a bridge can cost millions of dollars, in addition to passive financial losses.

1.3. Vulnerability of Concrete Bridges to Fire

Generally, structural members made of concrete possess excellent fire resistance properties. This is attributed to the good thermal properties of concrete, including low thermal conductivity and high heat capacity, which delay the progression of temperature inside the concrete member. Further, concrete loses its strength at a much lower rate, as compared to steel. However, concrete members still experience degradation in structural capacity as sectional

temperatures rise. The level of degradation is dependent on temperature-dependent mechanical properties (strength and stiffness) of both concrete and steel, as well as any sectional loss resulting from fire-induced spalling.

Figure 1.1 (a) conceptually illustrates moment and shear capacity degradation of a rectangular concrete beam in a bridge exposed to the high temperatures during a fire. The flexural (M_n) and shear (V_n) capacities of the beam at room temperature are constant throughout their entire length (blue shaded areas). After exposure to a certain fire duration, the flexural ($M_{n,T}$) and shear ($V_{n,T}$) capacities are reduced to the orange shaded areas in each diagram. During fire exposure, the initially applied bending moment (M_u) and shear force (V_u) are decreased to account for a reduction of the combined loads ($M_{u,T}$ and $V_{u,T}$) during a fire incident. Since the flexural and shear strength of the beam continue to degrade during fire exposure, they will eventually reduce to a level below the applied bending moment or shear force, respectively. Failure of the rectangular concrete beam would typically occur due to degradation of its flexural capacity ($M_{n,T}$), as the high temperatures predominantly reach the flexural reinforcement and its shear capacity degrades slowly.

I-shaped girders are the most popular type of superstructure member in concrete bridges. Their slender cross-section reduces the girder self-weight and allows construction of longer spans but can present a different fire behavior compared to rectangular girders. The lower thermal mass of I-shaped sections allows a faster progression of temperatures in the web of the girder, which results in faster degradation of its shear capacity. This behavior is conceptually illustrated in Figure 1.1 (b) through degradation of moment and shear capacities of an I-shaped concrete beam during fire. It can be seen that the degraded shear strength ($V_{n,T}$) is lower for the I-shaped section as a result of the higher temperatures in the web. The accelerated degradation of the sectional shear capacity could lead to shear failure of the I-shaped section prior to flexural failure.

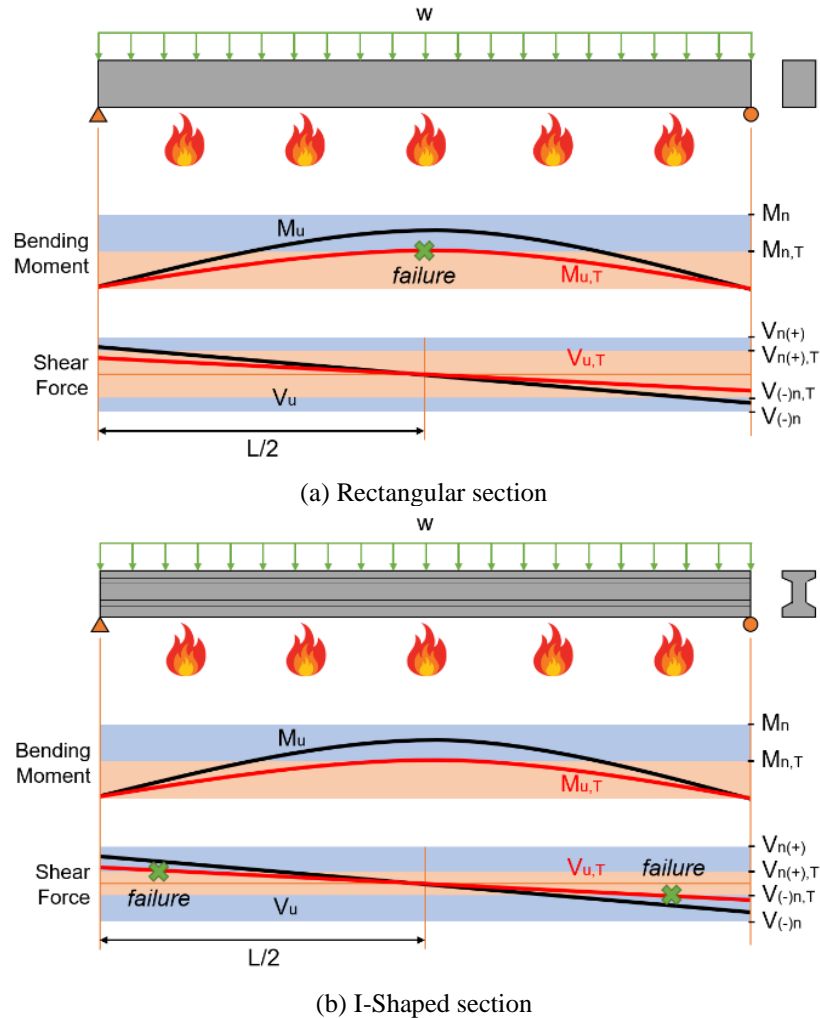


Figure 1.1: Variation of bending moment and shear force at ambient and fire conditions

Shear forces can also govern under certain loading configurations due to the presence of high concentrated loads, such as a tanker parked near the supports of a bridge, potentially leading to early failure under shear limit state. In the case of bridge girders made with superior types of concrete, such as ultra-high performance concrete (UHPC), the shear capacity under fire conditions can be compromised. This can occur due to the reduction or elimination of shear reinforcement as a result of UHPC's inherently high shear strength. Additionally, UHPC members are often much slenderer, resulting in faster temperature propagation within the web and degradation of its shear capacity during fire. The severity of bridge fires and UHPC's susceptibility to fire-induced spalling are other factors that can aggravate the fire response of these girders.

Therefore, shear failure becomes a critical limit state that requires careful consideration in the evaluation of the fire performance of I-shaped bridge girders.

In current practice, fire hazard in buildings is overcome through provision of active and passive fire protection systems prescribed in buildings codes and standards [42]. The active systems comprise of detection or suppression systems that activate in the presence of fire. As part of the passive system, fire resistance is provided to structural members. For concrete members, a prescribed minimum concrete cover (thickness) encasing rebars and minimum cross-sectional dimensions are required to meet fire resistance requirements for structural fire safety [43]. However, there are no specific fire-related provisions in standards for structural members in bridges [10]. Even if designers were to extend fire resistance provisions developed for buildings to bridge structures, it will not yield adequate fire safety due to considerable differences among the key influencing features (fire temperatures, structural characteristics, etc.). While retrofitting existing bridges with fire protection systems can be complex and costly, addressing fire safety in the design of modern bridges allows for practical and economically feasible solutions that align with the emerging need for more resilient infrastructure.

1.4. Ultra-High-Performance Concrete

Among several promising new structural materials, UHPC has gained special attention in the bridge industry due to its superior mechanical properties and enhanced durability characteristics [44]. UHPC consists of a highly compacted cementitious composite designed with low water-to-cementitious materials ratio (less than 0.25), and high contents of fine mineral admixtures and supplementary cementitious materials [45]. UHPC mixtures are typically made with high steel fiber content and without any coarse aggregates. However, some researchers have introduced coarse aggregates in UHPC for cost optimization [46,47]. Additionally, heat and

pressure curing (90°C to 200°C) have been applied to achieve higher strength [48,49]. Overall, UHPC provides high levels of compressive and tensile strength, high toughness and a ductile behavior in tension, which is dependent on the type and volume of steel fibers incorporated [50].

The U.S. Department of Transportation - Federal Highway Administration [51] defines UHPC-class materials as those exhibiting compressive strength above 150 MPa, pre- and post-cracking tensile strength above 5 MPa, and enhanced durability through a discontinuous pore structure. These properties represent a significant improvement from normal strength concrete (NSC), high strength concrete (HSC), and fiber reinforced concrete (FRC), as shown in Figure 1.2. The highly compact nature of UHPC contributes to its high compressive strength, far surpassing NSC's and HSC's strength that usually range between 20-50 MPa and 70-100 MPa, respectively. While the tensile strength of NSC and HSC range between 1 and 3 MPa and is considered too low to be accounted for in structural design, the addition of steel fibers in UHPC contributes to an improved performance in tension. UHPC presents a ductile behavior after cracking in tension and higher levels of strains when compared to FRC. Overall, these properties contribute to enhanced flexural and shear response of UHPC members, which is taken into consideration in the structural design of a bridge to optimize steel bar reinforcement [52,53]. Previous studies under room temperature conditions have demonstrated the high shear strength of UHPC, allowing a reduction or removal of shear reinforcement (stirrups) without a decrease in ductility or moment capacity, even under predominant shear loading [54,55].

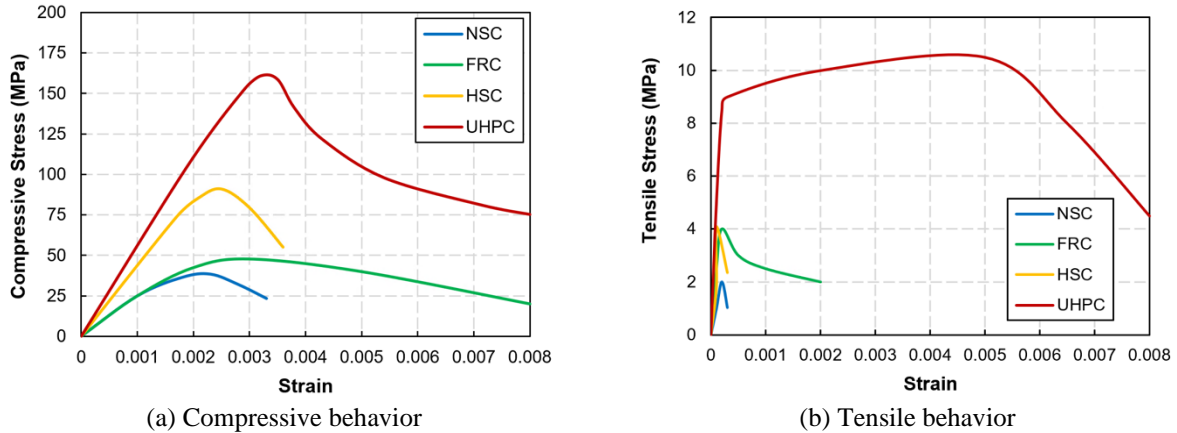


Figure 1.2: Comparison of stress-strain response of different types of concrete

UHPC is being adopted for a wide range of applications in highway infrastructure projects due to its superior mechanical properties. Figure 1.3 presents the documented use of UHPC in bridge projects in the United States over the past 26 years. While most of these applications have been on the connection between members and deck overlays, UHPC has been used in superstructure members (deck and girders) in several bridge projects throughout the world [20,44,51,56]. The first UHPC bridge in Canada was constructed in 1997 and was followed by at least 26 additional UHPC bridges [21]. Malaysia is the country with the largest number of UHPC bridge superstructures to date, with over 120 bridges built between 2010 and 2020 [44]. In China, at least 20 bridges with UHPC composite decks had been built as of 2019 [57]. Several UHPC bridges have also been built in France, Switzerland, South Korea, and other parts of the world [44]. Overall, the use of UHPC in bridge superstructures allows for the design of slender cross-sections, which leads to reduced dead loads that allow for the construction of longer spans. However, some knowledge gaps result in the lack of complete design guidelines and standards for UHPC structures, which has limited its wide application. Considering the increasing amount of research in this field, it can be expected that a significantly larger number of UHPC bridges will be constructed in the coming years [58].



Figure 1.3: Bridges with UHPC applications in the United States [59]

While UHPC offers enhanced mechanical properties in ambient conditions, its performance under elevated temperatures has raised concerns in the field of fire safety. Previous studies have shown that UHPC structures do not present the same level of fire resistance as conventional concrete members [60,61]. At high temperatures, UHPC experiences fast degradation of its mechanical properties and is highly susceptible to fire induced spalling [62], which is the breaking up of surface layers during fire exposure. Such spalling can expose internal layers of concrete, reinforcing bars or prestressing strands to higher temperatures, even at early stages of fire exposure [63]. The occurrence of spalling is the result of internal tensile stresses from pore pressure build-up during free water evaporation and development of differential thermal gradient in the concrete section [64]. It is a complex phenomenon, considered stochastic in nature and influenced by various factors. Due to its very compact microstructure and low permeability, UHPC is more prone to such spalling, since water vapor cannot freely dissipate from the concrete section [65,66]. Moreover, the high moisture content of concrete members in the harsher outdoor environment, combined with the high thermal gradients in bridge fire scenarios, produce ideal conditions for occurrence of fire-induced spalling in concrete bridge members [32,67].

1.5. Research Approach

The research topic addressed in this dissertation includes three interrelated broader topics: fire safety, bridge girders, and concrete. Fire safety is becoming a critical topic of consideration in infrastructure design due to the high severity of petrol-based fires near bridges. On the other hand, the design of modern concrete bridge members is made with optimized and slenderer cross-sectional shapes. Besides, there is an increasing interest in the use of superior concrete products, such as UHPC, to increase the durability and improve the design of concrete bridges. However, the use of concretes of higher strength and slender concrete sections reduces the fire resistance of concrete members. The interrelation between these three topics form the foundation for comprehending the performance of concrete bridge girders under fire conditions through a combination of material science, fire safety, and structural engineering.

1.5.1. Hypothesis

This study is developed based on the following research hypothesis: “Modern bridge girders have slender cross sections and are made with superior concrete products for improved durability and design efficiency. Exposure to bridge fire conditions lead to concentration of heat in their web and fast degradation of their shear capacity. Thus, the fire performance of concrete girders is fundamentally different than building members and require assessment with due consideration to specific temperature-dependent material properties and realistic fire exposure.”

1.5.2. Objectives

The primary objective of this dissertation is to develop a comprehensive understanding of the response of concrete bridge girders exposed to fires and to formulate recommendations for their fire design. This study systematically addresses the following specific objectives:

1. Carry out a state-of-the-art review on the characteristics of bridge fires and on the behavior of concrete bridge girders at elevated temperatures. This includes reviewing studies on fire resistance tests and numerical studies carried out on concrete members, as well as on the effect of temperature on UHPC material properties.
2. Conduct material property tests to evaluate specific properties of concrete at elevated temperatures:
 - a) Undertake pore pressure measurements on concrete specimens during heating to analyze the effect of pore pressure build-up mechanism on fire induced spalling.
 - b) Undertake direct shear strength tests on UHPC specimens exposed to different levels of temperature to quantify the effect of temperature on the shear strength of UHPC.
3. Develop a numerical tool to trace the response of concrete bridge girders under fire:
 - a) Incorporate temperature-dependent material properties of constituent materials (concrete and steel) for heat transfer and stress analyzes, as well as the non-uniform temperature distribution of bridge fire models.
 - b) Validate the developed numerical model by comparing thermal and structural predictions from the model with results measured in fire tests.
4. Conduct a set of parametric studies using the developed numerical model to quantify the influence of various critical factors on the fire performance of concrete bridge girders. Also, illustrate the applicability of the model for real bridge fire evaluations.
5. Formulate design guidelines for fire resistance design of concrete bridge girders based on the results generated from these studies.

1.5.3. Methodology

The research objectives stated above will be addressed through a set of experimental and numerical studies. Experiments will be carried out on concrete specimens to measure pore pressure build-up at elevated temperatures and evaluate the susceptibility of UHPC structures to fire induced spalling. Additionally, direct shear strength tests on UHPC specimens will be carried out to establish a rational approach for evaluation of shear capacity degradation at high temperatures.

As part of the numerical studies, a finite element-based model is developed in ABAQUS to evaluate the fire response of concrete bridge girders. The thermo-mechanical analysis takes into consideration non-linear material (thermal and mechanical properties) models for concrete and steel. Additionally, non-uniform temperature fields are established through fire dynamics simulations carried in FDS-PyroSim to consider realistic fire conditions of burning vehicles under a bridge. The model is validated using data from fire resistance tests on concrete members.

The validated numerical model is used to conduct a case study on the fire-induced collapse of a bridge, as well as on parametric studies to quantify the effect of critical factors on the fire performance of concrete bridge girders. Finally, results from parametric studies are utilized to propose guidelines for fire design of modern concrete bridge girders.

1.5.4. Dissertation Layout

This dissertation is organized in eight chapters. Background information on the proposed research topic and motivation, as well as research objectives are discussed in this first chapter. Chapter 2 provides a detailed state-of-the-art review of the advancements in bridge engineering, with a focus on modern concrete bridge girders, material properties of UHPC at elevated temperatures, and on the fire resistance of concrete bridge girders. Chapter 3 presents the development of experimental studies, which included the pore pressure build-up measurements

and shear strength degradation at elevated temperatures. In Chapter 4, the development of a numerical tool for evaluating the fire resistance of concrete bridge girders is presented, including details on its development and validation. The applicability of this tool is demonstrated in Chapter 5 through a comprehensive evaluation of a real bridge fire incident. In Chapter 6, parametric studies have been carried out to evaluate the influence on different parameters on the fire resistance of concrete bridge girders. Based on the results from these studies, design recommendations for fire evaluation and design of concrete bridge girders under fire conditions are outlined in Chapter 7. Finally, Chapter 8 summarizes key findings from this dissertation, discusses its research impact and provides recommendations for future work.

2. STATE-OF-THE-ART REVIEW

2.1. General

Over the last decades, the majority of research in structural fire engineering has focused on building members subjected to standard fire conditions. Less attention has been given to bridge structures, especially for concrete bridge members under realistic fire conditions. The rapid rise of hazardous materials transportation in urban areas has resulted in an increased number of bridge fire incidents, often leading to severe consequences. As a result, concerns regarding the fire safety of bridge structures have intensified. Concurrently, advances in concrete technology have led to the development of newer concretes, such as High-Strength Concrete (HSC) and Ultra-High-Performance Concrete (UHPC), which have gained popularity in the bridge industry due to its higher strength and durability characteristics. However, the fire response of UHPC structures is still a concern due to its high degradation at elevated temperatures and susceptibility to fire induced spalling. This chapter provides a state-of-the-art review on the advancements in bridge engineering, with a special focus on the design of UHPC bridge girders. Previous studies on the behavior of UHPC at elevated temperatures, both at material and structural level, as well on the characteristics of bridge fires, are reviewed. The fire problem in concrete bridge girders is also discussed, with special attention to the factors of influence, as well as approaches used for fire resistance evaluation and previous studies on the fire resistance of concrete bridge girders.

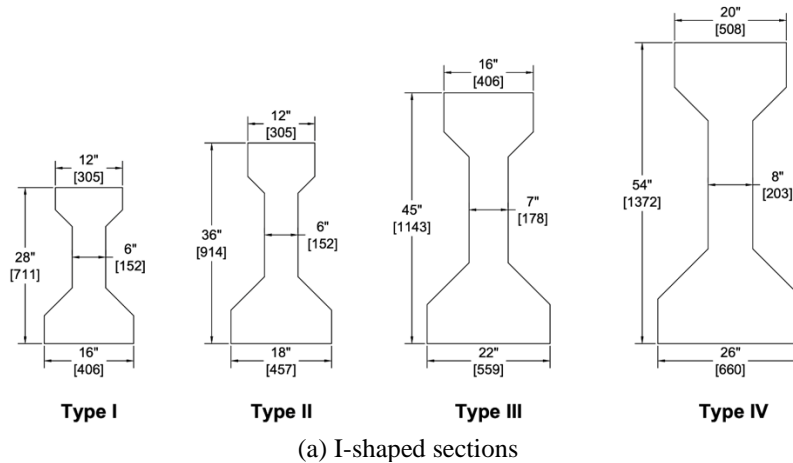
2.2. Advancements in Bridge Engineering

The design of bridge structures in the United States follows the specifications from the American Association of State Highway and Transportation Officials (AASHTO) LRFD Bridge Design Manual. For concrete bridge girders, the axial, flexural and shear forces have to be considered when analyzing the mechanics of both prestressed and non-prestressed concrete

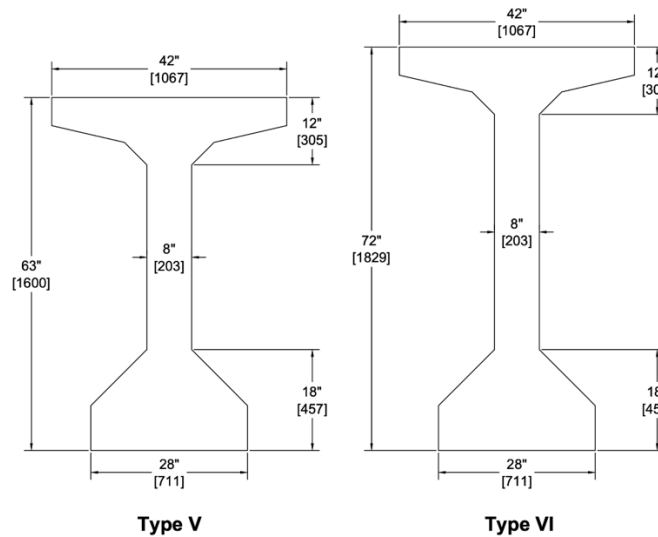
members. In the case of prestressed members, prestressing strands are used to counteract tensile stresses and associated cracking, allowing it to overcome longer spans. I-shaped sections are also commonly used in concrete bridge girders due to its compact and efficient cross-sectional shape. These sections place the majority of the material in the areas (flanges) where it most effectively resists bending stresses, resulting in a high strength-to-weight ratio. To facilitate the design and construction of prestressed concrete bridges, optimized standard cross-sectional shapes have been created. They allow an optimization of the design process and easy fabrication of concrete girders in precast plants, accelerating the construction of concrete bridges. Throughout the years, sections and design methods evolved as new materials have been introduced to the construction industry, including prestressing strands and concretes of higher strength. To make use of superior materials such as UHPC, specific methods are being developed, as presented herein.

2.2.1. Modern Cross-Sectional Shapes

In the 1950's, the AASHTO together with the Precast/Prestressed Concrete institute (PCI) and the Federal Highway Administration (FHWA) published a set of standard sections for prestressed concrete bridge girders that have been commonly used in highway bridge projects in the United States. These sections are suitable for projects with span ranges varying from 15 to over 48 meters and present a span-to-depth ratio of approximately 0.04-0.05 [68]. They are illustrated in Figure 2.1 and include both I-shaped (types I-IV) and bulb-tee sections (types V-VI). Bulb-tee sections have a bulbous bottom flange that accommodates additional prestressing strands, while the wider top flange can better withstand compressive stresses on the upper part of the girder. Based on this concept, other series of standardized sections have been developed by the department of transportation from different states in conjunction with local precasters to support the development of optimized designs.



(a) I-shaped sections



(b) Bulb-tee sections

Figure 2.1: Standardized AASHTO-PCI bridge girder cross-sections

Over the years, various shapes and sizes of structural elements have evolved to meet specific construction requirements [69]. With the increasing use of prestressed concrete in bridge construction, the need to design sections capable of spanning even greater distances became apparent. This led to the introduction of wide-flanged sections, specifically engineered for bridge spans of up to 60 meters [68]. One notable example of such a girder section is the Nebraska University (NU) girders, which were developed in the early 1990's through a PCI research grant [70]. These innovative girders feature larger flanges to accommodate a greater number of strands or tendons, enabling the construction of longer bridge spans while minimizing the overall volume

of concrete required. The larger bottom bulb of these girders can house nearly 40% more strands compared to the standard bulb-tee design. This, in turn, facilitates improved girder spacing and a reduction in the number of girder lines needed for a given span. These sections have been developed for both pretensioning and combined pre- and posttensioning applications.

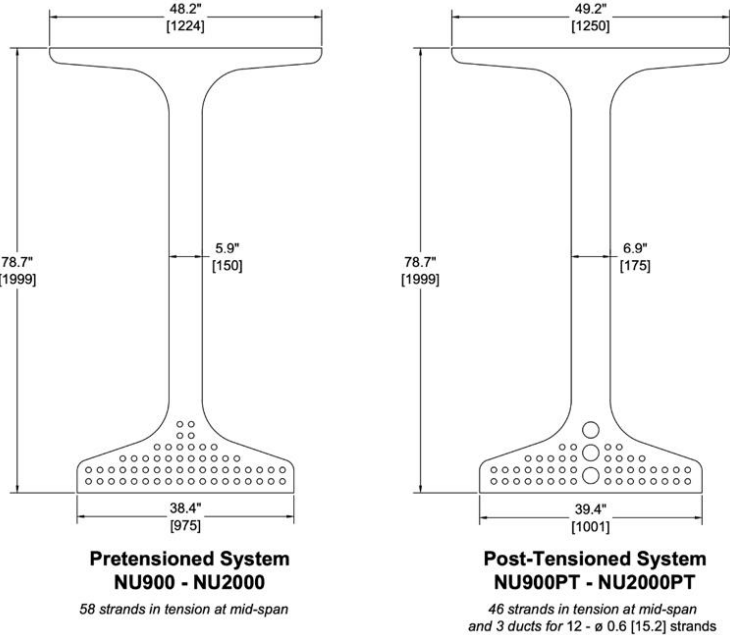


Figure 2.2: Nebraska University wide-flanged sections

Despite the significant effort devoted throughout the last few decades to develop optimized girder sections for prestressed concrete bridges, their adaptability to bridges made with newer concrete types such as UHPC bridge girders is constrained. This is attributed to the fact that UHPC has a significantly higher unit cost when compared to conventional concrete, and therefore, sections should be even more optimized to take advantage of its superior mechanical properties in order to become a competitive material in bridge superstructure. As part of an extensive research program focused on the mechanical and structural behavior of UHPC in bridge applications, the FHWA has proposed an optimized section inspired on the PCI bridge design example of a Florida I-beam FIB-102 [71]. This section can span a maximum of 61 m with high strength concrete. In comparison to the FIB-102, the proposed UHPC girder exhibits a similar cross-sectional area and

weight per unit length. It is reinforced with 95 strands of 17.8 mm diameter, with 3 strands positioned in the top flange and 92 strands positioned in the bottom flange, stacked in 7 layers. The strands are spaced at a minimum distance of 51 mm center-to-center, ensuring a minimum cover thickness of 51 mm. As a result, the UHPC girder is able to span 91 m, as opposed to 61 m for conventional concrete, with a similar weight per unit length.

Another section type for UHPC bridge girders has been proposed in the second phase of a research report published by the PCI [72]. In this project, a design concept known as the "decked I-beam" is proposed, integrating an I-shaped girder with a deck slab in a single component. The decked slab extends outward from the top flange of the girder and serves as the bridge deck itself, providing a driving surface for vehicles, as illustrated in Figure 2.3. To enhance the load-carrying capacity of the deck while minimizing the amount of concrete used, parallel ribs are integrated into the decked (ribbed) slab. This system has been used to develop a family of UHPC bridge girders for the state of Nebraska by adapting the girder depth to increase its stiffness and be used in longer span lengths [73]. The authors claim that the proposed section is adequate for cold climates, as UHPC presents higher durability and that it can present an accelerated construction process.

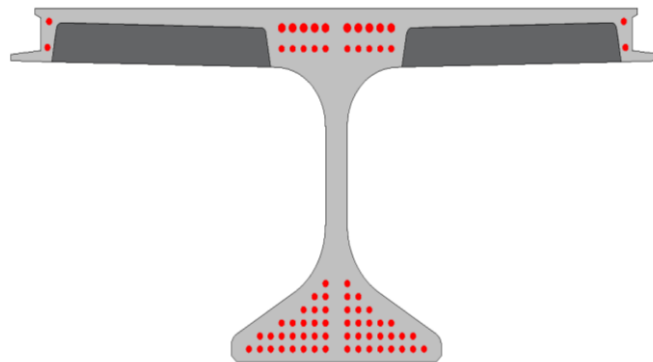


Figure 2.3: Proposed decked I-beam section for UHPC bridge girders

2.2.2. Design Methods and Procedures

The design of concrete structures in the United States is based on the specifications of ACI 318-19 Building Code Requirements for Structural Concrete [43] and AASHTO LRFD Bridge Design Specifications (BDS) [10]. These specifications assume that flexural strength is governed by the yielding of steel and the crushing of concrete, relying on well-established mechanical models that do not consider concrete's tensile strength [68]. However, these methods are not applicable to UHPC structures due to fundamental differences in its mechanical properties and, consequently, on the structural response of UHPC members. The intrinsically high compressive strength and tensile strain-hardening characteristics of UHPC contribute to resisting bending and shear stresses, resulting in different failure modes, and should be considered in the design. To address these differences, the AASHTO Committee on Bridges and Structures is working on the development of a guide specification for structural design with UHPC to supplement their bridge design manual [74]. Additionally, research reports from other institutions, such as the PCI also provide some guidance for the design of UHPC bridge girders [72]. Internationally, other documents have also been made available for design engineers, such as the French National Addition to Eurocode 2 [75] and the Canadian Highway Bridge Design Code [76].

2.2.2.1. Flexural Capacity of UHPC Beams and Girders

The flexural capacity of a concrete beam at ambient conditions is typically estimated by applying principles of cross-sectional strain compatibility. Mechanical models (stress-strain relations) of concrete and steel are employed to determine the stresses generated on strained cross-sections and calculate the flexural strength based on the equilibrium of forces. In conventional concrete beams, the tensile strength of concrete is ignored while the steel reinforcement carries all

the tensile stresses. For simplification, a calibrated rectangular compression stress block with height a is used to calculate the flexural strength M_n based on stress equilibrium:

$$a = \frac{A_s f_y}{\beta_1 f'_c b} \quad (2.1)$$

$$M_n = A_s f_y \left(d - \frac{a}{2} \right) \quad (2.2)$$

where A_s is the area of reinforcing steel, f_y is the yield stress of reinforcing steel, d is the effective depth of the section, and a is the depth of the rectangular stress block and can be evaluated by applying equilibrium principles. The coefficient β_1 is used to replace the actual compressive stress distribution by an equivalent one of simple rectangular outline, which is usually considered 0.85 for rectangular beams made of normal strength concrete.

The analysis of beams made with discrete steel fiber reinforcement, including UHPC, takes into consideration the contribution of concrete's tensile strength to carry the tensile stresses on the bottom of the beam. Some analytical methods have also been proposed to determine the flexural capacity of UHPC members based on the strain compatibility approach, as illustrated in Figure 2.4. The procedure specified by ACI 544 [77] for design of fiber reinforced concrete beams can be used to analyze the flexural capacity of UHPC beams, as demonstrated by Shafieifar et al.[78]. This method takes into consideration the contribution of the tensile stresses in concrete as uniformly distributed over an area of height $(h - e)$. The flexural capacity of a fiber reinforced member $M_{n,FR}$ is calculated according to Equation (2.3).

$$M_{n,FR} = A_s f_y \left(d - \frac{a}{2} \right) + f_t b (h - e) \left(\frac{h + e - a}{2} \right) \quad (2.3)$$

The beam height, depth, and width are represented by h , d , and b , respectively; A_s refer to the cross-sectional area of rebars and f_y to the yield strength of steel; a is the height of the concrete compression block; c is the distance from the top fiber to the neutral axis; and e is the distance

from the top fiber to the beginning of the concrete tension block. This method considers a maximum compressive strain at the top fiber of 0.003 and the depth of the of the neutral axis (c) is calculated by considering equilibrium of forces at the cross-section.

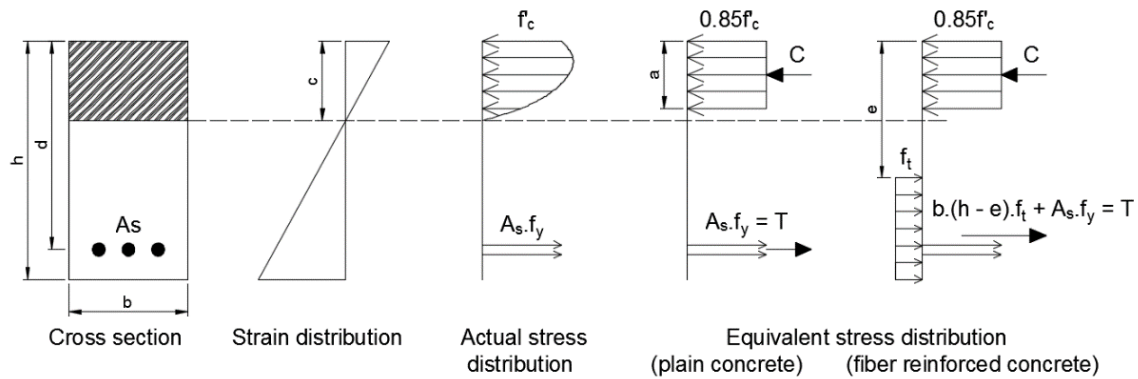


Figure 2.4: Strain and flexural stresses distribution assumption in a reinforced concrete beam

The French and Canadian design approaches consider a linear strain variation and a triangular compressive stress block for UHPC. In contrast, these methods present different stress distributions in the concrete tension zone. Both limit the concrete compressive strain and the steel tensile strain based on UHPC crushing and reinforcing steel rupture, respectively. According to El-Helou and Graybeal [79], although these approaches can predict some aspects of the structural response of UHPC beams, they do not account for the different behavior, these members exhibit before and after crack localization. This could lead to excessive deflections and hinging of the beam around the localized crack in some cases. Another approach proposed by the FHWA [80], considers the flexural behaviors and expected failure modes associated with UHPC members by restricting the tensile strain in beam sections to the UHPC strain at crack localization. The method includes bilinear elastic-plastic relations for steel and concrete (in tension and compression). The nominal flexural capacity is taken as the lesser of the curvature values associated with strain limits of UHPC and steel on the sectional compatibility analysis.

2.2.2.2. Shear Capacity of UHPC Beams and Girders

The shear capacity (V_n) of a conventional reinforced concrete beam is computed by considering the contribution of concrete (V_c) and shear reinforcement in web (V_s) to the shear strength, as shown in Equation (2.4) and illustrated in Figure 2.5. The shear strength contribution of the concrete (including the contributions from aggregate interlock V_i , dowel action of the main reinforcing bars V_d , and that of the uncracked concrete V_{cz}) can be calculated using Equation (2.5), according to ACI 318 [43]. This equation takes into consideration the member-factored axial load (N_u) and its gross area (A_g). ρ_w is the longitudinal reinforcement ratio and λ is a modification factor reflecting the lower tensile strength of lightweight concrete and is assumed to be 1.0 for normal weight concrete. The shear strength contribution of the web reinforcement is calculated using Equation (2.6) where A_v is the area of shear rebars, f_{yt} is the yield strength of the steel, and s is the spacing between them.

$$V_n = V_c + V_s \quad (2.4)$$

$$V_c = \left(2 \lambda \sqrt{f'_c} + \frac{N_u}{6 A_g} \right) b_w d \quad (\text{With reinforcement}) \quad (2.5)$$

$$V_c = \left(8 \lambda_s \lambda (\rho_w)^{1/3} \sqrt{f'_c} + \frac{N_u}{6 A_g} \right) b_w d \quad (\text{Without reinforcement})$$

$$V_s = \frac{A_v f_{yt} d}{s} \quad (2.6)$$

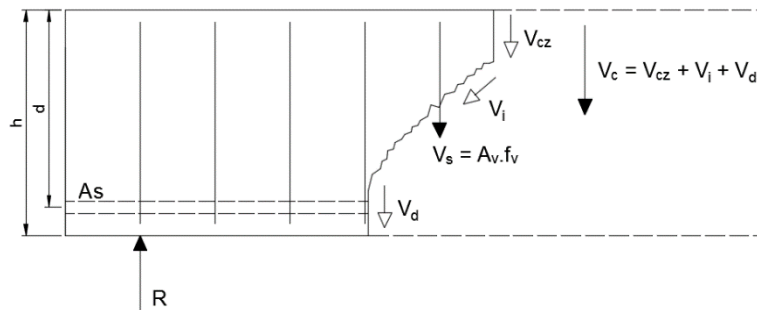


Figure 2.5: Forces at a diagonal crack in a concrete beam with stirrups

For concrete bridge girders, AASHTO LRFD BDS [10] incorporates the simplified version of the Modified Compression-Field Theory (MCFT), known as the SMCFT (Simplified MCFT), which was derived by Bentz et al. [81]. While the ACI 318 is based on empirical equations derived from extensive testing, the AASHTO method is a more mechanistic approach, offering a more rational design. Both approaches can be simplified or detailed, taking into account the effect of prestress and other parameters into the shear capacity calculations.

For fiber reinforced concrete, the shear strength contribution of the steel fibers in UHPC (V_f) is added as a third component to Equation (2.4). This is the procedure adopted in some design guidelines and recommendations, such as the French National Addition to the Eurocode 2 [75] and the Canadian Highway Bridge Design Code [76]. In the French method, V_f can be calculated using Equation (2.7), in which $\sigma_{Rd,f}$ is the mean value of the post-cracking strength perpendicular to the shear crack of inclination θ ; b_w is the width of the web, and z is the effective shear depth. The value of $\sigma_{Rd,f}$ is obtained from uniaxial tensile stress-strain results derived from a specified inverse analysis of the results of a flexural prism test and includes a partial safety factor and an orientation factor. The inclination angle of the principal compression stress with respect to the longitudinal axis is determined from elastic stress transformation evaluated at the center of gravity of the beam at the expected force demand at the ultimate limit state. The value of θ is taken as equal to or greater than 30° .

$$V_f = \sigma_{Rd,f} b_w z \cos \theta \quad (2.7)$$

The French shear design methodology for beams concludes by requiring that the stress in the compression field be lower than the compressive resistance limit and the flexural reinforcement be able to accommodate the increase in tensile force due to the applied shear force.

2.2.3. Projects Utilizing UHPC in Bridge Superstructures

While there has been significant interest and investment on the development of UHPC for bridge applications over the last decades, its use in bridge superstructure members is limited. Built in 1997, the Sherbrooke Pedestrian Overpass in Sherbrooke, Quebec, Canada, is considered the first UHPC bridge in the world. It consists of a precast, post-tensioned space truss made with formerly known reactive powder concrete and spans 60 m over the Magog River [82]. However, the Bourg-Lès-Valence bridges in France are considered the first two UHPC road bridges in the world. These bridges are 20.5 and 22.5 m long and composed by five 889 mm-deep pi-shaped UHPC girders and were opened to the public in 2001 [83]. Both Canada and France built several other bridges in the years following these projects, as well as other countries in Asia and Europe. A wide variety of shapes and design solutions have been used in these projects, most commonly u-shaped and pi-shaped girders [84].

In the United States, only four bridges have been built using UHPC girders, as detailed in Table 2.1. The Mars Hill bridge in Iowa, the first application, features a 33.5 m single-span design consisting of three precast, prestressed 1,140 mm-deep bulb-tee beams [85]. Virginia's Route 624 bridge, comprising ten spans over Cat Point Creek, incorporates UHPC bulb-tees, each with a depth of 1,140 mm and a span length of 24.8 meters [86]. In Buchanan County, Iowa, extensive research by FHWA led to the construction of a UHPC bridge with pi-shaped girders, combining a unique cross-section with a central 15.6-meter-long span [87]. Lastly, the Hawkeye Bridge in Iowa employs K-UHPC, utilizing local materials, and features girders designed to be 1,600 mm wide, 711 mm deep, and 1320 mm long, with post-tensioning performed on longitudinal strands in the bottom of the girders, seven on each flange [88]. These projects collectively demonstrate the versatility and adaptability of UHPC technology in varying bridge construction scenarios. This

was made possible due to extensive research on UHPC mechanical behavior, both at material and structural levels, under ambient conditions. However, there is lack of data on fire response of UHPC structural members and this is mainly due to limited studies on the fire response of UHPC.

Table 2.1: Applications of UHPC bridge girders in the United States

Bridge / Location	Year	Bridge span length (m)	Section shape / Depth (mm)	UHPC	Reinforcement
Mars Hill Bridge Wapello County, IA	2006	33.5	I-shaped 1,14 mm	$f'_c = 206$ MPa With steel fibers	47 - $\varnothing 15.2$ mm low-relaxation prestressing strands – no shear reinforcement
Route 624 over Cat Point Creek Richmond County, VA	2008	24.8	I-shaped 1,143 mm	$f'_c = 215$ MPa $f'_t = 10.1$ MPa With steel fibers	No information available
Jakway Park Bridge Buchanan County, IA	2008	15.6	Pi-shaped 838 mm	$f'_c = 148$ MPa With steel fibers	9 - $\varnothing 15.2$ mm low-relaxation prestressing strands in each flange
Hawkeye Bridge Buchanan County, IA	2015	15.8	Pi-shaped 711 mm	$f'_c = 186$ MPa With steel fibers	7 - $\varnothing 15.2$ mm low-relaxation prestressing strands in each flange

2.3. UHPC at Elevated Temperatures

The successful and safe implementation of UHPC as a novel construction material for bridges relies on the thorough consideration of all factors that can influence its performance, including fire conditions. Over the last years, there has been some research interest on the fire performance of UHPC structures, mostly due to the fast degradation of its mechanical properties at elevated temperature, as well as its high vulnerability to fire-induced spalling. These studies have shown that UHPC undergoes a complex process of deterioration during heating, which is fundamentally different than in conventional concretes. The low porosity of UHPC, while advantageous with respect to strength and durability in ambient conditions, becomes a liability during heat exposure. It restricts the release of internal moisture and water vapor, leading to internal pressure buildup, which contributes to the occurrence of fire-induced explosive spalling. These processes lead to rapid degradation of its thermal and mechanical properties at elevated

temperatures, resulting in strength and stiffness loss and potentially compromising the integrity of UHPC members with reduced fire resistance. While these degradation processes are well understood for NSC and HSC, there have been limited studies on UHPC thermal characterization.

2.3.1. Temperature-Dependent Properties for UHPC

Temperature-dependent material properties are critical to determine how structural members will behave when exposed to elevated temperatures and to develop efficient fire protection measures. These properties can be grouped into three categories. The first consists in thermal properties, namely density, thermal conductivity, specific heat, and thermal expansion, which are used to trace the thermal response (temperature progression) of a member exposed to fire. The second category is of the mechanical properties, usually comprising of elastic modulus, compressive and tensile strength, and stress-strain response, which is used to determine the structural capacity of members exposed to elevated temperatures. Lastly, (fluid) transport properties indicate the ability of a concrete to let gases and fluids migrate through its porous system network, and usually includes porosity and permeability. These properties degrade with temperature as a result of load-induced thermal strain, as well as chemical and physical changes in the material microstructure.

Degradation of UHPC at elevated temperatures results from moisture evaporation, dehydration and decomposition of cementitious products, as well as transformations (phase changes) in aggregates. In conventional concretes, the primary changes in the cement paste are the evaporation of free water, dissociation of calcium hydroxide at 400°C, and of calcium-silicate-hydrate at different levels of temperature up to 900°C [89]. Due to its low water-to-cement ratio (lower than 0.25), UHPC presents higher contents of un-hydrated cement clinker, as well as lower amounts of low-density C-S-H and higher amounts of high and ultra-high-density C-S-H [90].

Additionally, the use of thermal and pressure curing (common in UHPC fabrication) results in the formation of xonotlite, a more stable form of C-S-H than tobermorite found in conventional concretes [91]. While tobermorite undergoes several processes of degradation at different levels of temperature from 20°C to 800°C, xonotlite experiences only one process around 775°C due to its better chemical organization [92]. Another important aspect of UHPC composition is the use of higher content of mineral admixtures, such as silica fume, which minimize the formation of portlandite (calcium hydroxide) [93]. In the aggregates, degradation is related to the nature of the rock (quartz, dolomite, etc.), which can lead to significant thermal expansion at elevated temperatures. Siliceous-based aggregates experience a volumetric expansion of 5.7% at 573°C due to a phase transformation from α to β form [94]. Carbonate and calcareous based aggregates experience transformation of calcium carbonate into lime between 600-800°C, respectively [95]. In summary, the rise in sectional temperature results in weakening of chemical bonds and a differential volumetric behavior (shrinkage of the cementitious paste and expansion of the aggregates). The combination of these processes creates internal stresses that lead to microcracking and changes material properties at elevated temperatures.

For conventional types of concrete, including normal-strength concrete (NSC) and high-strength concrete (HSC), thermal and mechanical properties at elevated temperatures have already been reported in several studies. They have also been included in standards and guidelines, such as Eurocode 2 [96] and the ASCE manual [97]. For UHPC, some temperature-dependent properties have also been investigated in previous studies. However, for being a novel structural material with limited research, these properties have not been incorporated in any code or standard yet.

2.3.1.1. Thermal Properties

From a review of the literature, test data on the high-temperature thermal properties of UHPC from seven studies have been compiled [98–104]. These properties include mass loss, thermal conductivity, specific heat, and thermal expansion. Generally, they are obtained through testing methods and procedures prescribed by ASTM or ISO standards. More comprehensive details on these methods can be found elsewhere [105]. In most cases, the test results are utilized to formulate best-fit equations and establish relationships to describe how a specific thermal property varies with increasing temperatures, which have been used when available.

Variation in UHPC density is presented in terms of mass loss in Figure 2.6, which is governed by moisture evaporation (up to 300°C) and dehydration of cement compounds (between 300°C and 500°C). After 500°C, mass loss tends to stabilize due to the low moisture content in UHPC specimens and any further mass loss can be attributed to degradation of aggregates, as reported by Kodur et al. [104]. Chen et al. [98] reported high levels of mass loss at lower levels of temperature, which can be attributed to higher moisture contents in the specimens. Likewise, variance from the different studies can result from differences between specimen compositions, test equipment and procedures employed in the tests. The relations reported by Xue et al. [99] presented a significant increase of mass loss after 500°C, which can also be attributed to variations in specimen composition and testing procedures.

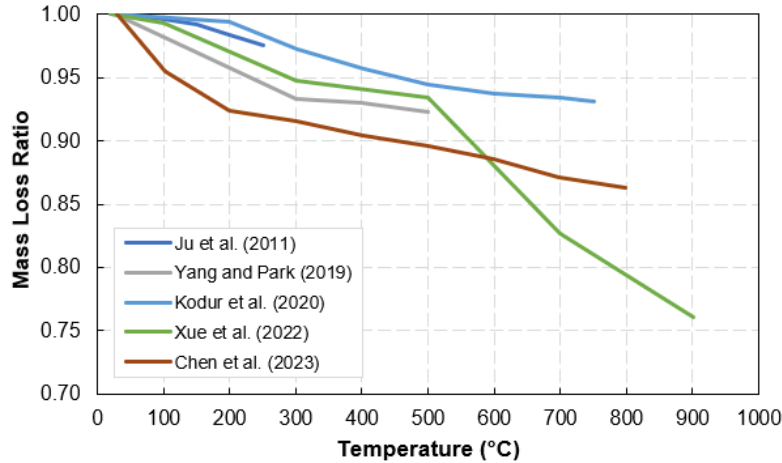


Figure 2.6: Comparison of UHPC mass loss obtained from different studies

Thermal conductivity represents the ability of a material to conduct heat and is defined in terms of a heat rate conducted through a unit area per unit temperature gradient. Conventional concretes present thermal conductivity in the range of 1.3-2.5 W/m-K, depending on the type of aggregate used in its composition. HSC tends to present slightly higher values than NSC due to its lower water-to-cement (w/c) and use of supplementary cementitious materials, such as slag and silica fume. For UHPC, thermal conductivity has been measured in even at higher levels, reaching almost 3 W/m-K at ambient conditions [104,106]. This is due to the fact that UHPC has a very compact matrix, with low porosity and low moisture content. Besides, UHPC usually includes metallic fibers that can contribute to heat conduction. With increase in temperature, thermal conductivity tends to decrease due to moisture variations and disintegration of the cementitious matrix, stabilizing for temperatures higher than 400°C, as shown in Figure 2.7.

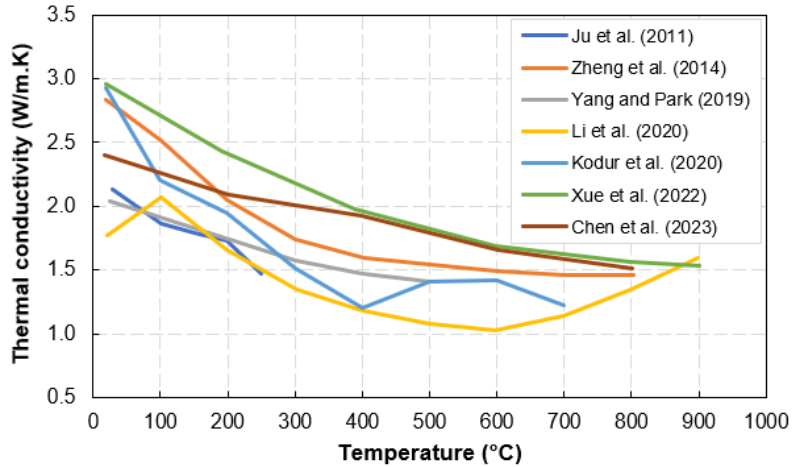


Figure 2.7: Comparison of UHPC thermal conductivity obtained from different studies

The amount of heat required to raise the temperature of a unit mass by one degree (Celsius or Kelvin) is measured in terms of specific heat, which is needed to determine the thermal mass. Specific heat is inversely proportional to thermal conductivity, which means that the higher the thermal conductivity, the lower the specific heat. From results reported in previous studies (Figure 2.8), there is little variation on this property with increasing temperatures. At certain temperature ranges evaporation of moisture leads to increased specific heat values, and aggregate phase transitions can generate peaks for some specific rock types. The specific heat peak at 600°C in the data from Xue et al. [99] can be attributed to addition of coarse aggregates in the mixture.

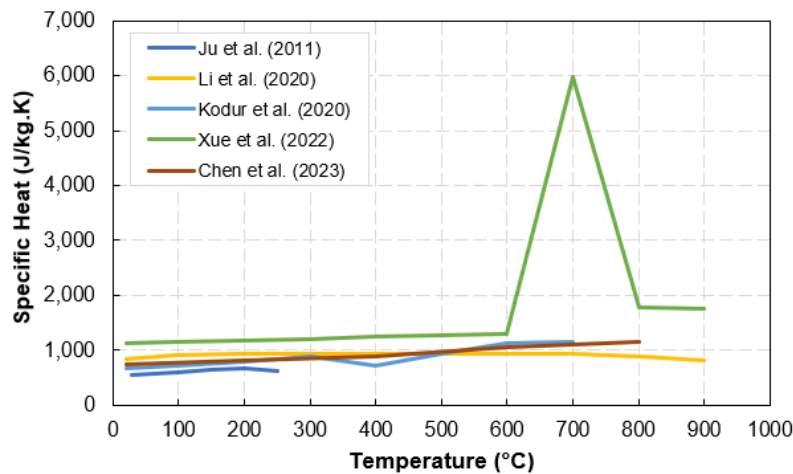


Figure 2.8: Comparison of UHPC specific heat obtained from different studies

Thermal expansion is used to describe the increase of size in a material due to rise of temperature as a result from heat energy absorption. Figure 2.9 presents a comparison between results obtained from different studies. Overall, it can be seen that thermal expansion increases almost linearly with the increase of temperature up to 600°C. After this level of temperature, some studies reported expansion reduction, as seen in the relations proposed by Kodur et al. [104], Xue et al. [99], and Li et al. [100]. These studies also reported challenges to measure thermal properties of UHPC at higher levels of temperature due to its high susceptibility to fire-induced spalling, which can damage testing equipment and compromise these measurements. For this reason, some studies were not able to report thermal relations at higher levels of temperature, as seen in the data reported by Ju et al. [103] and Yang and Park [101].

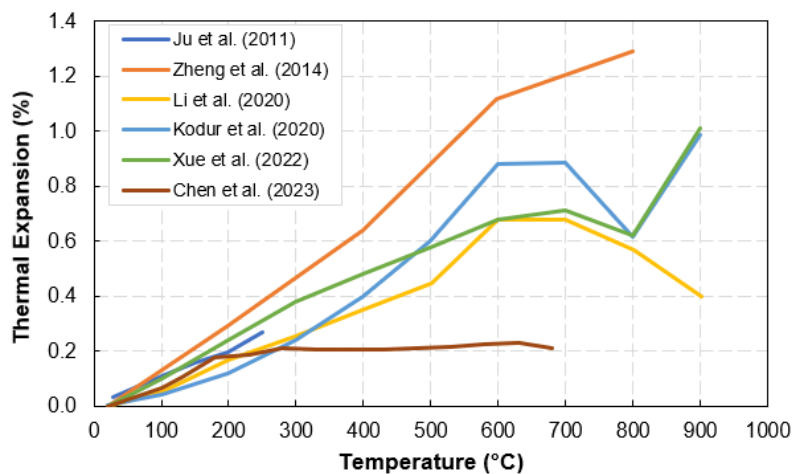


Figure 2.9: Comparison of UHPC thermal expansion obtained from different studies

2.3.1.2. Mechanical Properties

While studies on UHPC thermal properties at elevated temperatures are limited, research on its mechanical properties has received more attention. Results from six experimental studies test data on high-temperature mechanical properties of UHPC have been compiled here [107–112]. The properties investigated in these studies include elastic modulus, compressive strength, tensile strength, and flexural strength. Unlike thermal properties, there is no standard ASTM or ISO test

procedure for measuring the mechanical properties of concrete at elevated temperatures. A RILEM technical recommendation can be used to evaluate mechanical properties at elevated temperatures (up to 750°C) by extending test methods available for ambient conditions. Specimens can be tested in three testing regimes (unstressed, stressed, and residual), varying the order in which heat and load will be applied to the specimen. The procedure adopted in most studies is the unstressed regime, in which the specimen is first heated to the targeted temperature for a specific period of time and then tested mechanically while it is still hot. This procedure is typically preferred as it does not require sophisticated equipment while it still provides the strength of the hot specimen. More details on the test methods available for characterizing the mechanical properties and the testing regimes can be found elsewhere [105].

Figure 2.10 presents the variation in compressive strength with increase in temperature in UHPC specimens from different studies. In the tests conducted by Tai et al. [107], Zheng et al. [102] and Sanchayan and Foster [109], compressive strength increased in the 100-300°C temperature range. This can be attributed to the fact that this temperature caused thermal curing of the specimens, as a result of pozzolanic reactions of SCMs. On the other hand, other studies presented a decrease of strength of about 10% when exposed to temperatures as low as 100°C [110–112]. Overall, the results show that UHPC loses approximately 50% of its compressive strength when exposed to the temperature range of 500-700°C.

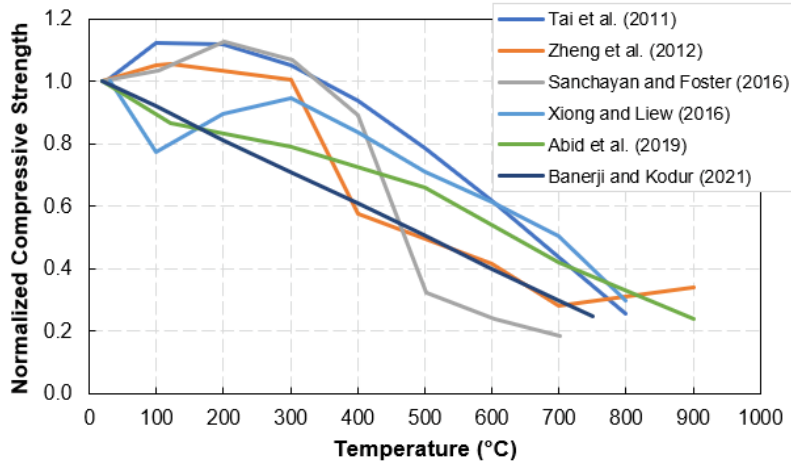


Figure 2.10: Comparison of UHPC compressive strength obtained from different studies

The effect of temperature in the elastic modulus of UHPC is also an important parameter for determining the fire behavior of UHPC structures. It has also been previously studied and their results are plotted in Figure 2.11 for comparison. Overall, they follow a similar decay trend throughout the entire temperature range, except for a single study that reported an increase of 10% in the elastic modulus for specimens exposed to 100°C. In some studies, it has been reported a reduction of 50% of the elastic modulus of UHPC when exposed to temperatures in the range of 250-450°C, which could lead to excessive deflections of structural members during fire exposure.

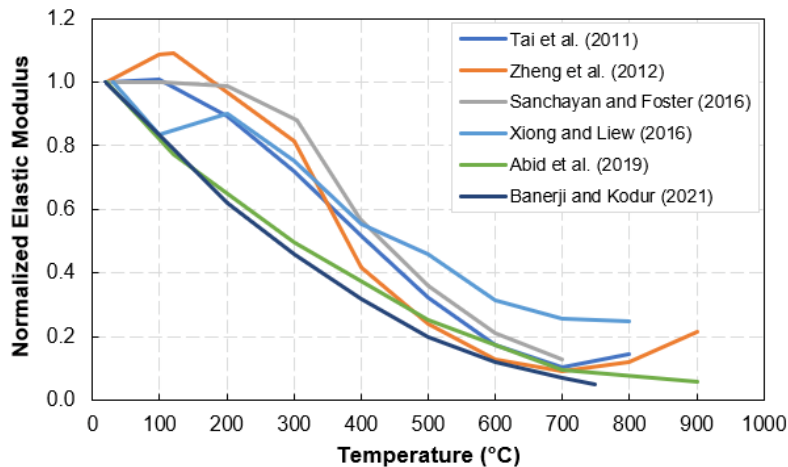


Figure 2.11: Comparison of UHPC elastic modulus obtained from different studies

Tensile strength is another important parameter for the design of UHPC members. However, the effect of temperature on this property has been less investigated. Figure 2.12 presents a summary of the results obtained in the four studies found in the literature. A linear decay of strength is observed on these results, indicating that UHPC loses approximately 50% of its tensile strength in the temperature range of 450-550°C.

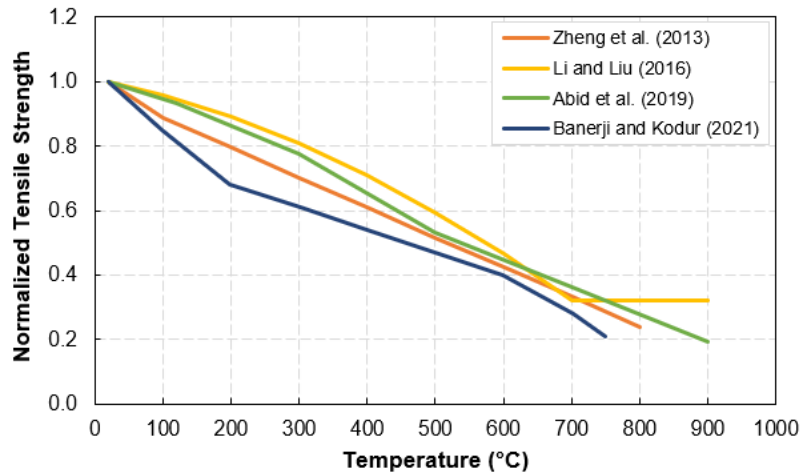


Figure 2.12: Comparison of UHPC tensile strength obtained from different studies

The presence of steel fibers makes UHPC a desirable structural material for flexural members. However, only two studies have been found in the literature with tests on the effect of temperature on the flexural strength of UHPC at the material level. These results are plotted in Figure 2.13 and demonstrate a big variance between them. Shear strength is another important property of UHPC, which has never been studied at elevated temperatures at the material level. Specific material properties, such as flexural and shear strength can provide insightful data for the design of UHPC members subjected predominantly to these types of stresses.

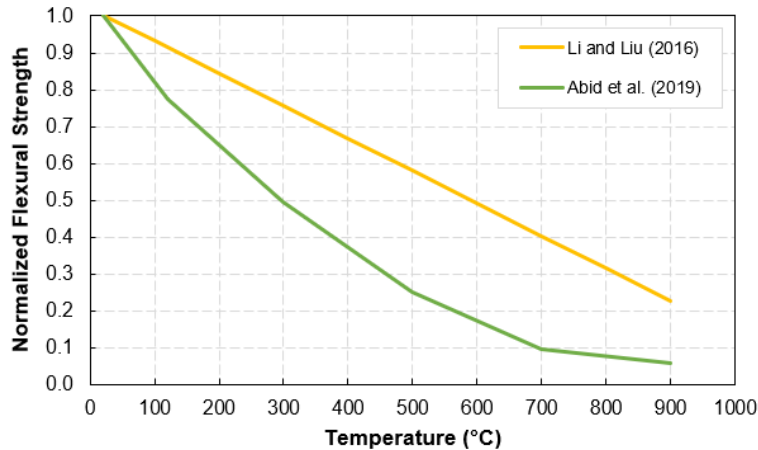


Figure 2.13: Comparison of UHPC flexural strength obtained from different studies

2.3.1.3. Fluid Transport Properties

Fluid transport properties are important for understanding fire induced spalling of UHPC, specifically in terms of the pore pressure build-up mechanism. These properties represent the ability of concrete to transport fluids and gases through its pore system network and are typically expressed in terms of porosity and permeability. There are different methods and procedures that can be used to measure these properties at ambient conditions, but none of them has been developed specifically to evaluate the behavior of hot specimens. In this case, specimens are typically tested in the residual regime, in which they are exposed to the targeted temperature level and after cooled down tested for the fluid transport property of interest.

Porosity of concrete is typically measured through mercury intrusion porosimetry, which provides the volume of pores in concrete, as well as its pore size distribution. Figure 2.14 presents the results obtained in tests carried out in different studies with specimens exposed to elevated temperatures [98,101–103,111]. Overall, the porosity of UHPC is reported to be equal or less than 5% at ambient conditions, with exception of one study that reported 10%. This is significantly lower than NSC and HSC specimens. The increase in porosity with temperature can be attributed to microcracking of concrete with temperature as a result of differential thermal expansions.

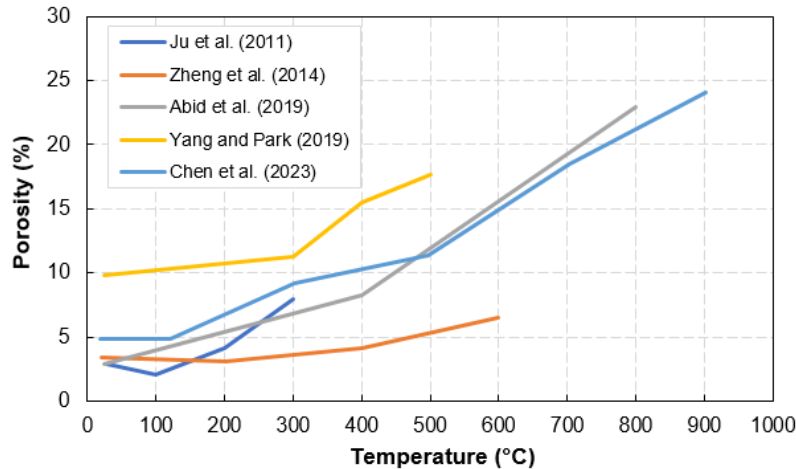


Figure 2.14: Comparison of UHPC porosity obtained from different studies

Permeability is a very important measure of the ability of concrete to let the passage of moisture and gases flow through its pore system network. The permeability of UHPC, HSC, and NSC is considered to be in the order of 10^{-18} , 10^{-17} , and 10^{-16} m², respectively [113,114]. Very few studies have reported results on these tests and most of them were limited to the temperature of 300°C, as shown in Figure 2.15. One recent study by Li et al. [115] has been able to measure UHPC permeability with hot specimens and at higher temperature levels. From the results obtained in these studies, it can be seen that UHPC permeability increases significantly with temperature. This is attributed to cracking of concrete microstructure, which connects previously unconnected pores and creates channels that result in the increase of the material permeability.

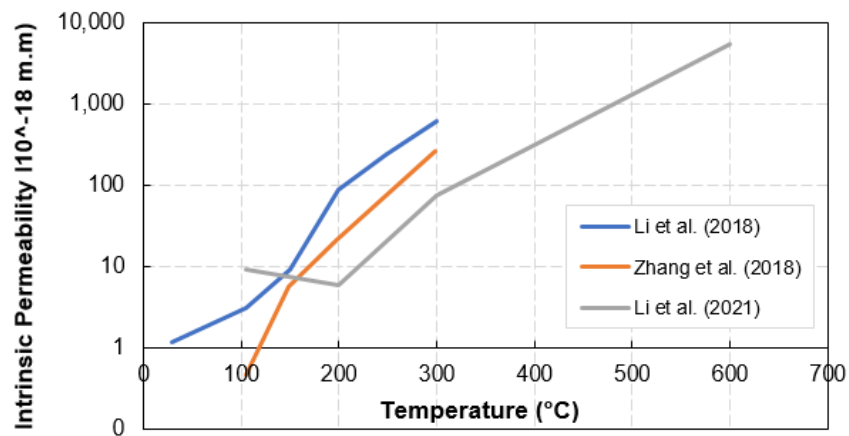
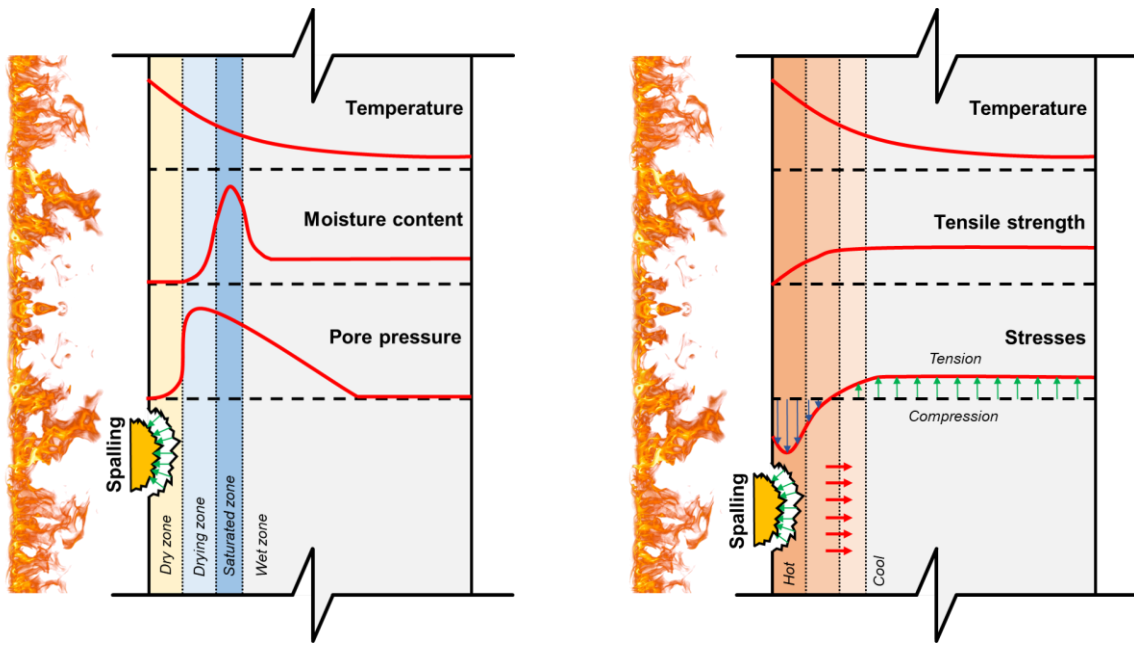


Figure 2.15: Comparison of UHPC permeability obtained from different studies

In the lack of intrinsic permeability test results, water sorptivity can provide an indicative metric of permeability. However, only one study in the literature has reported results for this type of test and it still requires more investigation in order to be related to the actual permeability coefficient used to measure fluid transportation inside of concrete [116]. Overall, measuring UHPC properties at elevated temperatures can be challenging due to its high susceptibility to fire induced spalling. Several studies have reported the difficulty in conducting these measurements, especially at higher levels of temperature (more than 600°C), due to loss of specimen or even damage to the equipment.

2.3.2. Fire-Induced Spalling

Spalling can occur in concrete structures when exposed to rapidly rising temperatures and it can occur at different levels of magnitude and intensity. There have been numerous studies in the literature over the last three decades investigating the mechanisms behind its occurrence and influencing factors. It is widely accepted that spalling results from internal tensile stresses generated by one or both of two main mechanisms: (a) pore pressure build-up during moisture evaporation; and (b) differential thermal expansion due to thermal gradients. As schematically illustrated in Figure 2.16, heating the surface of a concrete member creates high thermal gradients between the exposed surface and the inner regions. With increased temperatures, tensile strength of concrete gets reduced, making it more vulnerable to the increasing tensile stresses generated by both mechanisms. In the pore pressure build-up mechanism (a), tensile stresses are generated by moisture evaporation in the saturated layer, which will be discussed in more details in the following section, whereas in the differential thermal expansion mechanism (b), indirect tensile stresses arise between the hot, expanding surface and the cooler, contracted inner regions. The level of influence of each one of them is unknown, but both of them are believed to contribute to concrete spalling.



(a) Pore pressure build-up mechanism

(b) Differential thermal expansion

Figure 2.16: Schematic illustrating fire-induced spalling mechanism in concrete

Previous studies have shown that multiple factors influence the occurrence of spalling, including heating conditions, structural configuration, and concrete properties. Among different factors, concrete strength is believed to be one of the main influencing factors due to the high susceptibility of HSC and UHPC members to such spalling. Most researchers agree that this behavior derives from the low permeability of these concretes, which difficult the release of water vapor during moisture evaporation and result in pore pressure build-up. Besides, the inclusion of fibers, especially polypropylene, has shown to be effective in mitigating or reducing spalling.

Currently, there is not a specific test method to evaluate fire induced spalling in concrete. Some researchers have employed tests both at the material and structural level to evaluate different parameters. It is commonly agreed that real scale tests provide a more realistic response of the various factors that influence its occurrence, as some influencing factors cannot be scaled down. However, small scale tests can be used to measure specific properties or simulate the behavior of a portion of a structure in order to obtain insights on the magnitude of specific properties.

2.3.2.1. Pore Pressure Build-Up

Pore pressure build-up (also known as hygro-thermal mechanism) is considered one of the main governing processes of fire induced spalling [117–120]. This mechanism operates by transforming free water and physically bound water into steam at high temperatures. As this expansion happens within the concrete pores, it creates pore pressure, which manifests as tensile stresses. If these stresses, combined with other thermal stresses developed in the concrete during heating, surpass the tensile strength of concrete, fragments of concrete detach from the member's surface [65,121,122].

The magnitude of stresses induced by pore pressure buildup depends on the heating conditions, moisture migration and evaporation within concrete [63,89,123,124]. As temperatures rise and water evaporates, a pressure gradient forms, driving water vapor both inward and outward through the concrete member [65,125]. Water vapor migrating through the network of concrete pores condenses upon reaching cooler regions, forming a saturated layer known as a "moisture clog" [120,126,127]. This clog impedes further inward vapor migration [128,129]. With continued heating, the moisture clog eventually reaches boiling temperature, initiating evaporation. This process creates high hydraulic pressures in concrete pores at the front of the moisture clog, as illustrated in Figure 2.16 (a) [130].

The fluid transport characteristics of concrete, such as porosity and permeability, play crucial roles in these processes [64,131–133]. Concretes with lower porosity offer less space for water evaporation [134], and those with lower permeability hinder water vapor movement through their pore networks [115]. Concrete's tensile strength also influences its ability to resist pore pressure release and susceptibility to damage [135], which is particularly challenging in High Strength Concrete (HSC) and Ultra-High Performance Concrete (UHPC) due to their densely

packed microstructure [62,136–140]. Several fire resistance tests have highlighted that HSC and UHPC structures are highly prone to fire-induced spalling, primarily due to their low permeability that restricts water vapor release and leads to pore pressure buildup [110,139,141–143]. To mitigate this issue, previous research has shown the effectiveness of incorporating fibers into concrete to reduce pore pressure and enhance resistance to fire-induced spalling [115,144–146]. Polypropylene fibers, in particular, have proven effective because their high thermal dilation and low melting temperature (approximately 160°C) contribute to increased concrete permeability. The differential thermal expansion of these fibers induces microcracking around their tunnels, providing pathways for water vapor release [115]. Alternatively, the melted polypropylene fibers can be absorbed by the cementitious matrix, creating channels through which water vapor can migrate and evaporate [145,147].

Data on stress evolution from pore pressure buildup in concrete during heating is necessary for estimating the spalling risk in concrete structures. In one of the pioneering studies, Kalifa et al. [65,144] introduced the PTM (pore pressure, temperature, and mass) test, showing that HSC specimens develop higher peak pressures compared to conventional concretes. This study also demonstrated that increasing polypropylene fiber content reduces peak pressure, a finding corroborated by other studies [118,119,148,149]. It has been observed that peak pressure occurs at varying distances from the heating surface as heating time increases, and that polypropylene fibers facilitate moisture penetration into deeper concrete regions, delaying peak pressure occurrence [150,151]. In UHPC, Ozawa et al. [146] measured pore pressures as high as 11 MPa in specimens containing only steel fibers and exposed to the standard fire curve. Other studies have confirmed the positive effects of polypropylene fibers and coarse aggregates in reducing pore pressure and spalling depth in UHPC specimens [140,147]. However, relatively low pore pressures

(less than 2 MPa) have generally been reported in UHPC [147,151,152]. This might be due to instrumentation issues that fail to capture peak pressure, as well as the development of cracks and temperature-induced spalling in the specimens, preventing the measurement of realistic pressure magnitudes.

Measuring pore pressure during rapid heating is a challenge due to high temperature gradients and explosive spalling, which can damage pressure sensors and prevent data acquisition throughout the entire process [105]. To address this, pioneering studies introduced the idea of guiding pore pressure from the concrete specimen to an external pressure gauge located outside the furnace [65,125,153]. Over the past two decades, this concept has been employed in various experimental programs [140,146,147,149,154–156]. However, there is no standardized testing method for pore pressure measurements. Consequently, some researchers have developed their own equipment and procedures, resulting in inconsistent test setups and methods. Key differences include the type of gauge head used to capture steam from concrete, the means of transferring pressure to the sensor, the heating rate, and the maximum temperature during the test [117,155]. Recently, many studies have effectively used sintered metal heads attached to the end of a steel pipe filled with silicon oil to transfer pressure from the specimen to the sensor [65,132,149,154,157]. Nonetheless, these studies still vary in other test parameters, such as heating procedures and specimen dimensions, leading to significant differences in measured pore pressure values [117,155].

2.3.3. Structural Behavior of UHPC Members at Elevated Temperatures

While the characterization of material properties at elevated temperatures is important for deriving constitutive relations and to understand the effect of temperature on specific properties, structural level evaluations hold significant importance for ensuring a comprehensive

understanding of the fire response of UHPC structures. Extensive research has been carried out over the last few years to evaluate the fire resistance of NSC and HSC structures, particularly on concrete columns. These studies highlighted critical factors governing the fire behavior of concrete structures and resulted in fire design provisions to be included in codes and standards. As UHPC is a new structural material, there are very limited experimental studies on fire resistance of UHPC structures in the literature. Some research has also been conducted through numerical models, but there are many limitations due to the lack of proper validation or due consideration to all influencing factors, including fire-induced spalling, as discussed herein.

2.3.3.1. Experimental Studies

As a pioneer experimental study on the fire resistance of real-scale UHPC beams, Kahanji et al. [139] tested seven rectangular UHPC beams with a 100x200 mm cross-section and a 1,750 mm span. The simply supported beams were exposed to the standard fire curve while subjected to different load levels (20, 40, and 60% of the ultimate capacity at room temperature). Beams were made with UHPC containing 2% and 4% of steel fiber reinforcement and one of the beams contained 0.4% of polypropylene (PP) fiber reinforcement. The authors reported that all beams experienced spalling during fire tests. Besides, it was noted increased resistance to spalling in the beams with higher contents of steel fibers and no spalling in the beam with PP fibers. Some of the specimens that presented higher levels of spalling failed abruptly under shear mode and these specimens presented significantly lower fire resistance than the other beams.

Hou et al. [158,159] tested eight rectangular UHPC beams, four of them with supplementary fire insulation. The simply supported beams had a 200x400 mm cross-section and a 4,500 mm span. They were exposed to the standard fire curve (ISO 834) while subjected to different load levels (30 and 50% of the ultimate capacity at room temperature). As part of the test

variables, the authors varied rebar cover thickness (25 and 35 mm) and tested beams with 2% and 0.2% steel and polypropylene fibers, respectively. It was reported that the insulated beams did not experience any spalling during fire tests and that they resisted fire for additional 30 minutes when compared to uninsulated beams. The uninsulated beams experienced some spalling depending on the level of fiber reinforcement. Comparing with results of similar NSC beams, the authors noted that UHPC beams presented lower fire resistance under similar testing conditions.

At Michigan State University, Banerji et al.[61] tested four UHPC rectangular beams with 180x270 mm cross section and 3,658 mm span. All beams were reinforced with steel fibers and two of them also had PP fibers. Only one of the beams reinforced with PP fibers was reinforced with stirrups. They were exposed to design fire curves with a cooling phase starting at 90 minutes of fire exposure, while subjected to varying load levels (40, 45, 50, and 60%) applied in two points. It was observed high levels of explosive spalling in the compression zone (on the sides) of the beam sections and lower fire resistance than NSC and HSC beams. Also, it was reported that higher load levels induced cracking of the beams, aiding in pore pressure release and thus less spalling in those beams. The beam reinforced with PP fibers and stirrups did not fail and resisted the whole design fire exposure, which was attributed to the lower levels of fire-induced spalling.

To investigate the fire response of prestressed UHPC beams, Yan et al. [160] tested eight post-tensioned beams (two with unbonded tendons). This is the only experimental study on the fire resistance of prestressed UHPC beams found in the literature. The authors reported the successful use of hot-air curing to mitigate fire-induced spalling in all beams. The curing process consisted in the application of hot air on the surface of the members for two days after casting, gradually increasing the temperature from 50°C in the first 24 hours to 150°C over an additional 24 hours. As a result, the specimens presented a significantly lower moisture content in the surface

layers, reducing the chance of pore pressure build-up during heating. All beams were exposed to the standard fire curve and the testing variables included cover thickness (42.5, 52.5, and 62.5 mm) and load ratio (0.3 and 0.5). As expected the beams with higher concrete cover thickness and lower load ratio presented less deflections and higher fire resistance times. The authors did not report any significant spalling in all beams (resulting from steamed curing) and verified that the unbonded beams presented lower fire resistance due to the rapid loss of prestress during heating.

Following up with an investigation on the shear performance of UHPC beams at elevated temperatures, the study led by Yang et al. [161] presented results on fire resistance test on ten hot-air cured UHPC beams. Specimens were fabricated with varying reinforcement conditions (shear and longitudinal) and were exposed to the standard fire curve while subjected to different load ratios (0.25, 0.35, and 0.45) in varying shear span ratios (2.0 to 3.5). The authors reported lower fire resistance with increasing shear span ratios and with increasing load ratios. While this behavior is similar to what should be expected at ambient conditions, it should be noted that the specimens were partially insulated with fire protection to ensure shear failure at the load application location. Additionally, it was verified that increasing shear reinforcements (stirrups) and longitudinal reinforcement resulted in higher fire resistance due to reduction of shear failure brittleness in UHPC beams. This indicates that UHPC experiences fast degradation of its shear capacity at elevated temperatures and exhibit a different shear behavior than in ambient conditions.

Table 2.2 summarizes key parameters in the aforementioned experimental studies on UHPC beams at elevated temperatures. Overall, it can be seen that all specimens have been tested under similar conditions of fire exposure and loading conditions. The inclusion of PP fibers and the use of hot-air curing proved to be effective strategies to mitigate fire-induced spalling in UHPC at the structural level. Shear reinforcement (stirrups) appear to have a significant impact on the

overall fire performance of UHPC beams due to its contribution to prevent the advance of spalling as well as to resist the rapid degradation of shear strength at elevated temperatures. Other factors that can affect the fire response of UHPC beams, such as other fire exposure conditions, varying fiber dosage, and non-rectangular cross-sectional shapes (such as T- or I-shaped girders) are still to be studied to address all the influencing factors that can affect UHPC flexural members.

Table 2.2: Summary of experimental studies on UHPC beams at elevated temperatures

Authors (Year) / Reference	Cross-section / Span length	Reinforcement	UHPC	Loading / Fire exposure
Kahanji et al. (2016) [139]	100x200 mm 1,750 mm	Tensile: 2Ø16 mm	$f_c = 100.6-178.7$ MPa Fibers: 2% or 4% (ST) + 0.4% (PP)*	R=20-60% ISO 834
Hou et al. (2019) [158,159]	200x400 mm 4,500 mm	Tensile: 3Ø25 mm Comp.: 2Ø10 mm Shear: Ø8 mm @60 mm	$f_c = 121.8$ MPa Fibers: 2% (ST) + 0.2% (PP)	R=30-50% ISO 834 Insulation
Banerji et al. (2020) [61]	180x270 mm 3,658 mm	Tensile: 3Ø13 mm *Comp.: 2Ø10 mm *Shear: Ø10 mm @100 mm	$f_c = 145-173$ MPa Fibers: 1.5% (ST) + 0.11% (PP)*	R=40-60% Design fire
Yan et al. (2022) [160]	250x350 mm 6,000 mm	Tensile: 2Ø22 mm + 3Ø15 mm (HS) tendons Comp.: 2Ø18 mm Stirrups: Ø10 mm @100-150mm	$f_c = 158-176.8$ MPa Fibers: 2% (ST)	R=30-50% ISO 834
Yang et al. (2023) [161]	250x350 mm 2,200 mm	Tensile: 6Ø32 or 8Ø25 mm Stirrups: Ø8 mm @ varied	$f_c = 138.6-145$ MPa Fibers: 2.65% (ST)	R=25-45% ISO 834

(*): Only some of the beams contained this reinforcement

(HS): High strength (1860 MPa) low-relaxation seven-wire monostrand tendons

(f_c): Compressive strength at fire test day

(ST): Steel fibers; (PP): Polypropylene fibers

(R): Ratio between the applied load during test and the beam capacity at ambient conditions

2.3.3.2. Numerical Studies

Alternative to testing, fire response of UHPC members can be evaluated using numerical models. In recent years, a significant number of numerical models on the fire response of concrete members have been developed, mostly based on the finite element method using software programs such as ABAQUS, ANSYS, and SAFIR. In these models, structural members are discretized into meshed representations and assigned non-linear material models for both steel and concrete components. Thermal and structural analysis are carried out, either in coupled or

uncoupled mode, considering predefined loading and exposure conditions to evaluate the overall fire response of the member. Typical results extracted from these models include temperature distributions and deflections, which are compared to the specified failure criteria (such as deflection limits) to determine the fire resistance of the member. Alternatively, macroscopic analysis can be undertaken by developing programs using programming languages such as FORTRAN, PYTHON, or MATLAB. In this method, the analysis of a critical section can be used to predict the fire response of a concrete member, but it can be more complex than using available commercial programs if the user does not have experience with the coding language. Nevertheless, results from these models have been successfully validated against experimental data and have been used to investigate the influence of specific factors through parametric studies.

There have been a few numerical studies on the fire response of UHPC flexural members, as summarized in Table 2.3. Most of these studies incorporate thermal and mechanical properties of UHPC based on previous high temperature tests on material properties, such as the ones presented in section 2.3.1. The models developed in the commercial software ABAQUS do not include fire induced spalling of UHPC [158,160,162,163]. This is based on the high complexity and computational cost for accurately tracing spalling progression in these models. Besides, authors assumed that under certain conditions, such as presence of polymeric fibers and hot-air curing, spalling may not significant and, therefore, do not affect the overall fire behavior of the member. The other studies presented in Table 2.3 are based on the extension of a numerical model developed by Kodur and Dwaikat [164] for NSC and HSC beams. The authors have updated the material models and, most significantly the spalling sub-model for UHPC. An important aspect of a spalling sub-model is the criteria for spalling occurrence, which has been discussed in detail by these authors [163,165]. Other studies in the literature have proposed different means of tracing

fire-induced spalling in concrete during heating. Despite the efforts and advancements on this, spalling is still considered as stochastic in nature by several researchers and the fact that these models are based a number of assumptions can limit their applicability in practice.

Table 2.3: Numerical studies on UHPC beams at elevated temperatures

Authors (Year) / Reference	Overview	Spalling model	Material model
Hou et al. (2019) [158]	Developed in ABAQUS and validated using their own experimental data	No spalling model – Authors assumed thermal curing	Based on experimental data from tests conducted by previous studies
Ren et al. (2020) [163]	Developed in ABAQUS and validated using data from Hou et al. [158]	No spalling model – Authors assumed use of hybrid fibers	Same as Hou et al. [158]
Ren et al. (2021) [166]	Macroscopic FE model – extended from Kodur and Dwaikat [164]. Validated using tests from Hou et al. [158], Kahanji et al. [139] and Banerji et al. [61]	Spalling sub-model from Kodur and Dwaikat [164] developed for HSC	Same as Hou et al. [158]
Ren et al. (2021) [137]	Same model presented in Ren et al. (2021) [166]	Modified the spalling sub-model from Kodur and Dwaikat [164] with different constitutive relationships and spalling criterion	Same as Hou et al. [158]
Banerji and Kodur (2022) [165]	Macroscopic FE model – extended from Kodur and Dwaikat [164]. Validated using test data from Banerji et al. [61]	Modified the spalling sub-model from Kodur and Dwaikat [164] to account for loading stresses, thermal gradients, varying permeability and spalling through the beam length	Based on experimental data from their own previous tests [104,112]
Yan et al. (2022) [160]	Developed in ABAQUS and validated using their own experimental data	No spalling model	Based on experimental data from previous studies [102,106]
Simwanda et al. (2023) [162]	Developed in ABAQUS and validated using data from Kahanji et al. [139]	No spalling model	Based on experimental data from previous studies [104,112]

2.4. Characteristics of Bridge Fires

A key parameter for assessing the realistic fire behavior of a structural member is reproducing the fire environment. Standard temperature-time heating curves have been used as a metric to evaluate the fire resistance of structures for more than a century, as required by established codes and standards [167]. The ISO 834 [168] fire curve, usually referred as the “standard fire” curve, has been widely adopted for assessing building structures, with similar versions specified in other standards, including ASTM E119 [169] and Eurocode 1 [170]. These

curves have been designed to emulate a building fire scenario, which encompasses burning of cellulose-based materials in a closed environment. However, bridge fire scenarios present a very distinct behavior than usually encountered in buildings. Unlike the typical fuel source found in buildings, bridge fires often result from the combustion of petrochemicals such as gasoline, diesel, or other highly flammable substances. This leads to a much higher fuel load and heat release rate, resulting in a completely different time-temperature curve. Besides, while buildings are enclosed spaces with restricted oxygen supply, bridges are open spaces with abundant oxygen available, enabling complete combustion of the fuel load during a fire incident. Additionally, the large scale of bridge structures and varying ventilation conditions can result in uneven distribution of heat, creating thermal gradients on the surface of structural members.

Over the years, other fire curves have been created to represent fire scenarios resulting from combustion of hydrocarbon substances. Unlike the standard fire curve used for buildings, there is a big variance among different fire hydrocarbon curves developed by different research and standard institutes. These differences arise from the numerous types of petrochemical fuels and environments in which they can burn (inside of tunnels, under or over bridges, inside a facility, etc.). As illustrated in Figure 2.17, hydrocarbon fire curves present a rapid rise of temperatures in the first five minutes of burning, typically above 1000°C, while standard fire curves take 90-120 minutes to reach the same level. The RABT ZTV curves were developed in Germany to represent the fire scenarios of a train and a car fire based on results of experimental tests [171]. These curves have a maximum temperature of 1200°C and a burning duration of 30 to 60 minutes, followed by a linear cooling phase. The RWS (Rijkswaterstaat) curve was developed in the Netherlands to represent the burning of 50 m³ of oil or gasoline with a fire load of 300 MW [171]. As a result, the fire curve presents a peak temperature of 1350°C and lasts for around 120 minutes. In the United

States, a hydrocarbon fire curve is prescribed by ASTM E1529 [172], which presents a linear increase of temperature from 1000°C at the early stages of fire exposure to almost 1200°C after 240 minutes of fire exposure. Alternatively, Eurocode 1 [170] presents the following equations to define standard, hydrocarbon and external fires:

$$T_{Standard\ fire}(^{\circ}C) = 345 \log(8.t + 1) + T_0 \quad (2.8)$$

$$T_{Hydrocarbon\ fire}(^{\circ}C) = 1080(1 - 0.325e^{-0.167t} - 0.675e^{-2.5t}) + T_0 \quad (2.9)$$

$$T_{External\ fire}(^{\circ}C) = 660(1 - 0.687e^{-0.32t} - 0.313e^{-3.8t}) + T_0 \quad (2.10)$$

where t is the time (minutes) and T_0 is the ambient temperature (°C). The external fire curve is designed to assess structures on the external side of a building and for this reason presents lower temperatures than all the other fire curves. The hydrocarbon fire curve presents a rapid rise of temperature to 1100°C in the first 30 minutes of fire exposure, which is kept constant through the entire fire duration. Overall, these fire curves assume a fictitious surface temperature progression, which can overestimate or underestimate the response of bridge members assessed under such conditions. Therefore, evaluation of bridge structures under realistic fire conditions requires a comprehensive understanding of a bridge fire scenario in order to determine the realistic temperature fields that bridge structures can experience.

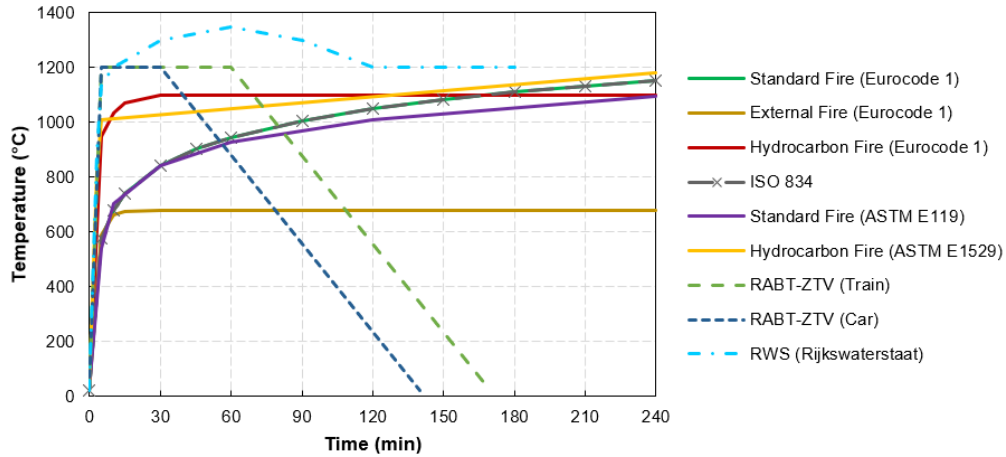


Figure 2.17: Petrol-based fire curves according to different sources

2.4.1. Bridge Fires Load and Intensity (Heat Release Rate)

An alternative to evaluate the fire performance of bridge structures under realistic fire conditions is the use temperature fields defined based on fire load and intensity. The fire load represents the amount of combustible material available to burn during a fire and is typically expressed in relation to the burning floor area (MJ/m^2). On the other hand, the fire intensity is expressed in terms of heat release rate (HRR), which represents the amount of energy (heat) released per unit of time during a fire. In other words, it represents how fast the fuel load is being consumed during the burning process and is typically expressed in mega-watts (MW) [173]. Experimental ranges and representative HRR for different vehicle types are included in the NFPA 502 report [174], as presented in Table 2.4.

The heat released during combustion is propagated to the surface of structural members through convection and radiation. The rate at which thermal energy is transferred to the surface of structural members is determined by the total heat flux (\dot{q}''_{tot}) [175]:

$$\dot{q}''_{tot} = \varepsilon \left[\dot{q}''_{inc} - \sigma(T_{surf})^4 \right] + h(T_{gas} - T_{surf}) \quad (2.11)$$

where ε is the emissivity factor, \dot{q}''_{inc} is the incident radiative heat flux, σ is the Stefan–Boltzmann constant, h is the convective heat transfer coefficient, T_{gas} and T_{surf} are the temperatures of the gas and on the surface of the member.

Table 2.4: HRR for typical vehicles based on NFPA 502 [174]

Vehicle Type	Experimental (Representative) HRR	
	Peak HRR (MW)	Time to peak HRR (min)
Passenger car	5-10 (8)	0-54 (10)
Multiple passenger cars	10-20 (15)	10-55 (20)
Bus	25-34 (30)	7-14 (15)
Heavy goods truck	20-200 (150)	7-48 (15)
Flammable/Combustible liquid tanker	200-300 (300)	-

2.4.2. Fire Tests on Bridge Girders

There are only three fire tests on bridge girders using real-fire sources to replicate a bridge fire scenario with a controlled HRR published in the literature. The tests conducted by Takehara et al. [176] and Alos-Moya et al. [177] were made on composite steel-concrete girders using a fuel load lower than usually encountered in tankers. Results from these tests showed that fire temperatures can reach 1200°C within few minutes of fire exposure and that significant thermal gradients are developed along all directions of the bridge. The only real-bridge fire test in concrete bridge girders reported in the literature was conducted by Beneberu and Yazdani [178]. The main objective of the study was to evaluate the performance of girders strengthened with carbon fiber-reinforced polymer under hydrocarbon fire exposure. The authors reported being limited to 4.23 m³ of aviation fuel and one hour of testing. Temperatures quickly rose above 900°C in the first five minutes of fire exposure and reached peaks above 1100°C throughout fire exposure. Overall these studies highlighted the challenges related to conducting open-pool fire experiments due to

the influence of wind that can change the direction of the flames. Additionally, the lack of a standardized test method for conducting such measurements and complexities associated with its execution can impose challenges for the development of similar experimental tests.

2.4.3. Approaches for Modeling Bridge Fire Scenarios

Modeling bridge fire scenarios can be more advantageous due the high costs and logistic complexities associated with experimental programs. Despite the lack of standards and specific guidelines for modeling bridge fires, several studies have been conducted and developed their own approaches for modeling these scenarios. Liu et al. [179] groups these approaches into three categories: (1) temperature curve method; (2) intermediate method, and (3) computational fluid dynamics (CFD) method. The temperature curve method refers to the use of nominal temperature-time relations to represent the fire scenario in a closed furnace, such as the ones presented in Section 0. This method is commonly accepted for testing of structural members in buildings but is not well accepted for analysis of bridge structures because they cannot describe the non-uniform field of temperatures in bridge members [179]. Previous studies have shown that a significant thermal gradient can be developed in all directions of bridge structures during a fire event, especially in long-span bridges, which can lead to unrealistic failure predictions [180–183].

In intermediate methods, a combination of theoretical and numerical modeling is used to analyze the flame, thermal conditions and heat transfer mechanisms to determine the temperature fields [179]. These models can include flame radiation models and localized fire models in a more simplistic and less accurate way than CFD models. On the other hand, CFD models comprise of a more refined method for modeling bridge fires. CFD models are based on the principles of fire dynamics and energy conservation equations to formulate a balance of a meshed model. The Fire Dynamics Simulator (FDS) developed by the National Institute of Standards and Technology

(NIST) is an open-source software that is commonly used for modeling fire-driven fluid flow. In these models, the fire source is specified based on heat released per unit area (HRRPUA) and it takes into consideration ventilation conditions and geometry of structural members, which are modeled as obstructions for heat flow. Results from FDS models can be transferred to finite-element (FE) models to trace the fire response of bridge girders in previous studies.

As opposed to the aforementioned methods, CFD models can describe the temperature gradient based on convection and radiation mechanisms. To model the fire source, fire intensity is commonly expressed in terms of unit area (HRRPUA), representing the ratio between the HRR and the area over which the fire is occurring [31]. Figure 2.18 presents the HRRPUA used in some previous studies for modeling fires on bridges, most commonly ranging around 2,500 kW/m² [28,182,184–189]. Alos-Moya et al. [182] investigated various HRR levels and found that 1000 kW/m² best represented the response of a steel bridge during a fire incident. They also examined different discretization sizes for transferring temperatures from FDS to finite element models, focusing solely on steel girders. On another study, Peris-Sayol et al. [28] identified factors such as fire location, vertical clearance, and wind effects that influence bridge fire behavior. Further studies by Lu et al. (2023) and Saglik et al. (2022) explored the effects of fire on various bridge types and connections. Gong and Agrawal [189] and several other studies used similar ranges of HRRPUA for evaluating the behavior of bridges in specific incidents. Overall, these studies demonstrate that this range of parameters is appropriate for modeling bridge fires.

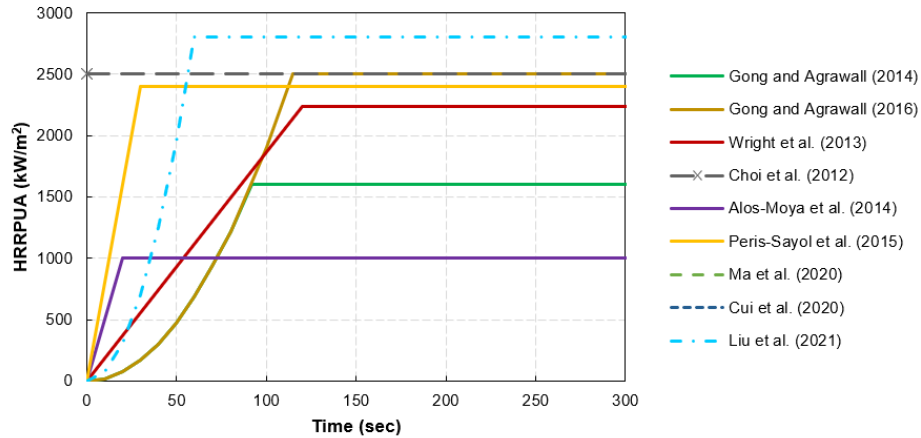


Figure 2.18: HRRPUA in bridge fires adopted by different studies

2.4.4. Current Fire Safety Provisions for Bridges

In buildings, fire hazard is mitigated to certain extent through a set of active and passive fire protection systems. Active systems, which includes suppression systems like sprinklers, help limit the growth of a fire and have been installed in very few critical bridges, such as Akashi Kaikyo bridge in Japan, the Seohae Bridge in Korea [32], and the Osman Gazi Bridge in Turkey [190]. However, installation of those systems in bridges present several practical challenges. On the other hand, passive protection through provision of fire resistance to structural members is more appropriate for bridge structures. However, in current practice, bridges are not specifically required to be designed with any fire safety provisions [10,18,76]. Some non-mandatory provisions in standards, such as NFPA 502 [174] “Standard for Road Tunnels, Bridges, and Other Limited Access Highways” contains very limited general recommendations to consider fire hazard in bridges. In France, Cerema [191] published guidelines for analyzing the fire resistance of road bridges, including the idealization of the fire scenario, assessment of the fire resistance, and the assessment of bridges after fire. However, most of the standards and guidelines available are based on the fire provisions used for buildings and do not fully account fundamental differences in fire scenarios, material characteristics, and structural configurations of bridge structures.

2.5. Fire Resistance of Concrete Bridge Girders

Despite the growing interest to investigate and develop fire safety strategies to bridge structures, most of the studies carried out so far have focused on steel or composite steel-concrete bridges. As already demonstrated, concrete bridges can also be vulnerable to fire hazard. Specifically, modern bridges structures with slender cross-sections and made with concretes of higher strength can present faster degradation under fire conditions and result in low fire resistance ratings. Other factors such as loss of prestress and high severity fire exposure can accelerate degradation of concrete bridges under fire exposure. However, current codes and standards do not present specific requirements for fire design of concrete bridges as well as specific requirements for evaluating the fire resistance of bridge structures in general. Some limited experimental and numerical studies have been carried out to evaluate the fire response of concrete bridge girders made with conventional concretes when exposed to standard fire curves, as presented herein.

2.5.1. Factors Influencing Fire Response of Concrete Bridge Structures

The behavior of a concrete member during fire exposure is influenced by a number of factors related to the properties of the structural materials (concrete and steel), structural configuration (boundary conditions and reinforcement configuration) and exposure conditions (applied load and fire exposure conditions). Studies have demonstrated that concretes of higher strength experience faster degradation at elevated temperatures due to its lower permeability and that members with slender cross-sections experience higher temperatures during fire exposure, resulting in faster degradation of its structural capacity. Additionally, higher loading ratios and exposure to fires of higher severity (higher temperatures) also contribute to faster degradation at elevated temperatures. These influencing factors have been thoroughly studied for building structural members and are well documented in the literature.

While the fire response of prestressed concrete members for building applications has also been thoroughly evaluated, a very scarce number of studies have evaluated the response of prestressed concrete bridges. When exposed to elevated temperatures, prestressing steel can experience relaxation, leading to the loss of the initial prestress. At critical temperatures, this can result in excessive deflections and compromise the structural integrity of the concrete member. For conventional prestressed concrete members, this critical threshold can be at temperature levels as low as 400°C. Besides, during fire exposure, significant restraint forces can be developed at the ends of a prestressed concrete beam, which can have either a positive or negative effect depending on their location along the depth of the cross-section.

Another important aspect of concrete bridge structures that may result in a different behavior than conventional building members is the use of slender cross-sectional shapes. While in buildings, concrete beams are designed with conventional rectangular shapes, slender I-shaped and T-shaped sections are typically used to reduce self-weight. These geometries experience higher temperatures during fire exposure, which can lead to a different governing failure limit state in bridge members, such as shear failure instead of flexural failure due to the high concentration of heat in the web. Previous studies have reported that concrete beams subjected to predominantly flexural loads can experience unexpected shear failure at elevated temperatures as a result of slender web sections [139,161,192].

Overall, the fire response of concrete bridge girders can be significantly different than building members due to the lack of active fire protection systems and harsher exposure conditions. Unlike buildings, bridges are subjected to fires resulting from hydrocarbons and are exposed to the harsher outdoor environment conditions. These conditions can result in higher moisture contents (from snow or rain) and increase the susceptibility to fire induced spalling.

2.5.2. Approaches for Evaluating Fire Response of Concrete Bridges

The fire resistance of concrete structures can be evaluated through experimental tests or numerical models. Both methods present advantages and drawbacks. In general, experimental tests are known to provide a more realistic response of concrete members at elevated temperatures, specifically in terms of fire-induced spalling, but they are also costly and time-consuming. On the other hand, numerical models can be used to simulate a number of scenarios more economically, but the accuracy of the results will depend on the level of refinement of the model. These methods can complement each other, as experimental tests are useful for validating the numerical model, which in turn can be used to evaluate a number of influencing factors.

Fire resistance tests are typically conducted following a standardized test method, such as the procedures prescribed by ISO 834 [168], ASTM E119 [169], and EN 1363 [193]. These methods are similar in the fact that tests are conducted in a laboratory furnace where the specimen is exposed to a standard fire curve while temperature and deflections are monitored to determine the failure time of the specimen. While this test may be adequate to represent a building compartmented fire, it cannot be representative of a bridge fire scenario for two main reasons. First, specimens are uniformly heated in these tests, whereas thermal gradients are typically developed in bridge fire scenarios. Second, the furnace length is usually limited to a distance that can accommodate building members, and the loading conditions are restricted by the testing facility. Therefore, numerical models can better represent the loading and fire conditions a bridge girder is expected to experience during a fire incident.

An important aspect to evaluate fire resistance is the definition of failure criteria. There are different criteria that can be used to determine failure of a member during fire exposure, and a combination of multiple criteria has been commonly used. The most common criteria to evaluate

beams and bridge girders is the specification of a deflection and/or a rate of deflection limit. The threshold for the deflection and rate of deflection criteria is typically $L^2/(400d)$ and $L^2/(9000d)$, respectively, where L is the span length and d is the girder depth, both in mm, as per ASTM E119 [169] and ISO 834 [168]. Other studies have used the BS 476-20 [194] threshold, which limits the deflection in $L/20$ or $L/30$. Another alternative to determine failure of a concrete girder during fire exposure is the use of the critical temperature criterion. In this method, failure is said to occur when a critical temperature limit is reached at the reinforcement or strands, in which most of the strength and bearing capacity is lost. For prestressed concrete girders, the critical temperature is assumed to be 400°C, while in reinforced concrete members 593°C is typically adopted. While these methods can be easily employed to determine failure of a member both experimentally or through numerical models, they are not directly related to the structural capacity of the member. In steel bridges, some studies have proposed to limit strains in the steel section, movement of the girder on the supports, or even buckling behavior through out-of-plane displacements in the web.

As an alternative, strength limit criterion can be employed in addition to the other criteria. This criterion is based on the assessment of a member capacity to withstand the effects imposed by the applied loading and can be employed to assess failure under dominant flexural and shear loading. However, strength-based criteria are difficult to be determined both experimentally and numerically. While failure can easily be verified in both methods, the gradual loss of capacity cannot be directly determined through either of those methods. However, based on the temperatures measured at different locations of the cross-section and temperature-dependent material properties of both steel and concrete, the loss of capacity during fire exposure can be calculated. Overall, there is no standardized method or criteria to determine failure of a concrete member at elevated temperatures and authors have been proposing their own criteria.

2.5.3. Previous Studies on the Fire Resistance of Concrete Bridge Girders

A review of the literature demonstrates that very limited studies have been conducted on the fire resistance of concrete bridges, as shown in Table 2.5. It can be seen that only three experimental studies have been published, from which only one was done with real fire exposure, while the other two comprised of furnace tests using the hydrocarbon fire curve. The fire test carried out by Beneberu and Yazdani [178,195] evaluated the response of three prestressed I-shaped girders spanning 9.6 m subjected HL-93 live load and exposed to a real-fire scenario resulting from the burning of aviation fuel as explained earlier in section 2.4.1. The NSC girders were 700 mm-deep and were reinforced with 12 low relaxation high-strength steel strands with a 12.7-mm diameter. Two of the three girders were strengthened with carbon fiber-reinforced polymer and one of those was insulated with fire protection. The authors reported temperatures of exposure around 900°C and that one of the girders (not strengthened) experienced much lower temperatures due to wind conditions. The maximum strand temperature (almost 500°C) and deflection (18 mm) was reported in the strengthened girder without fire protection. Also, severe damage due to spalling was reported by the authors, which could have resulted in collapse of the girders if the experiment had been conducted for a longer duration. In the experimental program carried out by Wu et al. [196] four prestressed box girders and two prestressed T-shaped girders were tested in a furnace with exposure to the hydrocarbon fire while subjected to their cracking load at midspan. The results obtained by this study shows that strand temperatures in the box girders were lower than the T-shaped girders due to their higher thermal inertia and the fact that these girders were exposed to fire from only one side. This contributed to a rapid increase in midspan deflections and lower fire resistance of the T-shaped girders (90-120 minutes) when compared to the box girders (160-180 minutes). Lastly, the study conducted by Song et al. [197]

tested three prestressed box girders exposed to the hydrocarbon fire curve while subjected to two concentrated forces representative of 55% of the girder capacity at ambient conditions. The concrete used in the fabrication of the specimens was reinforced with polypropylene fibers, which significantly reduced the spalling levels. The authors observed high temperature and fracture of the steel strands (with loss of prestress), leading to fire resistance levels ranging between 65 and 75 minutes. Overall, these fire tests showed that concrete bridge girders can present higher fire resistance than steel bridge girders. However, there is a number of other influencing factors that can affect the fire response of these girders that have not been studied yet.

Table 2.5: Summary of studies on the fire resistance of concrete bridge girders

Author (Year) / Reference	Type of study	Specimen details	Testing/Analysis parameters	Key findings
Beneberu and Yazdani (2018, 2019) [178]	Experimental	Prestressed I-shaped girders strengthened with carbon fiber reinforcement Span = 9.6 m	Real-fire exposure (open pool fire using aviation oil) under HL-93 live load	Large damage to girders without thermal insulation
Wu et al. (2020) [196]	Experimental and numerical (ABAQUS)	Prestressed box and T-shaped girders Span = 4.3 m	Furnace testing - hydrocarbon fire under mid-span cracking load	Higher deflections and lower fire resistance in the T-shaped girders
Song et al. (2023) [197]	Experimental	Prestressed box girders – reinforced with PP fibers Span = 5.7 m	Furnace testing - hydrocarbon fire under two concentrated forces (load ratio = 0.55)	Loss of prestress with fire exposure despite of the positive effect of PP fibers to prevent spalling
Zhang et al. (2017) [198]	Numerical (ANSYS)	Prestressed T-shaped girders Span = 20 m	Exposed to four standard fire scenarios while subjected to a distributed load	Girders experience failure when exposed to the more severe fire curves due to increased rate of deflections
Zhang et al. (2017) [199]	Numerical (ANSYS)	Prestressed box girders Span = 20 m	Hydrocarbon fire exposure	Increasing levels of prestressing resulted in reduced deflections
Song et al. (2020) [200]	Numerical (ANSYS)	Prestressed box girders Span = 30 m	Hydrocarbon fire exposure	Studied different variables
Wu et al. (2020) [201]	Numerical (FDS-ABAQUS)	Prestressed box girders Span = 58 m	Exposed to real-fire conditions and live load	Significant loss of capacity after fire exposure
Timilsina et al. (2021) [202]	Numerical (FDS-ABAQUS)	Reinforced concrete T-shaped girders Span = 14.86 and 12.38 m	Exposed to real-fire conditions and live load	Significant loss of capacity after fire exposure

A few numerical models have also been conducted to evaluate the fire resistance of concrete bridge girders. Zhang et al. [198] developed a 3-D finite element model in ANSYS to evaluate the behavior of prestressed T-shaped bridge girders exposed to three fire scenarios and a design fire curve, while subjected to a distributed load. The girder experienced failure after 101 minutes of exposure to the hydrocarbon fire curve under rate of deflection criterion, while it failed at 147 minutes of exposure to the standard fire curve under strength-based (flexure) criterion. In another study, Zhang et al. [199] evaluated the response of box girders exposed to the hydrocarbon fire curve under varying levels of prestress. The authors reported that deflection increases more rapidly in the girders with lower prestress levels, reaching failure limit states after 180 minutes of fire exposure. In a similar study, Song et al. [200] evaluated prestressed box girders exposed to the hydrocarbon fire curve with a number of variables. The authors reported that the concrete cover thickness, load level, and fire exposure position were the variables that presented significant influence of the fire resistance ratings, while the degree of prestress and the fire exposure length did not have significant influence. Wu et al. [201] coupled FDS results to a finite element model in ABAQUS to trace the fire response of prestressed box girders, demonstrating a positive response of these members under realistic fire exposure. Even without failure, the authors highlighted that some level of permanent damage may have happened due to cracking and loss of prestress. Lastly, Timilsina et al. [202] evaluated the residual capacity of a fire damaged concrete bridge through a coupled FDS-ABAQUS model, demonstrating severe levels of damage and need of replacement of the bridge. Overall, it can be seen that most of these studies have evaluated box girders under hydrocarbon fire curve, and very limited have focused on standardized I-shaped sections, which are more common in modern bridge constructions.

2.6. Current Knowledge Gaps

Based on the detailed literature review presented, it is clear that there is very limited information on the fire response of concrete bridges in the literature, specifically for modern bridges made with newer concrete types, such as UHPC. Optimized cross-sectional shapes have been proposed for UHPC bridge girders, but they do not take into consideration fire performance as a key consideration. Besides, various shapes (I-shaped, T-shaped, and Pi-shaped sections) have been used in bridges and their fire resistance can be significantly different from that of rectangular beams commonly applied in buildings. The influence of fire induced spalling on the fire response of concrete bridge girders exposed to fire scenarios, especially for UHPC members, still lacks thorough understanding. While some studies have characterized some temperature-dependent properties of UHPC, specific properties have not been studied yet, including pore pressure development and degradation of shear strength at elevated temperatures. Based on this review of the literature, the following key knowledge gaps have been identified:

1. Lack of data and testing procedures for measuring high temperatures spalling-related properties of concrete, such as pore pressure build-up in concrete. Similarly, there is a lack of data on the degradation of shear strength of UHPC at elevated temperatures and its influence on the fire resistance of structural members.
2. Lack of validated numerical models for tracing the fire resistance of concrete bridge girders. Current numerical models do not account for newer types of concrete, such as UHPC. There is also limited information on the failure criteria to be adopted for evaluating the fire resistance of bridge girders.

3. Limited studies on the fire resistance of concrete bridge girders subjected to realistic fire conditions representative of petrol-based fires. Further, current studies do not account for the wide range of parameters that affect the fire resistance of bridge girders.
4. There is a lack of guidelines in codes and standards for fire design of concrete bridges, specifically girders which are highly vulnerable to fire exposure.

3. EXPERIMENTAL STUDIES

3.1. General

While material-level properties of NSC and HSC at elevated temperatures have already been studied, the literature review in the previous chapter shows that there is very limited data for UHPC. These properties are important to model the thermal response (temperature progression) and the structural response (strength and deflections) of concrete structures under fire conditions. The fire behavior of UHPC structures is quite complex and more research is still needed to develop a thorough understanding on the effect of temperature on other specific properties of UHPC. This chapter presents results from experimental tests conducted to measure pore pressure build up in concrete and to investigate the effect of temperature on the shear strength of UHPC. Specimens cast as part of a bigger research project at Michigan State University were used to measure pore pressure build-up in NSC and UHPC specimens during heating, aiming to provide insights on the contribution of this mechanism to spalling. In addition, direct shear strength tests were conducted on UHPC specimens heated to different temperature levels in order to measure the loss of shear strength with temperature. The following sections present details on fabrication of specimens, test procedures, and a discussion of the results obtained in these experimental tests.

3.2. Fabrication of Test Specimens

Specimens made of NSC and UHPC in different shapes and sizes were cast for the testing purposes of this experimental program. The mixtures and specimens were prepared by previous graduate students as part of a larger experimental program led by Prof. Kodur at Michigan State University. The following sections present details on the materials and mix composition of the of the concrete batches used in this study, as well as details on the fabrication of the specimens.

3.2.1. Materials and Batch Mix Proportions

The specimens used in the tests were fabricated from three batches of concrete, namely normal-strength concrete (NSC), UHPC reinforced with steel fibers (UHPC-ST) and UHPC reinforced with both steel and polypropylene fibers (UHPC-ST-PP). Table 3.1 presents the mix proportions and properties of the three concrete batches used in this study. The conventional NSC mixture comprised of Type I-Portland cement, Class C-fly ash, natural (silica) sand, and carbonate coarse aggregates of 12.7 mm maximum diameter [203]. A water-to-cement ratio of 0.45 was used in this mixture, in addition to water reducer admixture in 6.1 kg/m^3 to achieve a slump of 100 mm. The UHPC mixtures were designed by Metna Co. with a controlled amount of coarse aggregates to facilitate the mixing procedure (energy required) and reduce the unit cost of the mixture [204]. All batches of UHPC included Type I-Portland cement, slag, silica fume, silica sand, limestone powder, natural sand, and carbonate coarse aggregates of maximum diameter of 12.7 mm [54]. A very low water-to-binder ratio of 0.14 was used in the UHPC mixtures, in addition to 48 kg/m^3 of Chryso 150, a polycarboxylate-based superplasticizer, to achieve proper workability in the fresh state. In the UHPC-ST and UHPC-ST-PP mixtures, straight steel fibers with 0.2 mm diameter and 13 mm length were added in 1.5% by volume fraction. For the UHPC-ST-PP mixture, 13 mm-long polypropylene fibers, with a melting point of 160°C , were added in 0.11% by volume fraction. Table 3.2 summarizes the properties of steel and polypropylene fibers used in the composition of the UHPC mixtures [204].

Table 3.1: Concrete batch mix proportions and properties

Component	NSC (kg/m ³)	UHPC (kg/m ³)	UHPC-ST (kg/m ³)	UHPC-ST-PP (kg/m ³)
Coarse aggregate (carbonate)	970	517	517	517
Fine aggregate (natural sand)	838	544	544	544
Limestone powder	-	184	184	184
Silica sand	-	299	299	299
Silica fume	-	224	224	224
Slag	-	102	102	102
Cement (type I)	312	510	510	510
Fly ash (class C)	78	-	-	-
Steel fibers (1.5% vol.)	-	-	127	127
Polypropylene fibers (0.11% vol.)	-	-	-	1.6
Water	140	121	121	121
Water reducer admixture	6.1	48	48	48
Water-cement ratio (w/c)	0.45	0.24	0.24	0.24
Water-binder ratio (w/b)	0.45	0.14	0.14	0.14

Table 3.2: Properties of the fibers used in the UHPC mixtures [204]

Fiber Type	Diameter (mm)	Length (mm)	Aspect ratio (Lf/Df)	Tensile strength (MPa)	Density (kg/m ³)	Melting temperature (°C)
Steel	0.2	13	65	960	7850	-
Polypropylene	0.018	13	722	570-660	910	170

3.2.2. Mixing and Curing Procedures

All the batch mixes were prepared by the local ready-mix company and supplied to the Civil Infrastructure Laboratory (CIL) at Michigan State University, where the specimens were cast and cured. For the NSC mixture, the standard mixing procedure employed by Shafer Redi-Mix Inc. was used in the fabrication of the specimens. The fresh concrete mixture was poured into metallic and wooden forms and compacted with steel rods to ensure proper distribution and compaction of the concrete inside the forms. After casting, NSC specimens were covered with a 0.15 mm thick heavy-duty polyethylene film to prevent loss of moisture and deposition of dust on

the surface of the specimens. After 24 hours, the specimens were demolded and stored in a curing chamber (at 25°C temperature and 60% relative humidity) until the day of testing [203].

Mixing and casting of the UHPC specimens occurred in April, 2018 following a special mixing procedure developed with Metna Co. to ensure a uniform and workable mixture. The procedures consisted in first mixing the dry components, starting with coarse and fine aggregates, followed by the addition of the binders (silica fume, slag, limestone powder, and cement) with one third of the water content in form of ice to control the reaction time. The truck drum mixer was turned into high speed (0.25 revolutions per second), then the remaining water and superplasticizer was incorporated and mixed for five minutes. The mixer was then reversed to ensure uniform distribution of all ingredients, and mixed for another five minutes. After that, a small portion of the mixture was poured off the truck for casting of the UHPC specimens. Then, steel fibers were added to the mixture and mixed for another five minutes, followed by casting of the UHPC-ST specimens. Finally, polypropylene fibers were added to the mixture and mixed again for another five minutes for casting of the UHPC-ST-PP specimens. After casting, specimens were cured at room temperature for the first 24 hours, then demolded and stored in the curing chamber [204].

For measuring compressive strength and splitting tensile strength of the three batch mixes, specimens were tested at 28 and 90 days after casting and results are presented in Table 3.3. While the compressive and tensile strength of the NSC was much lower than the UHPC, there was not much difference between the UHPC batches with and without polypropylene fibers.

Table 3.3: Concrete batch mix proportions and properties

Property (Age)	NSC (kg/m ³)	UHPC (kg/m ³)	UHPC-ST (kg/m ³)	UHPC-ST-PP (kg/m ³)
Compressive strength (28th day)	39	151	145	160
Compressive strength (90th day)	42	164	167	173
Split tensile strength (28th day)	3	6	15	14
Split tensile strength (90th day)	3	7	16.5	15

3.2.3. Specimens Configuration and Instrumentation

The fresh batches were cast into molds of different shapes and sizes based on the testing purposes. For pore pressure tests, cubic molds were of 100x100x100 mm³ of internal dimensions, while cylindrical molds were of two sizes: (i) 75 mm-diameter and 150 mm-height; (ii) 100 mm-diameter and 200 mm-height. Pore pressure probes were mounted at the center of the molds before placing concrete as shown in Figure 3.1. The probes comprised of aggregate-shaped sintered metal heads of 5 mm in length fitted on capillary steel pipes of 2 mm diameter (Figure 3.2). The sintered metal heads were fabricated and provided by Dr. Roberto Felicetti, from Politecnico di Milano, Italy [154].



(a) Cubic molds



(b) Cylindrical molds

Figure 3.1: Molds with pore pressure probes before casting [66]



Figure 3.2: Sintered metal heads used in pore pressure measurements [66]

For undertaking direct shear strength tests, prismatic specimens measuring 40x50x150 mm were cast. These dimensions are lower than JSCE-SF6 [205] prescription, which consists of specimens of 150x150x500 mm. The decision of scaling the specimens down was made to accommodate limitations in the testing equipment, such as the furnace size and the strength test machine. Besides, handling large scale specimens at high temperatures poses a risk and limitation for this type of test. For preparation of the specimens, a 5 mm-notch was made all around the specimens with the help of a power saw in order to induce shear failure through the shear plane. This procedure was proposed by Mirsayah and Banthia [206] and has been followed by other studies as well. Figure 3.3 presents a notched specimen used for shear strength test.

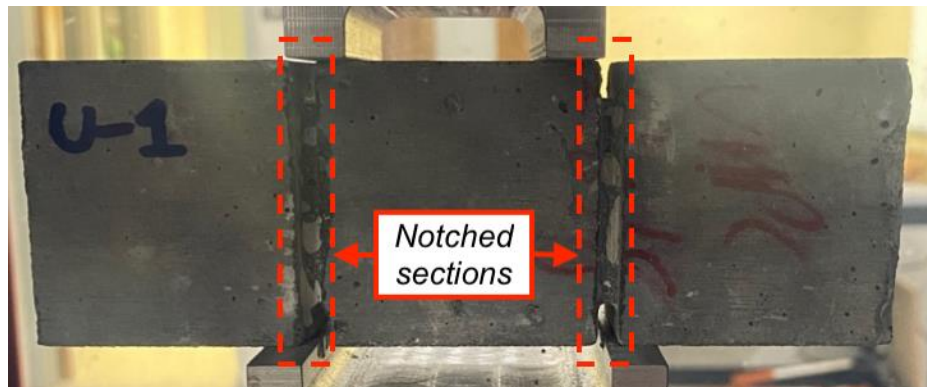


Figure 3.3: Notched prismatic specimens for shear strength tests

3.3. Pore Pressure Build-Up Measurements

The build-up of pore pressure inside of concrete is the primary mechanism that can lead to fire induced spalling of concrete structures during heating. Specifically, concretes of higher

strength such as HSC and UHPC exhibit lower permeability and thus higher susceptibility to this phenomenon. However, measuring pore pressure can be challenging due to the lack of a standard test procedure and guidelines. Previous researchers have developed their own experimental set-up and testing procedures to conduct these tests, which have led to inconsistencies in the measured pore pressure values. Therefore, as part of the current experimental study, a number of pore pressure measurements have been undertaken to investigate the effect of different parameters on pore pressure build-up in concrete during heating, as well as its influence on the fire induced spalling mechanisms [66].

The experimental method used in this study was developed based on the analysis of previous studies reported in the literature. It aims to simulate the thin web of an I-shaped bridge girder, as illustrated in Figure 3.4, which presents a critical situation for this mechanism due to the formation of a symmetrical plane through which no moisture transfer can occur. The rapid increase of temperatures in this region lead to formation of a quasi-saturated layer and high pore pressure, which can result in delamination or holes in the web. Thus, cubic specimens have been insulated with a ceramic fiber blanket on four sides to establish mono-directional heating flow through the specimen. Additionally, some cubic specimens were sealed using aluminum foils and heat-resistant epoxy in addition to the application of the insulation blanket to prevent loss of moisture through the sides of the specimen and reduce the measured pore pressure values. Other influencing factors such as specimen shape and size, as well as varying heating rates have been used in this experimental program, as presented herein.

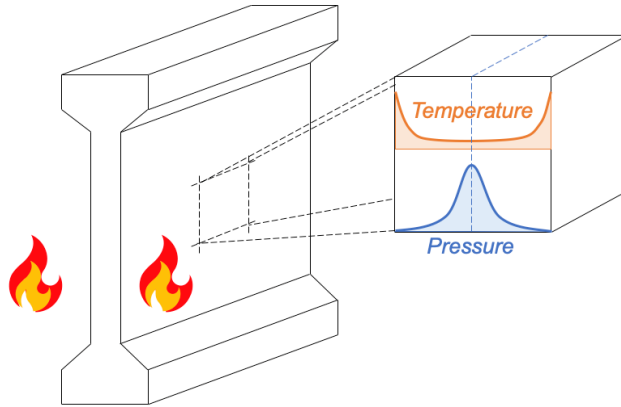
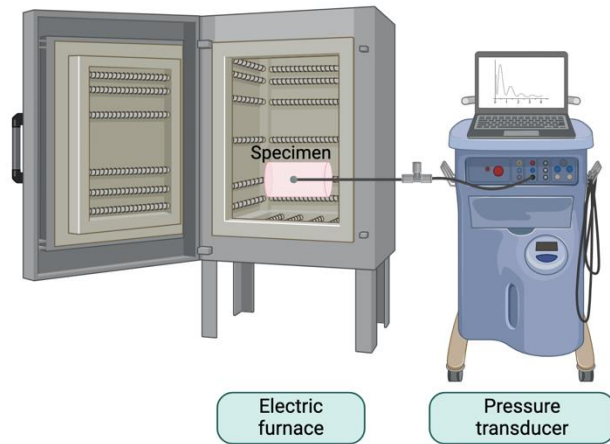


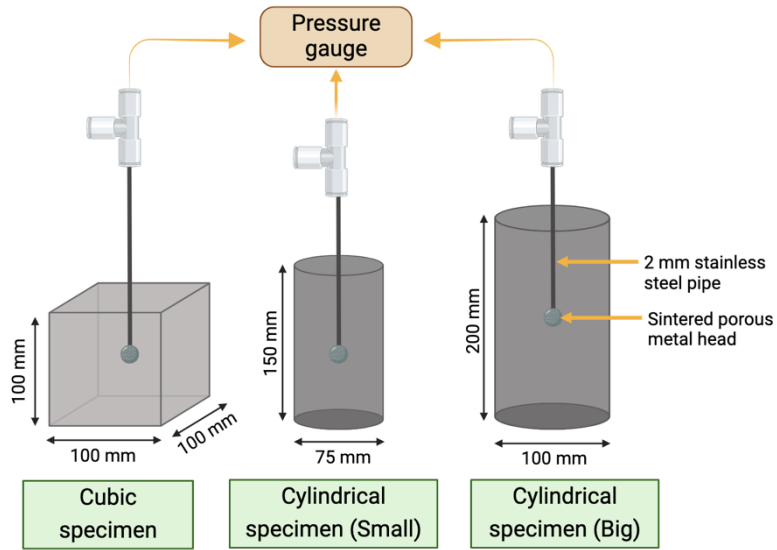
Figure 3.4: Pore pressure build-up in the web of an I-shaped concrete girder exposed to fire

3.3.1. Test Set-Up and Procedure

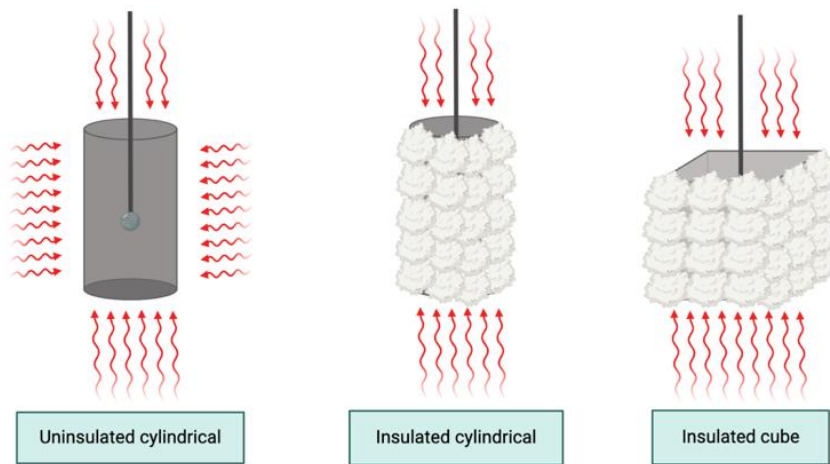
As part of this experimental program, a test set-up for pore pressure measurement was designed and implemented. Figure 3.5 (a) presents the experimental setup, where pressure was captured using a sintered metal head attached to a steel pipe embedded within the concrete specimen. The pipe was filled with thermally-stable silicon oil to transfer the pressure to a pressure transducer outside of the heating chamber. Figure 3.5 (b) illustrates how the steel pipe, filled with thermally stable silicone oil, was connected to a pressure transducer via probes, which in turn was linked to a data acquisition system for real-time pressure measurement. The thermal expansion of silicone oil was disregarded in the reported pore pressure values due to its minimal effect at temperatures below 200°C, as noted in previous studies [117,155]. To prevent exposure of the silicone oil to high temperatures during specimen heating, the section of the steel pipe inside the furnace was insulated with a ceramic fiber blanket. The pressure transducer had a maximum reading capability of 4.0 MPa and the electric furnace used for heating of the specimens is capable of heating at a rate of 10°C/min.



(a) Testing equipment



(b) Pore pressure sensor inside specimens of different shapes and sizes



(c) Insulation and heating exposure conditions

Figure 3.5: Schematic of the pressure testing equipment, specimens, and set-up

The testing procedure involved heating the specimen at various predetermined rates up to 600°C. At this temperature, the specimen contained minimal moisture, which limited further pore pressure accumulation. The chosen heating rates were selected to match those commonly used for material characterization. These rates were specifically chosen due to the susceptibility of high-strength concretes like UHPC to cracking and fire-induced spalling, conditions that could create openings through which pore pressure might be released, thus compromising measurements.

Throughout heating, pore pressure within the concrete specimens and furnace temperature were monitored at regular intervals. Once the furnace reached 600°C, the temperature was maintained constant until the test concluded. The test finished when the measured pore pressure returned to its initial level (below 0.05 MPa). Test durations varied depending on the specific conditions of each experiment; in some cases, tests ended prematurely due to occurrences such as explosive spalling or excessive thermal cracking in the concrete specimens.

3.3.2. Calibration of Pore Pressure Tests

Table 3.4 presents a summary of the test parameters together with the peak pore pressure values measured in each of the 21 tests conducted. Cubic and cylindrical specimens were tested under varying heating rates. Lower heating rates were used for UHPC specimens to minimize the chances of fire induced spalling (since spalling prevents the measurement of pore pressure build-up), as noticed in trial specimens and previous studies [104,112]. Sealed specimens were sealed using aluminum foils of 14 µm thickness and heat-resistant epoxy in addition to the application of the insulation blanket. Specifically, the epoxy material is a commercially available resin used for industrial applications and can resist temperatures up to 280°C. A similar procedure of sealing the unexposed sides of cubic specimens has been conducted in a previous study by Felicetti et al. [154] as a way of creating a more representative simulation of a portion of a concrete member exposed

to heating. Insulation and sealing variables were used to assess pore pressure development in cubic specimens made with NSC and UHPC-ST. The significance of all studied variables on pressure measurement will be analyzed in section 3.3.4.

Table 3.4: Testing parameters and measured peak pore pressure

Concrete type - Specimen #	Specimen geometry	Dimensions (mm)	Insulation	Sealing	Heating rate (°C/min)	Peak pore pressure (MPa)
NSC-1	Cube	100x100x100	Yes	No	10	0.59
NSC-2	Cube	100x100x100	Yes	No	10	0.50
NSC-3	Cube	100x100x100	Yes	No	5	1.08
NSC-4	Cube	100x100x100	Yes	No	5	1.31
NSC-5	Cube	100x100x100	Yes	Yes	10	1.12
NSC-6	Cube	100x100x100	Yes	Yes	5	1.76
NSC-7	Cube	100x100x100	Yes	Yes	2.5	0.84
NSC-8	Cylinder	75x150	Yes	No	10	0.88
NSC-9	Cylinder	75x150	No	No	10	0.82
NSC-10	Cylinder	75x150	No	No	5	0.85
UHPC-ST-1	Cube	100x100x100	Yes	No	1	0.70
UHPC-ST-2	Cube	100x100x100	Yes	No	1.5	0.40
UHPC-ST-3	Cube	100x100x100	Yes	No	2	0.10
UHPC-ST-4	Cube	100x100x100	Yes	No	5	0.10
UHPC-ST-5	Cube	100x100x100	Yes	Yes	1.5	0.40
UHPC-ST-6	Cube	100x100x100	Yes	Yes	1	0.18
UHPC-ST-7	Cylinder	75x150	No	No	1	4.00*
UHPC-ST-8	Cylinder	100x200	No	No	1	0.09
UHPC-ST-9	Cylinder	100x200	No	No	1.5	4.00*
UHPC-ST-PP-1	Cube	100x100x100	Yes	Yes	1	0.70
UHPC-ST-PP-2	Cylinder	75x150	No	No	1	1.72

(*) Reached pressure gauge limit of 4.00 MPa

Thermocouples were employed to monitor temperature progression during the tests. Initial trials revealed that placing a thermocouple within the same steel pipe used for pore pressure measurement could result in some pressure leakage, potentially compromising measurement

accuracy. Therefore, it was decided not to measure temperatures inside the concrete specimens simultaneously with pore pressure. To measure temperature progression within specimens of similar conditions, a second series of tests was conducted on duplicate specimens. These specimens were cast with thermocouples positioned in the same locations as the pore pressure probes used in the initial set. Figure 3.6 illustrates the temperature increase over time during fire exposure for different types of concrete subjected to varying heating rates.

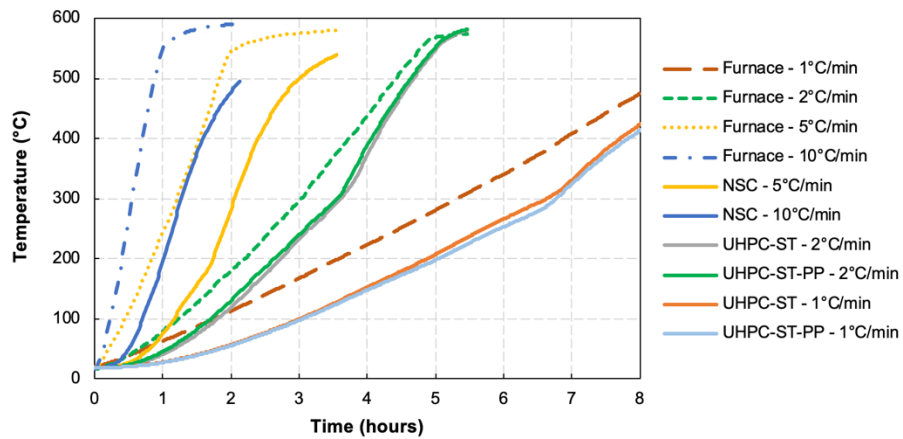


Figure 3.6: Progression of temperatures in the specimens under varying heating rates

3.3.3. *Checking the Validity of the Proposed Test Set-Up*

To ensure the accuracy and reliability of the experimental configuration, a series of pore pressure tests conducted in this study were used to validate the findings by repeating tests and comparing them with previously published results [117,154]. Four cubic specimens of Normal Strength Concrete (NSC) were subjected to unidirectional heating rates: 10°C/min (NSC-1 and NSC-2) and 5°C/min (NSC-3 and NSC-4), and the measured pore pressure during these tests are presented in Figure 3.7. Initially, pore pressure increases gradually, accelerates to peak pressure, and then gradually decreases, forming a bell-shaped curve. These results clearly demonstrate that the heating rate influences both the timing and magnitude of peak pressure. However, slight variations in peak pressure among specimens subjected to similar conditions can be attributed to

concrete heterogeneity and the degradation of concrete properties as temperature increases. Variations in concrete components (such as aggregate or cement paste) around the sensing head may result in different captured moisture contents by the pore pressure probe. Additionally, concrete degradation at elevated temperatures can lead to the formation of microcracks, creating pathways through which water vapor escapes, thereby causing pore pressure variations among similar specimens. Overall, there is substantial agreement between the results obtained under similar testing conditions, indicating that the proposed experimental setup yields reliable outcomes.

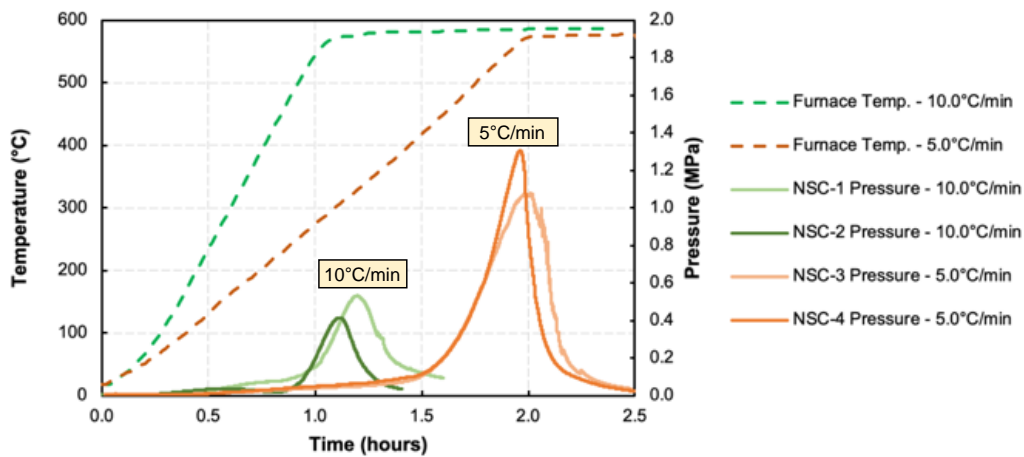


Figure 3.7: Pore pressure measurements in NSC specimens for validation

The results shown in Figure 3.7 also indicate that pore pressure accumulation was more pronounced in specimens subjected to a lower heating rate (NSC-3 and NSC-4). This phenomenon can be attributed to the formation of thermal cracks in concrete, which increase in both size and number under higher heating rates. These microcracks connect previously isolated pores, creating pathways through which water vapor can migrate, thereby reducing the maximum pore pressure observed. Another explanation for this behavior relates to the specific location where moisture clog forms within the concrete specimen, as depicted in Figure 3.8. At higher heating rates, water vapor may not migrate as far from the specimen surface due to rapid evaporation, resulting in the

formation of the moisture clog closer to the exposed surface and farther from the location of the pressure probe. Therefore, in the results presented in Figure 3.7, the lower measured peak pressure in specimens subjected to higher heating rates ($10^{\circ}\text{C}/\text{min}$) do not necessarily indicate lower overall pore pressure. Instead, it suggests that the peak pressure might be occurring at a different location within the specimen, away from where the pressure probe is positioned.

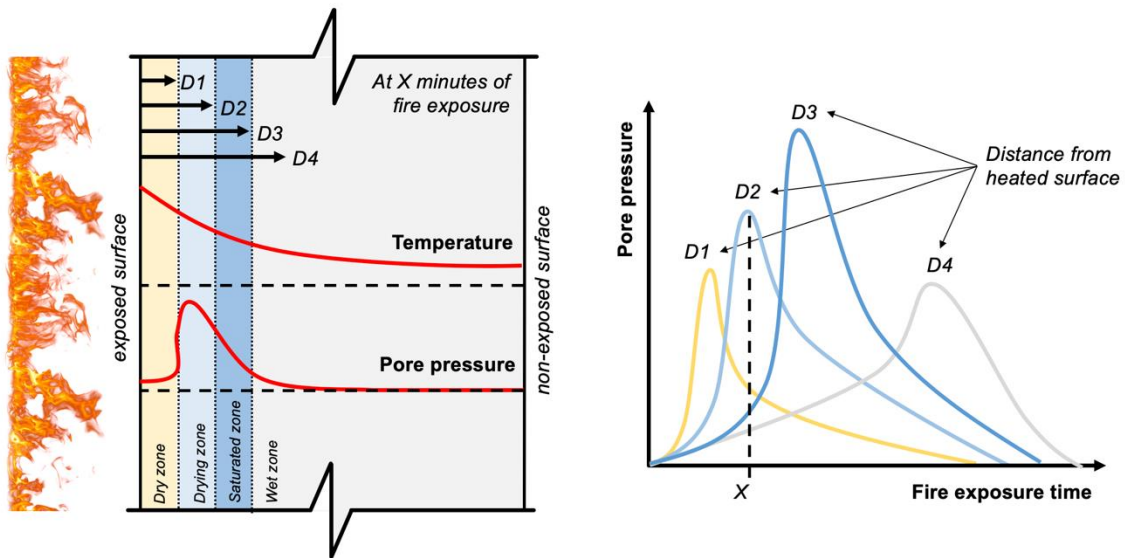


Figure 3.8: Schematic of pore pressure variation along the distance from the heated surface

To further assess the measured pore pressure results, Figure 3.9 compares the peak pressures obtained from pore pressure measurements in Figure 3.7 with those reported in other studies. The studies by Kalifa et al. [65] and Felicetti et al. [154] were selected for comparison due to similarities in their experimental setups: (a) similar concrete compositions and compressive strength ranges; (b) pore pressure probes positioned 50 mm from the heated surface; and (c) specimens heated at a consistent rate of $10^{\circ}\text{C}/\text{min}$. However, there are notable differences: Kalifa et al. [65] tested larger specimens ($300 \times 300 \times 120 \text{ mm}^3$) heated from one side, resulting in higher moisture content within the specimens available for pore pressure buildup. In contrast, Felicetti et al. [154] subjected specimens to an imposed compressive load, which reduces pore size and restricts crack formation that typically facilitates pore pressure release.

As depicted in Figure 3.9, the maximum pore pressure observed in this study is lower compared to previous studies. This difference can be attributed to variations across different experimental programs, including the age and moisture content of the specimens, as well as other inherent characteristics and exposure conditions. These fundamental differences in test setups and procedures make direct comparisons between studies challenging. Despite these variations, it is generally acceptable to conclude that the results obtained in this study fall within a reasonable range. Therefore, the experimental setup proposed in this study demonstrates the ability to reliably track the evolution of pore pressure over time.

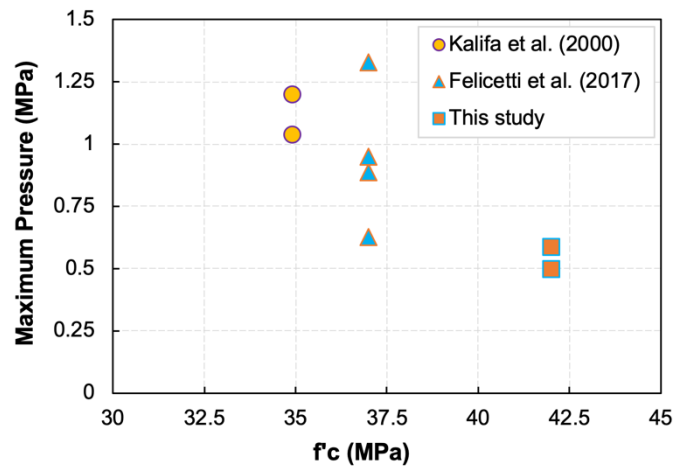


Figure 3.9: Comparing maximum pressure measured with other similar studies

3.3.4. Results and Discussion

The data generated from the tests clearly demonstrate that specimen geometry and test conditions exert a significant influence on pore pressure build-up. Therefore, the results from pore pressure measurements are presented across different influencing parameters, including concrete strength (NSC and UHPC), specimen shapes (cubic and cylindrical), and exposure conditions (insulated and sealed) and varying heating rates.

3.3.4.1. Evolution of Pore Pressure in UHPC Cubic Specimens

Four cubic UHPC-ST (reinforced solely with steel fibers) specimens were subjected to varying heating rates to assess pore pressure build-up during heating. Given UHPC's susceptibility to explosive spalling, the specimens were tested at lower heating rates (1.0, 1.5, 2.0, and 5.0°C/min). Additionally, these specimens were insulated on their sides to ensure a uni-directional heating condition. Figure 3.10 displays the results of pore pressure measurements from these UHPC specimens. The highest pore pressure was observed in the specimen exposed to a heating rate of 1.0°C/min (UHPC-ST-1), followed by the specimen exposed to 1.5°C/min (UHPC-ST-2). In contrast, specimens subjected to 2.0 and 5.0°C/min (UHPC-ST-3 and UHPC-ST-4) did not exhibit a distinct peak in pressure and showed minimal pore pressure buildup compared to those exposed to lower heating rates. Figure 3.11 illustrates the condition of specimens tested at higher heating rates (2.0 and 5.0°C/min), revealing significant cracking in UHPC-ST-3 and explosive spalling in UHPC-ST-4 during the tests. This behavior is attributed to the dense microstructure of UHPC, which inhibits the release of pore pressure, as well as differential thermal expansion of UHPC components that generates internal stresses within the specimens. The development of cracks and spalling compromises pore pressure measurements due to the sudden release of water vapor during heating.

Overall, the pressure level measured in UHPC specimens is notably lower than anticipated, considering the dense nature and explosive tendencies of UHPC. It was expected that UHPC specimens would exhibit higher pressures compared to NSC specimens. However, previous studies have already documented similar relatively low pore pressure values in UHPC [140,146,151]. This behavior is attributed to UHPC's high susceptibility to cracking and spalling, which leads to premature pressure release before reaching peak pore pressure. Another contributing factor to this

behavior is the low permeability of UHPC, which restricts moisture penetration into deeper regions of the specimens and results in the formation of moisture blockages closer to the heated surface. As seen in these results, lower heating rates (e.g., 1.0°C/min) allow pore pressure to accumulate to higher levels in UHPC specimens. However, unlike NSC specimens that typically exhibit a bell-shaped curve after reaching peak pressure, UHPC specimens show an abrupt decrease in pore pressure, indicating the formation of cracks or similar mechanisms that facilitate pressure release. These findings suggest that the dynamics of pore pressure buildup and measurement in UHPC differ from those in conventional concretes. This is influenced by the complexities involved in conducting tests, such as the use of lower heating rates, as well as the propensity for cracking and spalling, which can compromise pore pressure measurements.

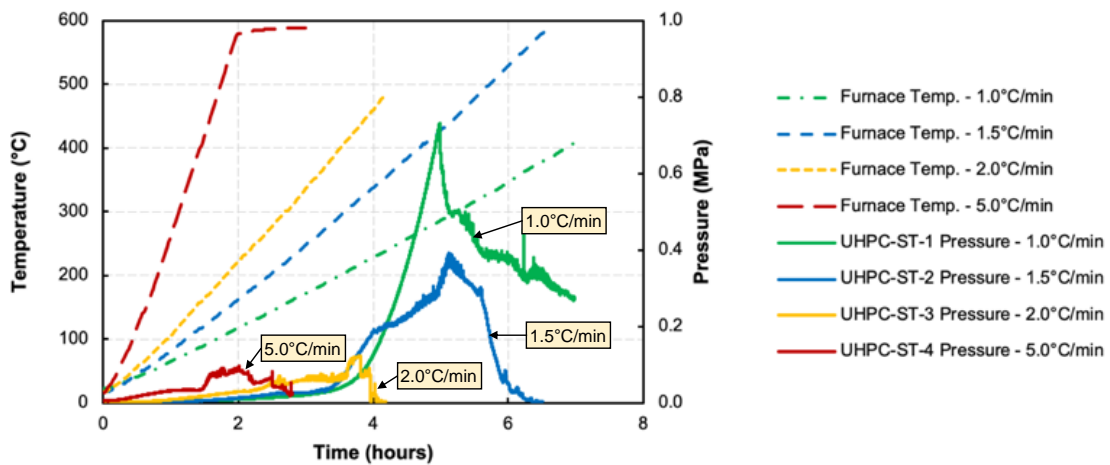


Figure 3.10: Pore pressure build-up in UHPC specimens subjected to varying heating rates



Figure 3.11: Cracking and spalling of UHPC specimens after testing

3.3.4.2. Evolution of Pore Pressure in Cylindrical Specimens

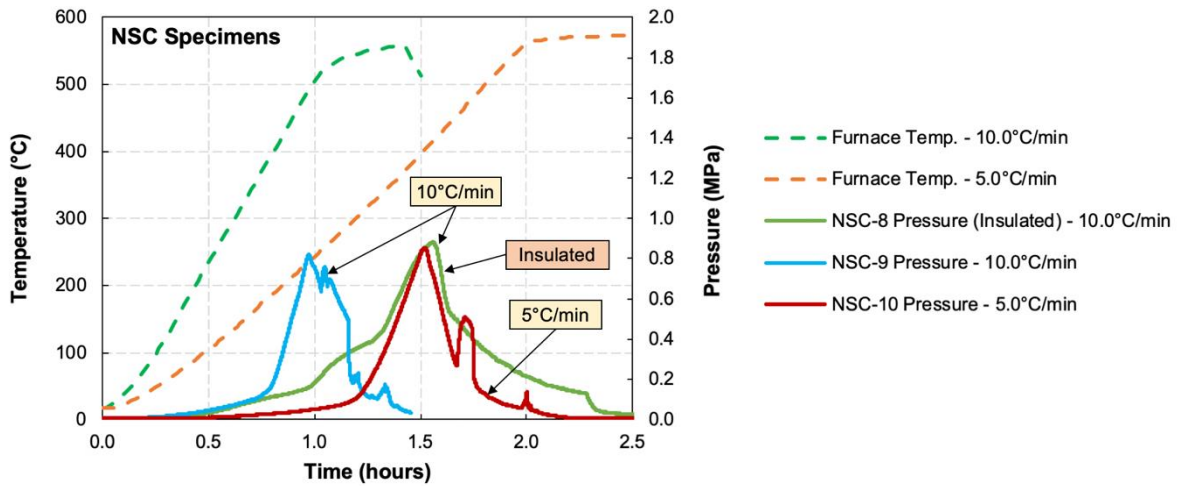
The next set of tests aimed to evaluate pore pressure development in cylindrical specimens made of NSC and UHPC, with and without polypropylene fibers, under various heating rates and insulation conditions. Figure 3.12 (a) illustrates the results from pore pressure tests conducted on NSC cylindrical specimens with 75 mm diameter and 150 mm height. The measured peak pressure was very close across all the specimens, ranging between 0.82 MPa and 0.88 MPa. One of the cylindrical specimens (NSC-8) was insulated to simulate uni-directional thermal flow, similar to the cubic specimens. Comparing this insulated specimen with an uninsulated one (NSC-9) heated at 10°C/min, it is observed that the peak pressure for the uninsulated specimen occurred at 60 minutes, while for the insulated specimen it occurred at 90 minutes. This delay can be attributed to the presence of insulation, which slows the propagation of heat within the specimen, consequently delaying pore pressure buildup. Alternatively, the delay could be due to the insulated specimens experiencing heating from both the top and bottom, resulting in the sensor probe being 75 mm from the heated surface. In contrast, uninsulated specimens are heated from all sides, placing the sensor probe 37.5 mm from the heated surface. The increased distance between the probe and the heated surface results in a longer path for moisture migration and pore pressure

buildup. Thus, it can be inferred that the peak pressure measured in the insulated specimen occurs between the sensor probe and the heated surface, and may not represent the highest pressure level reached inside the specimen. Furthermore, the uninsulated specimen heated at a lower rate of 5.0°C/min exhibited a similar curve to the insulated specimen heated at 10.0°C/min. This highlights the high influence of heating rate, which affects the rate of moisture migration through the concrete pore system and the distance it travels to reach the sensor probe. It is important to note that pore pressure curves for cylindrical specimens (as shown in Figure 3.12) did not exhibit a well-defined bell shape as observed in cubic specimens. This reflects the occurrence of microcracks within the concrete that result in some pressure release during the heating process.

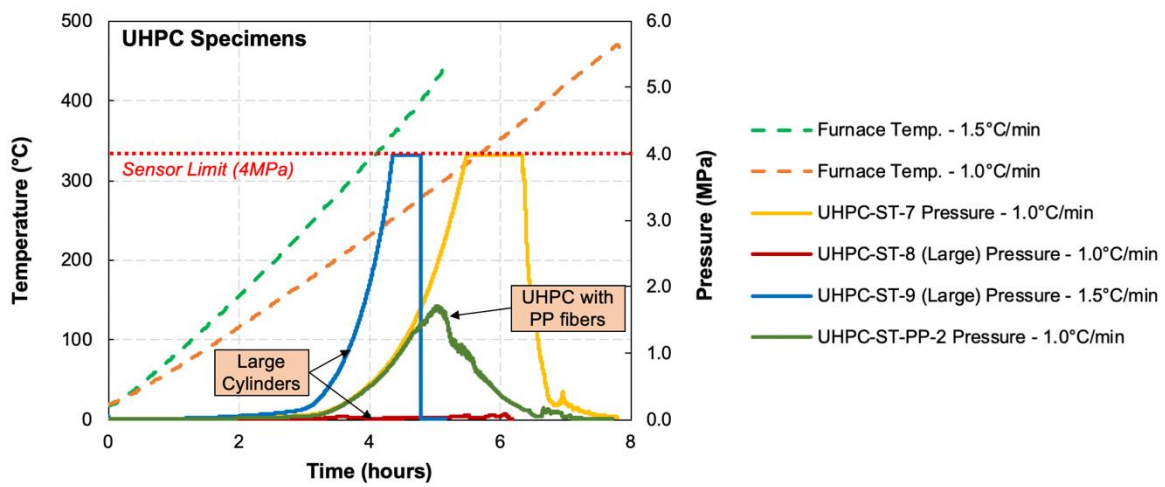
Small (75 mm diameter and 150 mm height) and large (100 mm diameter and 200 mm height) cylindrical UHPC specimens were tested to investigate the impact of specimen dimensions on pore pressure buildup. The results from these tests are illustrated in Figure 3.12 (b). Firstly, it is important to note that significantly higher pressure values were recorded in these specimens, surpassing the sensor limit of 4.0 MPa. Consequently, a flat reading was obtained at this maximum pressure level. The larger UHPC specimens (UHPC-ST-8 and UHPC-ST-9) were identical in composition to the smaller specimens (UHPC-ST-7 and UHPC-ST-PP-2) and were tested without any sealing or insulation under two heating rates: 1.0°C/min and 1.5°C/min. The larger specimen subjected to 1.5°C/min (UHPC-ST-9) exhibited a bell-shaped pore pressure buildup and exceeded the 4.0 MPa limit. In contrast, the larger specimen subjected to 1.0°C/min (UHPC-ST-8) did not show any distinct pressure peak during heating. Post-test observations revealed that this specimen (UHPC-ST-8) experienced explosive spalling, as shown in Figure 3.13, which compromised pressure measurements during the test. The other specimen (UHPC-ST-9) also exhibited cracking but managed to develop a pressure peak due to the higher heating rate. This highlight, once again,

the unpredictable nature of fire-induced spalling and the high susceptibility of high-strength concretes to this phenomenon.

In the smaller UHPC cylindrical specimens exposed to a heating rate of $1.0^{\circ}\text{C}/\text{min}$, a similar trend was observed. The small UHPC specimen (UHPC-ST-7) reached the sensor pressure limit of 4.0 MPa, indicating that the peak pressure was significantly higher in this specimen. Unlike the larger specimen that also reached the pressure sensor limit but exhibited an abrupt drop at the end of the test, the smaller specimen maintained the bell-shaped curve throughout its pressure curve decline. This suggests that pore pressure build-up was fully developed in this specimen and that the peak pressure in UHPC specimens can be notably higher than in NSC specimens. The other small UHPC specimen (UHPC-ST-PP-2), reinforced with polypropylene fibers, exhibited a pore pressure buildup of 2 MPa. This can be attributed to the polypropylene fibers melting at lower temperatures (approximately 160°C), which creates channels for water vapor to migrate and evaporate without generating such high pressure peaks [115,146,149,207]. Additionally, the shorter distance between the heated surface and the pressure sensor inside the smaller UHPC specimens facilitated the capture of pore pressure closer to its peak values.



(a) NSC specimens



(b) UHPC specimens

Figure 3.12: Pore pressure build-up in cylindrical specimens subjected to varying heating rates



Figure 3.13: Explosive spalling of a large UHPC cylindrical specimen (UHPC-ST-8)

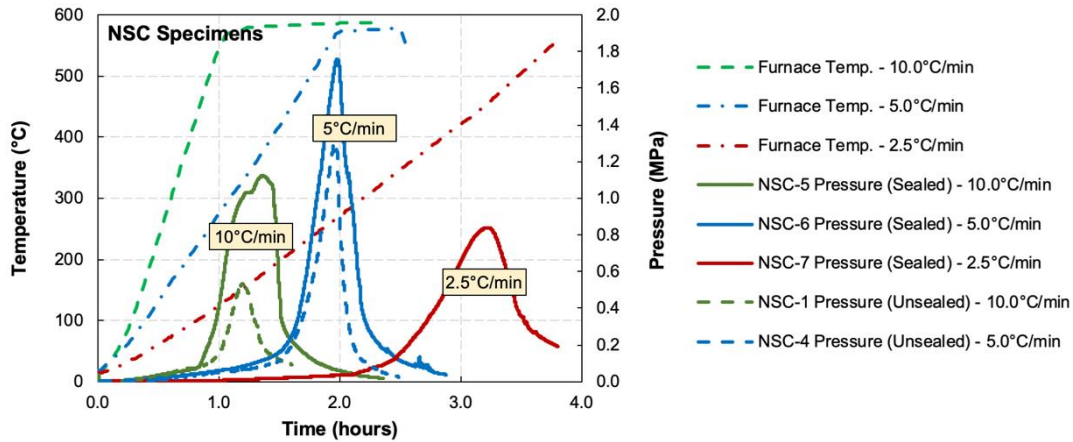
3.3.4.3. Evolution of Pore Pressure in Sealed Specimens

To assess how heat transfer affects pore pressure development, all cubic specimens were insulated to replicate a mono-directional heat flux. It is important to note that thermal insulation restricts heat transfer, though moisture loss can still occur through the sides of the specimen. Sealing the specimen before applying thermal insulation prevents moisture loss through the sides and establishes a mono-directional moisture flow. Felicetti [154] tested different sealing materials and demonstrated that using heat-resistant epoxy resin with aluminum foils was the most effective approach. Consequently, three NSC cubic specimens and three UHPC cubic specimens were sealed prior to insulation and tested under different heating rates.

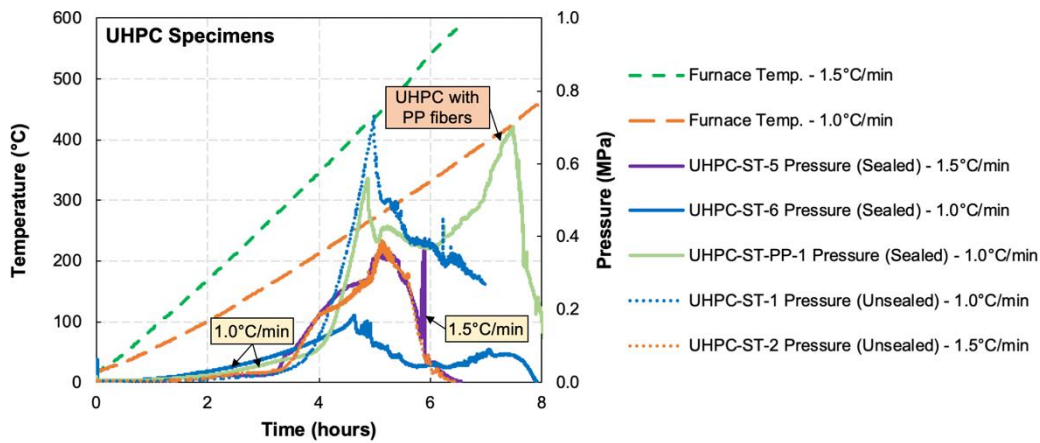
Figure 3.14 (a) shows the pore pressure buildup results in sealed NSC specimens subjected to heating rates of 2.5°C/min, 5.0°C/min, and 10.0°C/min. Comparing these results with unsealed (but insulated) NSC cubic specimens, it can be seen that specimens heated at 5.0°C/min (NSC-4 and NSC-6) and 10.0°C/min (NSC-1 and NSC-5) reached peak pressure at very similar heating durations (1.2 hours and 2.0 hours, respectively). This reaffirms that the timing of peak pressure is influenced by the sensor probe's location relative to the exposed surface. However, sealed specimens exhibited significantly higher peak pressures compared to unsealed specimens. Under a heating rate of 5.0°C/min, for instance, the maximum measured pore pressure increased from 0.55 MPa to 1.12 MPa (from NSC-4 to NSC-6), and under a 10.0°C/min heating rate, it rose from 1.20 MPa to 1.76 MPa (from NSC-1 to NSC-5). These findings demonstrate that sealing the specimen sides reduces moisture loss and results in higher pore pressure levels. A third sealed NSC cubic specimen tested at an even lower heating rate of 2.5°C/min (NSC-7) showed a lower peak pressure (0.84 MPa) compared to other heating rates. This can be attributed to the slower migration of moisture through the concrete pore system under lower heating rates, leading to the

formation of a moisture clog closer to the heated surface. Thus, these results confirm that the heating rate significantly influences peak pressure, a critical consideration in designing future experimental setups for pore pressure measurements.

Figure 3.14 (b) provides a comparison between the results obtained from tests on sealed UHPC cubic specimens with unsealed UHPC specimens exposed to the same heating rates. Both sealed and unsealed specimens exhibited similar behaviors. For instance, the specimen exposed to a lower heating rate of 1.0°C/min (UHPC-ST-6) showed a lower peak pressure compared to a similar specimen exposed to a higher heating rate of 1.5°C/min (UHPC-ST-5). The fluctuating pressure curves in both specimens reflect the occurrence of cracking and other physical processes inherent to UHPC, contributing to unpredictable pore pressure behavior. A third sealed cubic specimen, composed of UHPC reinforced with both steel and polypropylene fibers (UHPC-ST-PP-1), displayed two distinct pressure peaks during heating. After reaching the first peak, there was a sudden pressure drop due to cracking, followed by a gradual buildup leading to a second, higher peak of pressure before gradually decreasing again. The presence of polypropylene fibers facilitated higher peak pressures. Overall, these results demonstrate the challenges associated with measuring pore pressure build-up in high-strength concretes like UHPC, primarily due to their susceptibility to cracking and spalling during heating.



(a) NSC specimens



(b) UHPC specimens

Figure 3.14: Pore pressure build-up in sealed specimens subjected to varying heating rates

3.4. Shear Strength Measurements

Shear strength of concrete helps to resist vertical concentrated forces applied in flexural members as well as interfacial shear resulting from the applied prestressing forces. The shear strength of UHPC is generally higher than other types of concrete due to its intrinsic higher tensile strength. Steel fibers have a significant contribution to these properties and its effect has been studied for different types of concretes and fibers, mostly aiming a reduction of conventional shear reinforcement. However, when exposed to elevated temperatures, concrete experiences degradation of its mechanical properties which can lead to rapid loss of a member capacity. This

can be an issue for UHPC girders due to the use of slender web sections and the lack of shear reinforcement, leading to early shear failure and lower fire resistance.

Determining the level of degradation of shear strength through experimental tests provides important information that can help guide the design of structures to resist fire incidents. Direct shear strength tests offer a simple way of measuring the shear strength of concrete. This section presents results of an experimental program conducted to determine the degradation of UHPC shear strength exposed to elevated temperatures [208]. UHPC specimens made with and without steel and polypropylene fibers were exposed to different levels of temperature, varying from 20 to 750°C, and then tested under direct shear through a modification of the JSCE-SF6 [205] method. Details on the test set-up and procedure, as well as results and their validity are discussed herein.

3.4.1. Test Set-Up and Procedure

The equipment for evaluating the shear strength of UHPC at elevated temperatures consisted of an electric heating furnace and a strength testing machine. A cylindrical electric furnace capable of heating at a specified heating rate (maximum to 10°C/min) and maintaining a target temperature for a specified period of time was utilized to heat the specimens. For loading, a 2670 kN load-controlled Forney compressive testing machine was utilized. This machine has a digital interface that allows the control of different test parameters, such as loading rate and the failure point, and is capable of capturing the resulting deflection during the test. To apply shear load, a special apparatus was developed based on JSCE-SF6 [205] test method. It consists of a loading block and a support block, both made of steel with two loading knife edges each. A narrow span of 0.15 mm (0.006 in) is left between the edges of the loading and the support blocks to impose a concentrated shear stress over the specimen's notched section, where failure is expected.

Figure 3.15 shows a schematic illustration and a photograph of the final test set-up adopted for undertaking shear strength tests.

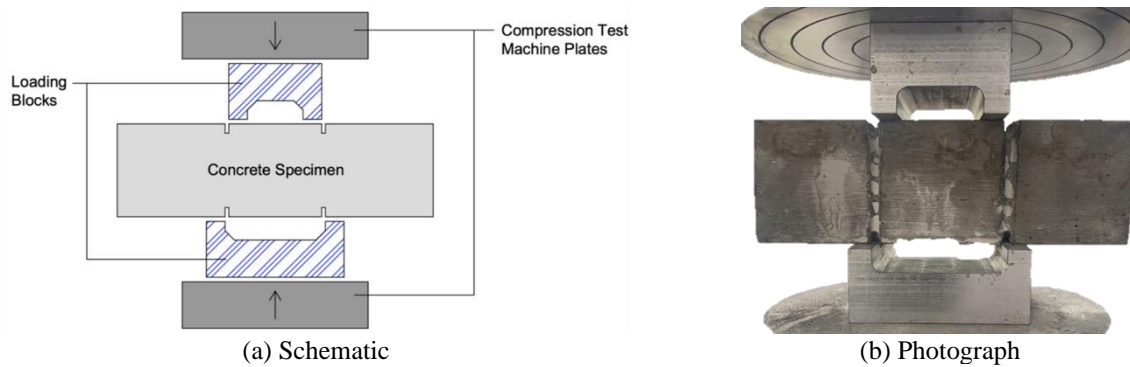


Figure 3.15: Specimen and apparatus for shear strength test

The UHPC specimens were tested in the unstressed testing regime. This testing regime aimed to simulate the fire behavior of concrete in a structural member with a small pre-load, such as the web of beam exposed to predominant flexural loads. Therefore, specimens were first heated to a targeted temperature without the application of any load. A heating rate of $2^{\circ}\text{C}/\text{min}$ was selected based on previous studies [112]. After reaching the targeted temperature, specimens were kept in that temperature for 30 to 45 minutes, so the targeted temperature was reached in the inner parts of the specimen. Figure 3.16 presents the targeted and measured temperatures inside of the furnace during heating of the specimens. Two specimens were heated at the same time in the furnace. While the first specimen was removed from the furnace to be tested, the other one remained in the furnace at the targeted temperature until the first test was completed.

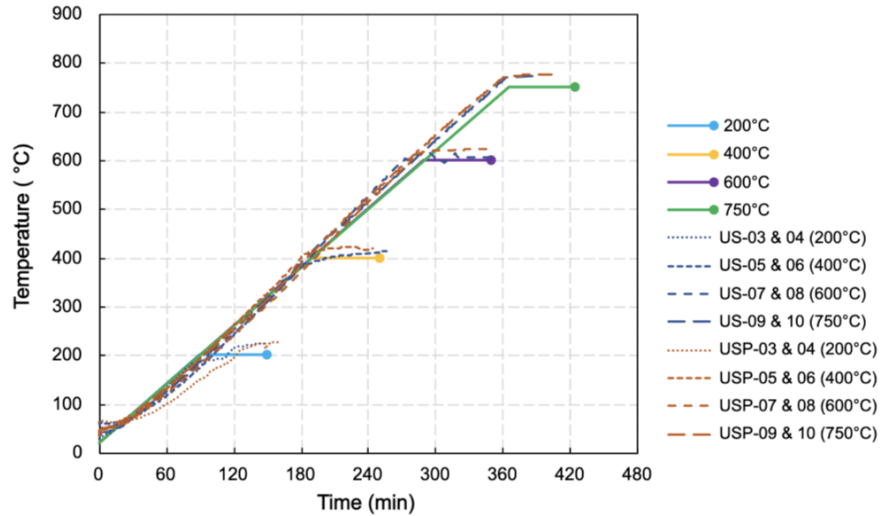


Figure 3.16: Targeted and measured temperatures in the furnace during heating of the specimens

The heated specimens were moved into the strength test machine where the shear test apparatus was installed. The process of moving the specimen from the furnace to the strength test machine and initiating the test took approximately two minutes. The test was conducted by applying load continuously until failure. Load was applied at a rate of 2 kN/min, which is within the shearing stress rate of 0.06 to 0.1 MPa/second prescribed by JSCE-SF6 [205]. Displacement was measured during the test by the movement of the loading plates generated by the strength test machine. Applied load and displacement data were recorded at a frequency of 0.55 Hz. Figure 3.17 presents the increase of loading ratio during one of trial tests.

The heated specimens were moved into the strength test machine where the shear test apparatus was installed. The process of moving the specimen from the furnace to the strength test machine and initiating the test took approximately two minutes. The test was conducted by applying load continuously until failure. Load was applied at a rate of 2 kN/min, which is within the shearing stress rate of 0.06 to 0.1 MPa/second prescribed by JSCE-SF6 [205]. Displacement was measured during the test by the movement of the loading plates generated by the strength test

machine. Applied load and displacement data were recorded at a frequency of 0.55 Hz. Figure 3.17 presents the increase of loading ratio during one of trial tests.

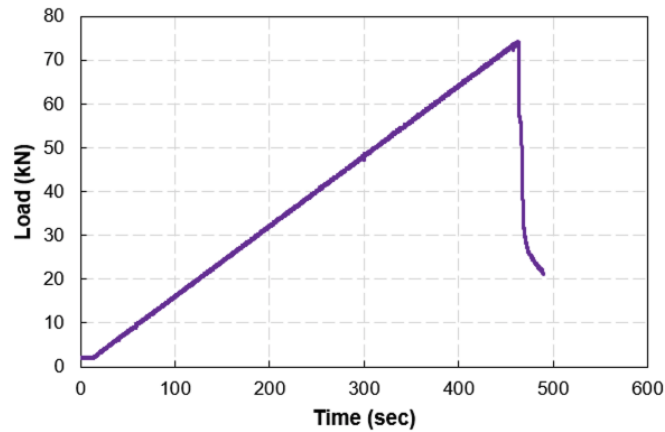


Figure 3.17: Targeted and measured temperatures in the furnace during heating of the specimens

3.4.2. Results and Discussion

Table 3.5 presents a summary of results from the tests conducted, including maximum temperature of exposure and the ultimate shear strength. The peak load (P_{max}) obtained in the tests was converted to ultimate shear strength (τ_{max}) through the following equation:

$$\tau_{max} = \frac{P_{max}}{2 (b_{eff} \cdot d_{eff})} \quad (3.1)$$

where b_{eff} and d_{eff} are the effective width and depth of the specimen, respectively. These dimensions were determined as the average of two measurements taken on each notched section of each specimen before the test. It should be noted that this equation assumes an elastic response and represents the average stress distribution between both shear sections.

Table 3.5: Summary of test results

Concrete type	Specimen designation	Temperature (°C)	Shear strength (MPa)	Shear strength reduction (%)
UHPC	U-01	20.0	26.3	100.0%
	U-02	199.8	18.4	70.0%
	U-03	414.3	16.4	62.4%
	U-04	614.9	5.6	21.3%
UHPC-ST	U-S-01	20.0	38.3	100.0%
	U-S-02	20.0	37.7	98.4%
	U-S-03	223.9	20.2	52.7%
	U-S-04	223.9	27.2	71.0%
	U-S-05	414.3	25.6	66.8%
	U-S-06	414.3	35.8	93.5%
	U-S-07	614.9	27.5	71.8%
	U-S-08	614.9	10.8	28.2%
	U-S-09	772.0	14.2	37.1%
	U-S-10	772.0	17.6	46.0%
UHPC-ST-PP	U-SP-01	20.0	49.6	100.0%
	U-SP-02	20.0	20.9	42.1%
	U-SP-03	227.9	19.7	39.7%
	U-SP-04	227.9	38.6	77.8%
	U-SP-05	423.2	35.7	72.0%
	U-SP-06	423.2	32.7	65.9%
	U-SP-07	621.8	25.8	52.0%
	U-SP-08	621.8	23.0	46.4%
	U-SP-09	775.6	13.9	28.0%
	U-SP-10	775.6	12.6	25.4%

Shear stress-displacement curves for multiple specimens tested at different levels of temperature are shown in Figure 3.18. It can be seen in these graphs that for some specimens there were a lot of fluctuations with abrupt increase and decrease of load. This behavior reflects crack openings and the effect of steel fibers bridging cracks in the specimen. Some variation can also be observed between specimens tested under similar conditions, as shown in Table 3.5. These

variations can be attributed to fiber orientation due to the fact that steel fibers are randomly dispersed in the mixtures.

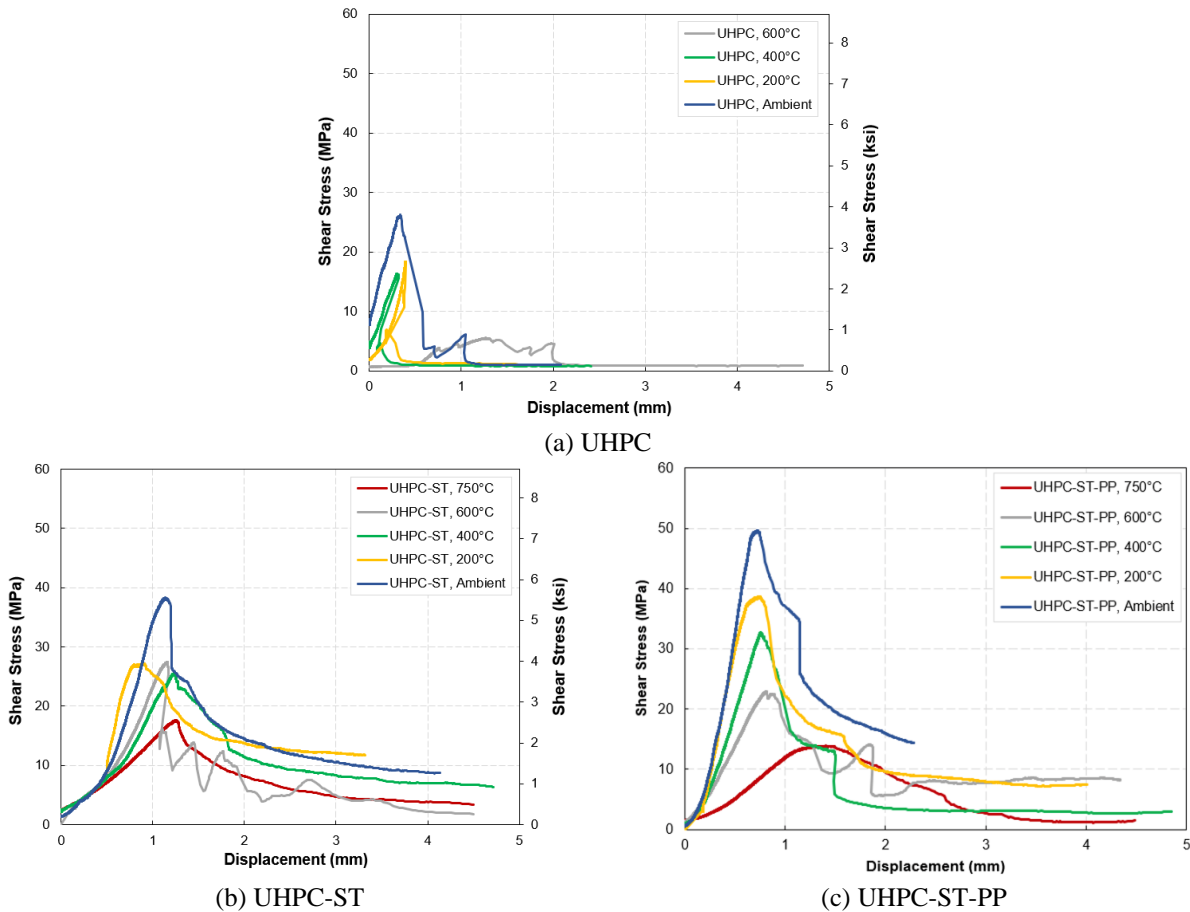


Figure 3.18: Shear stress-displacement curves for specimens at different levels of temperature

As expected, plain UHPC specimens presented an abrupt and sudden failure, as well as lower shear strength than the specimens reinforced with steel fibers. These specimens lost their ability to carry load instantly after cracking, without a residual load-carrying capacity beyond the peak load. There was not much difference in the behavior of specimens exposed to 200°C and 400°C, even though there was a decrease of approximately 35% in shear strength, when compared to the specimen tested at ambient conditions. For the specimen exposed to 600°C, there was a very significant decrease of shear strength of about 80% and a well-defined load peak cannot be observed. It should be noted, however, that the shear strength obtained for plain UHPC represents

a significant portion of the shear strength of UHPC-ST specimens. Besides, these strength values are much higher than obtained for plain conventional concretes in previous studies [206].

Fiber reinforced UHPC specimens were able to support higher shear stresses than plain UHPC. The specimens containing steel and polypropylene fibers sustained higher shear stresses than the specimens reinforced only with steel fibers. This can be attributed to the fact that polypropylene fibers melt around 160°C, creating voids inside concrete that help relieve some of the thermal stresses generated due to the development of high pore pressure during heating [209]. However, a steep degradation of shear strength was still observed when specimens were exposed to higher levels of temperature. In both situations, degradation of shear strength reached 50% of its original strength at room temperature. While it is possible to see a clear degradation on the peak of stress for specimens containing polypropylene fibers, the peak of stress in specimens containing only steel fibers was very similar along the temperature range between 200°C and 500°C.

Figure 3.19 presents shear strength as a function of the temperature of exposure. It can be seen that shear strength decreases with the increase of temperature and such behavior is dependent on the type of fiber reinforcement in the specimens. Such relationship can be used to model the fire behavior of UHPC beams exposed to fire and help to predict the shear capacity of the fire exposed UHPC beams. The linearized shear strength of each UHPC mixture as a function of the temperature of exposure T , in Celsius degrees, is presented in Equations (3.2) to (3.4). The R^2 for the UHPC-ST mixture is lower than for the other mixtures, but still presents a significative relation.

$$\tau_{T,UHPC}/\tau_{UHPC} = 1.013 - T \times 1.2 \times 10^{-3} \quad (R^2 = 0.93) \quad (3.2)$$

$$\tau_{T,UHPC-ST}/\tau_{UHPC-ST} = 1.004 - T \times 0.7 \times 10^{-3} \quad (R^2 = 0.80) \quad (3.3)$$

$$\tau_{T,UHPC-ST-PP}/\tau_{T,UHPC-ST-PP} = 1.041 - T \times 0.9 \times 10^{-3} \quad (R^2 = 0.96) \quad (3.4)$$

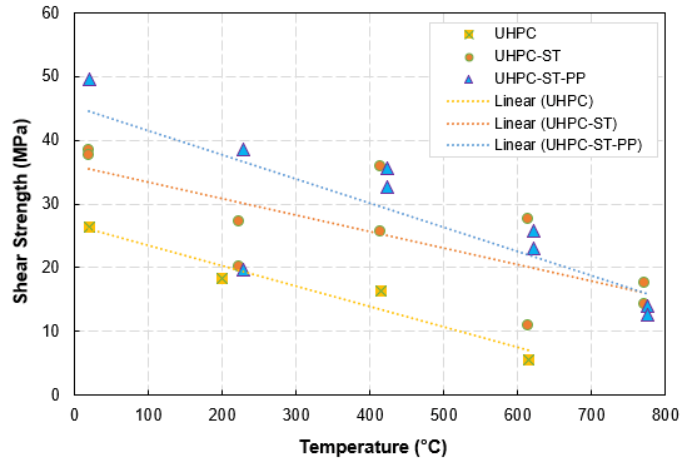


Figure 3.19: Degradation of shear strength with temperature

3.5. Summary

As part of the experimental studies conducted in this dissertation, measurements were performed to assess pore pressure build-up and shear strength degradation of UHPC at elevated temperatures. These tests provide crucial insights into two key factors that influence the fire response of concrete bridges, particularly of UHPC members. Based on the pore pressure build-up measurements, the following observations are drawn:

1. The location of the pressure peak can vary within a concrete specimen depending on its permeability and the heating rate applied during testing. Less permeable concretes exhibit peak pressures closer to the heated surface, whereas more permeable ones allow water vapor to migrate deeper. Therefore, consideration to sensor placement is crucial for accurately measuring the maximum pressure levels in a concrete specimen.
2. Heating rates higher than 2°C/minute induce cracking and spalling in UHPC, leading to the premature release of pore pressure and compromising measurement reliability. In contrast, lower heating rates facilitate water vapor to penetrate into deeper layers of NSC specimens, resulting in higher pressure levels.

3. Sealing and insulating specimen sides with aluminum foils and heat-resistant epoxy enhance pressure measurements by reducing moisture loss through unexposed surfaces and establishing a mono-directional moisture flow through the specimens.
4. Smaller specimens, due to their higher surface area relative to volume, facilitate easier outward movement of free moisture, which hinders the formation of moisture clogs and thereby limits the attainment of peak pressure.
5. The absence of a standardized procedure for pore pressure measurements limits the applicability of test results for development of predictive models to mitigate fire-induced spalling in concrete structures. Addressing these influencing factors, future experimental programs can be designed toward developing a standardized test procedure.

Based on the findings from shear strength measurements at elevated temperatures, the following observations are drawn:

1. The JSCE-SF6 method with the modifications proposed in this study can be effectively used to obtain shear characteristics of UHPC at elevated temperatures.
2. Both steel and polypropylene fibers improved shear strength of UHPC at elevated temperatures. While steel fibers had more contribution due to its ability of bridging cracks in the specimen, polypropylene fibers contributed to a higher shear strength through melting during the heating process, which reduced the formation of microcracks during heating and increased its ability to resist higher loads.
3. The three types of UHPC experienced some loss of shear strength when exposed to 200°C, but the effect of temperature became more pronounced when exposed to temperature levels higher than 400°C. Without fibers, UHPC experienced much faster

degradation and the contribution of polypropylene fibers became less pronounced at higher levels of temperature.

The relations and observations derived from these experimental tests provide important insights on specific characteristics of concrete at elevated temperatures, as well as for the design of future experimental programs. Due to the lack of guidelines and standardized procedures for evaluating pore pressure build-up and shear strength degradation at elevated temperatures, more research is needed in order to establish reliable failure criteria for evaluating the fire resistance of concrete bridge girders.

4. NUMERICAL STUDIES

4.1. General

As discussed in Chapter 2, a limited number of numerical studies have been conducted on the fire resistance of concrete bridge girders, and almost none of them account for UHPC. While existing models contribute to understanding the fire response of concrete beams used in buildings, they do not account for the specific design parameters and failure modes that can govern the fire resistance of concrete bridge girders. Among the limitations in existing numerical models, evaluating I-shaped girders while subjected to thermal loads representative of bridge fires with failure criteria specifically designed for bridge girders are some of the relevant factors that can differentiate the fire behavior of building and bridge members. To address some of these gaps, this chapter presents the idealization, development and validation of a numerical tool that can trace the fire response of concrete bridge girders under combined effects of thermal and structural loading. This tool comprises of a fire dynamics model that generates the field temperatures representative of bridge fires, coupled with a finite element-based thermo-mechanical model that performs heat transfer and stress analyses of I-shaped concrete bridge girders. It takes into consideration temperature-dependent material models for different types of concrete (NSC, HSC, and UHPC), as well as steel reinforcing bars and prestressing strands. In addition, a submodel is used to trace degradation of flexural and shear capacity of the member through a sectional analysis and determine failure through both deflection and strength-based criteria.

4.2. Idealization

The problem of tracing the fire behavior of concrete bridge girders was idealized through a combination of different methods of analyses to arrive at the most accurate response possible at the current state of knowledge. Figure 4.1 depicts the proposed procedure for analyzing the fire

resistance of concrete bridge girders. It consists of a fire dynamics model developed in FDS-PyroSim to generate field temperatures that are used as input in a finite element model developed in ABAQUS. A submodel is used to evaluate degradation of the member capacity during fire exposure and determine failure under a strength-based criterion.

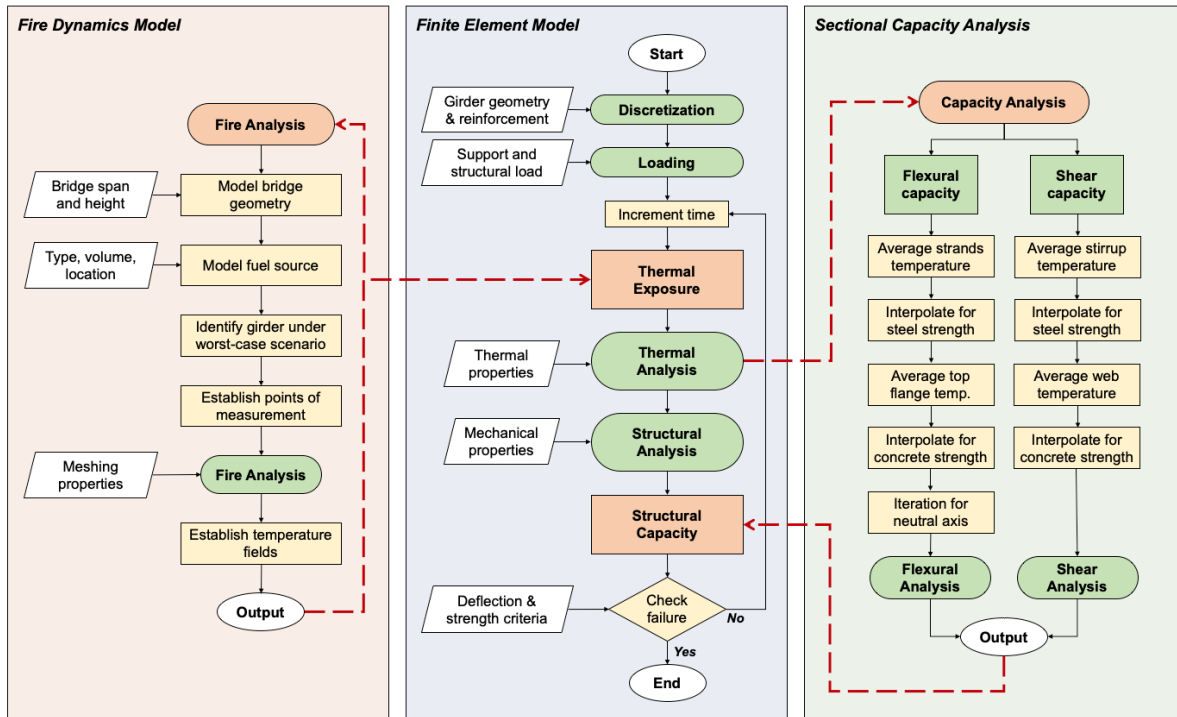


Figure 4.1: Proposed procedure for evaluating the fire resistance of concrete bridge girders

The model mainstream relies on the ABAQUS coupled thermo-mechanical analysis, which is carried out in incrementing time steps. At each step, the analysis is undertaken in four stages: first, computation of transient temperature field resulting from fire exposure; second, a heat transfer analysis assesses temperature distribution across the girder’s cross-section; then, calculation of stress and deformation response due to combined effects of thermal and mechanical loading is determined; finally, stability is evaluated through a strength-based criterion. For computation of field temperatures resulting from fire exposure, either uniform predefined temperature-time curves or results from the FDS-PyroSim analysis can be employed. To calculate degradation of flexural and shear capacity of the girder at each time step of fire exposure, a strength

analysis submodel is developed considering the temperatures derived from the thermal analysis. Deflections and strength criteria are then utilized to assess failure and determine the girder's fire resistance under the specified loading conditions.

4.2.1. Fire Dynamics Output Formulation

In a fire, heat is transferred from flames and hot gases to the surface of structural members through convection and radiation, contributing to the overall net heat flux (\dot{q}_{tot}''). The radiative heat flux (\dot{q}_{rad}'') can be computed as the difference between the incident radiation absorbed (\dot{q}_{inc}'') and the radiation emitted from the surface, which is calculated using the Stefan Boltzmann constant (σ) and the emissivity factor (ε). Similarly, the convective heat flux (\dot{q}_{con}'') can be determined as the difference between the gas temperature (T_g) and surface temperature (T_s) multiplied by a convective factor (h), as summarized in Equation (4.1).

$$\dot{q}_{tot}'' = \dot{q}_{rad}'' + \dot{q}_{con}'' = \varepsilon(\dot{q}_{inc}'' - \sigma T_s^4) + h(T_g - T_s) \quad (4.1)$$

Fire dynamics models, such as the ones developed using FDS, are based on computational fluid dynamics principles and have limited capability in calculating solid-phase heat transfer. In addition, FDS models operate with varying length and time scales, and make different assumptions about boundary conditions than finite element-based models used for heat transfer analysis. For instance, FDS models predict the heat flux to relatively simple solid surfaces, while finite element models assume a global gas temperature enveloping a more detailed structural member [175]. Therefore, these differences should be accounted for accurately transferring thermal results from the FDS to the ABAQUS model.

To facilitate this process, Wickstrom et al. [175] introduced the concept of adiabatic surface temperature (AST). This AST is a theoretical temperature derived by FDS for estimating both convective and radiative heat exchanges. This temperature is a practical measure influenced by the

heat flux from radiation and convection onto a surface, along with the gas temperature surrounding it. It serves as a representative temperature for calculating the heat flux towards a surface under exposure to fire, facilitating the integration of fire model outcomes into thermo-mechanical models, which has been largely used in previous studies in the literature [184,187,210]. By assuming the structural member as a perfect insulator, the surface temperature (T_s) in Equation (4.1) is assumed to be the AST (T_{AST}) in Equation (4.2), which would make the total net heat flux (\dot{q}_{tot}'') for this ideal surface to be equal zero for thermal equilibrium.

$$0 = \varepsilon(\dot{q}_{inc}'' - \sigma T_{AST}^4) + h(T_g - T_{AST}) \quad (4.2)$$

The net heat flux in the finite element model is presented in Equation (4.3) and it considers the effective gas temperature ($T_{g,eff}$) to calculate the heat flux by convection and radiation. If T_s is assumed to be equal to $T_{g,eff}$, then $\dot{q}_{net,FE}''$ would be zero. Therefore, by assuming that $T_{g,eff} = T_{AST}$ from the CFD model (Equation (4.4)), then temperatures from the fire model can be transferred to the finite element without potential errors from different model assumptions.

$$\dot{q}_{tot,FE}'' = \varepsilon(\sigma T_{g,eff}^4 - \sigma T_s^4) + h(T_{g,eff} - T_s) \quad (4.3)$$

$$\dot{q}_{tot,FE}'' = \varepsilon(\sigma T_{AST}^4 - \sigma T_s^4) + h(T_{AST} - T_s) \quad (4.4)$$

4.2.2. Finite Element Formulation

Fire resistance analysis using the finite element approach is usually carried out in two main stages, namely thermal and structural analysis. In the thermal analysis, temperatures at the boundaries and within the member are generated as a function of the fire resistance time. Nodal temperatures are then used as input to the structural analysis, in which stresses, strains and deformations are calculated as a combination of the thermal and mechanical loads acting on the body. In general purpose finite element programs such as ABAQUS, this can be done as a coupled

analysis (thermal and structural response calculated step by step) or uncoupled (temperatures are used as a thermal load), which does not affect the results obtained in the model.

In the thermal analysis, temperatures are usually assumed to be constant throughout a certain length of the member and for that reason the thermal analysis can be simplified to a two-dimensional heat transfer problem. Thus, the governing differential equation for transient heat transfer can be used to describe this mechanism:

$$\rho c_{(T)} \frac{dT}{dt} = \nabla(k_{(T)} \nabla T) \quad (4.5)$$

where ρ represents the material density, $c_{(T)}$ and $k_{(T)}$ are the temperature-dependent specific heat and thermal conductivity, T is the temperature, t is time, and ∇ is the spatial gradient operator.

Heat propagates through the member via conduction, where temperature differences drive heat flow from hotter to cooler regions. This is described by Fourier's Law, which relates the heat flux q_b (the rate of heat transfer per unit area) to the temperature gradient within the material:

$$k \left(\frac{dT}{dx} \eta_x + \frac{dT}{dy} \eta_y \right) = -q_b \quad (4.6)$$

where k is the material thermal conductivity; $\frac{dT}{dx}$ and $\frac{dT}{dy}$ are the temperature gradients in the x and y directions; η_x and η_y are the vector components normal to the boundaries in the cross-section plane for heat flux orientation; and q_b is the boundary heat flux acting on the boundaries and is negative because heat flows from high to low temperature regions.

The boundary conditions dictate how heat interacts with the external environment. If the boundary is exposed to fire, the heat flux q_b is influenced by convective and radiative processes and is calculated according to Equation (4.7). However, if the boundary is not exposed to fire, the heat flux is determined by the ambient conditions, according to Equation (4.8).

$$q_b = -h_f(T - T_f) \quad (4.7)$$

$$q_b = -h_0(T - T_0) \quad (4.8)$$

For determining the heat flux in the interface of the structural member, radiation and convection coefficients need to be specified, as presented in Equation (4.4). The convection heat transfer coefficient (h_{conv}) is assumed as 25 W/m².K and 50 W/m².K for standard and hydrocarbon fire curves, respectively, as recommended by Eurocode 1 [170]. The Stefan-Boltzman constant (σ) is assumed to be 5.67x10⁻⁸ W/m².K⁴ and the emissivity factor (ε) is related to the visibility of the structural member to fire. For concrete structures, the emissivity factor is usually taken as 0.8 (80% of the heat radiated reaches the surface of the member) as recommended by Eurocode 2 [96]. Some researchers recommend using lower values of ε for regions less exposed to radiation, such as the top flange and the top of the bottom flange in I-shaped girders.

Within each finite element of the structural member, temperatures at discrete nodes (T_e) are interpolated using shape functions. Thermal equilibrium within the element is achieved by relating heat storage ($[C_e^t].T_e$) and heat conduction ($[K_e^t]T_e$) to the applied thermal load (Q_e):

$$[C_e^t].T_e + [K_e^t]T_e = Q_e \quad (4.9)$$

where $[C_e^t]$ is the specific heat matrix of the element, T_e is the time derivative of the temperature vector (T_e), $[K_e^t]$ is the thermal stiffness matrix, and Q_e is the applied thermal load vector [211].

In structural analysis, ABAQUS utilizes the principle of virtual work [212]. According to this principle, the work done by external loads is stored in the material as strain energy. The variation in strain energy (δU) is determined by integrating the product of stresses (σ) and infinitesimal strains ($\delta\varepsilon$) over the volume (V):

$$\delta U = \int_V \delta\varepsilon . \sigma \, dv \quad (4.10)$$

The strain vector includes thermal strain (ε_{th}), mechanical strain (ε_{me}), creep strain (ε_{cr}), and transient strain (ε_{tr}). Transient strain applies specifically to concrete elements. The variation in work done by external forces (δV) can be computed as the product of the external nodal forces $\{F_e^n\}$ and the variation in nodal displacement $\{\delta u\}^T$, as following:

$$\delta V = \{F_e^n\}\{\delta u\}^T \quad (4.11)$$

Displacements in each node $\{u_e\}$ are related to the element displacement through a shape function matrix. The virtual work in Equation (4.10) can be rewritten in matrix form as:

$$[K_e]\{u_e\} - \{F_e^{th}\} = \{F_e^n\} \quad (4.12)$$

where $[K_e]$ is the element stiffness matrix, $\{u_e\}$ represents nodal displacements, $\{F_e^{th}\}$ denotes external thermal forces, and $\{F_e^n\}$ are external nodal forces [211,212].

Based on the formulation presented here, the numerical model developed in ABAQUS is capable of predicting temperatures, stresses, strains, and displacements for 3D structural members.

4.2.3. Capacity Assessment Formulation

The strength failure criterion (limit state) is based on ASTM E119 [169] prescriptions and is said to be achieved when the structural member is unable to resist the applied load effects. The reduced flexural capacity of a reinforced concrete member exposed to fire can be evaluated at the sectional level by extending room temperature capacity equations with due consideration to temperature induced degradation in the constituent material properties [213]. In the case of a simply supported beam made with plain concrete (no fibers) and subjected to a bending moment, the top portion (layers) of the concrete section is under compression, while the bottom portion (layers) is under tension. Like at room temperature, the tensile strength of concrete can be neglected in the bottom portion of the beam. The compressive and tensile forces developed in the concrete and steel reinforcement, respectively, can be equated considering temperature-dependent

strength of concrete ($f'_{c,T}$) and steel ($f_{y,T}$) for any specific temperature profile developed during fire exposure. The following equations can be used to evaluate the forces at a section, considering the depth of an equivalent rectangular compressive stress block at elevated temperatures (a_T).

$$a_T = \frac{A_s f_{y,T}}{\beta_1 f'_{c,T} b} \quad (4.13)$$

$$M_{n,T} = A_s f_{y,T} \left(d - \frac{a_f}{2} \right) \quad (4.14)$$

where A_s is the area of reinforcing steel, b is width of the concrete beam and d is the effective depth of the section. These geometrical variables can be considered to remain the same as at room temperature, which is usually the case for A_s . However, if a reduction in cross-section due to concrete spalling is to be considered, the width of the concrete beam b can be considered to be temperature-dependent b_T . If temperatures in the concrete are not beyond a certain temperature level (typically 300°C), usually there is not any reduction in compressive strength. This can be accounted for through a layered approach or through the isotherm approach, in which different strength levels are attributed according to the temperature level achieved in each layer.

An equivalent procedure can be adopted for beams made of fiber reinforced concrete, including UHPC reinforced with steel fibers. In this case, room temperature equations can be modified to take into consideration temperature-induced yield strength of the steel reinforcement ($f_{y,T}$) and tensile strength of fiber reinforced UHPC ($f_{t,T}$). The flexural capacity ($M_{n,FR,T}$) can be calculated using Equation (4.15), which consider the contribution of the tensile stresses of concrete as uniformly distributed over an area of height $(h - e)$. It is worth noting that a_f will also take into consideration degradation of UHPC's compressive strength and that occurrence of fire-induced spalling be accounted by modifying the width of the concrete beam (b).

$$M_{n,FR,T} = A_s f_{y,T} \left(d - \frac{a_f}{2} \right) + f_{t,T} b (h - e) \left(\frac{h + e - a_f}{2} \right) \quad (4.15)$$

The above procedure can be extended to evaluate the reduced shear capacity in beam at a given fire exposure time. The reduced shear capacity of a beam made with plain concrete ($V_{n,T}$) or with fiber reinforced concrete ($V_{n,FR,T}$) can be evaluated by extending the room temperature shear capacity equations as shown in Equations (4.16) and (4.17).

$$V_{n,T} = V_{c,T} + V_{s,T} \quad (4.16)$$

$$V_{n,FR,T} = V_{c,T} + V_{s,T} + V_{f,T} \quad (4.17)$$

These equations take into consideration degradation of shear strength in concrete ($V_{c,T}$), shear reinforcement ($V_{s,T}$), and steel fiber reinforcement ($V_{f,T}$) due to temperature as shown in Equations (4.18), (4.19), and (4.20), respectively. This approach also takes into consideration temperature-induced degradation of concrete compressive strength ($f'_{c,T}$), yield strength of shear stirrups ($f_{yt,T}$), and steel fiber reinforcement ($\sigma_{Rd,f,T}$).

$$V_{c,T} = \left(0.16 \lambda \sqrt{f'_{c,T}} + 17 \frac{\rho_w V_{u,T} d}{M_{u,T}} \right) b_w d \quad (4.18)$$

$$V_{s,T} = \frac{A_v f_{yt,T} d}{s} \quad (4.19)$$

$$V_{f,T} = \sigma_{Rd,f,T} b_w z \cos \theta \quad (4.20)$$

Since specific temperature-dependent values of the post-cracking strength perpendicular to the shear crack ($\sigma_{Rd,f,T}$) have not been measured and reported in the literature, it is proposed in this study the use of the same strength reduction factors used for steel in Eurocode 3 [214]. Also, it should be noted that temperatures used to account for degradation of properties of steel fibers will be taken to be the same as temperature in the concrete at the same depth.

4.2.4. Limitations and Applicability

The proposed numerical model provides a solution to trace the fire response of concrete bridge girders, but its applicability is constrained by some assumptions made during development. One limitation is the use of tie constraint between concrete and steel rebars/prestressing strands, assuming a perfect bond between them under fire conditions. This is a simplification commonly used in this type of numerical studies. In reality, concrete experiences cracking and strength degradation during heating, leading to loss of bond between these components. To account for this behavior more accurately, the bond-slip response at elevated temperatures is required. However, there is very limited experimental data available on this behavior, especially for newer concrete types such as UHPC and prestressing steel, which limits its implementation in the model.

Another limitation of the model is related to the absence of a spalling submodel. While fire induced spalling is not a significant issue in NSC members, it can significantly affect the fire response of HSC and UHPC members, as demonstrated in the previous chapters. In this case, concrete members are assumed to be reinforced with polypropylene fibers in order to reduce pore pressure build-up during heating and the effects of fire induced spalling. More details about this assumption can be found in Section 4.4.3. Overall, the model is capable of tracing of the response of concrete bridge girders made with different types of concrete, including NSC, HSC, and UHPC.

4.3. Fire Dynamics Model

The Fire Dynamics Simulator (FDS) developed by the National Institute of Standards and Technology (NIST) is adopted for modeling bridge fires [215] through the graphical user interface PyroSim developed by Thunderhead Engineering. This model involves creating a control volume with defined boundary conditions, which is then discretized to delineate the analysis area. Within this volume, bridge components are modeled as obstructions, affecting the flow of flames and

gases. Material properties, including thermal and combustion characteristics, are assigned to these obstructions. A fire source and a combustion model are specified within the model to initiate the fire simulation. Finally, measuring devices (sensors) are incorporated at specific locations to record analysis outputs, such as temperatures. This section outlines the complete process of developing the fire model, including discretization, fire load, and measuring devices.

4.3.1. Discretization and Boundary Conditions

The control volume must be chosen to adequately represent the volume influenced by the fire and at the same time be small enough to allow the model to run within a reasonable computing time. Figure 4.2 presents the control volume and its boundary conditions of a bridge model utilized in this study. It includes the entire bridge structure, including its girders, deck, parapets, and abutment walls. The volume is discretized in approximately 300,000 parallelepiped cells of 0.20x0.20x0.20 m. The meshed boundaries are modeled as open vents to represent a fire in an open space. The size of the control volume varies depending on the bridge geometry (span length, clear vertical spacing, and width), which will be discussed in the next chapters for each parametric and case study.

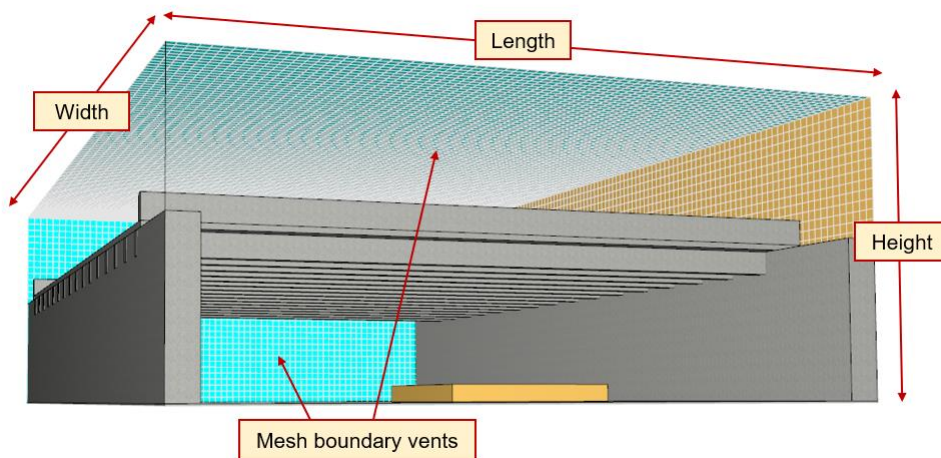


Figure 4.2: General view of the control volume of the FDS model

4.3.2. Model Components and Material Properties

The bridge structure is modeled as obstructions to the flow of heat and smoke. This included girders, deck, parapets and abutment walls, as illustrated in Figure 4.3. FDS limits the geometry of the model components to parallelepipeds, which means that none of the components can be modelled diagonally. Thus, girders are considered to have rectangular sections in the FDS model based on the bottom flange width and girder height. A layered surface composed by concrete was assigned to all bridge components (obstructions) in the model. Thermal properties of concrete were assumed from the PyroSim library and comprised of 2280 kg/m³ density, 1.8 W/m.K conductivity, 1.04 kJ/kg.K specific heat, and emissivity of 0.9. Since concrete is a non-combustible material with high thermal capacity, and only AST are collected for the thermo-mechanical analysis, these material properties can be considered adequate for the purpose of this analysis.

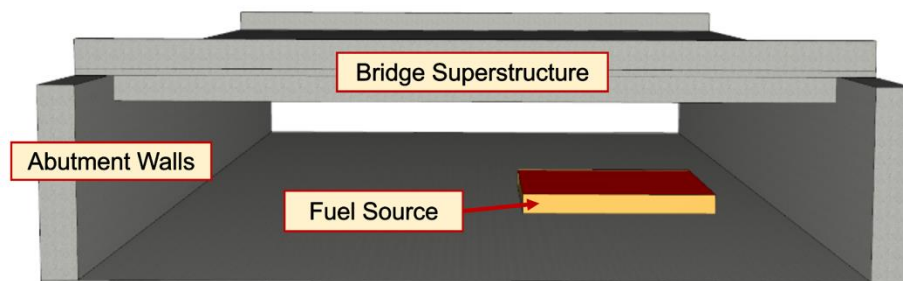


Figure 4.3: Obstructions modeled in the fire dynamics model

4.3.3. Fire Load and Combustion Reaction

In FDS, a fire source is typically specified by defining its characteristics such as size, location, intensity, and duration, often represented by creating an obstruction volume within the control volume. Fire intensity properties are then assigned to the burning surfaces of this volume by specifying the HRRPUA, ramp-up time, and extinguishing coefficient. As discussed in section 2.4.1, currently there is no standardized procedure or guidelines for modeling bridge fires, which results in varying heating procedures adopted by different authors. The only official guideline

available is the NFPA 502 [174] report that specifies the HRR of a tanker fire to be between 200-300 MW. However, fire intensity is specified in the model by the HRRPUA, which means that the resultant HRR can vary depending on the burning area defined in the model. As part of this study, two burning areas were considered as part of the variables of the parametric studies (Chapter 6). The two selected burning areas are 30 m² and 80 m², which represent the truck bed area of a tanker and an additional area of fuel spillage on the road, respectively. The burning area is considered to be 1 m above the ground level to represent the tanker height.

Figure 4.4 presents the HRRPUA-time curve adopted in this model. Based on the values suggestion by the NFPA 502 report [174], a HRRPUA of 2,500 kW/m² was selected as the fire intensity to result in a total HRR of approximately 200 MW based on the selected burning area. A t-squared ramp-up time of 60 seconds along with the selected HRRPUA were chosen based on studies in the literature that used values in the same range. A decay phase was not specified in this study, as the high fuel volume in a tanker is enough for burning for hours and would probably be extinguished before being totally consumed. The FDS model also requires a reaction mechanism to simulate the combustion behavior of the fuel being studied. In this case, the FDS6 N-Octane reaction was selected as it closely aligns with the chemical composition and burning characteristics of gasoline, ensuring a realistic representation of the fire dynamics within the simulation.

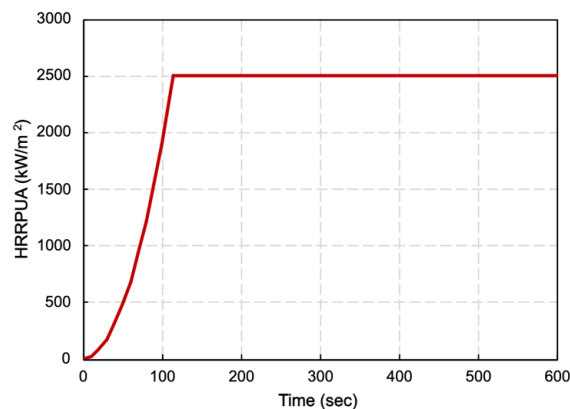


Figure 4.4: HRRPUA-time relation adopted for the fire source

4.3.4. Measuring Devices

The Solid-Phase Device in PyroSim is utilized for recording the AST at specific locations on the surface of bridge components. These measuring points included the bottom flange of girders and the bottom of the deck across both transversal and longitudinal directions of the bridge. These measurement lines are carefully positioned to intersect the burning area, ensuring the worst-case fire scenario is adequately captured. Figure 4.5 illustrates the distribution of data collection points (yellow dots) across the bridge. Given the high complexity and computational cost of mapping element or nodal temperatures to be input in the thermal/structural (ABAQUS) model, multiple devices are positioned along the girder's length in the FDS model. These devices, placed at one-meter intervals, facilitate the application of temperatures along the girder surface in the subsequent ABAQUS model.

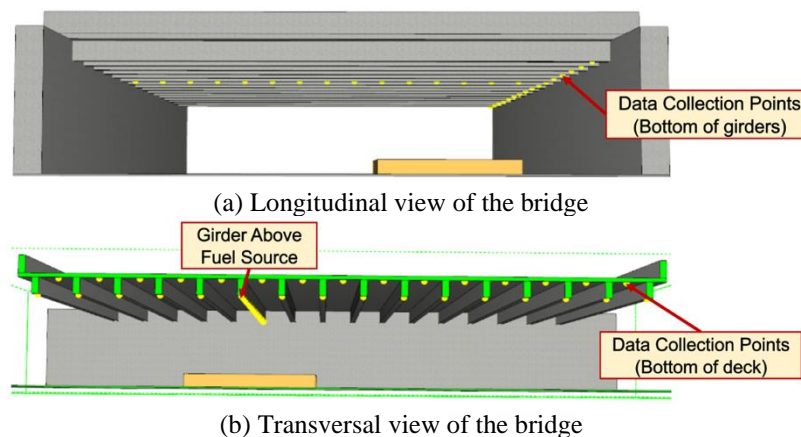


Figure 4.5: Data collection points on the bottom of the girders and the deck

4.4. Finite Element Model

The general-purpose finite element software ABAQUS [212] has been used to model the thermal and structural response of concrete bridge girders. In this approach, a comprehensive three-dimensional representation of the bridge girder is modeled considering temperature-dependent non-linear material models. The numerical model also incorporates various parameters

that significantly influences the fire resistance of concrete bridge girders. Such parameters include temperature-induced material property degradation, fire exposure conditions, the level and conditions of loading. This section outlines the complete process of developing this thermo-mechanical model, including discretization, material models, analysis details, and failure criteria.

4.4.1. Discretization

The three-dimensional finite element model was discretized in ABAQUS using eight-node-three-degrees of freedom thermally coupled brick elements (C3D8T) for concrete and two-node-three-degrees of freedom thermally coupled truss elements (T3D2T) for reinforcing bars and prestressing strands. C3D8T elements are capable of accounting for cracking of concrete in tension and crushing of concrete in compression, as well as creep effects and large strains. T3D2T elements can account for plasticity, large deflection and large strain effects of steel reinforcement. The interaction between concrete and steel elements is made using tie constraint by node-to-node interaction. A mesh sensitivity analysis was carried out to arrive at the best mesh size considering its effect on the model results and computational cost. As a result, the member is discretized using 25 mm and 50 mm seeded meshes in the transverse and longitudinal directions, respectively, as illustrated in Figure 4.6.

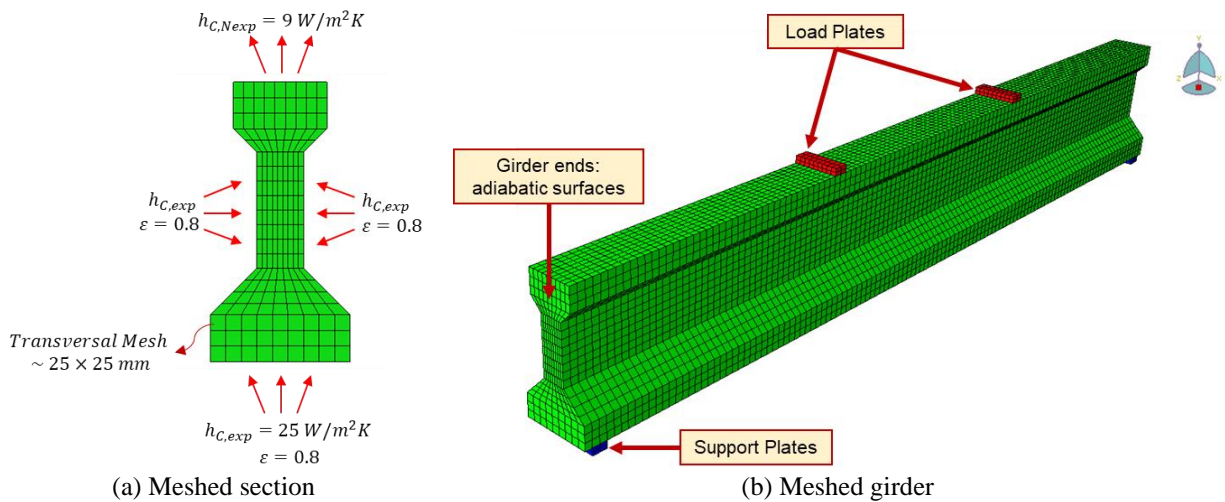


Figure 4.6: Meshed I-shaped girder used in the analysis

4.4.2. Material Models

Properties of concrete and steel strands are set as temperature-dependent in the analysis to account for degradation of thermal and mechanical properties, as detailed in APPENDIX A – TEMPERATURE-DEPENDENT MATERIAL MODELS. The progression of temperatures in the cross-section of a concrete member depends on the fire severity and its thermal properties, namely thermal conductivity, specific heat, density, and thermal expansion. Thermal properties of Normal-Strength Concrete (NSC) are defined based on the relationships provided in Eurocode 2 [96] for concretes made with carbonate aggregates. Thermal properties of HSC and UHPC are defined based on previous experimental studies and is presented comparatively to other types of concrete in Figure 4.7. For steel, both reinforcing bars and prestressing strands, thermal properties defined by Eurocode 2 [96] are adopted.

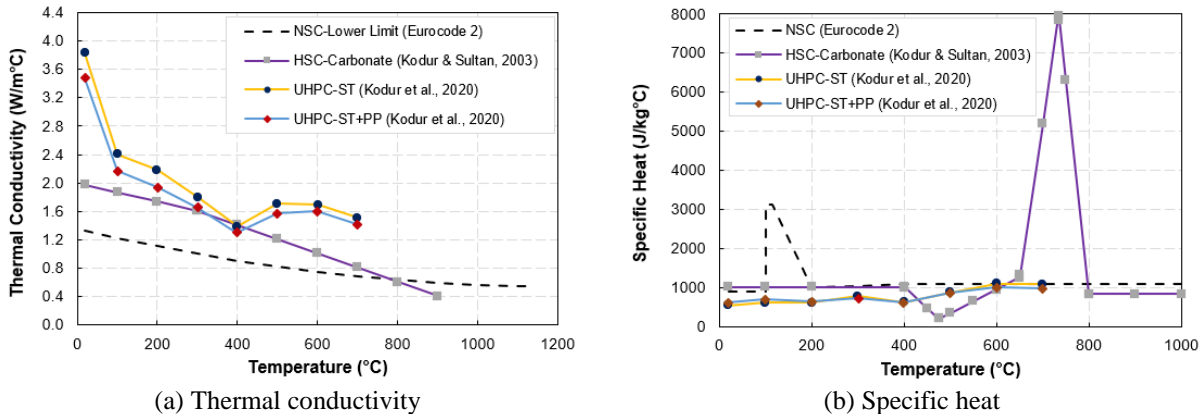


Figure 4.7: Thermal properties of different types of concrete

The metal plasticity model available in ABAQUS that utilizes Mises yield surface associated with plastic flow and isotropic hardening is used to model the mechanical behavior of steel. Temperature-dependent stress-strain relationships of steel reinforcing bars and prestressing strands are defined based on relationships from Eurocode 2 [96] and are presented in Figure 4.8.

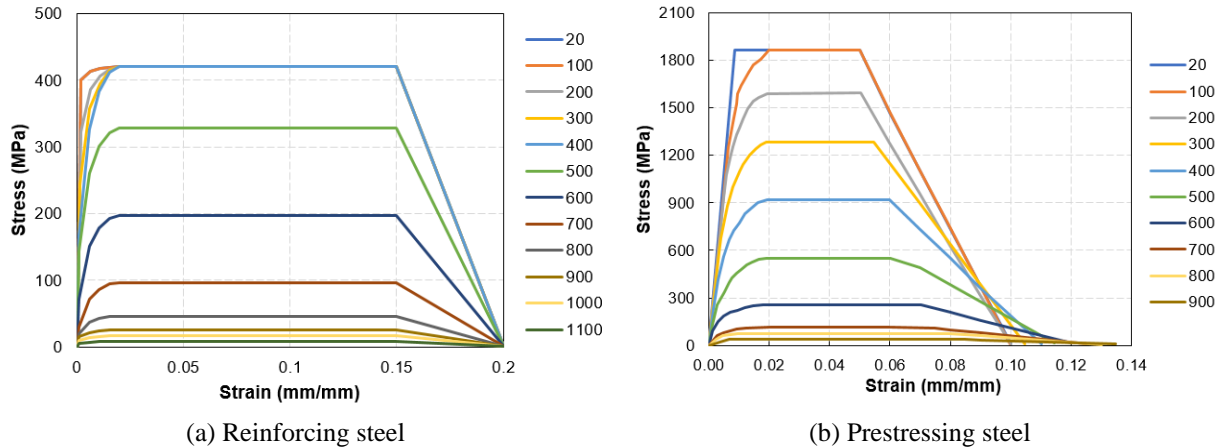


Figure 4.8: Stress-strain behavior of reinforcing and prestressing steel

The Concrete Damage Plasticity (CDP) model available in ABAQUS is used to model the nonlinear behavior of concrete (including NSC, HSC, and UHPC) because it presents a suitable stiffness behavior in the plastic stage. The CDP model is based on the theory of plastic flow and account for different laws of strength under tension and compression. It assumes isotropic damage evolution both in tensile and compressive plasticity, allowing the incorporation of strain hardening in compression and strain stiffening in tension, as well as an uncoupled damage initiation and accumulation in tension and compression. To define the CDP model a set of additional parameters are necessary (σ_{b0}/σ_{c0} , k_c , ψ , ξ , μ) and they are defined according to recommendations in the literature [216,217]. The ratio of biaxial to uniaxial compressive strength (σ_{b0}/σ_{c0}) influence the yield surface in a plane stress state and was set as 1.16. The failure surface in deviatoric plane (k_c) is the ratio of the distance between the hydrostatic axis to tensile and compressive meridians, set as 0.667. The dilation angle (ψ) describes the inclination of the failure surface towards the hydrostatic axis measured in the meridional plane, set as 15° . The eccentricity parameter (ξ) controls the deviation of the hyperbolic plastic potential from its asymptote and was set as 0.1. Finally, the viscosity parameter used for visco-plastic regularization of concrete (μ) was set as 0.

Temperature-dependent stress-strain relationships of NSC and HSC are defined based on relationships from Eurocode 2 [96] and their normalized behavior is presented in Figure 4.9. For UHPC, stress-strain relationships were adopted from the experimental study conducted by Banerji and Kodur [112], as shown in Figure 4.10. Stress-strain relationships of UHPC can be defined based on the type of fiber reinforcement used in the mixture (only steel or steel and polypropylene). In this study, UHPC is considered to be reinforced with both steel and polypropylene fibers to minimize the effects of fire-induced spalling.

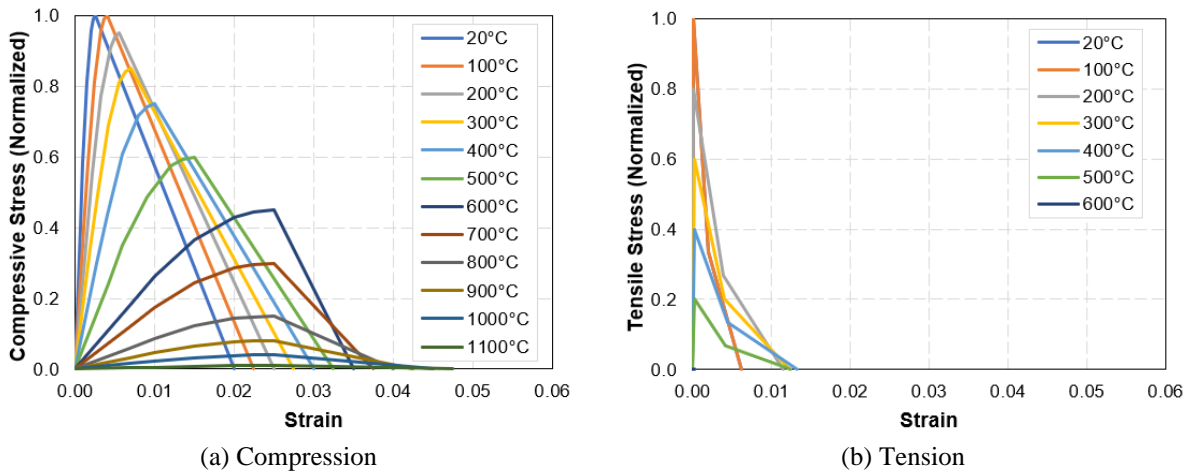


Figure 4.9: Temperature-dependent stress-strain relationships of NSC and HSC

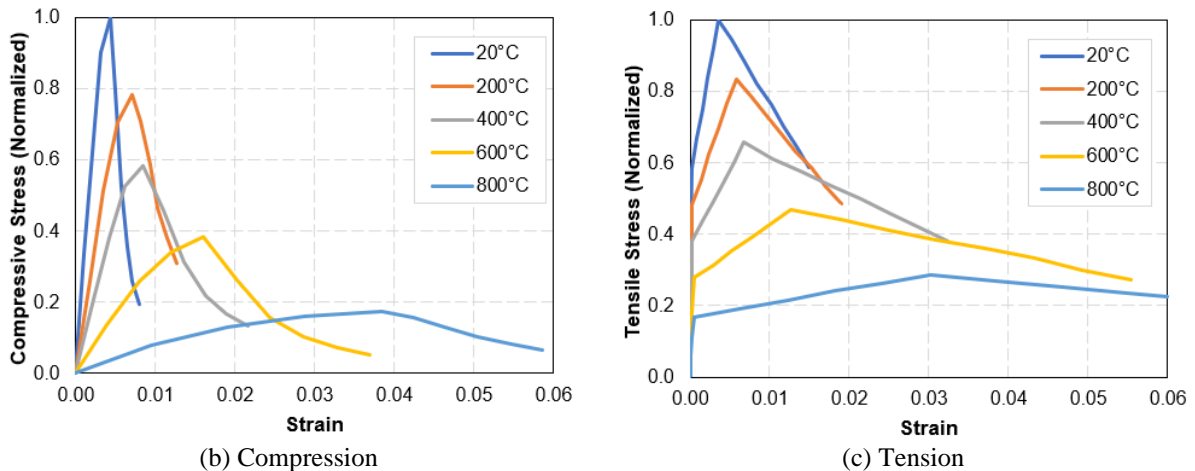


Figure 4.10: Temperature-dependent stress-strain relationships of UHPC

4.4.3. Fire-Induced Spalling of Concrete

Spalling is a major concern in concrete structures exposed to elevated temperatures, especially for those made with concretes of higher strength such as HSC and UHPC due to their lower permeability that hinders the release of vapor pressure during heating. As discussed in the literature review presented in Chapter 2, there are some alternatives that can be adopted to mitigate the effects of fire induced spalling of concrete. Such alternatives include the incorporation of fibers, like polypropylene to reduce internal pressure build-up, as well as employing special curing regimes and admixtures that reduces moisture content and improve the thermal stability of the material. As an example, Kahanji et al. [139] reported that by adding a high dosage of polypropylene fibers (4 kg/m^3) the tested UHPC beam presented no spalling after being subjected to the standard fire curve for one hour. In the fire tests conducted by Yan et al. [160] on real-scale hot-air cured UHPC beams, no spalling occurred when the beams were exposed to the standard fire curve for more than two hours. The benefits of employing this and other mitigation alternatives have presented promising results in several studies in the literature [218,219].

While the applicability and reliability of these measures still require further research, spalling is a serious issue for UHPC structures and it should be considered in their fire design. However, including fire-induced spalling in numerical models can be quite complex due to a number of influencing factors and the interrelation between them. In addition, implementing microscopic spalling analysis in finite element models that result on element deletion have a huge computational cost and their applicability in commercial software such as ABAQUS is limited. The few models available in the literature are based on a number of assumptions and, despite having been checked against experimental tests, their applicability is limited due to the large number of influencing factors. Despite significant research advancements, fire-induced spalling of

concrete remains a highly variable phenomenon and is considered by several researchers as stochastic in nature, meaning that its occurrence and extent can be unpredictable and inconsistent.

Based on the factors discussed above and the focus of this study on the broader thermal and structural behavior of concrete bridge girders, fire-induced spalling is not explicitly considered in this finite element model. The material models integrated into the numerical model reflect the degradation effects of elevated temperatures in HSC and UHPC with addition of polypropylene fibers, which have been proven to mitigate spalling. To account for the possibility of concrete spalling and improve the safety of the model predictions, a simplified methodology could be employed in the strength analysis submodel. This would involve reducing the sectional dimensions of the concrete member based on temperature rates that are known to cause spalling.

4.4.4. Analysis Details

The finite element model uses coupled thermo-mechanical analysis to trace the behavior of concrete members under fire conditions. For structural analysis, steel plates are used in the location of supports and load points to reflect practical situations, reduce concentration of stresses at the boundaries, and improve the convergence of the finite element model. Support plates are pinned and rolled at the bottom center lines perpendicular to the girder. The load is applied as vertical downward pressure on two steel plates sitting at the top of the member, equally spaced from midspan. For thermal analysis, an initial temperature of 20°C is assumed in the entire model, while convective and radiative heating are applied at the bottom and sides of the flexural member. Different loading and fire exposure conditions, as well as support and restraint conditions, can be specified in the model for different scenarios, as needed.

4.4.5. Failure Criteria

Failure of concrete bridge girders under fire exposure is evaluated using deflection and strength limiting criteria. As discussed in 2.5.2, there are currently no specific failure criteria established for concrete bridge girders. Therefore, for determining failure under the deflection criterion, methods available for building members are applied. According to ASTM E119 [169], the maximum total deflection should not exceed $L^2/400d$ (mm), while BS 476-20 [194] limits is to $L/30$. The rate of deflection is limited to $L^2/9000d$ (mm/min) based on ASTM E119 [169] requirements. The strength criterion is assessed at each time step of the analysis by calculating the degrading flexural and shear capacity of the member and comparing it with the applied bending moment and shear force, respectively. This study follows the procedure for calculating the strength criterion presented in section 4.2.3. Temperature failure criterion is not used to assess the fire resistance of concrete bridge girders due to its limitations. Since concrete bridge girders usually have the same concrete cover thickness (51 mm), the failure time under temperature criterion would be practically the same for all girders exposed to the same fire scenario. Further discussion on the applicability of these failure criteria is included in Chapter 7, which also proposes parameters for determining the failure of concrete bridge girders under fire conditions.

4.5. Model Validation

The developed numerical model is validated using results from fire tests conducted on NSC, HSC, and UHPC beams at Michigan State University. The accuracy of the model predictions is verified by comparing cross-sectional temperatures and deflections during fire exposure.

4.5.1. Selection of Beams and Girders for Validation

The NSC and HSC beams tested by Dwaikat and Kodur [141] were selected for fire resistance analysis. Both beams were 3.962 m-long, had a cross section of 254x406 mm and were

reinforced with conventional steel bars. Three 19 mm diameter bars and two 13 mm diameter bars were used as tensile and compressive reinforcement, respectively. Shear reinforcement consisted of 6 mm diameter stirrups spaced 150 mm over the length of the beam. The supports were placed 171 mm from the beam ends to form a simply supported configuration. The load was applied in two points, spaced 864 mm from each other and distant 1,400 mm from each support. The flexural capacity of the NSC and the HSC beam is 136 kNm and 139 kNm, respectively, and they were both subjected to a load of 100 kN during fire exposure, representing 55% of the beam capacity.

UHPC beams tested by Banerji et al. [204] were also analyzed as part of the validation process. These beams had the same length, support and load configuration. However, a reduced cross section of 180x270 mm and only three 12.7 mm diameter tensile rebars were used to take advantage of UHPC mechanical properties. These beams are made with two UHPC mixtures, one containing only steel fibers (identified UHPC Beam) and another one containing both steel and polypropylene fibers (identified UHPC-PP Beam). Table 4.1 presents a summary of design parameters, loading and fire exposure conditions of these beams. Figure 4.11 presents a comparative illustration of their design parameters.

Table 4.1: Summary of design parameters of the NSC, HSC and UHPC beams

Beam	Cross section [mm x mm]	Concrete f _c (MPa)	Capacity at room temp.	Fire	Applied load (% of capacity)
NSC Beam	254 x 406	58.2	115 kN	ASTM E-119	100 kN (55%)
HSC Beam	254 x 406	93.3	140 kN	ASTM E-119	100 kN (55%)
UHPC Beam	180 x 270	173.0	84 kN	Design Fire 1	60 kN (60%)
UHPC-PP Beam	180 x 270	176.0	84 kN	Design Fire 2	43 kN (45%)

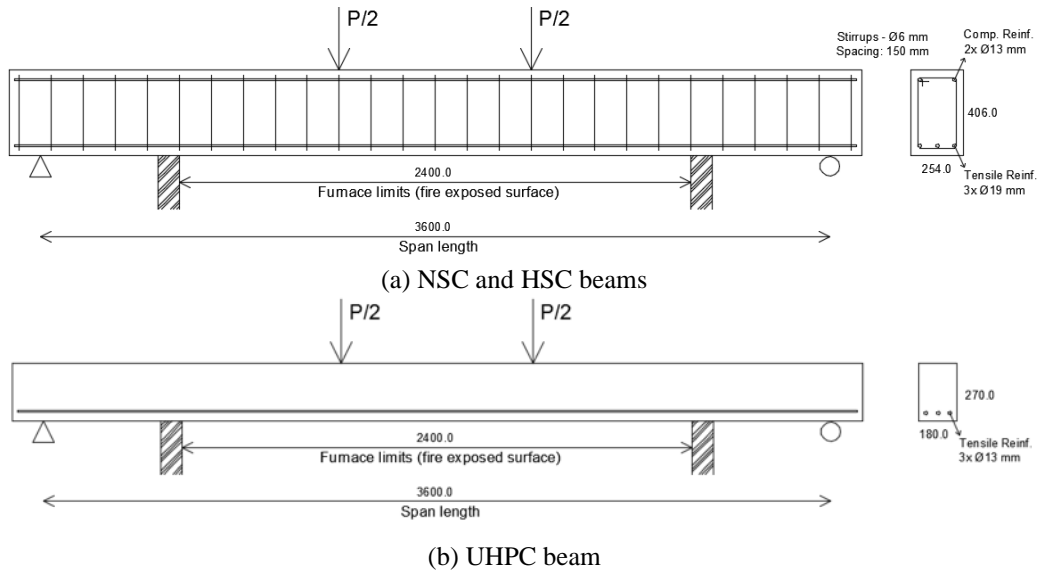


Figure 4.11: Design configuration of the reinforced concrete beams modeled

4.5.2. Thermal Response Validation

The measured and predicted temperatures in concrete (quarter and half-height) and rebars (center and corner) at mid-span of all beams are plotted in Figure 4.12 as a function of the fire exposure time. Measured temperatures refer to those obtained in experiments by Dwaikat and Kodur [141] for NSC and HSC beams, and those obtained by Banerji et al. [204] for UHPC beams. For the NSC and HSC beams, measured temperatures at the center rebars were not available, while measured temperatures at quarter-height of the UHPC beam could not be used due to malfunction of the thermocouple. Temperatures predicted by the model were obtained for the same points measured during experiments and presented a similar trend for all the beams analyzed. In all cases, temperatures predicted at the corner rebars had higher temperature rise than the center rebars due to their peripheral location that is exposed to heating from the side and bottom surfaces of the beam. As expected, temperatures measured and predicted in the concrete layers farther (half-height) from the fire exposed surfaces were lower than those closer (quarter-height) to the fire exposed surface. This behavior is due to the low thermal conductivity and high specific heat of concrete that delay the progress of temperature through the concrete cross-section.

Analysis of temperature data shows that the type of concrete has some influence on the temperature progression in reinforced concrete beams exposed to fire. It can be seen in Figure 4.12 (a) that the measured and predicted temperatures in rebars and concrete for the NSC beam are slightly lower than those presented in Figure 4.12 (b) for the HSC beam. This small variation can be attributed to the slight differences in thermal properties of those concretes due to the higher compactness of HSC and its higher susceptibility to fire induced spalling (in the case of measured temperatures). The UHPC beam followed the same trend, but temperatures in the quarter-height were very close to the ones on half-height due to the occurrence of spalling on the top part of the beam. It should be noted that the UHPC beam was exposed to a design fire with lower temperatures than the standard fire curve. Despite that, measured and predicted temperatures were higher than those obtained in NSC and HSC beams. The half-height of the UHPC beam reached 200°C around 70 minutes of fire exposure, while it happened after 150 minutes in the other beams exposed to a more severe fire curve. This can also be attributed to differences in thermal properties due to concrete compactness, as well as the fact that UHPC is reinforced with steel fibers, which present much higher thermal conductivity than concrete.

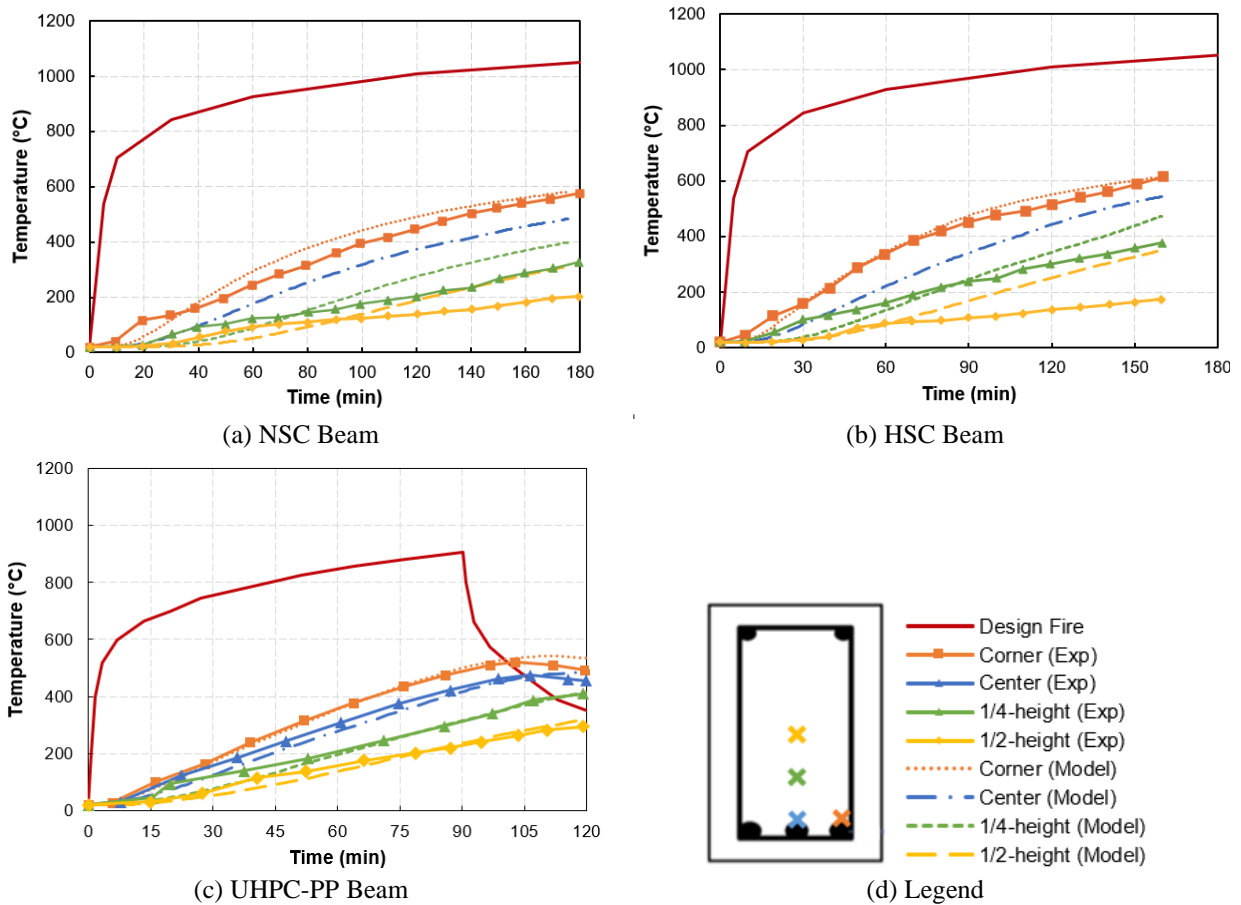


Figure 4.12: Measured and predicted temperatures at mid-span for the corner rebar in all beams

Overall, the temperatures predicted by the numerical model are in good agreement with test results. Difference between the measured and predicted temperatures are attributed to variations in the thermal properties assumed in the model, which can be influenced by several factors, including type of aggregate and moisture content. These differences were more pronounced in the inner regions of the beam and does not present high influence on the structural response. Overall, the thermal response can be considered validated for the purpose of this study.

4.5.3. Structural Response Validation

Figure 4.13 presents the measured and predicted midspan deflections for all beams as a function of fire exposure time. For NSC and HSC beams the mid-span deflection increases gradually with time at the beginning of fire exposure, and then becomes more pronounced towards

the failure point. For UHPC beams, increase in deflection occurred at a higher rate and resulted in earlier failure of the members. This behavior is related to the deterioration of strength and stiffness properties of concrete and steel with temperature. The initial deformations of a beam results from thermal gradients developed with the beam cross section and the applied loading. The effect of creep becomes more pronounced towards the end of the fire exposure with a significant increase of deformations due to the high stress levels that produce high creep deformations.

Deflections predicted by the model increase at a similar rate as those observed in the fire tests. In general, predicted deflections of the beams in the initial stages of fire exposure was very close to the experimental measurements. Despite the differences in the later stages, the model still predicted failure at a similar time. The UHPC-PP beam did not experience failure during two hours of fire experience, and model was able to capture some of the deflection recovery response. The difference between measured and predicted results is attributed to variations in the stress-strain relations assumed for concrete and steel at elevated temperatures, as well as small differences in the predicted thermal response. Overall, the model is capable of tracing the structural response of concrete members made with different types of concrete at elevated temperatures.

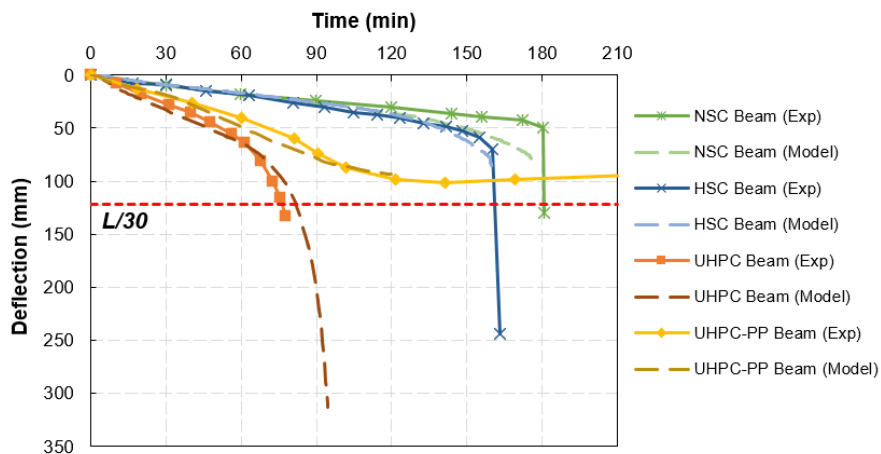


Figure 4.13: Measured and predicted mid-span deflection in all beams

4.5.4. Fire Resistance Ratings

Table 4.1 presents the fire resistance ratings obtained in the experimental tests and through the numerical model for concrete beams made with different types of concrete. It can be noted that the fire resistance of the beams decreased for beams made of concretes with higher strength, ranging from 180 min for the NSC beam to 80 min for the UHPC beam. The UHPC-PP did not experience failure due to the fact that it was exposed to a design fire curve with a cooling phase. Overall, this data demonstrates that the model was able to predict similar fire resistance ratings than what was obtained in the fire tests, highlighting the reliability of the model to predict the fire resistance of concrete members made with different types of concrete.

Table 4.2: Fire resistance ratings from experimental tests and numerical model results

Beam	Fire resistance rating (min)	
	Test	Model
NSC Beam	180	175
HSC Beam	160	159
UHPC Beam	78	81
UHPC- PP Beam	NF	NF

NF: No failure

4.6. Summary

This chapter presented the conception, development and validation of a numerical tool for tracing the fire behavior of concrete bridge girders. This model has been developed with commercially available software, such as ABAQUS and FDS-PyroSim, which facilitates the application of this tool in real practice. Coupling the fire dynamics model with the finite element model allows the analysis of bridge girders more realistically as it accounts for the non-uniform temperature distribution on the surface of structural members instead of simply adopting a prescribed standardized curve. The model is capable of discretizing bridge girders made with

varying shapes and sizes and incorporates non-linear material models to trace the thermal and structural response of bridge girders more accurately. In addition, the model incorporates a sectional analysis submodel to check flexural and shear strength degradation during fire exposure and determine failure based on the strength based criteria. The validity of the model has been checked by comparing temperature and deflection predictions from the model with results obtained in experimental tests, which included temperatures at different points within the member as well as midspan deflections. While the developed model present high complexity and is dependent on a number of variables, it can provide an accurate response of the behavior of concrete members exposed to elevated temperatures. Overall, the developed numerical model is an important tool for accurately generating data on the influence of several other parameters that can affect the fire resistance of concrete bridge girders, as well as for performing case studies, as will be presented in the next chapters.

5. MODEL APPLICABILITY

5.1. General

This chapter presents the application of the numerical model developed in Chapter 4 to assess the fire behavior of bridge structures in field applications. The studied case is the collapse of the I-95 overpass in Philadelphia on June 11, 2023, due to a tanker-induced fire incident [220]. This fire caused significant traffic disruptions to an important transportation system on the East Coast of the United States. The causes and mechanisms for early failure of this bridge, as well as the effectiveness of mitigation strategies that could have prevented the collapse of this overpass under similar fire incidents are analyzed. The studied alternatives include composite action between the steel girders and the concrete slab, as well as thermal insulation of the girder. While this bridge was made of composite steel girder-concrete slab, the analysis of its fire behavior provides valuable insights on the applicability of the proposed numerical model and methodology for assessing real bridge fire incidents considering the characteristics of real bridge fire scenarios. In addition, this chapter demonstrates the integration of fire mitigation strategies into the design of critical infrastructure, particularly bridges, to enhance their resiliency under possible fire scenarios.

5.2. Description of the Bridge Fire Incident

In the early hours of June 11, 2023, a truck-tractor combined with a tank-trailer was transporting 8,500 gallons of gasoline from Wilmington, DE, to a gas station in Philadelphia, PA. The driver lost control of the vehicle while navigating the I-95 northbound off-ramp onto Cottman Avenue, resulting in a rollover and collision with the east abutment wall of the southbound overpass beneath I-95. The off-ramp was marked with a 25-mph speed limit sign, in contrast to the 55-mph highway speed limit, and a truck rollover warning sign. The crash triggered a large

explosion, followed by an intense fire. The northbound I-95 overpass collapsed due to the fire, and the southbound overpass suffered significant damage. The truck driver, who perished in the incident, was the only casualty in this incident [15].

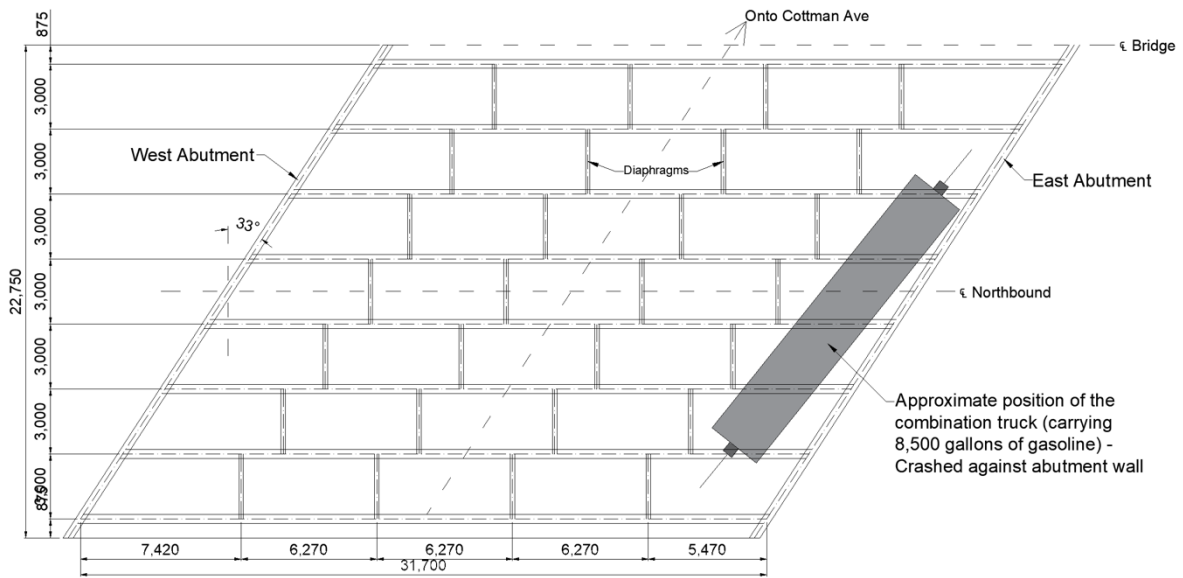
The precise time when the fire started and the bridge collapsed remains uncertain but can be approximated using data available to officials and testimonials from media sources, as summarized in Table 5.1. The preliminary report published by the National Transportation Safety Board [14], states that the incident occurred around 6:17 a.m., likely marking the crash time. Surveillance footage captured the tanker crash and shows it was followed by an explosion and fire of high intensity [221,222]. The Philadelphia Fire Battalion reported receiving the emergency call at 6:22 a.m. [223], with crews arriving shortly before 6:30 a.m. [41]. The nearest Philadelphia Fire Department (Engine 38) is less than two miles from the scene. However, dispatch audios [224], indicates some confusion regarding the fire's location. It was not confirmed if the overpass had collapsed by the time firefighters arrived or if any firefighting efforts occurred before the collapse. A commuter's video recorded at 6:21 a.m. shows the overpass already sagging and reports it collapsing about a minute later, around 6:22 a.m. [224]. Other videos shared on social media by commuters driving on I-95 depict large flames and black smoke emanating from the overpass, with some reports suggesting the collapse happened about ten minutes after their recordings. Based on the information available, it is estimated that the girder collapsed between 10 and 15 minutes after the tanker crash.

Table 5.1: Timeline of bridge fire incident on June 11, 2023

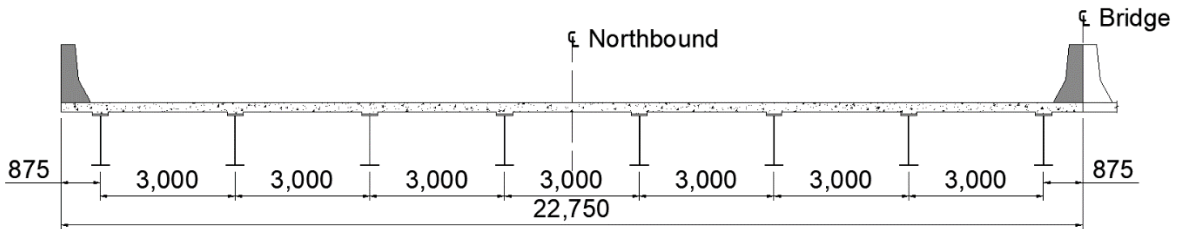
Estimated time (hh:mm)	Event
06:17 ~ 06:20 am	Tanker crashes the abutment wall and fire starts immediately
06:20 ~ 06:30 am	Videos of intense fire and bridge sagging posted on social media
06:22 am	Emergency dispatchers received a call for the accident response
06:28 ~ 06:30 am	Emergency crew arrived on the site
06:30 ~ 06:32 am	Bridge collapsed

5.3. Structural Characteristics of the Bridge

According to construction plans, the I-95 overpass spans 31.7 meters over Cottman Avenue and has a 33° skew. The superstructure consists of separate southbound and northbound structures with no connections between them. Each structure is made up of eight steel plate girders spaced three meters apart, topped by a reinforced concrete slab. Each bay contains four diaphragms, spaced 6.27 meters apart, which connect the steel girders. Transverse stiffeners are embedded in concrete diaphragms over the abutments at the support locations. The composite concrete slab is 216 millimeters thick and has a deck out-to-out width of 22.75 meters, accommodating four design lanes and two shoulders (one on each side). The bridge appurtenances include a concrete parapet at the outer edge and a concrete median separating the adjacent bounds. Figure 5.1 shows the top and cross-sectional views of the northbound overpass.



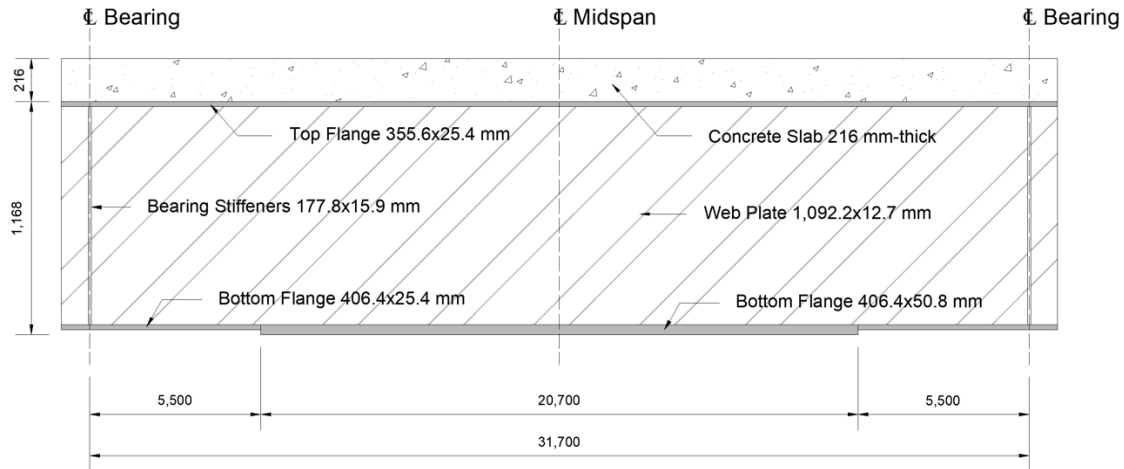
(a) Top view of the bridge structure



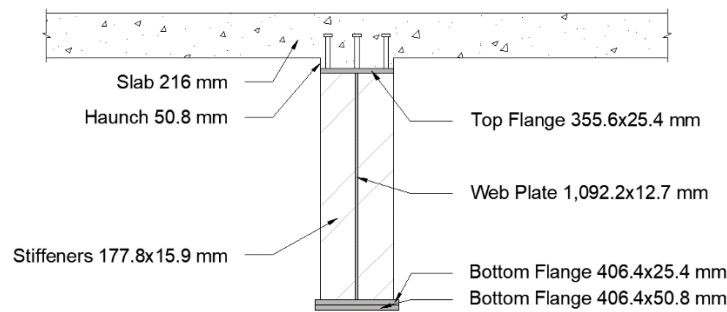
(b) Cross-sectional view of the bridge structure

Figure 5.1: Structural components of the I-95 overpass in Philadelphia

Figure 5.2 illustrates the typical steel plate girder and concrete slab from the I-95 overpass. The web plate is 12.7 mm thick and 1,092.2 mm high along the entire length of the girder. The top flange maintains a constant cross-section, being 25.4 mm thick and 355.6 mm wide. In contrast, the bottom flange is 406.4 mm wide but varies in thickness: it is 25.4 mm thick for 5.5 meters from each support and 50.8 mm thick in the middle of the girder. At each end support, a pair of 15.9×177.8 mm bearing stiffeners is placed. To connect the plate girders to the concrete slab, lines of three 22.2 mm-diameter shear studs, spaced 190.5 mm apart throughout the length of the girder, are used to achieve full composite action.



(a) Longitudinal view of the girder



(b) Transversal view of the girder

Figure 5.2: Layout of the composite girder from the I-95 overpass

The steel plate girder was manufactured using ASTM A709 Grade 50 steel, which has a yield strength of 345 MPa and an ultimate strength of 450 MPa. The concrete slab was made with 35 MPa compressive strength concrete and reinforced with ASTM A615 Grade 60 epoxy-coated steel rebar. Considering the girder's geometry and material properties, the flexural capacity of the composite section at mid-span is calculated to be 14,730 kN-m. The ABAQUS model developed in Chapter 4 was employed to assess the girder's capacity under ambient conditions by analyzing its load-displacement response. Figure 5.3 shows the room temperature analysis results of the I-95 overpass composite girder. The maximum moment applied to the girder nearly reached 17,000 kN-m, exceeding the capacity estimated through sectional capacity analysis. This difference is attributed to the simplifications in sectional analysis, which leads to lower capacity predictions.

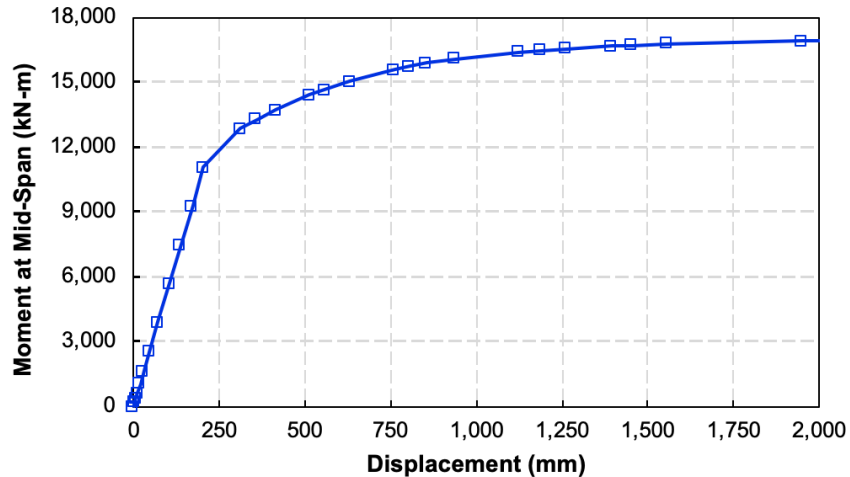


Figure 5.3: Moment-displacement relation for the I-95 composite girder at ambient conditions

5.4. Evaluating Fire Resistance of a Typical Girder Section

The numerical model developed in Chapter 4 is applied to trace the fire response of the I-95 overpass in Philadelphia. The analysis is performed on a typical girder section, considered representative of the entire bridge, as presented in Figure 5.4. The simply supported girder is modeled to carry its own weight, increased by 25%, considering no live loads applied on the bridge during fire exposure. The calculated factored self-weight is 27.5 kN/m, which includes the weight of the steel girder, concrete slab, haunches, bridge appurtenances (parapets and medians), and secondary steel members (diaphragms, stiffeners, connection plates, etc.). The resulting bending moment from the distributed load is 3,452.2 kN-m, approximately 25% of the girder's plastic moment capacity under ambient conditions. The girder is evaluated under exposure to three different temperature-time fire curves: “standard” fire, “hydrocarbon” fire, and “design” fire (which includes a cooling phase), as shown in Figure 5.5. The “standard” and “hydrocarbon” fires reflect the burning conditions of cellulose-based materials (typical in buildings) and hydrocarbon materials (common in vehicle fuels), respectively, as specified by Eurocode 1 [170]. The “design” fire curve, derived from a previous study [225], exhibits an intermediate temperature rise between the other curves and includes a cooling phase after reaching a peak temperature of 950°C. While

a uniform temperature distribution along the length of the girder was assumed in all scenarios, the girder has also been evaluated under the non-uniform field temperatures derived from the FDS-PyroSim model considering this girder geometrical characteristics, as presented in the next section.

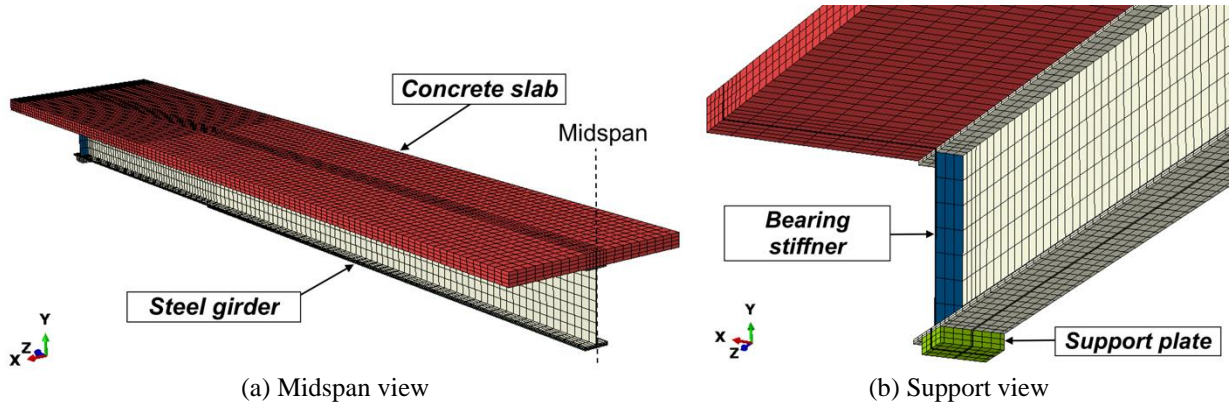


Figure 5.4: Discretization of I-95 overpass girder for nonlinear finite element analysis

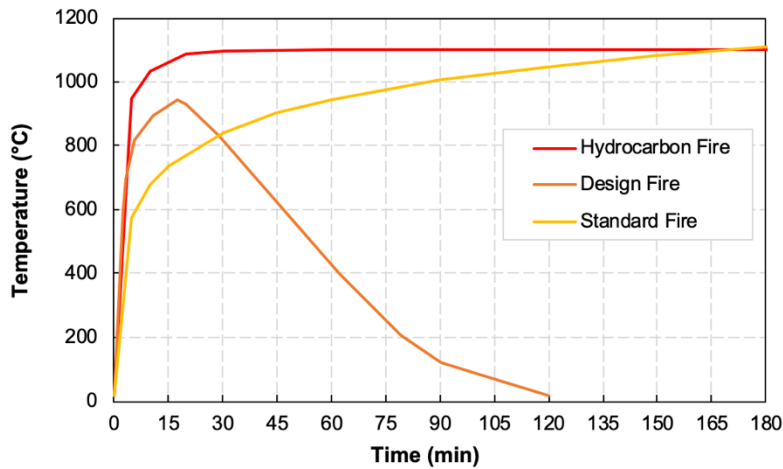
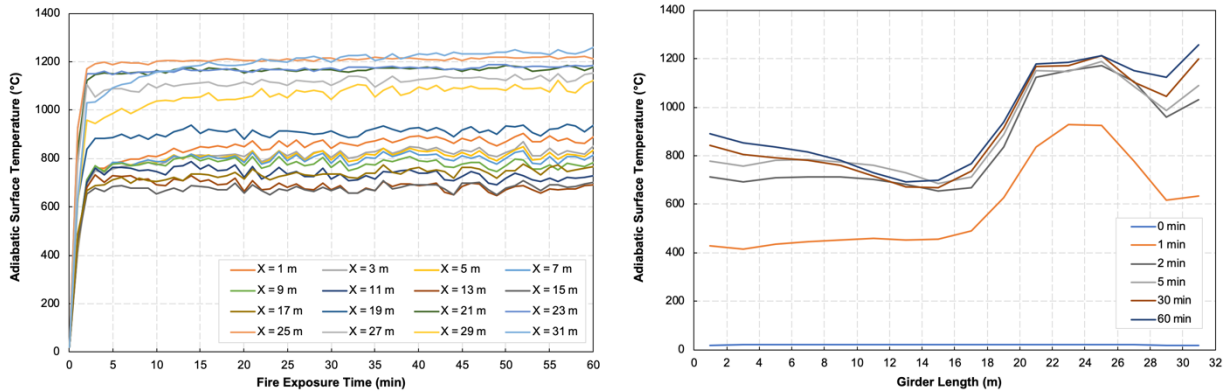


Figure 5.5: Temperature-time relations of the fire scenarios used in the analysis

5.4.1. Fire Development Response

Figure 5.6 presents the adiabatic surface temperatures measured at different points along the length of the girder (distant X from the end support) on the bottom flange of the girder. It can be observed that a significant thermal gradient was developed along the length of the girder, ranging from 650°C to 1200°C. The highest levels of temperature were measured at a point close to one the support locations, where the fire source was modeled (crashed tanker). This data

demonstrates that certain sections of the bridge experience higher temperatures sooner and more intensively than others, which should be accounted for a more realistic evaluation of the girder.



(a) AST as a function of fire exposure time (b) AST as a function of the girder length
 Figure 5.6: Temperatures measured throughout the girder length during fire exposure

5.4.2. Thermal Response

Figure 5.7 displays the results from the thermal analysis of the I-95 overpass girder section. The temperature progression over fire exposure time (up to 90 minutes) is plotted for selected locations, which included bottom flange, web mid-depth, top flange, and slab mid-depth. Results show that temperatures in the girder web rise significantly higher than those in other locations. This is attributed to the web's thinner profile (12.7 mm) compared to the flanges (25.4 mm and 50.8 mm for the bottom and top flanges, respectively). In addition, the larger web surface area contributes to accelerate the increase in sectional temperature. In contrast, the top flange temperatures are lower than those in the bottom flange and web, owing to the insulating effect of the concrete slab, which covers the top flange and absorbs heat through the heat sink effect. At the slab mid-depth, temperatures remain much lower than in the steel section due to concrete's lower thermal conductivity, which delays the penetration of heat into the slab.

As expected, the thermal response is significantly influenced by the severity of the fire. The girder exposed to the hydrocarbon fire curve experienced much higher temperatures compared to the other fire scenarios. Additionally, the temperature gradient between the steel girder and the

concrete slab is notably lower for the girder subjected to the standard fire curve. In the design fire scenario, the cooling phase caused a decline in sectional temperatures after reaching peak temperatures between 30 and 34 minutes of fire exposure. The thermal gradient along the girder length from the simulation fire (FDS-PyroSim) is also reflection on the temperatures measured at different locations (midspan and support). Overall, the temperatures predicted in the steel section are consistent with findings from previous studies on the fire resistance of steel bridges [210,226].

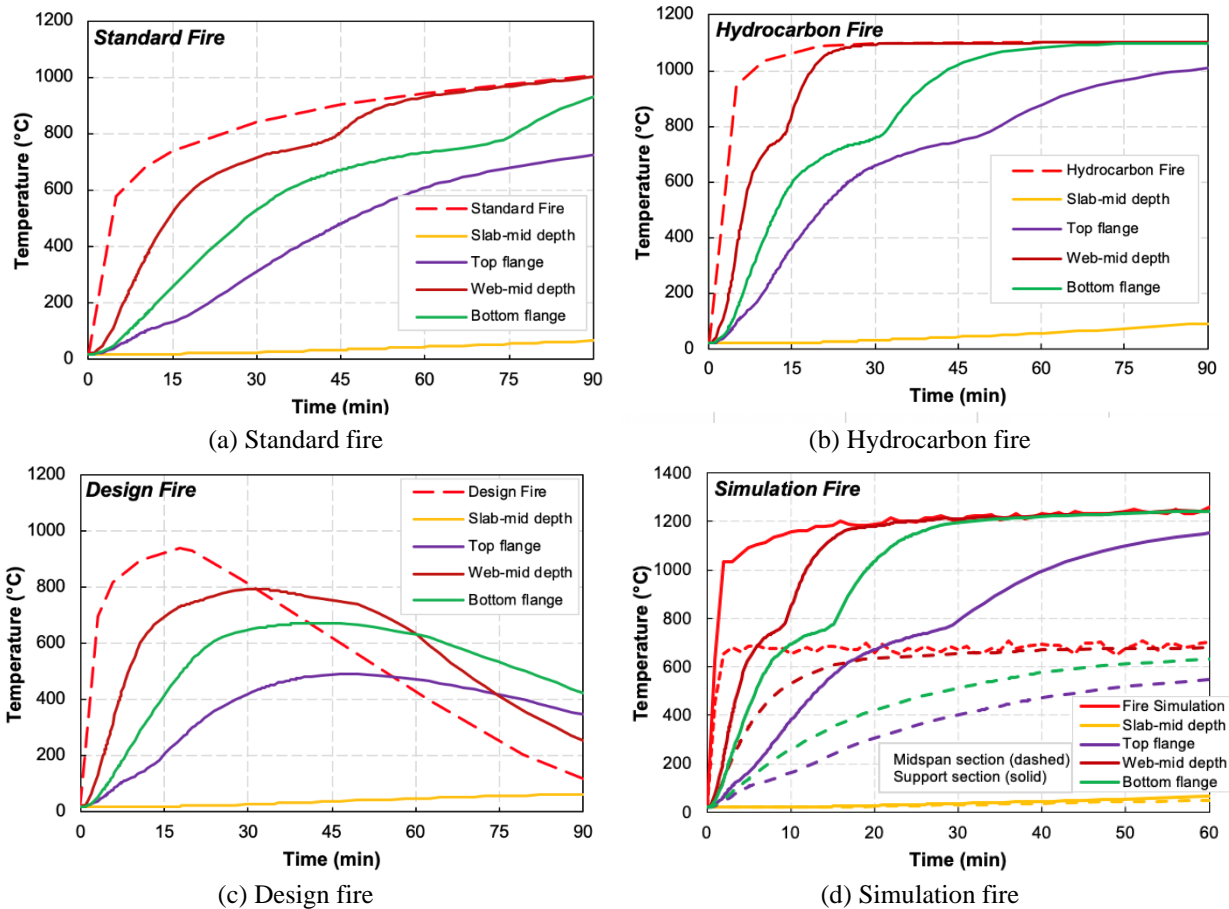


Figure 5.7: Thermal response of the girder exposed to different fire scenarios

5.4.3. Structural Response

The numerical model was also used to trace the structural response of the I-95 overpass girder section under the four fire scenarios. Figure 5.8 shows the progression of mid-span deflections of the girder with fire exposure time until it reached the point where the model stopped

converging due to run-away failure. These results indicate that the composite girder undergoes higher deflections as the severity of the fire increased, with the simulation fire causing the highest deflection rate. By comparing these results with observations from the actual incident, it can be deduced that the composite girder in I-95 overpass experienced sectional temperatures in the same range as in the case of a hydrocarbon fire scenario. These findings demonstrate the importance of considering the appropriate fire scenario in the analysis of bridges structures, as these fires present much higher severity than conventional building fires.

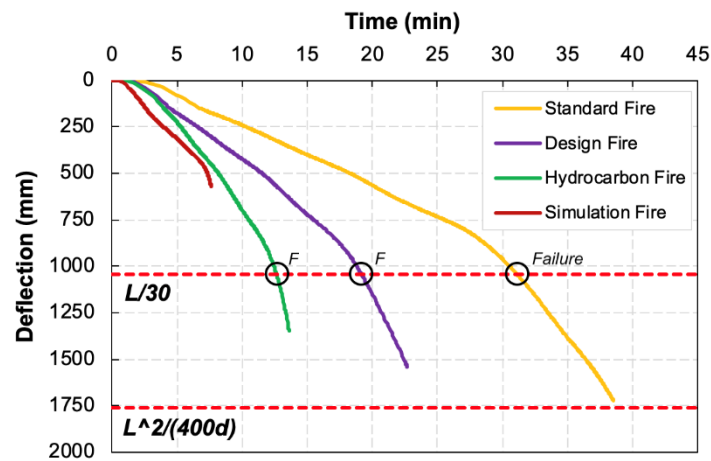


Figure 5.8: Deflection response of the girder exposed to different fire scenarios

The failure of the girder was analyzed under different criteria. In terms of deflections, two maximum deflection limits were assessed for comparison. It can be seen that the girder did not reach the failure limit of $L^2/400d$ by ASTM E119 [169]. On the other hand, the deflection limit of $L/30$ proposed by BS 476-20 [194] showed to be capable of capturing failure of this girder. The girder also reached the rate of deflection limit of $L^2/9000d$ in scenarios, resulting very similar fire resistance times as the $L/30$ limit. This demonstrates that deflection limits developed for building members are not capable of tracing the fire resistance of bridge girder accurately.

The analysis of moment capacity degradation under four distinct fire scenarios contributes to understanding the girder's structural performance under fire conditions (Figure 5.9). As fire

severity increases from the standard to the hydrocarbon fire curve, and then to the design fire curve with a cooling phase, there is a faster decrease in moment capacity with fire exposure. This progressive degradation illustrates the vulnerability of steel bridge girders to withstand bending moments due to thermal-induced material degradation. The hydrocarbon fire curve, being the most severe scenario, causes the highest rate of moment capacity degradation, suggesting the bridge structures could experience temperatures similar to those from the hydrocarbon fire curve. These findings demonstrate the importance of evaluating the fire performance of bridge structures based on strength-based failure criteria rather than relying on critical temperature limits for the steel section.

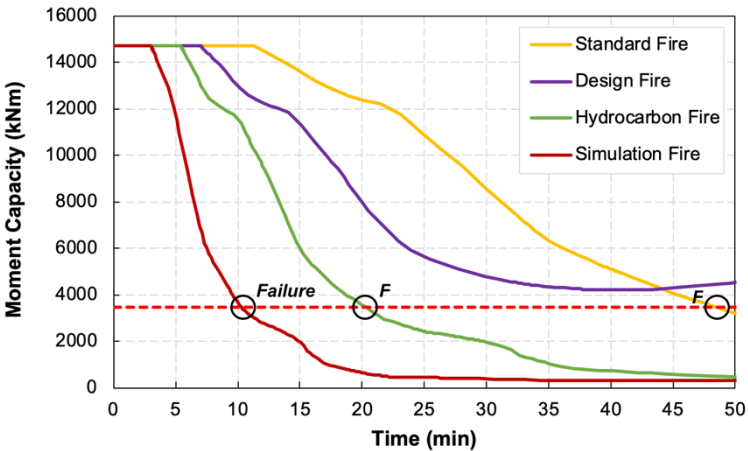


Figure 5.9: Degradation of moment capacity under different fire scenarios

It should be noted that the structural response of steel members exposed to fire is also dependent on the effects of thermal expansion. With increasing temperatures, steel members can experience large horizontal displacements and reach the bridge abutments, creating compression forces that can lead to different stress distributions and alter the deflection response of the bridge. This is particularly concerning in members with end restraint conditions or long-span bridges. Due to the limited information on the end conditions of this bridge, such effects were not considered in this model.

5.4.4. Failure Mode

The girder experienced the same failure mode while analyzed under exposure to all fire scenarios. This failure occurred at the intersection between the two bottom flange thickness, as illustrated in Figure 5.10, highlighting a potential point of vulnerability in steel members. This transition zone experienced a high concentration of stresses and plastic strains under fire exposure. The combination of high temperatures and varying flange plate thicknesses led to differential expansion rates, causing uneven thermal strain distribution at the interface. This ultimately triggered the yielding of steel and localized failure of the thinner plate near the intersection with the thicker plate. The actual failure of the I-95 overpass appears to be very similar to the one predicted through the model, as observed through photographs of the incident. However, this similarity cannot be confirmed due to the lack of close-up images of the collapsed girders that could help identify the actual failure mode developed at the incident.

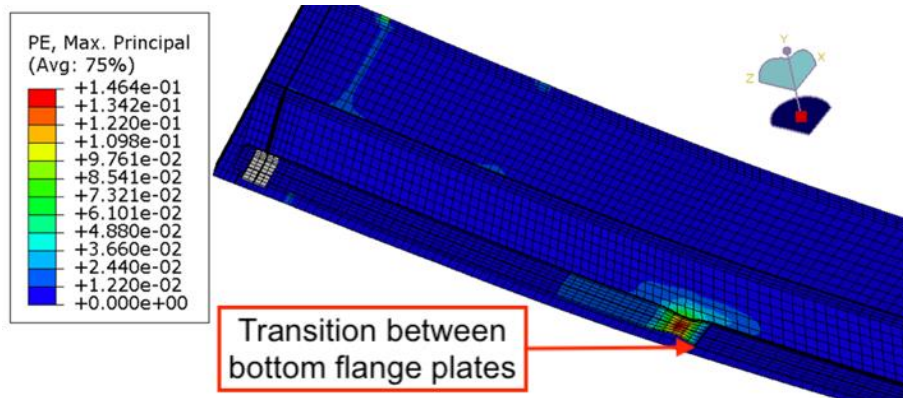


Figure 5.10: Failure mode of the girder on the numerical analysis

5.4.5. Fire Resistance Times

Table 5.2 summarizes the results from the fire resistance analysis under different fire scenarios. Based on the deflection criterion, the girder did not fail (NF) under the $L^2/400d$ limit in any of the analysed scenarios because the girder experienced failure under other limiting criteria before reaching the deflection limit. However, the $L/30$ limit was able to predict failure of the

girder 1-2 minutes prior to runaway of the model. When evaluating the rate of deflection criterion, results demonstrate that the girder experienced a higher deflection rate when exposed to the simulation fire and the hydrocarbon fire curve, reaching the deflection rate limit at 3 and 5 minutes of fire exposure, respectively. Regarding the strength criterion, the girder presented varying levels of fire resistance. It maintained its strength for 48 minutes under the standard fire scenario (similar to a building fire) and 20 minutes under the hydrocarbon fire scenario but did not reach failure when exposed to the design fire curve due to the cooling phase. Considering the high fire hazard risk associated with this bridge and its premature collapse during the fire incident (after approximately 10 minutes of fire exposure), it is likely that the bridge experienced a thermal field similar to that generated under hydrocarbon fire exposure. Some simplifications of the numerical model, such as variations in defined material properties and geometrical non-linearities, may cause discrepancies in the predicted fire resistance. Overall, the model effectively traces the fire behavior of the I-95 overpass in Philadelphia and can be used to develop design strategies to mitigate fire hazards in similar bridges to mitigate fire hazard in important infrastructure.

Table 5.2: Fire resistance times for the composite girder under different fire scenarios

Fire scenario	Fire resistance (min)			
	$L/30$	$L^2/(400d)$	$L^2/(9000d)$	Strength
Standard fire	32	NF	31	48
Hydrocarbon fire	12	NF	5	20
Design fire	18	NF	17	NF
Simulation fire	NF	NF	3	10

5.5. Strategies for Enhancing the Fire Resistance of Bridge Girders

The results of the numerical analysis presented above highlight the vulnerability of bridges to fire hazards. To design and construct more resilient infrastructure, it is essential to design critical bridges with adequate levels of fire resistance to withstand the adverse impact of fires. This section

explores two design strategies to improve the fire resistance of steel bridges: utilizing composite action between steel girders and concrete slabs, and implementing fire insulation measures. By assessing the performance of the I-95 overpass in Philadelphia with additional fire protection, this section aims to provide more clarification into the effectiveness of these strategies in reducing the vulnerability of steel bridges to fire hazards.

5.5.1. Composite Action

The first strategy to enhance the fire resistance of steel bridge girders involves utilizing composite action with the concrete slab. When the steel beam experience significant reduction of structural capacity during fire exposure, some of the forces carried by the steel girder are transferred to the cooler concrete slab. Additionally, the concrete slab helps slow the rate of temperature increase on the top flange through the heat sink effect. Previous studies have demonstrated that these beneficial actions from the slab can improve the fire resistance of steel bridge girders [227].

For the I-95 overpass, the steel girders were in composite action with the concrete slab. Therefore, the analyses on the girder were repeated without composite action to provide observations on the effectiveness of composite configuration. In this case, contact properties were assigned to the interface between the concrete slab and the steel girder, consisting of hard-contact in the normal direction and penalty contact tangentially, as in previous studies [227]. Figure 5.11 shows the increase in mid-span deflections with fire exposure time for the composite and non-composite bridge girder while exposed to the three fire curves from Figure 5.5. It can be observed that the non-composite girders experienced lower deflections in the early stages of fire exposure. This can be attributed to the restraint effect the concrete slab imposed on the steel girder during its expansion process. However, throughout fire exposure, the steel girder undergoes a rapid loss of

strength and stiffness, leading to the earlier failure of the non-composite configuration through the rate of deflection limit criterion.

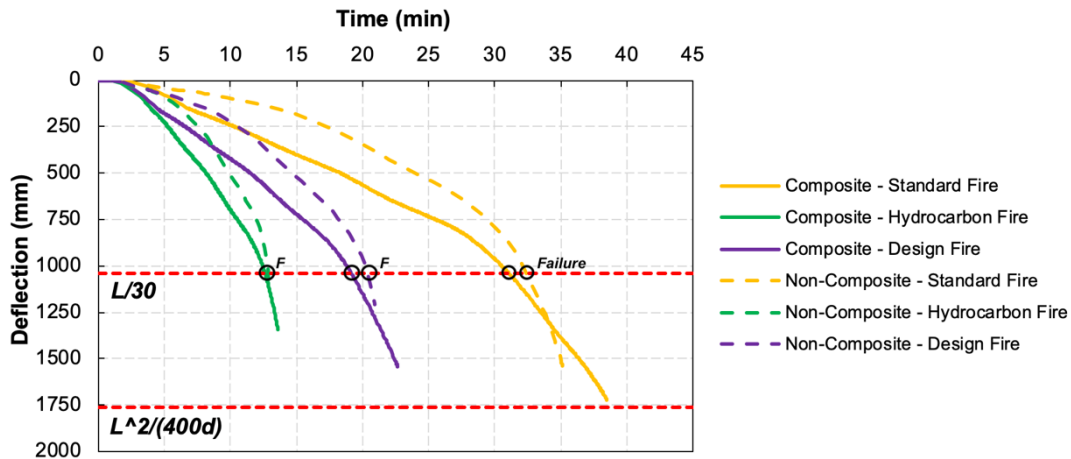


Figure 5.11: Deflection response of the composite and non-composite girder

Figure 5.12 presents the calculated degradation of moment capacity with fire exposure time of the non-composite girder exposed to the three fire curves is presented. The degradation pattern of the non-composite girder differs significantly from that of the composite configuration (Figure 5.8). In the non-composite case, the steel girder alone bears the entire applied moment, and its lower flexural capacity (due to the absence of composite action) reduces the time available to reach the applied moment threshold, resulting in earlier failure. Overall, these results highlight some beneficial effects of using composite action to improve the fire response of steel bridge girders. However, the increase in fire resistance provided by composite action might not be sufficient to achieve the desired fire resistance levels in certain scenarios, indicating that other alternatives, such as fire insulation, may need to be considered.

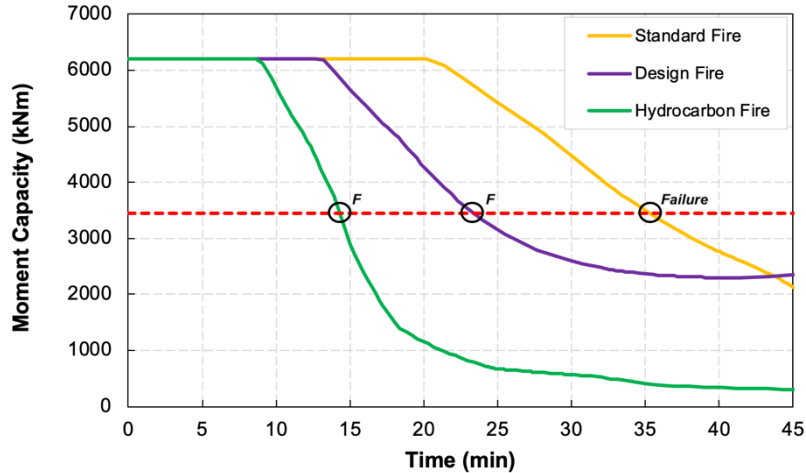
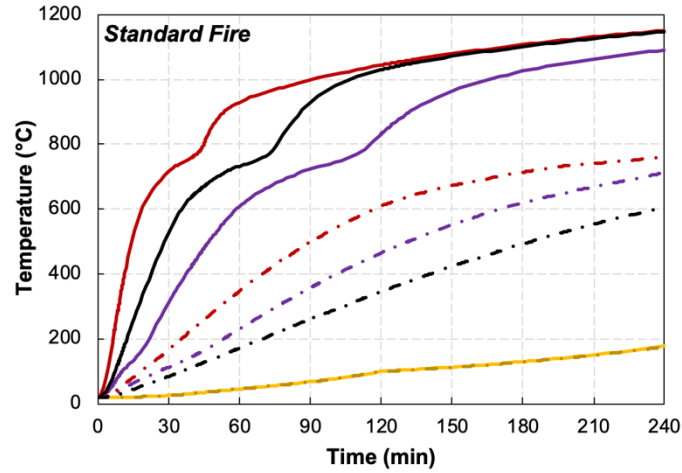


Figure 5.12: Degradation of moment capacity of the non-composite girder

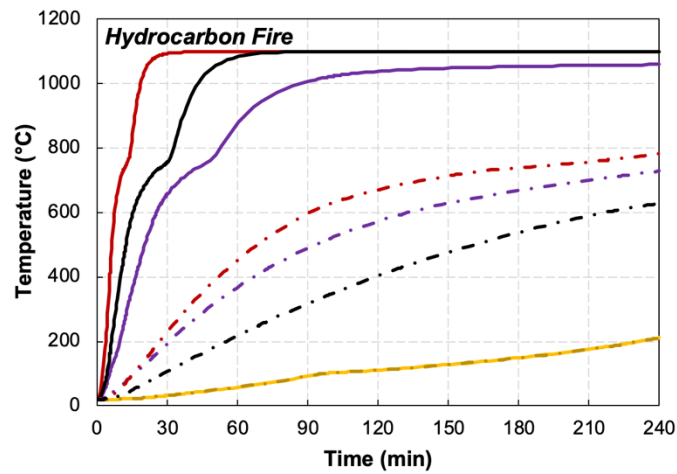
5.5.2. Fire Insulation

Another approach to improve the fire resistance of steel bridges involves using fire insulation materials on the steel girders to delay temperature increase in the steel section during fire exposure. This method is commonly employed in steel structural elements within buildings. Various types of insulating materials are available, including intumescent coatings, gypsum boards, and mineral wools. Since bridges face more severe weather conditions directly, spray-applied cementitious materials can offer enhanced durability and ease of application. Previous studies have already explored this strategy for enhancing the fire safety of steel bridges [228–230].

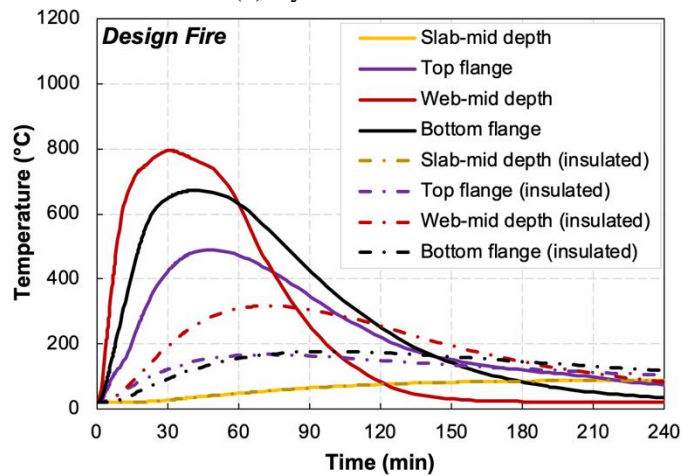
To assess the impact of fire insulation on the fire performance of the I-95 bridge overpass, the numerical model was updated to incorporate thermal insulation on the steel girder. Carboline type-5MD was chosen as the fire insulation material due to its superior effectiveness compared to similar options [230]. The insulation covers the entire steel girder with a total thickness of 12.7 mm. Figure 5.13 illustrates the thermal response of the insulated bridge girder compared to an unprotected steel girder section.



(a) Standard fire



(b) Hydrocarbon fire



(c) Design fire

Figure 5.13: Thermal response of the insulated girder exposed to different fire scenarios

As expected, the fire insulation significantly reduced the progression of temperatures in the steel girder. This effect is particularly pronounced during exposure to the hydrocarbon fire curve,

where the insulation notably delays the onset of elevated steel temperatures. For instance, after 30 minutes of fire exposure, the peak temperature in the steel girder reaches 1100°C compared to 230°C in the protected girder. It's important to note that unlike the unprotected steel girder, temperatures in the top flange of the protected girder are higher than in the bottom flange. This occurs because the bottom flange is covered by fire insulation from all sides, while the top flange is only protected from one side, leaving its top surface in contact with the concrete slab. Since the slab remains unprotected, temperatures rise at a similar rate as in the unprotected section, transferring some heat to the top flange of the steel girder. Overall, fire insulation demonstrated its effectiveness in reducing temperatures experienced by the steel girder across all fire scenarios.

Figure 5.14 illustrates the deflection response of the bridge girder with insulation, considering both composite and non-composite action between the steel girder and the concrete slab under standard and hydrocarbon fire scenarios. The deflection response is notably different from that observed in non-insulated composite and non-composite sections (Figure 5.8 and Figure 5.11, respectively). In all cases, the girder initially experiences slight negative deflections during the early stages of fire exposure (up to approximately 90 minutes). This is attributed to higher temperatures affecting the top flange of the steel girder, causing greater thermal expansion compared to the bottom flange. As the temperature of the section continues to rise throughout fire exposure, the strength and stiffness of steel start to degrade, resulting in increased deflection. Overall, the insulated girder demonstrated significantly improved fire resistance compared to the unprotected steel girder (Table 5.3).

The $L^2/400d$ deflection limit presented in Figure 5.14 is higher for the non-composite section due to its lower depth (no consideration to the concrete slab). The non-composite girders attained the maximum deflection at 229 and 185 minutes under the standard and hydrocarbon fire

exposure, respectively. Under the $L/30$ deflection limit, the girder attained failure about 30 minutes ahead, demonstrating an inconsistency between different methods. The rate of deflection limit was reached at later stages for these girders, and at 239 minutes of fire exposure for the composite girder exposed to the hydrocarbon fire curve. In summary, this analysis highlights the effectiveness of using fire insulating measure as a viable strategy for increasing the fire resistance of steel bridges.

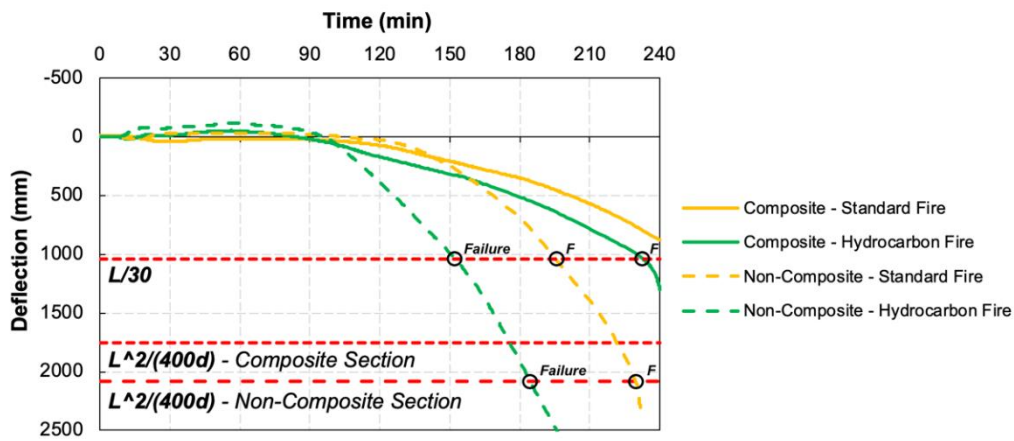


Figure 5.14: Deflection response of the insulated composite and non-composite girder

5.5.3. Fire Resistance with Enhanced Strategies

Table 5.3 summarizes the fire resistance outcomes from all conducted analyses. The girder exhibited varying fire resistance ratings based on different failure criteria. Generally, for composite girders, the rate of deflection criterion predominantly governed fire resistance, showing significant deviation from strength-based criteria. In these instances, the girder failed earlier under the strength criterion due to faster degradation of its flexural capacity. Overall, the fire resistance of steel girders is highly dependent on fire severity, with the lowest resilience observed during exposure to hydrocarbon fires. This highlights the importance of assessing bridge structures under realistic fire conditions. Furthermore, these findings emphasize the need for detailed analysis of bridge structures to design effective strategies for enhancing fire resistance. Both composite action and

fire insulation contribute to improving the fire resistance of steel bridge girders. While the impact of composite action on fire resistance is smaller, the contribution of fire insulation effect is very significant, particularly in hydrocarbon fire scenarios. These results suggest that the I-95 overpass girders with 12.7 mm of Carbolite type-5MD insulation could have survived the fire incident.

Table 5.3: Fire resistance results for the composite girder under different fire scenarios

Case	Composite action	Fire scenario	Fire insulation	Fire resistance (min)			
				$L/30$	$L^2/(400d)$	$L^2/(9000d)$	Strength
1	Yes	Standard	No	32	NF	31	48
2	Yes	Hydrocarbon	No	12	NF	5	20
3	Yes	Design	No	18	NF	17	NF
4	No	Standard	No	32	NF	31	36
5	No	Hydrocarbon	No	13	NF	8	14
6	No	Design	No	20	NF	18	24
7	Yes	Standard	Yes	NF	NF	NF	NF
8	Yes	Hydrocarbon	Yes	232	NF	239	NF
9	No	Standard	Yes	195	229	231	161
10	No	Hydrocarbon	Yes	151	185	202	130

5.6. Summary

This chapter demonstrated the applicability of the developed numerical model through a detailed analysis of the fire induced collapse of the I-95 overpass in Philadelphia on June 11, 2013. Based on the results obtained, the following conclusions can be drawn:

1. The developed numerical model was capable of properly simulating this bridge fire incident by predicting the fire temperatures generated by a tanker fire and the structural response of the girder under different exposure conditions.
2. The thermal response of the girder to the simulation fire was found to be similar to its response when exposed to a hydrocarbon fire. This demonstrates that bridge structures

are subjected severe fire conditions during tanker fire incidents and that this should be considered in the fire design of the bridge girders.

3. The failure mode identified in the model is the same as observed in the actual bridge fire incident. The transition in flange thickness revealed a weak point in the steel section, which led to failure of the girder due to yielding of the steel. This failure mechanism requires further investigation to improve fire design of composite girders.
4. Both composite action and supplementary fire protection can be used to enhance the resilience of steel bridges under fire. Fire insulation is a much more effective strategy for delaying the progression of temperatures in the steel section and thus ensuring slower degradation in capacity under fire exposure, reducing the risk of premature collapse.

6. PARAMETRIC STUDIES

6.1. General

The numerical model developed and validated in Chapter 4 is applied to quantify the effect of material and structural parameters, as well as fire exposure conditions, on the fire resistance of concrete bridge girders. Based on the hypothesis of this study (Chapter 1), I-shaped girders present lower fire resistance due to their slender cross-sections, which leads to rapid degradation in their shear capacity. Thus, the first set of analysis compare the fire response of I-shaped and rectangular bridge girders. Next, the effect of cross-sectional size is analyzed by comparing the fire resistance of different AASHTO standard cross-sectional shapes under different fire scenarios. The fire model developed using FDS-PyroSim is employed to evaluate the effect of non-uniform temperature distributions considering influencing parameters related to the bridge geometry (girder depth and spacing between girders), bridge geometry (span length and clearance height), and fire intensity (in terms of burning area). The effect of other design parameters, such as span length and concrete type, have also been analyzed to evaluate the effect of specific design characteristics that can affect the fire response of concrete bridge girders. Such information is crucial for predicting all possible failure modes and developing appropriate design recommendations for enhancing the fire safety of concrete bridge girders.

6.2. Effect of Cross-Sectional Shape

Initially, the numerical model was used to evaluate the fire behavior of a bridge girder with a standard AASHTO Type II cross section. In addition, a conceptual rectangular section with same width and depth was modelled to analyze the failure modes of different UHPC bridge girders, allowing for a comparison with the results from the I-shaped section. Figure 6.1 illustrates the details of the cross-section and the structural configuration of the girders. They were reinforced

with sixteen 12.7 mm-diameter reinforcing bars, distributed in two layers at the bottom part of the girder, spaced 51 mm from each other and from the cross-section contour. Both girders were 6,200 mm-long, with a clear span of 6,000 mm and two concentrated forces of 378 kN applied 1,000 mm from the girder mid-span, while exposed to a standard fire (ASTM E119). Thermal and mechanical properties of steel and UHCP were assumed as in Chapter 4.

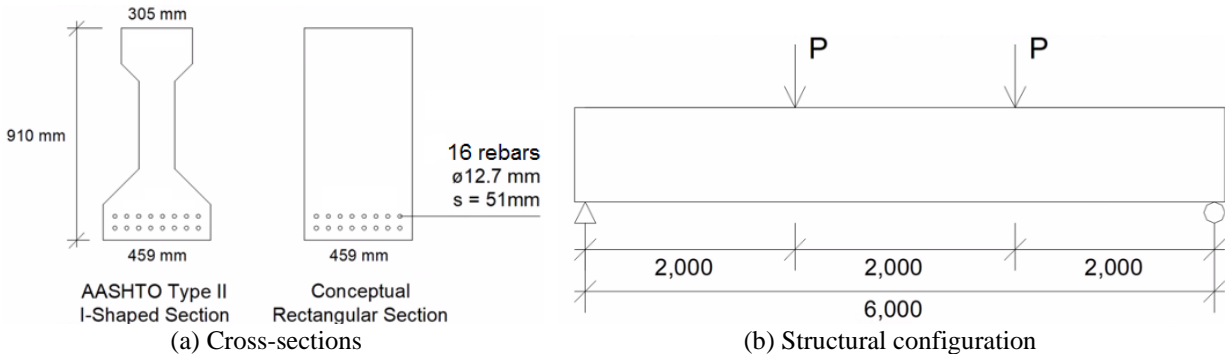


Figure 6.1: Details of the modelled UHPC bridge girder

6.2.1. Thermal Response

Figure 6.2 presents the progression of temperatures with fire exposure time at different points throughout the cross-section of the modeled UHPC bridge girders (both I-shaped and rectangular). Selected points include corner, center and top rebars, as well as at the center of the web and the top surface of the girder, as illustrated in Figure 6.1. It can be seen that the temperature progression in the corner and center rebars is very similar in both girders. However, temperature in other locations progresses more rapidly in the I-shaped girder. For instance, at 60 minutes of fire exposure, the temperature in the center of the web is below 40°C in the web of the rectangular girder, while it is past 350°C in the I-shaped girder (Figure 6.3). This is attributed to the slender cross-section of the I-shaped girder and resulting lower thermal mass, which allows a faster progression of temperatures throughout the girder cross-section. The thinner web also leads to rapid transmission of heat to the bottom and top flanges, which results in increased temperatures in the top layer of rebars, as well as at the compression zone of the I-shaped girder.

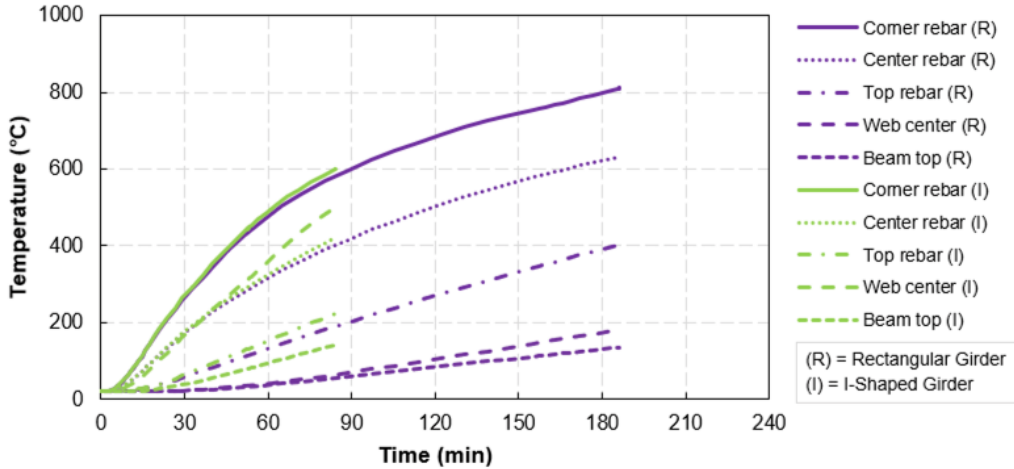


Figure 6.2: Progression of temperatures with fire exposure time in the UHPC bridge girders

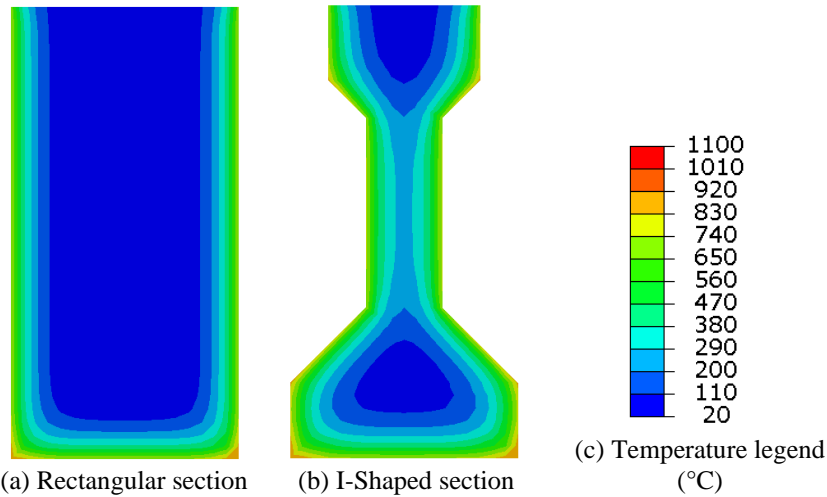


Figure 6.3: Isotherms of the two bridge girders after one hour of exposure

6.2.2. Deflection Response

The progression of midspan deflection with fire exposure time for both girders up to their respective failure time is presented in Figure 6.4. It can be seen that deflections were higher and increased much more rapidly in the I-shaped girder compared to the rectangular girder throughout the whole fire exposure. This results from the reduced moment of inertia of the I-shaped cross-section compared the rectangular cross-section. Furthermore, the faster degradation of strength and stiffness due to the higher temperatures to which the I-shaped girder experience compared to

the rectangular contributes to the rapid increase of midspan deflections in I-shaped girders during fire exposure, contributing to early failure and lower fire resistance.

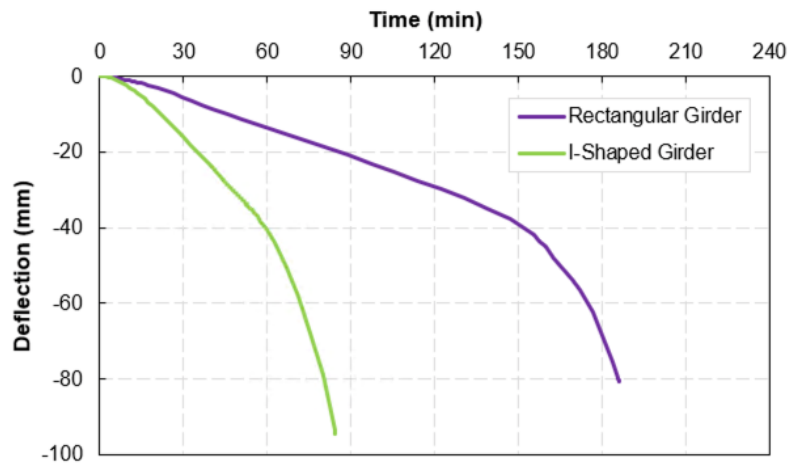


Figure 6.4: Progression of midspan deflections in rectangular and I-shaped girders

6.2.3. Strength Degradation

Figure 6.5 presents degradation of the flexural and shear capacities of both girders with fire exposure time. From the assessment of moment capacity degradation, it is clear that the I-shaped girder experience faster degradation than the rectangular girder, which is attributed to the higher temperatures attained in the section that lead to faster degradation of concrete and steel strengths. However, only the rectangular girder experienced failure under flexural limit state, which occurred after 186 minutes of fire exposure. The I-shaped girder did not reach the flexural limit state because it failed much earlier under the shear limit state, at 84 minutes of fire exposure, as can be seen in Figure 6.5 (b). Degradation of shear capacity in the rectangular girder occurred much more slowly compared to the I-shaped girder, attributed to the slower progression of temperatures in the web.

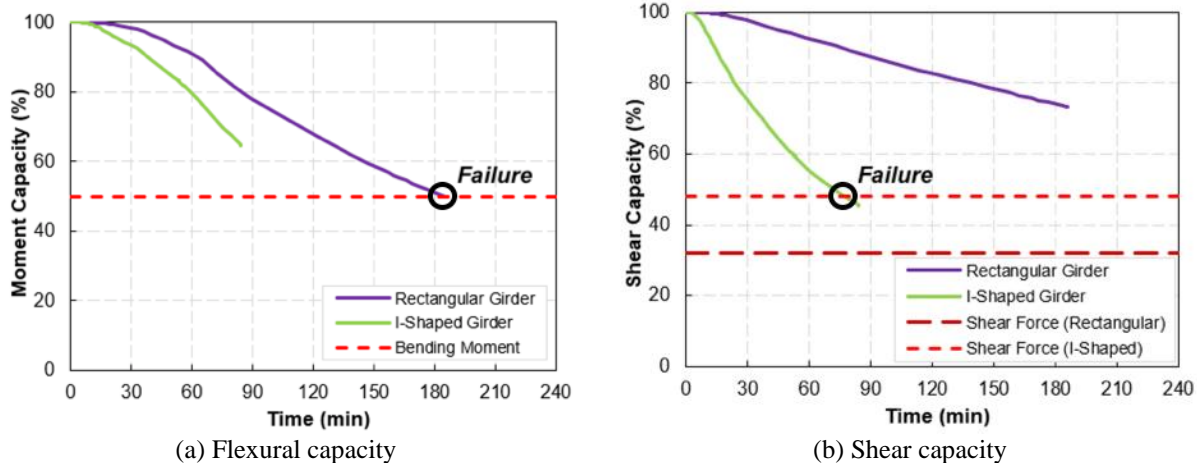


Figure 6.5: Degradation of flexural and shear capacities as a function of fire exposure time

To further assess the failure mode of these girders during fire exposure, principal plastic strain contours obtained through the ABAQUS finite element model at the estimated failure time are presented in Figure 6.6. It can be seen that the mode of failure changed from flexure (in the rectangular section) to shear (in the I-shaped section) due to concentration of strains on the bottom of the mid-span (rectangular) to the center of the web (I-shaped), respectively. While both girders presented similar degradation of the steel reinforcement strength, degradation of the concrete strength, especially in the web, was much more severe in the I-shaped section. This is a result of the lower thermal mass, which allowed higher temperatures in the web of the I-shaped section. Consequently, the failure mode switched from flexural to shear, highlighting a potential vulnerability of I-shaped girders that requires careful consideration in fire design.

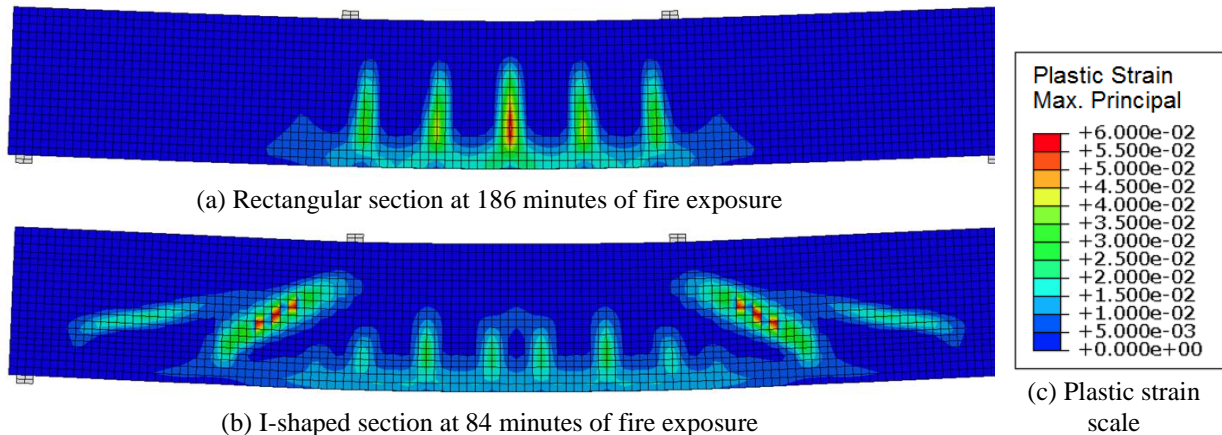


Figure 6.6: Principal plastic strains through the beam's longitudinal cross-sections

6.3. Effect of Cross-Sectional Size

In the next step of these parametric studies, standardized cross-sections for concrete bridge girders (AASHTO types I through IV) were modeled to evaluate the effect of cross-sectional size on the fire response of bridge girders made with UHPC. These sections were selected due to the fact that they are commonly used in bridge construction throughout the United States and that they cover different bridge spans. Figure 6.7 presents the dimensions and recommended location of prestressing strands in these sections. Based on their characteristics, four bridge girders were designed with low-relaxation prestressing strands of 12.7 mm-diameter, made of 1,862 MPa steel, and subjected to an initial prestress of 885 MPa (47%). The strands were distributed in layers inside of the bottom flange, spaced 51 mm from each other and from the girder contour. Table 6.1 presents key design characteristics of each girder, including the number of strands, span length and the applied load. The load was applied as two concentrated forces, each placed 1 m from the girder midspan for all girder types.

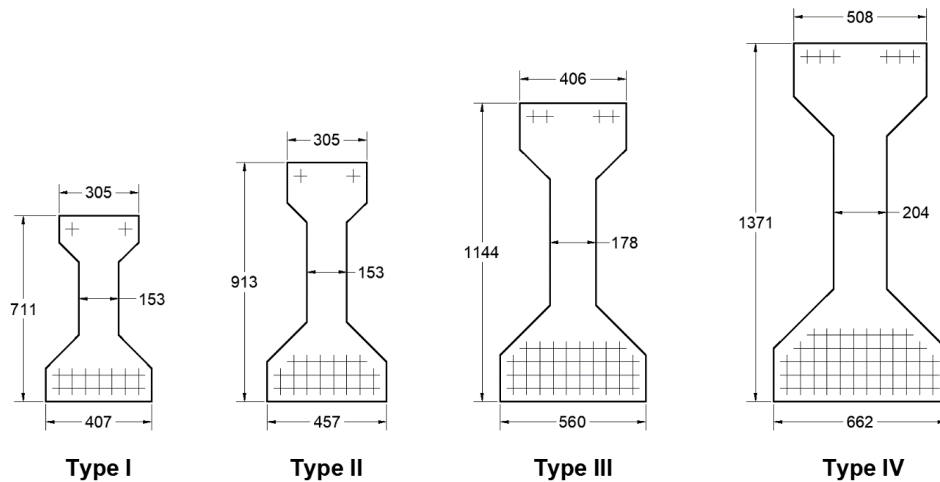


Figure 6.7: Cross-sectional dimensions and tensile reinforcement in AASHTO standard sections

Table 6.1: Design characteristics of the girders with each of the four cross-sections

AASHTO Girder	Web width (mm)	Girder height (mm)	Effective depth (mm)	Flexural reinforcement	Span (m)	Applied load (kN)
I	153	711	634.5	14 - Ø 0.5 mm	12	450
II	153	913	815.6	22 - Ø 0.5 mm	16	550
III	178	1,144	1,020.5	38 - Ø 0.5 mm	20	900
IV	204	1,371	1,227.4	54 - Ø 0.5 mm	24	1,250

6.3.1. Thermal Response

The four girders were modeled under both standard and hydrocarbon fire scenarios. Figure 6.8 illustrates the temperature progression over time at the center of the web and the bottom corner strand for each case. Generally, temperatures rise more quickly at the strand locations due to their proximity to the heated surface compared to the center of the web. It is important to note that these temperatures are measured at specific locations and can vary across the girder cross-section. Larger girder types contain more strands, distributed in multiple layers within the bottom flange (Figure 6.7). Thus, while strands in the first layer experience similar temperatures across all girder types, larger girders have several strands that are protected from high temperatures in the inner regions.

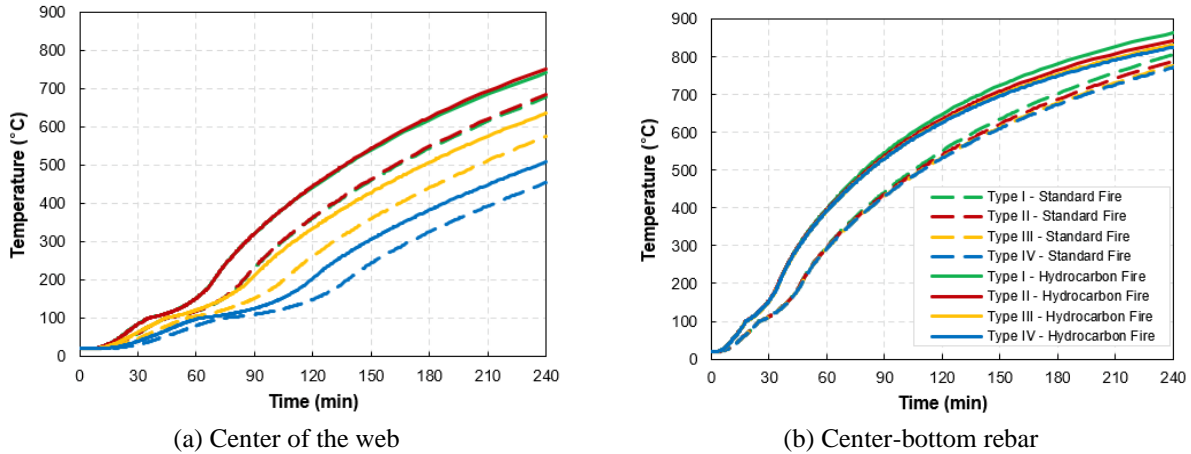
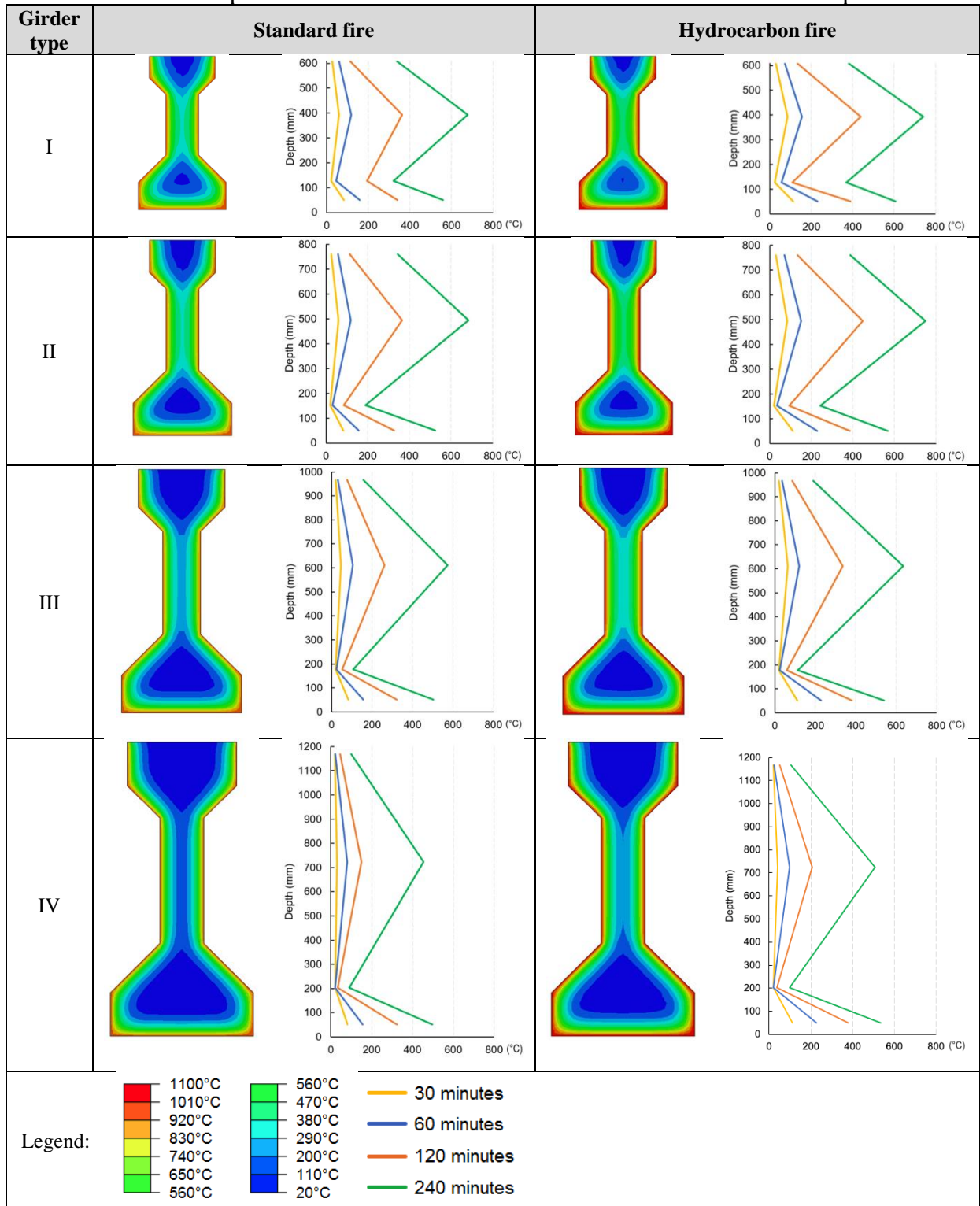


Figure 6.8: Temperature increase with fire exposure time

It can be seen that temperatures are higher in the center of the web in girders types I and II, as they have the same web width. Temperatures decreased in girders types III and IV as the web width increased, delaying the progression of temperatures to the center of the web. As expected, the girders exposed to the hydrocarbon fire curve experienced higher levels of temperature in the web as compared to the girders exposed to the standard fire curve. This behavior was also noticed in the temperatures at the bottom-corner strands. In general, there was not much difference in the temperatures at the bottom-corner strand, which is attributed to the fact that the same concrete cover thickness (51 mm) was used for all girders. A slight difference in temperatures was noticed in later stages of fire exposure in girders types I and II due to their lower concrete mass, which allowed heat progression into the bottom flange and contributed to increase the temperature in the bottom corner reinforcement.

The temperature contours generated by the finite element model are shown in Table 6.2. These contours represent temperatures throughout the cross section at 120 minutes of exposure to the standard and hydrocarbon fires and they illustrate the above discussion. It can be clearly seen a higher concentration of heat in the web of the small cross-sections and that temperatures were higher when the girders were exposed to the hydrocarbon fire curve.

Table 6.2: Temperature contours in standard sections after 2 hours of fire exposure



6.3.2. Deflection Response

The structural behavior of the four girder types exposed to the two fire scenarios (standard and hydrocarbon fire curves) is presented in Figure 6.9 in terms of midspan deflections. It can be observed that all curves present a similar trend, which can be divided into three stages. In the first stage, there is a rapid increase in deflection due to thermal expansion of concrete. During the second stage, the rate of deflection decreases as it is influenced by the degradation of material strength and stiffness as temperatures progress within the girders' cross-section. In the final stage, there is another rapid increase in deflection resulting from material creep and softening of the steel strands. The distinct response between each case shows that both the fire scenario and cross-sectional size present influence on the fire response of concrete bridge girders. In general, it can be noticed that the girders exposed to the hydrocarbon fire attained lower fire resistance, of about 30 minutes, than the same girder exposed to the standard fire curve.

Overall, the girders with smaller cross-sections (types I and II) experimented a faster increase of mid-span deflections when compared to the more robust girders (types III and IV), with higher thermal mass. This can be attributed to the faster progression of temperatures inside of these girders, which lead to a faster degradation of strength and stiffness of concrete and steel. Since the number of strands increase with the size of the concrete girder, the smaller girders had more strands in peripheral locations, which experienced higher levels of temperatures. This means that in larger sections most of the strands are located in the inner parts of the bottom flange where temperatures are not very high, delaying degradation of its strength and increasing its fire resistance. Consequently, despite their higher span lengths, larger sections can sustain its original strength longer, leading to higher fire resistance.

With regards to deflection limit states, the $L/30$ and $L^2/400d$ limits were assessed to determine failure based on the maximum deflections, as well as the $L^2/9000d$ maximum deflection rate. The failure time of each case is presented in Table 6.3. Overall, it can be observed that the $L^2/400d$ limit was not able to predict failure of the bridge in most cases and that the $L/30$ limit resulted in more conservative results than other failure criteria. The deflection rate criterion ($L^2/9000d$) was able to predict failure for the girders experiencing a significant increase in deflections towards the later stages of the analysis for most cases.

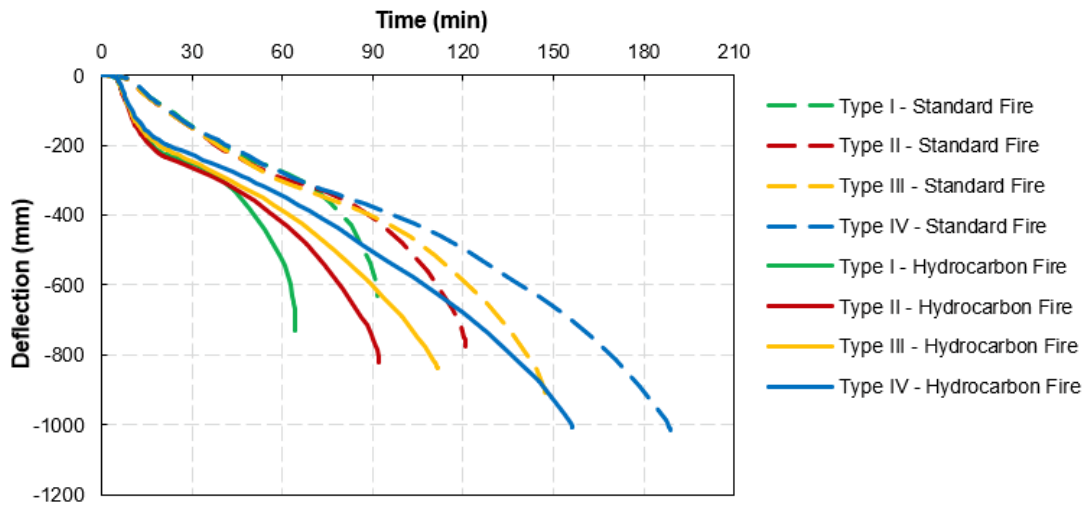


Figure 6.9: Midspan deflection during exposure to prescribed fire curves of standard sections

6.3.3. Strength Degradation

The structural capacity of the four girders during exposure to the standard and hydrocarbon fire scenarios were calculated based on the previously derived equations for flexural and shear strength degradation. The calculations take into consideration temperature-dependent degradation in mechanical properties of steel and concrete, obtained through the numerical model at different locations of the girders. Figure 6.10 presents the reduction of flexural and shear capacity with the applied bending moment and shear forces resulting from the applied loading present during fire exposure for all cases studied.

It can be seen that both the flexural and shear capacities degrade with fire exposure time in a similar trend. The reduction in flexural capacity is very small during the first 30 minutes of fire exposure, which is attributed to the fact that temperatures are very low within the cross-sections, including at strands locations. After this initial stage, temperatures start to progress through the concrete girder and reach the prestressing steel strands, leading to a faster degradation of the flexural capacity. This degradation occurs faster in the smaller cross-sections (types I and II) due to its lower concrete mass that allow the progression of temperatures more easily. Similarly, the girders exposed to the hydrocarbon fire curve presented faster degradation (approximately 30 minutes) than the same girders exposed to the standard fire curve.

A similar behavior was observed in degradation of the shear capacity. However, in this case, the girders of types I and II presented almost the same level of degradation. This is due to the fact that these girders have the same web width (153 mm), lower than the other girders. This slender shape allows a faster progression of temperatures and rapid degradation of concrete mechanical properties in the web region, which contributes to lower shear capacity in these UHPC girders. Overall, it can be observed that degradation of shear and flexural capacities occurred at a similar rate and resulted in similar failure times.

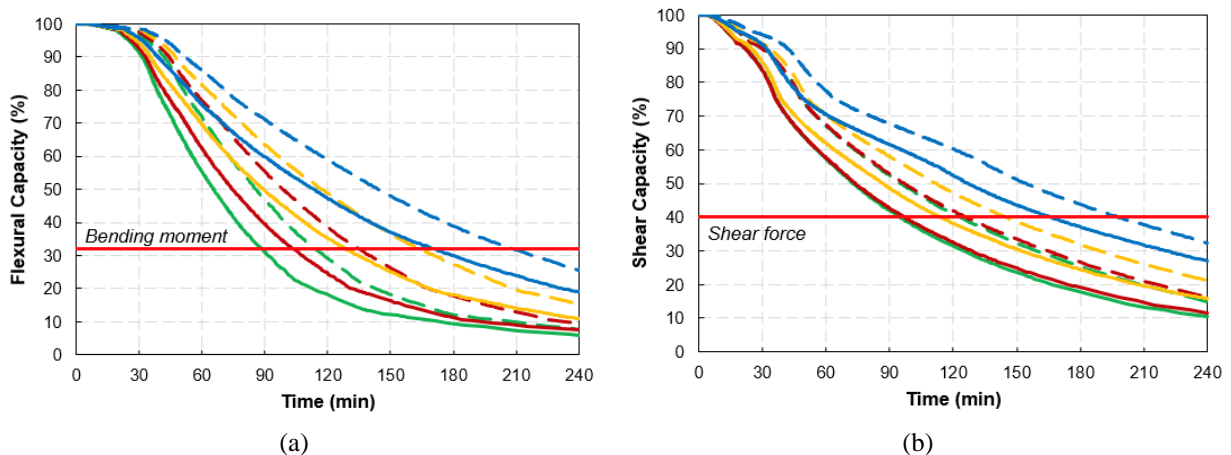


Figure 6.10: Flexural and shear capacity degradation during exposure to prescribed fire curves

6.3.4. Fire Resistance

Table 6.3 summarizes results obtained from these analyses, including fire resistance (failure times) obtained through each failure criteria. The analysis of AASHTO girders type I through IV made with UHPC under standard and hydrocarbon fire scenarios reveals that larger girder sections exhibit higher fire resistance, attributed to their increased thermal mass. Increasing fire severity from standard to hydrocarbon fire exposure resulted in a decrease of the fire resistance in approximately 30 minutes. While all four types of girders experienced failure during four hours of exposure to both fire scenarios, they varied according to different limiting criteria. The $L^2/400d$ and $L^2/9000d$ limits for maximum deflection and rate of deflection were not able to capture failure in all of the studied cases. On the other hand, the $L/30$ limit predicted more conservative fire resistance times than the other criteria. It should also be noted that flexural and shear strength degradation were very close in some of the cases and varying loading configurations could result in earlier shear failure. Overall, these results demonstrate the need of considering proper failure limits to analyze the fire response of concrete bridge girders.

Table 6.3: Summary of fire resistance results from different limit states

AASHTO Girder	Fire scenario	Fire resistance (min)					
		Deflection criteria			Strength criteria		Final
		$L/30$	$L^2/(400d)$	$L^2/(9000d)$	Flexural	Shear	
I	Standard	82	90	90	105	122	90
	Hydrocarbon	54	62	NF	78	99	62
II	Standard	108	NF	120	121	123	120
	Hydrocarbon	74	91	91	91	100	91
III	Standard	135	NF	147	140	145	140
	Hydrocarbon	99	NF	NF	112	117	112
IV	Standard	170	NF	188	178	202	178
	Hydrocarbon	136	NF	NF	142	168	142

* NF – No failure

6.4. Effect of Fire Exposure Conditions

The fire dynamics model developed using FDS-PyroSim is used to trace the development of bridge fires and determine the temperatures of exposure in concrete bridge girders under different design and exposure conditions. This section presents details on the parameters chosen for these parametric studies as well as results obtained in the analysis. Results include the adiabatic surface temperatures, which will be used for deriving a fire curve for evaluating the fire resistance of concrete bridge girders as part of the design recommendations in Chapter 7.

In these parametric studies, five influencing parameters are selected based on an analysis of previous bridge fire incidents and consideration to basic principles of fire dynamics that could lead to more or less severe fire exposure conditions. Table 6.4 presents the range of variables for each studied parameter, which includes the bridge geometry (girder depth and spacing between girders), bridge geometry (span length and clearance height), and fire intensity (heat release rate). In terms of girder depth, two standard AASHTO sections are selected (Type I and Type IV) to investigate the level of influence this parameter has to keep entrapped hot gases and smoke between the girders. In addition, two girder spacings (1.5 m and 3.0 m) are investigated, as they can also contribute to heat propagation between the girders. Since these parameters are related to each other, two concrete bridge structures are simulated in the fire model: short span bridge (12 m) with Type I girder and 1.5 m spacing; and medium span bridge (24 m) with Type IV girder 3.0 m spacing. In relation to the bridge geometry, two clearance heights (5.0 m and 8.0 m) are evaluated for each combination of girder type/spacing. As for the fuel source, the selected fire intensity ($2,500 \text{ kW/m}^2$) is simulated considering two different fuel spillage areas, 30 and 80 m^2 , which generates total HRR of 75 and 200 MW, respectively. The fuel source was placed adjacent to the abatement walls as this would lead to higher temperatures, based on previous studies

[28,231]. The combination of these variables resulted in eight fire scenarios, and the results from the analysis of each one of them are presented in the following sections.

Table 6.4: Key variables studied as part of parametric studies

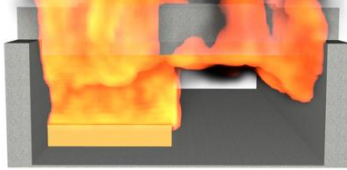
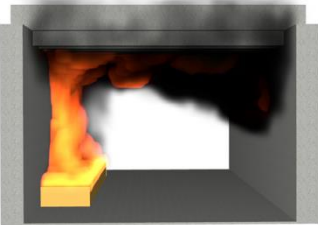
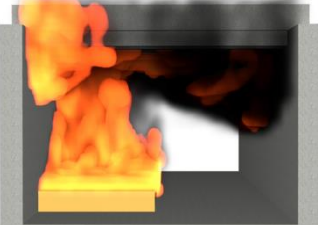
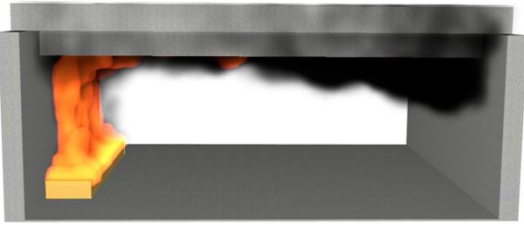
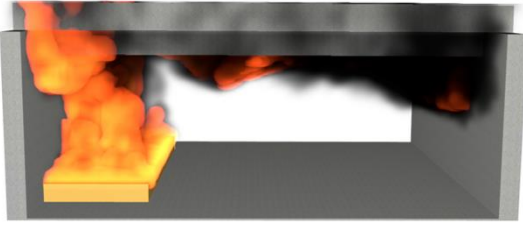
Parameter		Variables
Girder geometry	Girder depth (D)	700 mm (AASHTO Type I) 1,400 mm (AASHTO Type IV)
	Girder spacing (S)	1.5 m (shorter girder spacing) 3.0 m (larger girder spacing)
Bridge geometry	Bridge length (L)	12 m (short span) 24 m (medium span)
	Bridge height (H)	5.00 m (minimum clearance) 8.00 m (intermediate clearance)
Fire intensity	Spillage area (A)	30 m ² (tanker area) – 75 MW 80 m ² (tanker + spill) – 200 MW

6.4.1. Fire Development Response

The development of a bridge fire under eight different scenarios is presented in Table 6.5 through pictures of the NIST Smokeview program used to visualize the results. Each picture reflects a 60 minute fire duration. Across all scenarios, the fire exhibited a similar behavior: initial combustion at the source led to a vertical flow of flames and hot gases against the abutment wall, followed by rapid spread through the channels between the girders and descent towards the opposite abutment wall. This is due to the entrainment of ambient air as a result of the buoyancy of the hot, moving flow, which forms a jet. In some scenarios, the amount of hot gases and smoke filled the entire space between the girders and it is possible to see the flames breaching the sides of the bridge. This is the case of the bridges exposed to a fire of higher intensity (200 MW), which presented a higher volume of flames and smoke when compared to a bridge of similar characteristics but lower fire intensity (75 MW). Comparatively, bridges with reduced clearance heights (5 m) and shorter span lengths (12 m) exhibited larger flame and smoke, attributed to

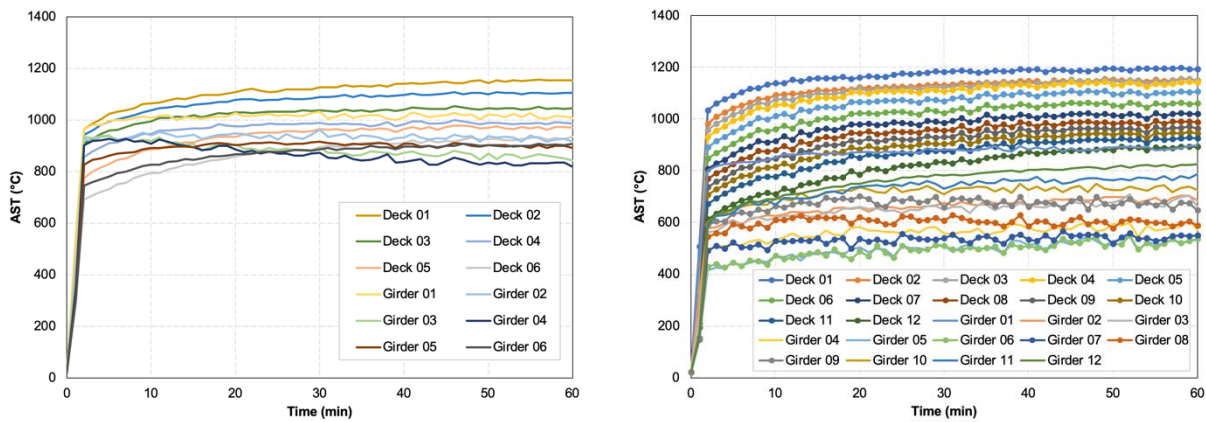
limited space for dissipation. On the other hand, bridges with higher clearances (8 m) and medium spans (24 m) exhibited slightly lower fire spread.

Table 6.5: Development of bridge fires under different scenarios

Bridge geometry	75 MW Fire	200 MW Fire
Clearance: 5 m Length: 12 m		
Clearance: 5 m Length: 24 m		
Clearance: 8 m Length: 12 m		
Clearance: 8 m Length: 24 m		

One of the key results from the fire model is the adiabatic surface temperatures (AST) measured at different points (every 2 m) along the length of the bridge. Figure 6.11 presents the AST recorded as a function of fire exposure time from two analyzed scenarios, that were exposed to the same fire intensity (total HRR of 75 MW) and minimum clearance (5 m), but two different bridge designs with varying spans: a short bridge spanning 12 meters and a medium bridge

spanning 24 meters. The results clearly show that higher thermal gradients are developed in the bridge with a medium span. The difference in thermal gradients in bridges of different span lengths can be attributed to the fact that longer bridge presents bigger volumes for heat propagation. Besides, the larger girder spacing adopted in these scenarios permits a faster propagation of heat. It is also possible to observe that the medium span bridge experienced slightly higher temperatures compared to the short span bridge. However, the average AST for all measured points throughout the bridge is higher for the short span bridge (965°C) compared to the medium span bridge (856°C). Graphs with results from all the scenarios analyzed are presented in APPENDIX C – FIRE DYNAMICS SIMULATIONS RESULTS.



(a) Short span bridge (12 m-long span)

(b) Medium span bridge (24 m-long span)

Figure 6.11: Adiabatic surface temperature measured along the length of the girder and the deck

Figure 6.12 presents the minimum and maximum temperatures recorded on the bottom of the girder and of the deck for each scenario analyzed as a function of heat release rate (HRR). The two total HRR used in the analysis were 75 MW and 200 MW, which represented the two burning areas of 30 m² and 80 m², respectively. It can be seen that the maximum temperatures recorded on the bottom of the girder (Figure 6.12 (a)) were higher in the short span bridges (L=12), as well as for the bridges with lower clearance (H=5). This can be explained by the fact that hot gases quickly concentrate on the space between the girders in short span bridges, leading to faster increase of

AST when compared to medium span bridges. For this reason, it is not possible to observe a significant difference in the maximum temperatures recorded on the deck surface (Figure 6.12b). This difference is observed for HRR of 75 MW, but it becomes less pronounced when the bridge is exposed to a higher fire intensity as the maximum registered AST becomes very similar. A similar trend can be noted when analyzing the minimum temperatures registered along the girder (Figure 6.12c), where it can be observed that a more significant gradient is developed for the medium span (L=24) and lower clearance (H=5) bridge. A similar trend is observed in the minimum temperatures recorded on the deck surface (Figure 6.12d), but much less significantly. Overall, it is clear that the studied parameters can affect the development of a fire on a bridge and that it can lead to significant thermal gradients along the bridge girder and deck.

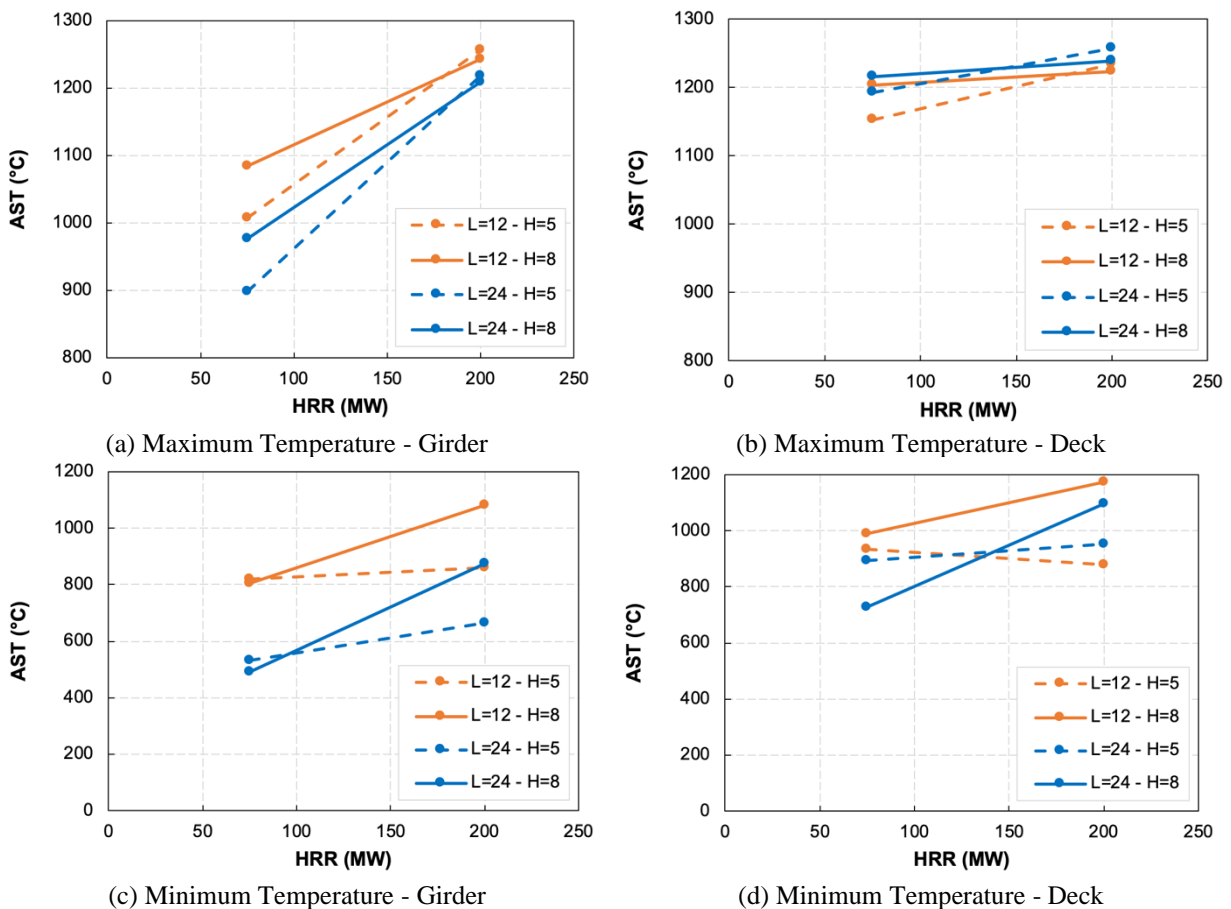
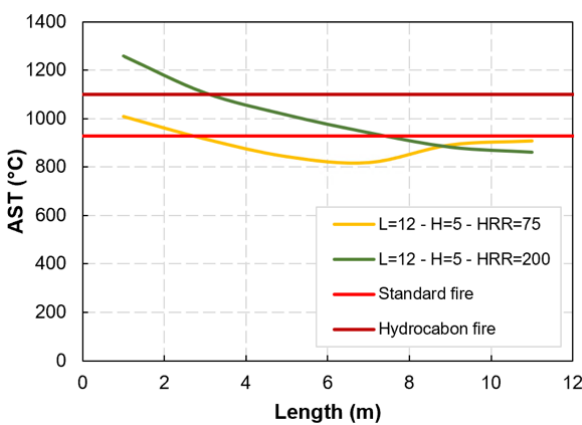
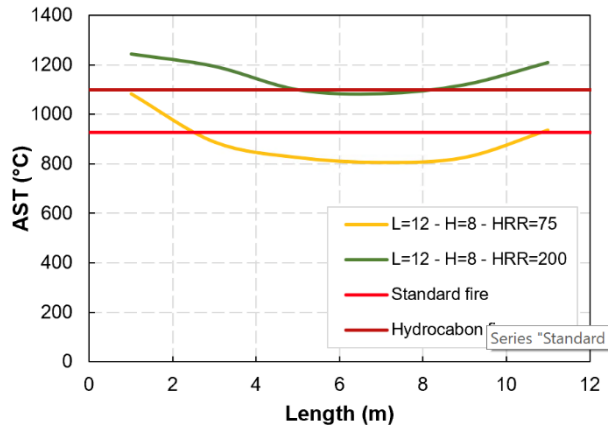


Figure 6.12: Maximum and minimum AST at the bottom of the deck and the girder

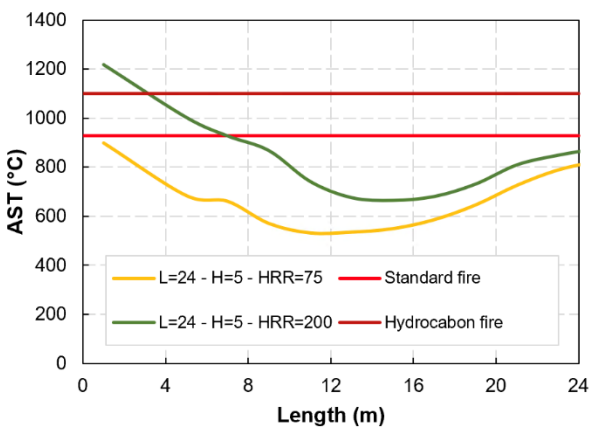
Figure 6.13 presents the measured AST from the fire simulations along the length of girder in comparison to temperatures from standard and hydrocarbon fire curves, all at 60 minutes of fire exposure. It can be observed that temperatures close to the support location (beginning of the girder) is higher than the hydrocarbon fire temperatures in all cases where the fire of higher intensity (HRR of 200 MW) was considered. The lowest temperatures were measured at midspan in almost all cases, with significant thermal gradients in the medium span bridge (L=24). Overall, these results demonstrate that bridges can experience severe fire temperatures and high thermal gradients depending on its geometrical features (span length and clearance height).



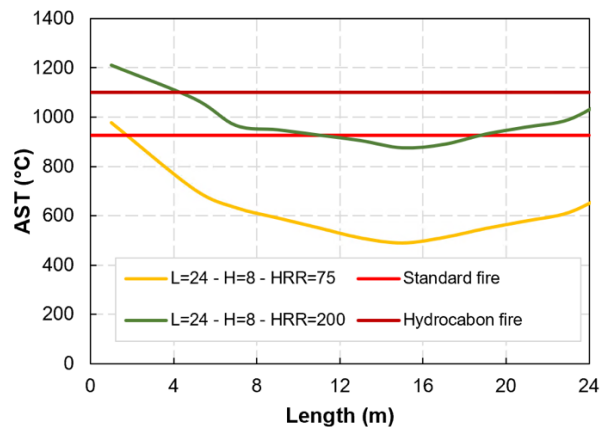
(a) Bridge with L=12 and H=5



(b) Bridge with L=12 and H=8



(c) Bridge with L=24 and H=5



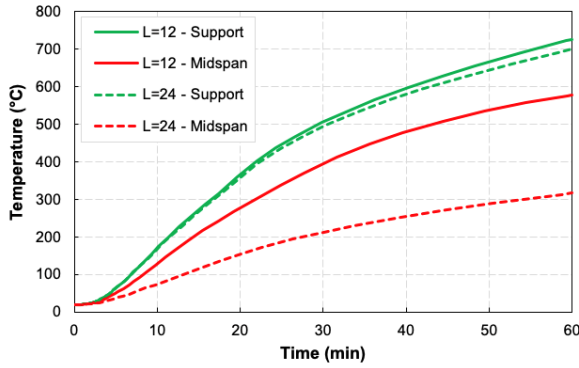
(d) Bridge with L=24 and H=8

Figure 6.13: AST as a function of bridge length compared to standardized fire curves

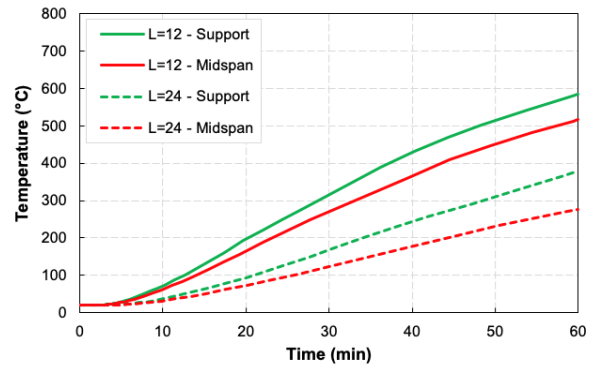
6.4.2. Thermal Response

The temperatures obtained in the fire model (FDS-PyroSim) were used as input in the finite element model (ABAQUS) to analyze the thermal response of bridge girders under realistic fire conditions. Figure 6.14 (a) and Figure 6.14b present the temperatures predicted by the thermal analysis at the corner prestressing strand location and at the center of the web, respectively, for girders from a short (12 m) and a medium (24 m) span bridge. Both selected scenarios consisted of bridges with a clearance height of 8 m exposed to a lower fire intensity (75 MW). These conditions were selected to be presented here due to the fact that they have produced the highest thermal gradients along the bridge length in each scenario. Results from all modelled scenarios are discussed in more details in APPENDIX D – THERMO-STRUCTURAL ANALYSIS RESULTS.

In order to analyze the thermal gradient developed along the bridge length in each scenario, temperatures at the support and midspan locations are plotted for comparison. Based on the results presented in the thermal analysis of both cross-sections, it can be observed that the thermal gradient from fire exposure is reflected on the temperatures measured within the girder along their lengths. For instance, while the temperatures at the corner rebar (Figure 6.14 (a)) were very similar for both girders at the support locations, there is a significant difference in the temperatures measured at the midspan cross-section between both bridge span lengths. Much higher temperatures were measured for the short span bridge (almost 600°C) than in the medium span bridge (slightly higher than 300°C). In this case, temperatures at the support location are very similar in both girders because they were analyzed right above the fire source, but as the bridge span increases, heat is dissipated to the environment and reduces the temperatures within the structural member at this location, as illustrated in Figure 6.15. A similar trend was also observed in the temperatures measured at the center of the web under similar exposure conditions (Figure 6.14b).



(a) Corner prestressed strand



(b) Web mid-height

Figure 6.14: Thermal response of girders from a bridge with higher clearance (8 m) exposed to a lower fire intensity (75 MW)

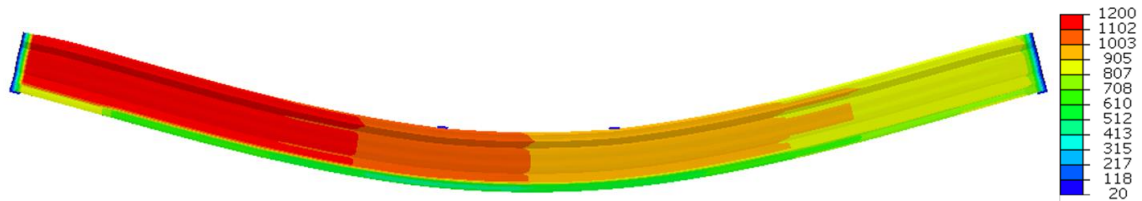
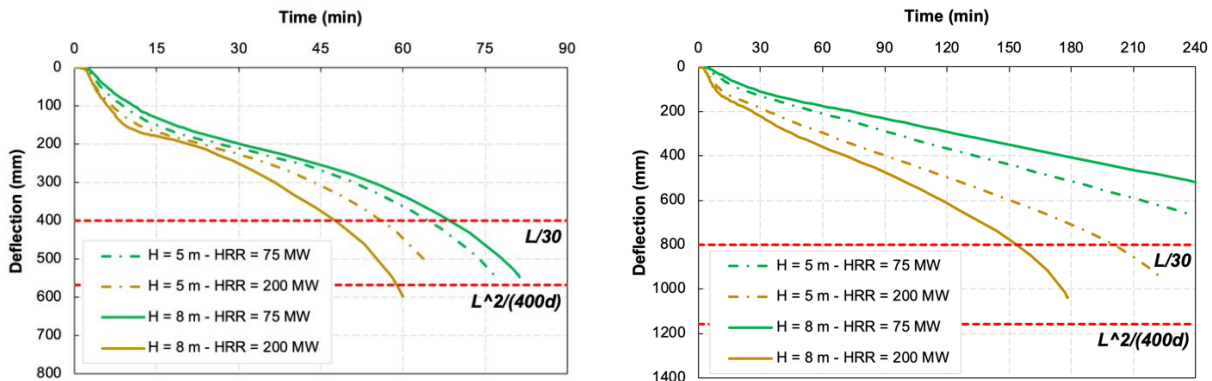


Figure 6.15: Thermal gradient developed along the length of a larger bridge girder (24 m) with a lower clearance (5 m) exposed to a lower fire intensity (75 MW)

6.4.3. Deflection Response

Midspan deflections predicted by the finite element model considering exposure to the fire scenarios developed by the FDS model are presented in Figure 6.16 for each combination of bridge geometry (short and medium span bridge girder). In general, the deflection response has been very similar for all girders analyzed and can be divided into three stages: (1) initially deflections are minimal, but as temperature increases the rate of deflection accelerates over time due to thermal strains and creep generated in concrete; (2) after a few minutes the deflection rate seems to stabilize and keep increasing steadily at a lower rate due to temperature-induced degradation of mechanical properties of steel and concrete; (3) deflections start to increase more rapidly again, indicating structural failure due to yielding of the prestressed steel strands.

Figure 6.16 (a) presents the results for the analysis of the short span bridge, with AASHTO Type I section and a span length of 12 m, considering two clearance heights (5 and 8 m) exposed to two HRR (75 and 200 MW). It can be seen that degradation of midspan deflections follows the fire development behavior discussed in Section 6.4.1, where the girders exposed to higher HRR experienced faster degradation. While a higher clearance height (8 m) slowed degradation of the girder exposed to lower HRR (75 MW), an opposite behavior was observed when comparing the same girder exposed to a higher HRR (200 MW). This can be attributed to the fact that heat gets dissipated more easily with higher clearance heights, resulting in lower fire temperatures on the girder, and consequently, reduced degradation and higher fire resistance of these girders. A similar trend is observed in Figure 6.16b in the analysis of the medium span bridge, with AASHTO Type IV section and a span length of 24 m.



(a) Short bridge (AASHTO Type I, 12 m-span) (b) Medium bridge (AASHTO Type IV, 24 m-span)
 Figure 6.16: Midspan deflection during exposure to fire model temperatures

Regarding deflection limiting criteria, both the maximum deflection and the rate of deflection were used to assess failure. For the short span bridge, with AASHTO Type I cross-section and a span length of 12 m, these limits are 400 mm, 567 mm and 25 mm/min. For the larger bridge, with AASHTO Type IV cross-section and a span length of 24 m, these limits have been calculated as 800 mm, 1,158 mm and 51 mm/min. From Figure 6.16 (a), it can be seen that the $L/30$ limit was reached between 45 and 70 min of fire exposure in the short span bridge. The

$L^2/400d$ limit was reached only by the girder with a clearance height of 8 m and exposed to a HRR of 200 MW, about 10 min later. The rate of deflection limit was reached at 76 and 63 min of fire exposure for the bridge with a clearance height of 5 m exposed to a HRR of 75 and 200 MW, respectively. For 8 m clearance height, the rate of deflection limit was reached at 80 min when exposed to a HRR of 75 and 200 MW, respectively. It should be noted that in both cases that the short span bridge was exposed to a HRR of 200 MW, the rate of deflection criteria was reached at 2 min of fire exposure, but it was recovered, and therefore not computed as the fire resistance of the girder. The medium span bridge presented a similar response, as can be observed in Figure 6.16. However, this bridge presented much slower increase of midspan deflections, reaching only the $L/30$ limit after 150 min of fire exposure. The higher fire resistance values obtained for the larger bridge is attributed to the higher thermal mass of concrete that contributes to delay the progression of temperatures within the girder and its strength degradation. Overall, these results demonstrate a significant difference between the fire resistance rating obtained through different criteria, and the importance of selecting appropriate criteria for determining the fire resistance of bridge girders.

6.4.4. Strength Degradation

The structural response of the girders is also analyzed in terms of strength degradation. Figure 6.17 presents the results for the calculated flexural and shear strength degradation for short span (AASHTO Type I section with a 12 m span length) and medium span (AASHTO Type IV section with a 24 m span length) bridge girders. In order to verify the effect of non-uniform fire exposure, the capacity of the girder is calculated for the temperatures in the midspan and near-support cross-sections for each analyzed fire scenario. As observed in the previous results, the short span bridge girder, experienced faster degradation of its flexural and shear capacities when

compared to the results from the medium span bridge. This is attributed to the higher temperatures experienced within this girder section as a result of its lower concrete mass, which leads to faster degradation of material mechanical properties and results in loss of capacity during fire exposure.

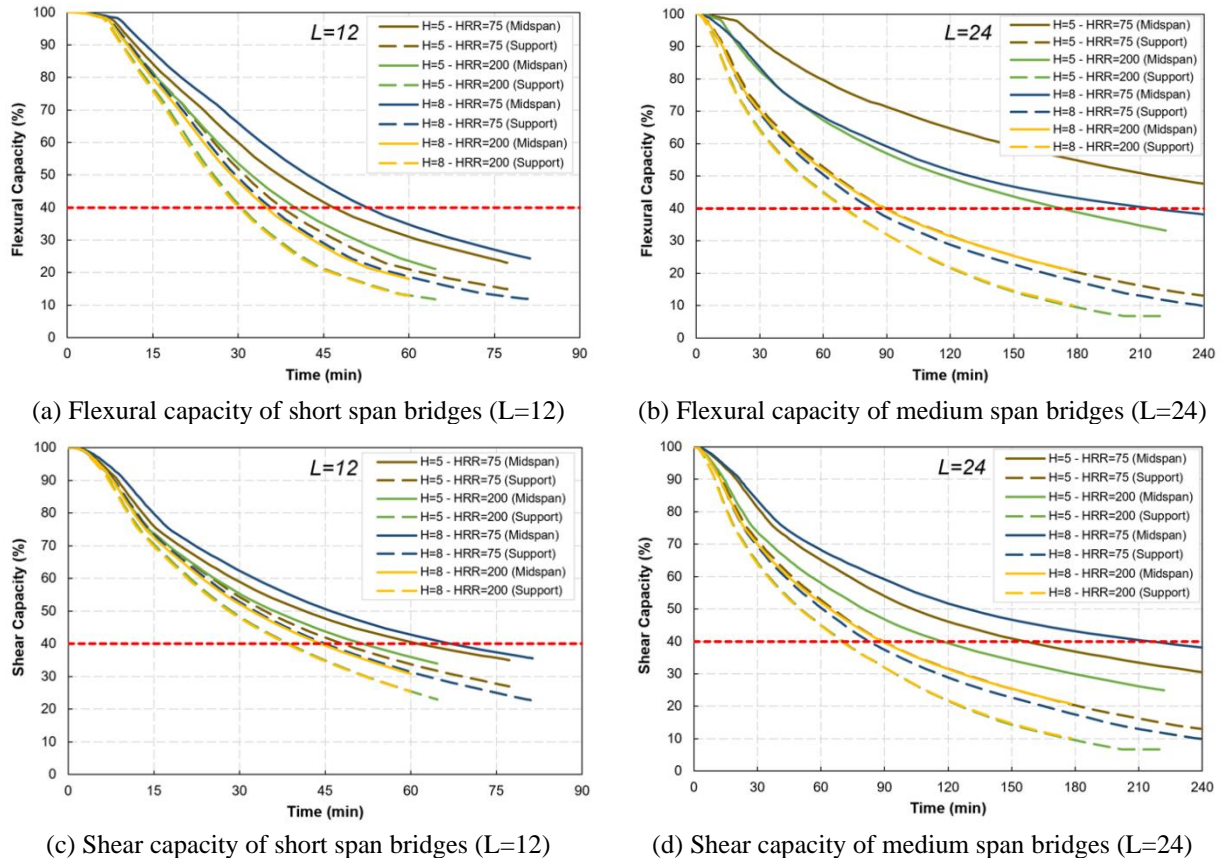


Figure 6.17: Flexural and shear capacity degradation during exposure to fire model temperatures

Similar to what was observed in the deflection-based criteria, the fire resistance of the short span bridge is much lower than the medium span bridge. The fact that the fire source was placed close to the girder supports contributed to a faster degradation of the girder shear strength at this cross-section, leading to early failure when compared to degradation of the flexural strength at midspan. Another factor that contributed to the faster degradation of shear strength is related the concentration of hot gases between the girders, which leads to increased temperatures on the web of the girders that resist most shear stresses. Results from all modelled scenarios are discussed in more detail in APPENDIX D – THERMO-STRUCTURAL ANALYSIS RESULTS. Once again,

it can be noted that the structural response of concrete bridge girders can be significantly affected by thermal gradients and fire temperature variations related to different bridge structures.

6.4.5. Fire Resistance

Table 6.6 presents a summary of the fire resistance results from the analyses of bridge girders subjected to non-uniform fire exposure. Results from the ABAQUS model considering the non-uniform temperatures of exposure generated in the FDS-PyroSim model demonstrate that bridge span length and clearance height present a significant influence on the fire resistance of concrete bridge girders. While the maximum temperatures recorded in all simulations was very similar for all the cases studied, it was observed that the minimum temperatures at the end of one hour of fire simulation had great variance in different scenarios. These differences between minimum and maximum temperatures demonstrate that a significant thermal gradient is developed on the surface of structural members exposed to open-air fires. Bridges with shorter span lengths (12 m) and higher clearance heights (8 m) experienced higher temperatures, while bridges with medium spans (24 m) and lower clearance heights (5 m) experienced higher thermal gradients. In addition to this, the effect of fire intensity was assessed in terms of total HRR considering a constant HRRPUA. While it was not observed significant difference in the temperatures recorded on the deck surface, it was observed that the higher HRR of 200 MW resulted in higher temperatures on the bottom of the girders compared to the lower one (75 MW). This can affect the structural response of concrete girders during fire exposure. Overall, the results demonstrate that bridge structures are exposed to significant thermal gradients during fire incidents, and several factors related to the bridge geometry and fire exposure conditions should be taken into consideration for realistic fire resistance assessment.

Table 6.6: Summary of fire resistance results from different limit states

Case	Span length (m)	Clearance height (m)	HRR (MW)	Fire resistance (min)					
				Deflection criteria			Strength criteria		Final
				$L/30$	$L^2/(400d)$	$L^2/(9000d)$	Flexural	Shear	
1	12	5	75	61	NF	76	46	46	46
2	12	5	200	52	NF	63 (2) ⁺	39	35	35
3	24	5	75	NF	NF	NF	240	86	86
4	24	5	200	193	NF	220	169	67	67
5	12	8	75	66	NF	80	50	42	42
6	12	8	200	44	58	58 (2) ⁺	32	36	36
7	24	8	75	NF	NF	NF	240	77	77
8	24	8	200	151	NF	177	84	67	67

* NF – No failure

⁺ Indicates that the bridge girder reached the limit at a previous fire exposure time but recovered

6.5. Effect of Girder Length

The effect of girder length on the fire resistance of concrete bridge girders was studied by modeling girders with AASHTO Type II sections and span lengths of 14, 16, and 18 m. The girders were considered to be made with UHPC and reinforced with 22, 0.5 mm-diameter prestressing strands and no shear reinforcement. They were exposed to the hydrocarbon fire curve while subjected to two concentrated forces of 225 kN each, which represented 40% of the girder flexural capacity at room temperature, as in the case presented in Section 6.2. Since these girders present the same cross-sectional dimensions and reinforcement configuration, and were exposed to the same fire curve, their thermal response is the same as presented in the previous case.

Figure 6.18 presents the progression of midspan deflections with fire exposure time for the girders considering different span lengths. Overall, it can be seen that they exhibit a similar trend but with increasing magnitudes as the span length increased. In the first few minutes of fire exposure (5-20 minutes), there was a rapid increase of midspan deflections due to thermal strains resulting from large thermal gradients. Following this, deflections increased more steadily as a

result of material strength and stiffness degradation. Towards the end, the girders failed due to yielding of the prestressing strands. As the span length increased, the progression of midspan deflections increased, and consequently, the failure occurred earlier. This is due to the larger span lengths, which result in higher bending moments and greater flexural demands on the girders, in addition to the effects of thermal strains that accelerates the degradation process. As a result, by increasing the span length by 2 m, the fire resistance of the girder was decreased by approximately 20 min.

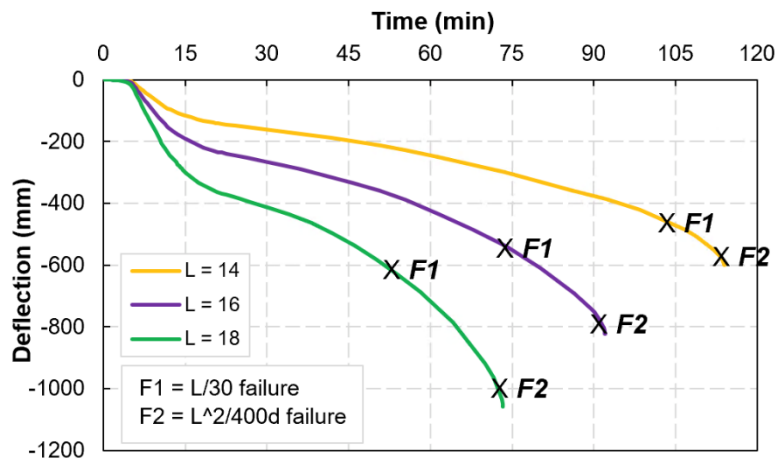


Figure 6.18: Progression of midspan deflections in girders with different span lengths

Table 6.7 presents the fire resistance of the three girders under different limits states. Deflection limits varied according to the girder length and, therefore, have been presented along the deflection curves in Figure 6.18 for each failure criterion. F1 indicates the deflection limit of $L/30$, while F2 indicates the deflection limit of $L^2/400d$. It can be observed that as the girder length decreases, there is a convergence between the two limits, indicating that they have been developed for building members with shorter span lengths. The rate of deflection limit of $L^2/9000d$ was not reached in any of these cases. Under the strength based criterion, the difference between the time reached by each girder was reduced by approximately 10 min. Overall, these results demonstrate that concrete girders with medium spans exposed to similar loading and fire

exposure conditions are more susceptible to earlier failure, highlighting the critical influence of span length on fire resistance of prestressed concrete bridge girders.

Table 6.7: Fire resistance times for concrete girders with different span lengths

Girder length (m)	Fire resistance (min)			
	$L/30$	$L^2/(400d)$	$L^2/(9000d)$	Strength
14	104	113	NF	103
16	73	91	NF	93
18	51	71	NF	84

NF: No failure

6.6. Effect of Concrete Strength

Another important parameter that can affect the fire resistance of concrete bridge girders is the type of concrete used in the girder composition. While concretes of higher strength (such as HSC and UHPC) provide higher capacity at ambient conditions, they experience faster degradation at elevated temperatures, which leads to a reduced fire resistance. The effect of concrete type was studied by comparing results from the analysis of girders with AASHTO Type II sections, with 22 prestressing strands and a span length of 16 m, made with three types of concrete: NSC ($f'_c = 50$ MPa), HSC ($f'_c = 100$ MPa), and UHPC ($f'_c = 170$ MPa). HSC and UHPC are assumed to have appropriate contents of polypropylene fibers in their mixture to mitigate fire-induced spalling, so it was not considered in the analysis. Shear reinforcement was provided only for the NSC and HSC girders, and consisted of 12.7 mm-diameter stirrups, spaced at 75 mm over the shear span of the girder. The three girders were exposed to the hydrocarbon fire curve while subjected to two concentrated loads, which represented 40% of their flexural capacity at room temperature, similar to the conditions presented in Section 6.2.

Figure 6.19 presents the progression of midspan deflections obtained in the model. It can be observed that the UHPC girder experienced higher levels of deflection compared to the NSC

and HSC girders, which is attributed to the faster degradation of UHPC mechanical properties with increasing temperatures. However, while the UHPC girder experienced failure by yielding of the steel strands, the NSC and HSC girders experienced flexural failure due to crushing of concrete and shear failure due to diagonal cracking, respectively. The failure mode of the NSC and HSC girders can be visualized in Figure 6.20 through the development of significant plastic strains in these regions of the girders. These results indicate that while UHPC experience faster degradation at elevated temperatures, its superior mechanical properties help provide a more predictable performance due to yielding of steel strands. On the other hand, despite being provided with shear reinforcement, the significantly lower tensile strength of HSC makes it more susceptible to shear failure during fire exposure. The faster progression of temperatures in I-shaped sections leads to quick degradation of concrete properties, making conventional concrete members susceptible to other failure modes, which should be considered in the fire design.

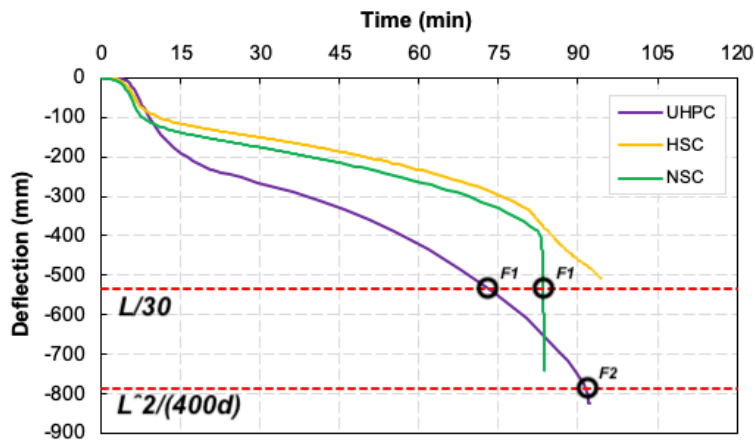
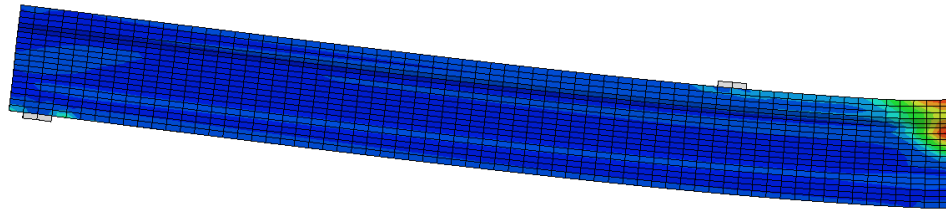
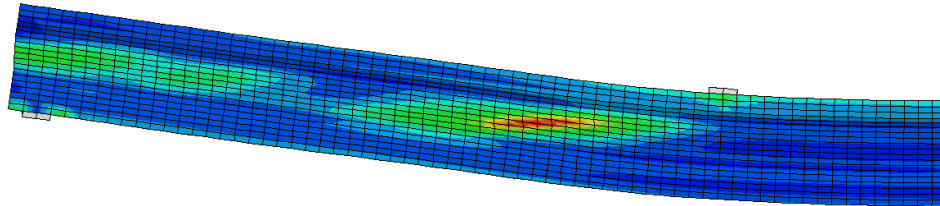


Figure 6.19: Progression of midspan deflections in girders made with different concrete types



(a) Failure of the NSC girder by crushing of concrete



(b) Failure of the HSC girder by diagonal cracking

Figure 6.20: Progression of midspan deflections in girders made with different concrete types

Table 6.8 presents the fire resistance time of the three girders under different limits states. The sudden increase in deflections of the NSC girder due to run-away of the model resulted in a fire resistance time of 83 min by both flexural and deflection limit states. While the HSC girder did not reach any of the deflection limits throughout the analysis, the development of large plastic diagonal strains indicates shear failure of the member during fire exposure, thus attaining a fire resistance of 82 min. Despite having a smoother increase in deflections and failure mode, the UHPC beam presented higher levels of deflections and reached the $L/30$ limit in 73 min of fire exposure. Considering just the strength and $L^2/400d$ limits, the UHPC girder presented a fire resistance of 91 min, which is slightly higher than the NSC and HSC girders. It should be noted that HSC and UHPC were considered to be made with polypropylene fibers. On the contrary, these girders could experience significant spalling and lower fire resistance. The distinct failure modes observed in these analyses highlight the importance of material selection in the fire design of concrete bridge girders. These insights emphasize the need for careful consideration of material properties and failure mechanisms in the design and application of concrete girders to ensure structural integrity and safety.

Table 6.8: Fire resistance times for girders made with different concrete types

Concrete type	Fire resistance (min)			
	$L/30$	$L^2/(400d)$	$L^2/(9000d)$	Strength
NSC	83	NF	83	83
HSC	NF	NF	NF	82
UHPC	73	91	NF	93

NF: No failure

6.7. Summary

This chapter presented results from parametric studies carried out to analyze the effect of different design and exposure parameters on the fire response of concrete bridge girders. Based on the results obtained in the numerical analyses, the following conclusions can be drawn:

1. I-shaped girders experience faster degradation during fire exposure than the similar rectangular-shaped girder. Its lower thermal mass leads to higher temperatures within the girder and faster degradation of concrete and steel strength and stiffness, resulting in earlier shear failure. The higher temperatures in the web of the I-shaped section lead to shear failure while a more robust rectangular section fails under flexural mode at later stages of fire exposure.
2. Smaller standard cross-sections, such as AASHTO types I and II, present lower fire resistance than the more robust sections types III and IV. This is attributed to the lower thermal mass in the smaller girder sections (types I and II) that allow a faster progression of temperatures and, consequently, faster degradation of the girder strength and stiffness.
3. Severe fires, such as hydrocarbon fires, can pose a significant hazard to bridge girders due to the faster progression of temperatures within the girders. The concentration of

- heat in the girder web accelerates degradation of its shear capacity and can make them vulnerable to shear failure, even when subjected to predominantly flexural loads.
4. Fire simulations predicted significantly high thermal gradients along the length of bridge girders, with temperatures higher than the hydrocarbon fire curve in support sections. The bridge span length and clearance height present high influence on the fire temperatures due to the loss of heat during a bridge fire. Bridges with shorter span lengths (12 m) and higher clearance heights (8 m) experienced higher temperatures, while bridges with medium spans (24 m) and lower clearance heights (5 m) experienced higher thermal gradients. A higher HRR resulted in higher temperatures on the bottom of the girders compared to a lower HRR.
 5. Concrete girders made with NSC and HSC can experience failure due to crushing of concrete (flexural) and diagonal cracking (shear) resulting from the high temperatures experienced within the cross-section of I-shaped girders. Due to its superior mechanical properties, especially tensile strength, UHPC girders are capable of sustaining its mechanical properties for longer fire exposure times, resulting in failure due to yielding of the steel strands. However, in these analyses, HSC and UHPC were considered to be made with polypropylene fibers to prevent spalling. On the contrary, these girders could experience significant spalling and lower fire resistance.
 6. Overall, results from parametric studies demonstrate that I-shaped concrete bridge girders are susceptible to different failure modes, including shear failure, resulting from the severe exposure conditions of bridge fire scenarios.

7. DESIGN RECOMMENDATIONS

7.1. General

To ensure structural safety under fire conditions, structural members in buildings shall be designed with appropriate fire resistance ratings, as required by current codes and standards. However, as discussed in the previous chapters of this dissertation, bridge design regulations do not provide specific fire safety requirements and provisions for design of bridge structures. Moreover, current parameters for assessing and determining the fire resistance of structural members have been developed for building members and do not account for the specific characteristics of bridge structures. Bridge girders are the most vulnerable structural members during a bridge fire due to their critical role in supporting the superstructure and its exposure conditions to the elevated temperatures. Based on results from the experimental and numerical studies carried out in this dissertation, this chapter proposes parameters for evaluating the fire resistance of concrete bridge girders. These parameters include appropriate thermal and structural loading conditions that bridge structures will experience during fire incidents, as well as failure criteria specifically designed for determining the fire resistance of concrete bridge girders. While the use of standardized sections in concrete bridges does not allow much customization in geometrical features when compared to steel bridges or building members, some design considerations can aid in achieving a safer design of bridge structures for fire incidents. This is particularly important for the design of modern bridge girders, which present reduced fire resistance when compared to conventional concrete bridge members. Therefore, the last section of this chapter includes preliminary design recommendations formulated to assist in the design of critical concrete bridge girders for adequate fire safety.

7.2. Fire Safety Measures in Bridges

A combination of fire safety measures is typically required to ensure structural fire safety in buildings. These measures include active or passive fire protection. Active fire protection includes the installation of detection or suppression systems that activate in the presence of fire to reduce its intensity and spread. However, the high installation and maintenance costs of such systems, particularly for bridges with large surface areas, make it unpractical. In addition, these active systems have been developed for building fires and are not applicable to bridge fires, which have higher magnitude. On the other hand, passive fire protection alternatives involve the use of construction materials to prevent fire growth and spread, without requiring activation. One of the most common alternatives is the provision of adequate fire resistance to structural members. While this is the only alternative to increase the fire safety of bridge structures, currently there are no standards or guidelines on how to achieve the desired levels fire safety in bridge structures.

7.3. Parameters for Fire Resistance Evaluation of Concrete Bridge Girders

When determining the fire resistance of structural members, either numerically or experimentally, appropriate thermal and structural loading conditions need to be considered in order to yield fire resistance ratings that will be representative of the member under real fire incidents. As demonstrated in Chapter 6, fire severity presents a significant influence on the thermal response of the member, and a severe fire result in faster degradation of material properties and the capacity of the member. In addition, the magnitude and position of the applied structural loading also affect the structural response of the member during the fire incident. Therefore, both thermal and mechanical loading conditions should be designed to represent the conditions to which bridge girders will be exposed in real bridge fire scenarios in order to result in accurate fire resistance predictions.

7.3.1. Fire Exposure Conditions

Bridge fires present unique characteristics, such as burning of highly flammable fuels (typically gasoline and other hydrocarbons) in an open air condition (good distribution of oxygen). The fact that bridges are open spaces facilitate the dissipation of heat to the environment, leading to a non-uniform exposure of structural members to elevated temperatures. These characteristics create thermal gradients along the surface of the bridge and affect the structure differently. The temperatures of exposure and thermal gradients generated are strongly dependent on the bridge geometry, including the span length and clearance height, as demonstrated in the parametric studies carried out in Chapter 6. Therefore, when evaluating the fire resistance of bridge girders, it is important to account for these factors to ensure an accurate assessment.

To evaluate the realistic fire severity in a bridge, fire dynamics modeling is to be carried out. FDS and PyroSim are among the tools available to determine the fire exposure conditions of a bridge member, as demonstrated in Chapter 4. However, these tools require specific knowledge on the principles of fire dynamics and fire modeling using this type of software in order to generate reliable results. Thus, an analytical method has been proposed to determine the temperatures along the surface of a bridge girder in order to facilitate the assessment of bridge girders exposed to fires.

This method aims at simplifying the process of deriving the fire exposure temperatures on bridge girders while taking into consideration parameters that can affect these results. The proposed methodology is based on the following assumptions:

1. Fire severity resulting from a tanker (carrying fuels and other flammable materials) crashing under a bridge represents the worst case fire exposure.

2. In a bridge fire, the fire source will be limited to the area of the burning source, typically the tanker. Spillage is also common during these incidents and can result in increased burning areas, affecting the intensity of the fire through the total heat release rate.
3. Depending on the incident, the fire source can be at different locations underneath the bridge. The worst case scenario would be the fire source in the mid-width of the bridge and closer to the girder support. This situation would result in higher temperatures, as demonstrated in previous studies [28,231].
4. Bridges are open spaces, which allows the dissipation of heat to the environment. Such conditions create a thermal gradient along the length of the girder. Therefore, the peak temperatures and resulting thermal gradients will be dependent on the bridge geometry, most importantly the bridge length (L) and clearance height (H).
5. A cooling phase is not needed for a bridge fire due to the large fuel volumes involved in bridge fires, which takes around four hours to be consumed, as presented in APPENDIX E – FIRE LOAD CALCULATION. This time should be enough for firefighters to extinguish the fire.

Based on these assumptions, the fire load has been simplified to a two-dimensional analysis that is based on the bridge span length (L) and clearance height (H), as illustrated in Figure 7.1. In this case, the fire source is assumed to be close to an abutment wall, creating a thermal gradient along the length of the girder (points 1 through 6) at a distance x from this wall.

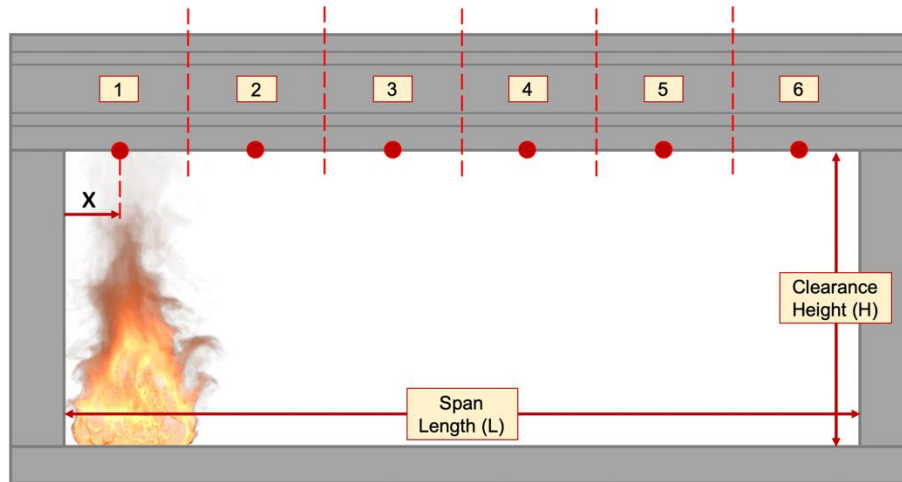


Figure 7.1: Proposed bridge fire model variables and thermal gradient along the girder length

The proposed method makes use of the data generated in the fire simulations carried out as part of the parametric studies (Chapter 6) to determine temperatures of fire exposure. A first review of this data shows that the highest temperatures measured along the length of girder in all case scenarios was at the first point of measurement, right above the fire source. Therefore, this is taken as the baseline for determining the fire temperatures on a bridge girder. Figure 7.2 (a) presents the temperatures measured at the point above the fire source in all scenarios with HRR of 200 MW, which is the worst case scenario studied. It can be seen that the magnitude of the fire temperatures is mostly influenced by the bridge length. The average temperature measured at each of the six points along the length of the girder considering four geometrical combinations is presented in Figure 7.2b. It is to be noted that as the measuring points distance from the fire source, temperatures decrease up to the mid-span, and then increase again close to the other abutment wall.

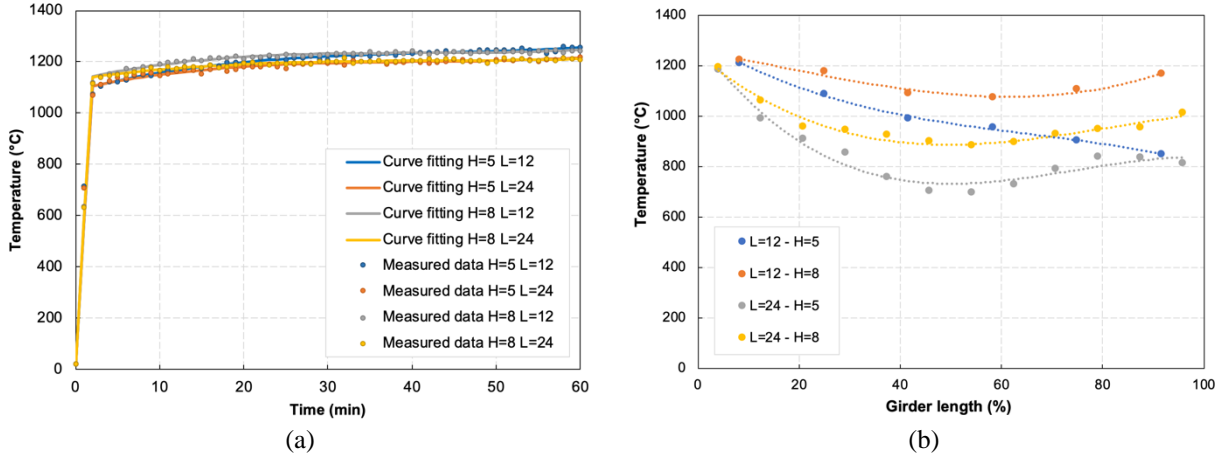


Figure 7.2: Fire development variables

Based on this data, the thermal exposure conditions proposed in this method consist in a space-temporal equation that takes into consideration both the span length and the clearance height of the bridge. First, the curve was fitted for the temperatures at the location right above the fire source in Equation (7.1), which can be used to determine the fire exposure temperatures for a bridge with span length L .

$$T_x = \phi[(0.00144 - 0.000028(L - 12))t^3 - (0.182 - 0.0037(L - 12))t^2 + (8.127 - 0.178(L - 12))t + 0.337(L - 12) + 1108] \quad (7.1)$$

T_x is the temperature of exposure on the girder (in °C) at a fire exposure time t (in min) for a bridge with length L (in m). The coefficient ϕ is introduced to account for the thermal gradient along the length of the girder and it is calculated through Equation (7.2) as a function of the distance x from the support, taking into consideration the bridge height H (in m).

$$\phi = (6.45 \times 10^{-5} - 3.33 \times 10^{-6}(H - 5))x^2 + (-8.89 \times 10^{-3} + 8.83 \times 10^{-4}(H - 5))x + 1 \quad (7.2)$$

Using Equations (7.1) and (7.2) it is possible to determine the temperature of exposure along the girder length as a function of the fire exposure time taking into consideration the bridge length L (in m) and height H (in m). To demonstrate the applicability of the proposed methodology,

temperatures predicted by the fire model in Chapter 6 are plotted against the curves established using the equations derived here for the same bridge geometry, as shown in Figure 7.3.

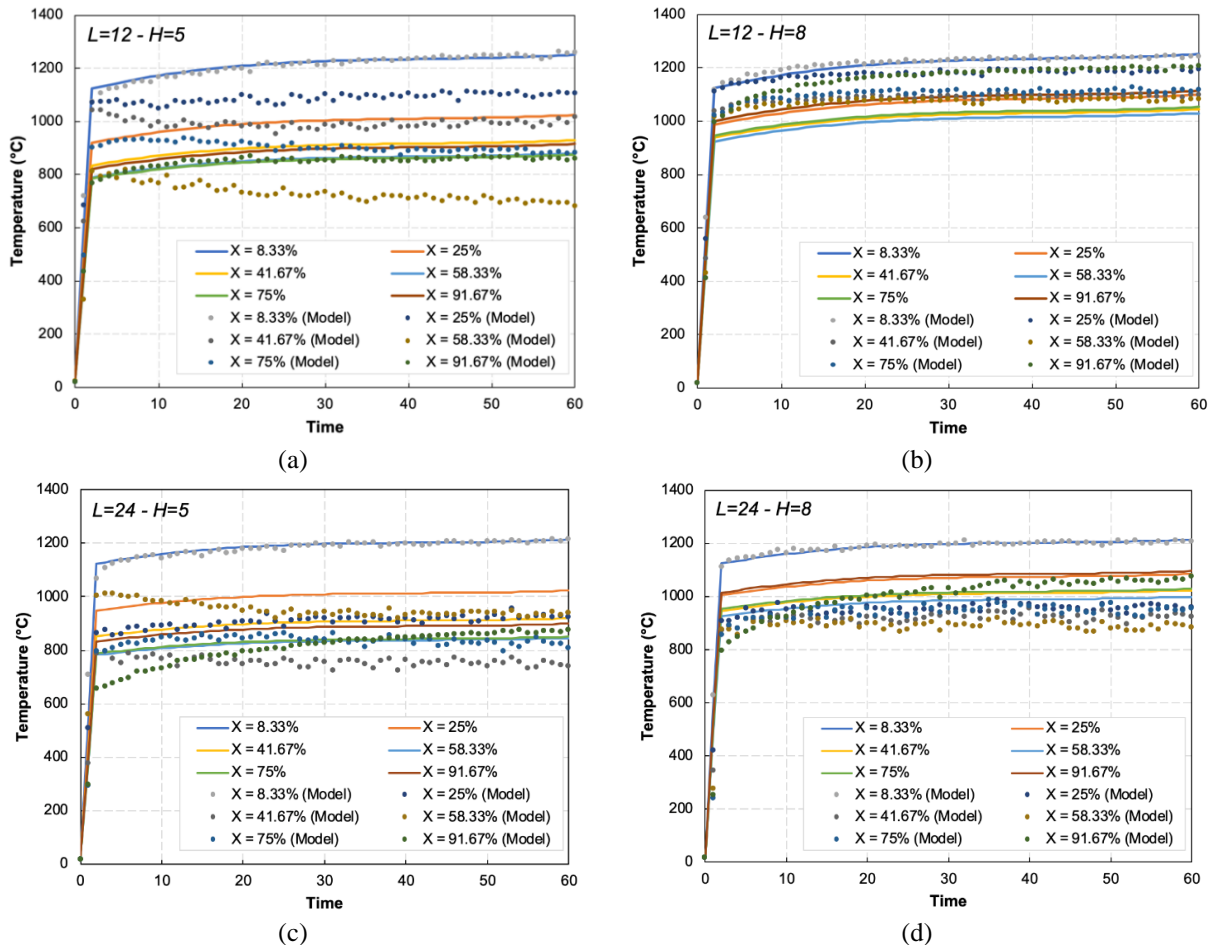


Figure 7.3: Comparison between temperatures predicted by the model and the fire curves

These figures demonstrate a strong correlation between the fire curve predicted by Equation (7.1) and the temperatures at the point directly above the fire source. However, the dynamic nature of fires complicates the prediction of the thermal gradient along the girder using a simplified equation. While there can be significant variance in the predicted thermal gradient, it is important to note that fire incidents will always exhibit some variability. Therefore, the proposed equations are considered acceptable for estimating exposure temperatures in bridge fires.

7.3.2. Structural Loading Conditions

In addition to thermal loading, the structural load to which a structural member is subjected during fire exposure also has a significant influence on its fire resistance. While thermal loading is time-dependent, structural loading remains constant during fire resistance evaluations. The load acting on a structural member during a fire comprises of dead and live loads. A common assumption in the fire engineering community is that structural members will be subjected to a reduced live load during a fire event. This is due to the fact that people will evacuate the structure at early stages of a fire. In a bridge fire, where most of the live load is comprised of vehicles traveling on the bridge, the live load can be almost null during a fire event. However, in worst case scenarios, a fire incident that result from overturn or crash of vehicles above the bridge, which can lead to burning under the bridge due to drainage of flammable liquids. In such case, a tanker and other heavy vehicles can be standing on the bridge during the fire event, imposing some level of design live load on the structure.

Bridge structures are designed for live loads based on the weight of the vehicles that will be crossing the bridge. At ambient conditions, the HL-93 loading method is specified in the LRFD Bridge Design Specifications by AASHTO. This method involves a combination of a uniformly distributed lane load with a design truck load or a design tandem load. The critical combination of these loads is used to determine the maximum stresses and forces on the bridge girder. However, this method has been developed for design purposes and is not applicable for fire resistance evaluation of a bridge girder. In fire evaluation, the magnitude of the applied load can be defined as a ratio of the member capacity at ambient conditions or as a ratio of the live load, if the actual value is known. In both cases, a 50% ratio is typically adopted in order to ensure that the evaluation captures the combined effects of mechanical and thermal stresses.

Another important parameter in establishing the loading conditions during a fire resistance test is the load configuration. Concentrated forces, such as those applied in four-point loading tests, offer significant advantages in experimental settings. They are easier to apply and control, allowing for precise placement of forces to simulate real-world conditions like vehicle axle loads. In four-point loading, a section of the girder is subjected to a constant bending moment, while other sections experience constant shear, which simplifies the analysis by isolating these effects. This clear distinction between bending and shear regions facilitates the identification of failure mechanisms and material behavior under mechanical stresses. On the other hand, distributed loads provide a more realistic simulation of the continuous forces acting on a bridge girder, such as the weight from the deck and bridge appurtenances, as well as the uniformly distributed traffic loads. However, distributed loads are more challenging to apply consistently in experimental settings and result in varying bending moments along the length of the girder.

Based on the factors discussed above, a four-point loading configuration is recommended to evaluate the fire resistance of bridge girders, as illustrated in Figure 7.4. This loading arrangement involves applying two concentrated forces at one-third of the girder supports, thus creating a balanced loading condition that subjects the member to constant bending moment and shear force at specific sections of the girder. In case of bridges with longer spans, the distance between the two applied forces can be reduced. To simulate the somewhat realistic conditions during a fire exposure, the applied load can be defined as a percentage of the girder capacity taking the total dead load and a portion of the live load (i.e. 30%) into consideration. By implementing these recommendations, the analysis can effectively assess the fire resistance and performance of the girder under sustained structural and thermal loads, providing critical insights into its safety and behavior during fire events.

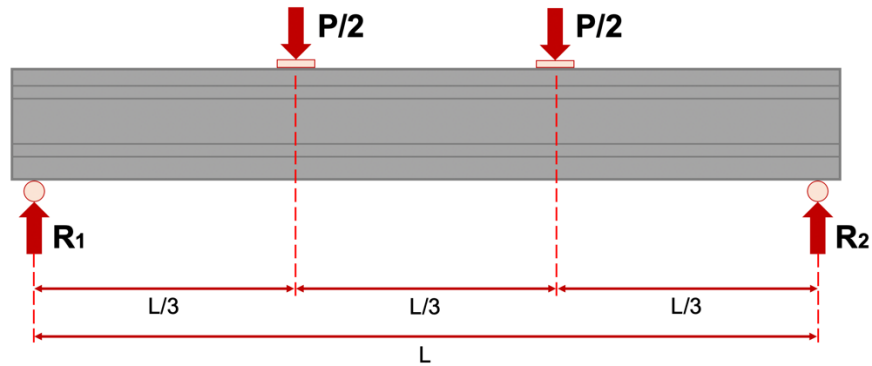


Figure 7.4: Proposed loading of bridge girders for fire resistance evaluation

7.4. Failure Criteria for Determining Fire Resistance Rating of Concrete Bridge Girders

To determine the fire resistance of a structural member, failure criteria must be adopted to establish when a structural member no longer is capable of meeting the desired performance requirements under fire exposure. Building codes and fire testing standards present different types of criteria to account for the various failure modes a structural member can experience while exposed to fire, as shown in Table 7.1.

Table 7.1: Failure criteria for flexural members based on different codes and standards

Type	Limits	Source
Maximum Deflection	$L^2 / (400d)$	ASTM E119; ISO 834-1
	$L/30$	BS 476-10
Maximum Rate of Deflection	$L^2 / (9,000d)$	ASTM E119; ISO 834-1; BS 476-10
Maximum Temperature	427°C (prestressing steel) 593°C (reinforcing steel)	ASTM E119
Strength	Flexural strength	ACI 216.1-14

L is the span length
d is the girder depth

In buildings, the most common approach to determine the fire resistance of flexural members is to limit the maximum deflection during fire exposure. Deflection limit state ensures that both functionality and safety of the bridge are maintained during and after the fire. However, current codes and standards present different limiting criteria, which can result in significantly

different fire resistance ratings depending on the method employed in the assessment. In addition, these methods have been developed for building members and do not account for the specific characteristics of bridge members. The rate of deflection limit is another limiting criterion related to the progression of deflections that can be used. By limiting the rate of deflection, early warning of potential failure (loss of strength) can be detected, ensuring the overall safety of the bridge during fire exposure.

Another failure criterion most commonly adopted for determining the failure of a structural member during fire exposure is the critical temperature criterion. This limit state defines failure as occurring when a critical temperature is reached at the reinforcement or strands, resulting in loss of strength and structural capacity. This is based on the fact that steel (rebars or strands) loses approximately 50% of its tensile strength around 500°C and this results in 50% of loss of flexural capacity. For prestressed concrete members, ASTM E199 [169] assumes the critical temperature to be 427°C, whereas for reinforced concrete members 593°C can be adopted. While these methods can easily be adopted to determining rational failure of a member both experimentally or through numerical models, they do not provide reliable assessment of the actual failure of a structural member. Besides, this limit state has been developed for determining the fire resistance of building members where most rebars and strands are located at peripheral locations. Bridge girders typically have several layers of reinforcing bars and strands, which means that most of them will be protected in the inner layers of the concrete girder. Therefore, adopting this criterion to assess the fire resistance of concrete girders would result in very conservative ratings.

Strength-based limiting criteria can be more appropriate for bridge girders, as they directly relate the degraded capacity of the member to ensure that it can sustain the applied loading during fire exposure. This method relies on the temperatures predicted within the member to estimate

strength degradation of steel and concrete and determine their capacity at different fire exposure times. Using simplified methods can facilitate the application of this method. However, current codes and standards do not present specific methods or calculation procedures for determining the degraded structural capacity in bridge girders at elevated temperatures. In addition, existing methods only address flexural strength, and do not account for shear capacity degradation, which can be a governing failure mode in I-shaped concrete girders.

Other specific criteria have been proposed to evaluate steel bridges, such as limiting strains in the steel section, controlling the movement of the girder on the supports, or addressing buckling behavior through out-of-plane displacements in the web. However, these criteria may also not be fully applicable to concrete bridge girders. Therefore, deflection and strength limiting criteria have to be chosen as the main criteria to assess the fire resistance of concrete bridge girders and the appropriate parameters for determining failure and is further discussed below.

7.4.1. Deflection Failure Criteria

Among the various deflection limiting criteria for assessing the fire resistance of flexural members, the $L/30$ and $L^2/(400d)$ limits are the most commonly used. Both consider the span length, but present different approaches and resulting deflection limits depending on the member span length, as illustrated in Figure 7.5. The $L/30$ limit, prescribed by BS 476, sets a fixed ratio of the span (3.33%) for any member length. In contrast, the $L^2/(400d)$ limit, prescribed by ASTM E119 and ISO 834, accounts for both the span length and the effective depth of the member, resulting in variable limits. It can be observed that the $L^2/(400d)$ limit is lower than the $L/30$ limit for shorter spans and higher for longer span lengths. This makes the $L^2/(400d)$ deflection limit more conservative for shorter spans, between 2 and 3% of the span length. However, for

spans longer than 12 m, this limit ranges between 4.7 and 5.6%. This variation highlights that the $L^2/(400d)$ limit is intended for building members and may not be suitable for bridge girders.

Throughout this dissertation, it has been observed that bridge girders rarely reach the $L^2/(400d)$ limit during fire exposure, indicating its inadequacy in capturing failure of bridge girders exposed to fires. On the other hand, the $L/30$ limit was reached at earlier stages of fire exposure, providing more conservative fire resistance ratings under the deflection limit state. Therefore, a new deflection limit state, $L^2/(500d)$, is proposed for evaluating the fire resistance of simply supported concrete bridge girders. This limit offers an intermediate deflection range of 3.8% to 4.4% for spans over 12 m. It is specifically designed for members exposed to the hydrocarbon fire curve, which results in higher deflections than building members, and takes the effect depth of the girder into account. Girders with smaller depths experience higher deflections than girders with deeper sections due to their lower moment of inertia and stiffness. By adapting the deflection limit prescribed by ASTM E119 and ISO 834, the fire resistance of concrete bridge girders can be assessed more accurately. It should be noted that the proposed deflection limit is only applicable for simply supported concrete bridge girders. Its ability to trace other types of girders, such as composite or continuous members, still needs to be evaluated in future studies.

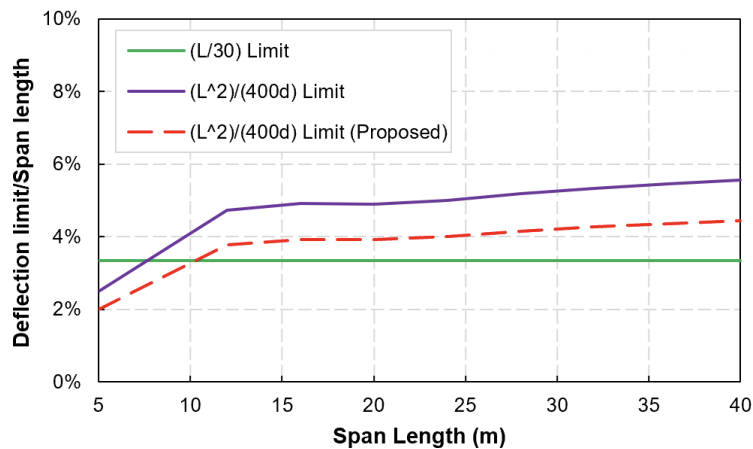


Figure 7.5: Deflection limit as a function of span length based on different methods

7.4.2. Strength Failure Criteria

Strength limit states provide an alternative to evaluate the fire resistance of bridge girders by evaluating degradation of mechanical properties with temperature while considering the applied loading. In this method, commonly used for beams in buildings, a sectional analysis is carried to determine the degraded capacity of the member at critical locations based on the temperatures reached within the cross-section at a specific fire exposure time. The degraded capacity is then checked against the external forces applied in the member, and if it becomes lower failure is said to happen. In the fire design of concrete members, usually only the flexural capacity is checked for the bending moment at the critical midspan section. However, as previously demonstrated, shear failure can occur in I-shaped bridge girders with slender cross-sections. Further, in bridge girders, the peak temperatures in the cross-section is reached at locations closer to support, since vehicles can crash against the abutment walls. Therefore, checking capacity degradation of bridge girders is important to ensure their safety during fire exposure.

To determine the degraded flexural and shear capacity degradation of a member during fire exposure, the procedure demonstrated in Section 4.2.3 can be employed. Considering the non-uniform temperature distribution along the length of bridge girders, it is recommended to evaluate the flexural capacity of the midspan cross-section and the shear capacity of a support cross-section, considering potential thermal gradients developed along the girder. The first step is to determine temperatures along the cross-section through a thermal analysis. This can be done for a specific fire exposure time (i.e. the desired fire resistance rating) or for several time steps to evaluate the degradation of member with fire exposure. Next, the degraded mechanical properties of concrete and steel for those levels of temperature are determined and the flexural and shear capacities of the girder is calculated. Finally, the degraded flexural and shear capacities are checked against the

applied bending moment and shear forces at the same locations. This intuitive approach offers a simplified alternative to evaluate failure of the member with consideration to both flexural and shear limit states.

7.5. General Recommendations for Fire Design of Concrete Bridge Girders

Based on the findings from the research work carried out as part of this dissertation, a set of recommendations have been formulated to assist in the design of concrete bridge girders for fire safety. These recommendations have been divided in three steps of the design process. First, due to the lack of fire resistance ratings in bridge design codes and standards, insights on how to establish appropriate fire resistance ratings for bridge structures are provided. Next, recommendations for the fire design of concrete bridge girders are made with consideration to material selection and structural design. Finally, fire protection alternatives are discussed. In general, these recommendations aim to assist design engineers and future researchers to advance the safety of concrete bridges to fires.

7.5.1. Required Fire Resistance Rating

In building design, fire resistance ratings for structural members are well-defined and laid-out in applicable building codes. These ratings are defined based the occupancy and height of the building, based on the time needed for evacuation and combat of the fire. However, current bridge design codes and standards do not include any fire resistance requirements. This gap creates an important barrier for designing bridge structures for fire safety, since appropriate fire resistance is essential to ensure the structural integrity and safety of a bridge member during and after a fire.

The fire resistance rating required for a bridge structure could be debated extensively, with considerations ranging from one to four hours, as in the case of buildings. A one-hour rating might be considered insufficient for critical bridges or bridges located in remote areas, potentially leading

to premature structural failure. On the other hand, a four-hour rating could be seen as overly conservative for a bridge carrying moderate traffic and located close to fire stations, resulting in unnecessary increased costs.

The appropriate fire resistance rating for a bridge will depend on several factors, including the bridge characteristics (geometry, structural materials and configurations), location (time required for emergency response), criticality for traffic (number of vehicles crossing the bridge daily, alternative routes, and need by emergency vehicles). Table 7.2 presents recommended fire resistance ratings for bridge structures based on these factors. For bridges located close to urban centers (where fire stations are close by and not carrying critical traffic), no fire resistance is required due to the expected rapid response time and lower impact of temporary closures. In urban areas with moderate traffic, a 1-hour rating is advised to ensure adequate safety and maintain traffic flow during fire incidents. For bridges in remote areas that carry critical traffic, a 1.5-hour fire resistance rating is recommended to account for longer emergency response times and the essential nature of the route. Finally, bridges situated in high-risk areas, such as industrial zones with high fire loads, and carrying critical infrastructure like emergency routes or utilities, should have a 2-hour fire resistance rating to withstand severe fire scenarios and prevent catastrophic failures.

The fire-based importance factor approach, originally proposed by Naser and Kodur, can be used to determine the appropriate fire resistance rating. In this approach, weightage factors are assigned to various parameters or characteristics of a bridge, resulting in a risk grade. By relating the proposed fire resistance ratings in Table 7.2 with the calculated risk grade of a bridge, fire safety requirements with response capabilities and the importance of the bridge to traffic.

Table 7.2: Recommended fire resistance for bridge structures

Fire resistance rating	Risk grade	Bridge characteristics
Not required	Low	Bridge located close to a fire station, not carrying critical traffic
1-hour	Medium	Bridge located in an urban area, carrying moderate traffic
1.5-hours	High	Bridge located in a remote area, carrying critical traffic
2-hours	Critical	Bridge located in a high-risk area (industrial zone, high fire load), carrying critical infrastructure (emergency routes, utilities)

7.5.2. Preliminary Guidelines for Fire Design

In the design of bridge structures, there is not much room for customization as most of concrete bridge girders are precast members made with standardized cross-sections. Designing concrete bridge girders with varying sectional dimensions (i.e. increased web thickness) and concrete cover thickness would require a significant amount of investment for updating equipment and procedures in precast plants, which would not be feasible. Therefore, other aspects related to the design of concrete bridge girders can be improved with regards to fire safety, such as batch mix composition and reinforcement configuration, as discussed herein.

7.5.2.1. Recommendations for Concrete Batch Mix Composition

Concrete consists in a combination of different materials to achieve the desired properties in the fresh and hardened states. By selecting and combining appropriate materials, a concrete batch mix can be designed to improve the fire response of structural members. Since aggregates occupy most of the volume of concrete, their properties at elevated temperature present a significant influence on fire behavior of a concrete member. For instance, carbonate aggregates (such as limestone) offer slightly better fire behavior compared to siliceous aggregates [232,233]. This is due to their lower thermal diffusivity, which contributes to slightly reduce heat propagation, as well as lower thermal strain coefficients and crack propagation characteristics, which contributes to slower degradation of mechanical properties at elevated temperatures [94,233].

Previous studies have shown that HSC members with carbonate aggregate concrete exhibit approximately 10% greater fire resistance than those with siliceous aggregate concrete [234,235]. Therefore, by selecting thermally stable aggregates, the performance of concrete bridge girders during fire exposure can be improved.

According to the literature review in Chapter 2, concrete mixtures with higher strength present lower fire resistance compared to conventional normal strength concretes. This is because high-strength concretes have a denser, more tightly packed composition, making them more prone to early cracking and spalling at elevated temperatures. As a result, concretes of higher strength experience faster degradation of mechanical properties when exposed to fire and are more susceptible to fire-induced spalling, resulting in lower fire resistance. This issue is particularly significant for UHPC bridge girders, as this type of concrete is especially more vulnerable to this degradation. To overcome these limitations, both metallic and synthetic fibers can be incorporated into the concrete mixture to improve the fire behavior of concrete structures. While metallic fibers increase the tensile strength of concrete, helping it resist the tensile stresses generated by differential thermal expansions and internal pressure build-up, synthetic fibers melt at lower levels of temperatures, creating voids that help accommodate the thermal expansions.

Polypropylene fibers are effective in enhancing concrete permeability due to their significant thermal expansion and relatively low melting point (at approximately 160°C). This thermal expansion causes microcracking around the fibers, forming pathways that allow water vapor to escape [115]. Additionally, as the fibers melt, they are absorbed by the cementitious matrix, forming channels that facilitate the migration and evaporation of water vapor [145,147]. The effectiveness of polypropylene fibers in reducing pore pressure build-up and fire-induced spalling has been demonstrated in the experimental tests presented in Chapter 3 of this dissertation.

Other studies in the literature have also demonstrated their capacity in mitigating fire induced spalling through real-scale fire tests [139,236–239]. Therefore, it is critical to incorporate an optimal amount of fibers, particularly polypropylene fibers in to minimize spalling and improve the fire performance of concrete bridge girders. Table 7.3 presents recommended fiber contents based on previous studies reported in the literature for different types of concrete, where HSC and UHPC refer to concretes with compressive strength higher than 60 and 150 MPa, respectively.

Table 7.3: Recommended fiber content to mitigate fire induced spalling

Concrete type	Recommended content of fibers
NSC	Not required
HSC	0.15-0.20% by volume of polypropylene fibers + 0.5% by volume of steel fibers
UHPC	0.20-0.30% by volume of polypropylene fibers + 1.5-3.0% by volume of steel fibers

7.5.2.2. Recommendations for Concrete Cover Thickness and Reinforcement Configuration

The design of concrete bridge girders offers little room for variation on some aspects of the reinforcement configuration. Tensile reinforcement typically consists of low-relaxation prestressed strands, comprised of seven high-strength steel wires. As per AASHTO LRFD Bridge Design Specifications [10], tensile strands are spaced 51 mm from each other and from the sectional contour (cover thickness). While this concrete cover thickness is required for durability purposes, it contributes to delay the progression of temperatures in the steel strands and to increase the fire resistance of the girders. Based on results from the thermal analysis, the critical temperature of 427°C in prestressing strands established by ASTM E199 [169] is reached at very early stages of fire exposure on the corner prestressing strands. One major difference between building and bridge members is that bridge members are heavily reinforced, and a bridge girder will contain prestressing strands distributed in several layers of the bottom flange while building members will have a much smaller number. Therefore, while a few of the prestressing strands reach the critical

temperature, a number of other strands will retain full-strength during fire exposure, enabling the concrete girder to maintain its structural capacity while exposed to fire. This can be effectively utilized for enhancing fire resistance by considering lower levels of loading present during a fire in a bridge. Additional fire resistance can be provided by increase the concrete cover thickness or the number of prestressing strands in peripheral locations within the girder.

Shear reinforcement offers more opportunity for customization in the design of concrete bridge girders. Previous research has demonstrated that reducing the spacing of stirrups and modifying tie configurations can improve the fire performance of NSC and HSC members. The confinement effect provided by shear reinforcement, combined with the higher porosity of the transition zone between the concrete and the steel bars have shown to reduce spalling progression and prevent buckling of the longitudinal reinforcement [209,234,240]. In the case of UHPC members, the concrete portion presents a higher contribution to the total shear capacity due to inherently higher shear strength of UHPC by the presence of steel fibers. For this reason, UHPC members tend to be designed with reduced or without shear reinforcement. However, results from these studies have shown that these members are susceptible faster shear strength degradation as a result of its slender sections and that increasing shear and longitudinal reinforcement can enhance fire resistance by reducing brittleness in UHPC beams [161]. While reducing shear reinforcement in UHPC bridge girders can facilitate the construction process and provide cost savings, still more research is needed in order to ensure that it will not impact the fire resistance of the girder. Therefore, the provision of shear reinforcement is recommended in modern concrete bridge girders made with UHPC to reduce fire-induced spalling and prevent shear failure during fire exposure.

7.5.2.3. Recommendations for Sectional Shape

While this research has explored the effect of fire on girders with different sectional shapes and sizes, state departments of transportation often have their own standardized sections developed in collaboration with local precast plants. Modern bridges, increasingly designed with superior concretes such as UHPC for enhanced strength and durability, tend to employ newer sectional shapes featuring even more slender cross-sections. Therefore, it is imperative to evaluate the thermal and structural response of these newer bridge designs, under fire conditions when used in critical locations. Assessing these factors will help ensure that the benefits of superior materials and innovative design are fully realized while maintaining safety and performance standards.

One alternative to overcome the limitations in fire performance of slender sections is to make use of U-shaped girders over the traditional I-shaped girders. As illustrated in Figure 7.6, the geometry of U-shaped girder also contributes to improved fire performance, as the enclosed shape can offer additional protection to the internal reinforcement against direct flame exposure due to the fact that only one side of the web is exposed to the elevated temperatures. Such fire exposure conditions require further investigations as differential thermal expansions can lead to failure under different failure modes.

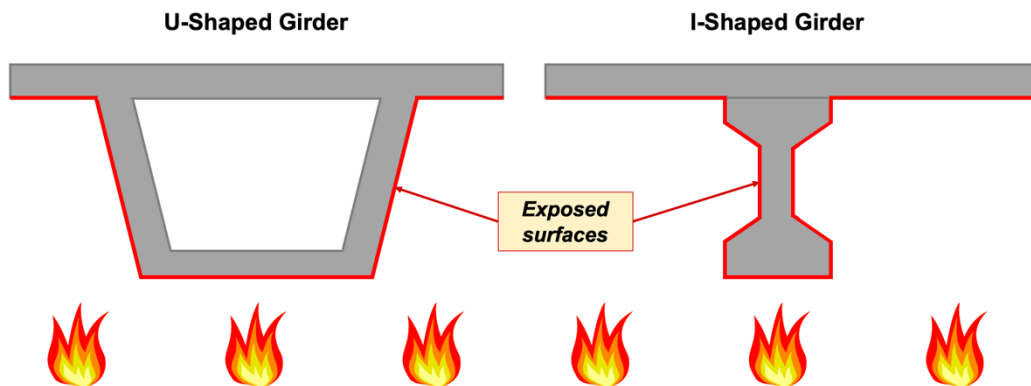


Figure 7.6: Fire exposure of I-shaped and U-shaped girders

7.5.2.4. Fire Protection Alternatives

If the previous design alternatives are not sufficient to obtain the required fire resistance, additional fire protection measures can be incorporated into the design of concrete bridge girders. These measures include passive fire protection alternatives to increase the fire resistance of structural members. This typically consists in the application of fire insulation materials on the surface of structural members, such as application of intumescent paints or spray-applied coatings to delay the progression of temperatures within the member and increase its fire resistance. These alternatives are usually used in the design of steel structures in buildings and their application in bridge structures would require further investigation to ensure that they can withstand the harsher outside environment, as well as regular maintenance for its continued performance. In addition, conducting advanced analysis, as demonstrated in the numerical studies conducted in this research, can result in more accurate fire resistance evaluation than the use of rational fire design measures. Alternatively, security measures can be adopted to prevent fires resulting from vandalism by implementing surveilling systems or access control in critical bridges.

7.6. Summary

This chapter presented the development of design recommendations to assist on the design of concrete bridge girders exposed to a fire. The first step was establishing parameters for the fire resistance analysis of bridge girders, including fire exposure and structural loading conditions. An analytical approach has been proposed to determine the spatial temperature distribution of fire exposure along bridge girders by taking into consideration the bridge geometrical features, specifically the clearance height and span length, considering a severe fire intensity. The proposed method facilitates the evaluation of bridge girders with due consideration to the thermal gradients developed in bridge fires and has been validated with results from the fire dynamics model

developed as part of this research. Additional insights on the structural loading of bridge girders have been provided to ensure structural loads representative of bridge structures are adopted. The next step was to establish failure criteria to determine the fire resistance of bridge girders. This included the evaluation of current methods used to determine deflection limits and its applicability to assess concrete bridge girders. Additionally, the use of strength-based limiting criteria, including flexural and shear limit states, is discussed as an alternative method to determine the fire resistance of concrete bridge girders. Finally, general recommendations for the design of concrete bridge girders under fire conditions have been proposed, including recommendations for the concrete batch mix composition, cross-sectional shape and reinforcement configuration.

8. CONCLUSIONS

8.1. General

Fire incidents on the vicinity of bridges have become more common over the last couple of decades due to increasing urbanization and transportation of hazardous materials. Typically, these fires result from incidents involving vehicles carrying significant amounts of fuels (hydrocarbons) or other flammable materials, which lead to the onset of very high temperatures in short periods of time. These conditions result in rapid degradation of structural members, leading to partial or full collapse of bridges. Also, following fire incidents, it requires detailed investigations, costly repairs, or even replacement of the structure. Such consequences can be attributed to the lack of specific fire safety provisions for bridge structures, leaving these important infrastructure members highly vulnerable to the effects of high temperatures exposure.

Bridge girders are the most vulnerable structural members during a bridge fire due to their critical role in supporting the superstructure and its exposure conditions to the elevated temperatures. While there has been some research on the fire response of steel bridges, the detailed review of the literature presented in Chapter 2 reveals that there is very limited information available on the effect of elevated temperatures on the fire performance of concrete bridge girders, especially in modern bridges incorporating HSC and UHPC. The optimized cross-sections developed for concrete bridge girders present a different behavior at elevated temperatures when compared to conventional concretes members made with NSC. Some of the key differences are related to slender webs/stems, which make these girders vulnerable to shear failure under fire conditions. Additionally, design provisions developed for conventional concrete members used in buildings cannot be directly applied in the design of modern bridge structures due to fundamental

differences in the material and structural characteristics, exposure conditions, and lack of active fire protection systems.

To develop a comprehensive understanding of the fire behavior of concrete bridge girders, experimental and numerical studies have been carried as part of the research work developed in this dissertation. Through experimental tests, the build-up of pore pressure in concrete and degradation of shear strength in UHPC have been measured at elevated temperatures, as detailed in Chapter 3. Pore pressure is one the main parameters that govern fire-induced spalling of concrete, but its measurement is quite complex due to a number of influencing factors. Therefore, this experimental program was been focused on analyzing the level of influence of different parameters that can affect measured results. Also, due to the high level of influence of shear strength on the fire response of concrete bridge girders, shear strength tests have been carried out to determine the level of degradation in shear strength with temperature. Overall, results from these tests provided important insights into key factors that influence the fire response of concrete bridges.

As part of the numerical studies, a finite element-based numerical model was developed in ABAQUS to trace the fire behavior of concrete bridge girders. The model is capable of accounting for the non-uniform temperature distribution of bridge fires obtained through fire dynamics simulations in FDS-PyroSim. In addition to thermal and structural analysis of the concrete bridge girders, a submodel was developed to analyze degradation of the member capacity based on the thermal response of the member, providing information on the effect of temperature on the degradation of the member capacity. The model was validated by comparing temperatures and deflections from the finite element model with results from fire resistance tests reported in the literature, as detailed in Chapter 4. The developed numerical model was then used to analyze fire-

induced collapse of an I-95 overpass in Philadelphia on June 11, 2023, in Chapter 5. In addition, the model was applied to evaluate the effect of different design and exposure parameters on the response of concrete bridge girders in Chapter 6. Considering the results obtained in the experimental and numerical studies, design recommendations have been outlined in Chapter 7 to improve the design of concrete bridge girders with regards to fire safety.

8.2. Key Findings

Based on the results obtained from the research work developed as part of this dissertation, the following key conclusions have been outlined:

1. When measuring the build-up of pore pressure in concrete during heating, the pressure peak will occur at a specific location inside of the specimen, which depends on the type of concrete being tested (its transport properties, such as porosity and permeability), moisture content and exposure conditions (exposed surfaces and heating rate). While concretes of lower permeability experience peak pressure close to the heated surface, water vapor can migrate to deeper layers in concretes of higher permeability. Higher heating rates (above 2°C/minute) induce cracking and spalling in UHPC, which results in pore pressure release, compromising pressure measurements. On the other hand, lower heating rates allow water vapor to migrate to deeper layers of NSC specimens, resulting in higher pressure peaks. Sealing and insulating the sides of the specimens with aluminum foils and heat-resistant epoxy led to higher pressure levels because it reduced the loss of moisture through unexposed surfaces. Using smaller specimens result in lower pressure measurements as they present higher surface area-to-volume ratio, allowing free water to be driven outwards more easily and hindering the formation of the moisture clog.

2. The modified JSCE-SF6 test method proposed in this dissertation was capable of measuring degradation of UHPC shear strength at elevated temperatures. Results from the tests showed that both steel and polypropylene fibers provided significant improvements in shear strength. While steel fibers bridged cracks in the specimen, polypropylene fibers reduced microcracking by lowering pore pressure build-up through their melting during the heating process. The three batches of UHPC specimens tested experienced loss of shear strength when exposed to 200°C, but the effect of temperature became more pronounced when exposed to temperatures higher than 400°C. Without fibers, UHPC experienced faster degradation and the contribution of polypropylene fibers became less pronounced at higher levels of temperature.
3. The developed numerical model is capable of tracing the fire response of concrete bridge girders, including modern girders made with UHPC. The model incorporates temperature-dependent thermal and mechanical properties of steel and concrete based on relations established in codes and studies available in the literature. In addition, the model is also capable of coupling field temperatures derived from fire models developed in FDS-PyroSim to the thermo-structural model developed in ABAQUS. A submodel is also included to assess the fire resistance of concrete bridge girders based on flexural and shear capacity degradation. The validity of the model is confirmed by comparing model predictions with results from fire tests on concrete beams.
4. The applicability of the model to field application is demonstrated by analyzing the fire induced collapse of the I-95 overpass in Philadelphia that occurred on June 11, 2013. The numerical model was capable of tracing the fire response of the bridge girder and reasonably predicting its failure mode and fire resistance. Based on the fire simulations

carried out, the bridge experienced temperatures higher than the hydrocarbon fire curve during the incident, emphasizing that bridge structures experience severe fires. While evaluating mitigation strategies, it was found that fire insulation is an effective strategy to increase fire resistance of bridge girders. If the girders in this overpass had been insulated with Carbolite type-5MD, 12.5 mm-thickness, the bridge could have resisted almost four hours of severe fire exposure.

5. By comparing the fire performance of bridge girders with rectangular and I-shaped sections, the main hypothesis of this dissertation has been confirmed: concrete girders with slender cross sections experience high concentration of heat in the web and faster degradation of their shear capacity. The analysis demonstrated that the failure mode changed from flexure to shear due to concentration of strains on the bottom of the mid-span (rectangular section) to the center of the web (I-shaped section), resulting from the faster degradation of the concrete strength in the web of the I-shaped section. While analyzing four standard I-shaped sections designed for bridges of various span lengths, it was observed that smaller standard cross-sections, such as AASHTO Types I and II, present lower fire resistance than the more robust sections Types III and IV. This is attributed to the lower thermal mass of smaller sections that allow a faster progression of temperatures and, consequently, faster degradation of the girder strength and stiffness. Other design parameters, such as girder length and concrete strength demonstrated a significant influence on the fire response of bridge girders.
6. Results from the fire simulations demonstrate that bridge span length and clearance height present a significant influence on the spatial distribution of fire exposure temperatures along the girder. A significant thermal gradient is developed on the

surface of structural members exposed to open-air fires. Bridges with smaller span lengths (12 m) and higher clearance heights (8 m) experienced higher temperatures, while bridges with longer spans (24 m) and lower clearance heights (5 m) experienced higher thermal gradients. In addition, it was observed that fires with higher fire intensity (200 MW) resulted in higher temperatures on the bottom of the girders and lower thermal gradients along the girder depth compared to the lower intensity-fire (75 MW). These conditions significantly affect the structural response of concrete girders during fire exposure, demonstrating the need to account for realistic temperature fields in the assessment of the fire response of concrete bridge girders.

7. Overall, results from numerical studies have demonstrated that the fire response of concrete bridge girders is significantly different than building members, thus requiring specific design recommendations that accounts for their specific exposure conditions. To assess the fire response of a concrete bridge girder more realistically, it was found important to establish appropriate temperature fields that accounts for the temperature levels and thermal gradients of bridge fires. In addition, the applied structural loading should reflect the loading conditions in bridges during fire events. Another important aspect is the definition of adequate failure criteria for determining the fire resistance of concrete bridge girders. Current limits have been developed for building members and cannot trace the fire response of bridge girders, with longer spans and exposed to fires of higher severity. Therefore, a new methodology has been proposed, including both deflection and strength limit states in the fire assessment of concrete bridge girders.

8.3. Research Impact

Bridges are an important part of transportation network and their resilience to extreme events, such as fires, is important to prevent excessive traffic disruptions and costly repairs or reconstructions after these incidents. The research conducted in this dissertation aimed to establish a comprehensive understanding of the behavior of concrete bridge girders under fire while addressing several key factors that affect their fire response. Through experimental and numerical investigations, this research has made the following contributions:

1. The pore pressure measurements performed in this study quantified the level of influence of different testing parameters on pore pressure evolution. Understanding how these parameters affect test results is important to assist in the development a standardized test procedure. This is important to make test results from different studies comparable, essential for advancing the knowledge on the pore pressure mechanism and its influence on fire-induced spalling of concrete.
2. While the JSCE-SF6 test method has already been implemented to evaluate the shear strength of steel fiber reinforced cementitious composites at ambient temperatures, this research has innovated by scaling down the specimens for testing UHPC at elevated temperatures. This allowed the quantification of UHPC shear strength at different levels of temperature in specimens reinforced with steel and polypropylene fibers. Such information is relevant for analyzing shear strength degradation in UHPC bridge girders, which can occur due to external forces, such as high concentrated forces close to midspan, or even on the interface of section variations due to prestressing forces.
3. The development of a numerical solution, capable of assessing the fire resistance of concrete bridge girders with due consideration to material property degradation and

- realistic fire exposure conditions, enables the analysis of bridge structures more realistically. Utilizing a commercially available tools like ABAQUS and PyroSim enhances the applicability of the numerical model for real-world applications.
4. The numerical model has been successfully applied to analyze the fire incident that led to the collapse of an I-95 overpass in Philadelphia on June 11, 2023, providing insights on the collapse mechanism and possible mitigation strategies.
 5. The parametric studies conducted in this research generated data on the influence of several factors affecting the fire resistance of concrete bridge girders, providing valuable insights on the level of influence of different design parameters (such as cross-sectional shape and size, span length, and material properties) and exposure conditions (fire temperatures and thermal gradients) on the fire response and failure mechanisms in concrete bridge girders, contributing to the collective knowledge in the field.
 6. Lastly, this research has developed a comprehensive methodology to assess the fire resistance of bridge girders effectively. By integrating experimental data, numerical simulations, and analytical techniques, this methodology offers a systematic approach to evaluate the fire resistance of concrete bridge girders, as well as on the safe fire design of concrete bridge girders.

In summary, the findings and methodologies presented in this study contribute to advancing the understanding and improvement of the fire resistance of concrete bridge girders, thereby enhancing the safety, durability, and resilience of bridge girders to fire hazard.

8.4. Recommendations for Future Work

The research work developed as part of this dissertation contributed to advance the state-of-the-art knowledge on the fire problem in concrete bridge girders by generating data through

experimental testing and numerical modeling. Still, additional research is needed to advance the field of structural fire engineering in concrete bridges. The following topics have been considered most relevant for future work in this area:

1. Further pore pressure measurements in concrete specimens will be required for developing a standardized test procedure capable of tracing the maximum pressure levels that could trigger fire-induced spalling in different types of concrete.
2. There are different methods that can be used to measure shear strength in concrete. For a better understanding on the applicability of the JSCE-SF6 test results at elevated temperatures, results from other test methods can be compared. The applicability of these results on the structural level design is still pending.
3. Fire tests on real-scale I-shaped concrete bridge girders under more realistic loading and fire exposure conditions are needed to provide insights into the fire behavior of modern bridge girders, especially made with HSC and UHPC. In addition, results from these tests will be useful for validating numerical models and ensuring their accuracy.
4. The developed numerical model can be refined to account for other important factors on the fire response of concrete bridge girders, such as the bond-slip behavior between concrete and steel at elevated temperatures, the confinement effect of shear reinforcement, as well as the developed of fire-induced spalling of concrete.
5. The design recommendations presented in this dissertation are preliminary and will need to be updated as more data on additional influencing factors becomes available. Future studies should consider the effects of composite action, restraint, and loading conditions to incorporate these into design codes and standards.

REFERENCES

- [1] Deng L, Wang W, Yu Y. State-of-the-Art Review on the Causes and Mechanisms of Bridge Collapse. *Journal of Performance of Constructed Facilities* 2016;30. [https://doi.org/10.1061/\(ASCE\)CF.1943-5509.0000731](https://doi.org/10.1061/(ASCE)CF.1943-5509.0000731).
- [2] Xu FY, Zhang MJ, Wang L, Zhang JR. Recent Highway Bridge Collapses in China: Review and Discussion. *Journal of Performance of Constructed Facilities* 2016;30. [https://doi.org/10.1061/\(ASCE\)CF.1943-5509.0000884](https://doi.org/10.1061/(ASCE)CF.1943-5509.0000884).
- [3] Proske D. *Bridge Collapse Frequencies versus Failure Probabilities*. Cham: Springer International Publishing; 2018. <https://doi.org/10.1007/978-3-319-73833-8>.
- [4] Wardhana K, Hadipriono FC. Analysis of Recent Bridge Failures in the United States. *Journal of Performance of Constructed Facilities* 2003;17:144–50. [https://doi.org/10.1061/\(ASCE\)0887-3828\(2003\)17:3\(144\)](https://doi.org/10.1061/(ASCE)0887-3828(2003)17:3(144)).
- [5] Pritchard B. *Bridge design for economy and durability: Concepts for new, strengthened and replacement bridges*. London: Thomas Telford; 1992.
- [6] Long AE, Basheer PAM, Taylor SE, Rankin BGI, Kirkpatrick J. Sustainable bridge construction through innovative advances. *Proceedings of the Institution of Civil Engineers - Bridge Engineering* 2008;161:183–8. <https://doi.org/10.1680/bren.2008.161.4.183>.
- [7] Torrent RJ. Bridge durability design after EN standards: present and future. *Structure and Infrastructure Engineering* 2019;15:886–98. <https://doi.org/10.1080/15732479.2017.1414859>.
- [8] Kodur VKR, Naser MZ. Fire hazard in transportation infrastructure: Review, assessment, and mitigation strategies. *Frontiers of Structural and Civil Engineering* 2021. <https://doi.org/10.1007/s11709-020-0676-6>.
- [9] Kodur VKR, Naser M. *Structural Fire Engineering*. 1st ed. New York: McGraw Hill; 2020.
- [10] AASHTO. *LRFD Bridge Design Specifications*. Washington, DC, USA: 2009.
- [11] Lichtenstein AG. The Silver Bridge Collapse Recounted. *Journal of Performance of Constructed Facilities* 1993;7:249–61. [https://doi.org/10.1061/\(ASCE\)0887-3828\(1993\)7:4\(249\)](https://doi.org/10.1061/(ASCE)0887-3828(1993)7:4(249)).
- [12] Hartmann J, Weingroff R. Happy 50th Anniversary National Bridge Inspection Standards. US Department of Transportation - Federal Highway Administration 2021. https://www.fhwa.dot.gov/highwayhistory/national_bridge_inspection_standards.cfm (accessed August 30, 2023).

- [13] U.S. Department of Transportation - Federal Highway Administration. Status of the Nation's Highways, Bridges, and Transit: 2004 Conditions and Performance. Washington, D.C.: 2004.
- [14] National Transportation Safety Board. Highway Accident Brief: Fire Damage to Bridge and Subsequent Collapse, Atlanta, Georgia, March 30, 2017. Washington, DC: 2018.
- [15] National Transportation Safety Board. Combination Vehicle Fire and Interstate 95 Overpass Collapse. Investigation No HWY23FH014 2023.
- [16] U.S. Department of Transportation - Federal Highway Administration. Deficient Bridges by Superstructure Material 2016. Bridges & Structures 2018. <https://www.fhwa.dot.gov/bridge/nbi/no10/mat16.cfm> (accessed August 30, 2023).
- [17] Minnesota Department of Transportation. Prestressed concrete bridges. Historic Bridges n.d. <http://www.dot.state.mn.us/historicbridges/prestressed-concrete.html#:~:text=First%20in%20the%20US%3A%20Walnut,Magnel's%20student%2C%20designed%20the%20bridge> (accessed August 30, 2023).
- [18] Taly N. Highway Bridge Superstructure Engineering: LRFD Approaches to Design and Analysis. Boca Raton, FL: CRC Press; 2015.
- [19] Xue J, Briseghella B, Huang F, Nuti C, Tabatabai H, Chen B. Review of ultra-high performance concrete and its application in bridge engineering. *Constr Build Mater* 2020;260. <https://doi.org/10.1016/j.conbuildmat.2020.119844>.
- [20] Zhou M, Lu W, Song J, Lee GC. Application of Ultra-High Performance Concrete in bridge engineering. *Constr Build Mater* 2018;186:1256–67. <https://doi.org/10.1016/j.conbuildmat.2018.08.036>.
- [21] Russell HG, Graybeal BA. Ultra-High Performance Concrete: A State-of-the-Art Report for the Bridge Community. McLean, VA: 2013.
- [22] Naser MZ. Autonomous Fire Resistance Evaluation. *Journal of Structural Engineering* 2020;146:04020103. [https://doi.org/10.1061/\(asce\)st.1943-541x.0002641](https://doi.org/10.1061/(asce)st.1943-541x.0002641).
- [23] Alavi AH, Hasni H, Lajnef N, Chatti K, Faridazar F. An intelligent structural damage detection approach based on self-powered wireless sensor data. *Autom Constr* 2016;62:24–44. <https://doi.org/10.1016/j.autcon.2015.10.001>.
- [24] Salehi H, Burgueño R. Emerging artificial intelligence methods in structural engineering. *Eng Struct* 2018;171:170–89. <https://doi.org/10.1016/j.engstruct.2018.05.084>.
- [25] Naser MZ. Mechanistically Informed Machine Learning and Artificial Intelligence in Fire Engineering and Sciences. *Fire Technol* 2021. <https://doi.org/10.1007/s10694-020-01069-8>.

- [26] Wickert D. Price tag for new I-85 bridge: Up to \$16.6 million. *The Atlanta Journal-Constitution* 2017.
- [27] Alos-Moya J, Paya-Zaforteza I, Hospitaler A, Loma-Ossorio E. Valencia bridge fire tests: Validation of simplified and advanced numerical approaches to model bridge fire scenarios. *Advances in Engineering Software* 2019;128:55–68. <https://doi.org/10.1016/j.advengsoft.2018.11.003>.
- [28] Peris-Sayol G, Paya-Zaforteza I, Alos-Moya J, Hospitaler A. Analysis of the influence of geometric, modeling and environmental parameters on the fire response of steel bridges subjected to realistic fire scenarios. *Comput Struct* 2015;158:333–45. <https://doi.org/10.1016/j.compstruc.2015.06.003>.
- [29] Peris-Sayol G, Paya-Zaforteza I, Balasch-Parisi S, Alós-Moya J. Detailed analysis of the causes of bridge fires and their associated damage levels. *Journal of Performance of Constructed Facilities* 2017;31. [https://doi.org/10.1061/\(ASCE\)CF.1943-5509.0000977](https://doi.org/10.1061/(ASCE)CF.1943-5509.0000977).
- [30] New York State Department of Transportation. *Bridge Fire Incidents in New York State*. New York, NY: 2008.
- [31] Hu J, Carvel R, Usmani A. Bridge fires in the 21st century: A literature review. *Fire Saf J* 2021;126. <https://doi.org/10.1016/j.firesaf.2021.103487>.
- [32] Garlock M, Paya-Zaforteza I, Kodur VKR, Gu L. Fire hazard in bridges: Review, assessment and repair strategies. *Eng Struct* 2012;35:89–98. <https://doi.org/10.1016/j.engstruct.2011.11.002>.
- [33] Stoddard RB. A case study: Evaluating fire damage. *ASPIRE* 2008:24–5.
- [34] Shutt CA. Protecting Against & Evaluating Fire Damage. *ASPIRE* 2008:18–22.
- [35] Hays H V., Pak-Harvey A. Fuel tanker explodes causing “catastrophic” damage on Indianapolis interstate. *USA Today (Online)* Available at: <https://www.usatoday.com/story/news/nation/2020/02/20/fire-indianapolis-jet-fuel-tanker-ignites-ramp-465-70/4826762002/> 2020.
- [36] Solis N, Curwen T, Hernandez S, Garcia K. Section of 10 Freeway damaged by fire will not need to be demolished, officials say. *Los Angeles Times* 2023.
- [37] Hall S, Evarts B. *Fire Loss in the United States During 2021*. 2022.
- [38] Bulwa D, Fimrite P. Tanker Fire Destroys Part of MacArthur Maze. *San Francisco Chronicle* 2007.

- [39] Yavuz F, Attanayake U, Aktan H. Economic Impact on Surrounding Businesses due to Bridge Construction. *Procedia Comput Sci*, vol. 109, Elsevier B.V.; 2017, p. 108–15. <https://doi.org/10.1016/j.procs.2017.05.301>.
- [40] City of Philadelphia. Updates on the I-95 fire and partial highway collapse 2023.
- [41] Guzman F, Hauck G, Nguyen T. Tanker fire causes part of Interstate 95 in Philadelphia to collapse; complete rebuild expected to take “months”: Updates. *USA Today* 2023.
- [42] International Code Council. *International Building Code*. 2018.
- [43] ACI 318. *Building Code Requirements for Structural Concrete*. Farmington Hills, MI, USA: American Concrete Institute; 2019. <https://doi.org/10.14359/51716937>.
- [44] Graybeal B, Brühwiler E, Kim B-S, Toutlemonde F, Voo YL, Zaghi A. International Perspective on UHPC in Bridge Engineering. *Journal of Bridge Engineering* 2020;25. [https://doi.org/10.1061/\(asce\)be.1943-5592.0001630](https://doi.org/10.1061/(asce)be.1943-5592.0001630).
- [45] Haber ZB, De la Varga I, Graybeal BA, Nakashoji B, El-Helou R. FHWA-HRT-18-036: *Properties and Behavior of UHPC-Class Materials*. McLean, VA: 2018.
- [46] Liu J, Han F, Cui G, Zhang Q, Lv J, Zhang L, et al. Combined effect of coarse aggregate and fiber on tensile behavior of ultra-high performance concrete. *Constr Build Mater* 2016;121:310–8. <https://doi.org/10.1016/j.conbuildmat.2016.05.039>.
- [47] Zeng X, Deng K, Liang H, Xu R, Zhao C, Cui B. Uniaxial behavior and constitutive model of reinforcement confined coarse aggregate UHPC. *Eng Struct* 2020;207:110261. <https://doi.org/10.1016/j.engstruct.2020.110261>.
- [48] Bajaber MA, Hakeem IY. UHPC evolution, development, and utilization in construction: a review. *Journal of Materials Research and Technology* 2021;10:1058–74. <https://doi.org/10.1016/j.jmrt.2020.12.051>.
- [49] Hamada H, Alattar A, Tayeh B, Yahaya F, Almeshal I. Influence of different curing methods on the compressive strength of ultra-high-performance concrete: A comprehensive review. *Case Studies in Construction Materials* 2022;17:e01390. <https://doi.org/10.1016/j.cscm.2022.e01390>.
- [50] Shafieifar M, Farzad M, Azizinamini A. Experimental and numerical study on mechanical properties of Ultra High Performance Concrete (UHPC). *Constr Build Mater* 2017;156:402–11. <https://doi.org/10.1016/j.conbuildmat.2017.08.170>.
- [51] Graybeal B. *Design and Construction of Field-Cast UHPC Connections*. McLean, VA: 2014.

- [52] El-Helou RG, Graybeal BA. Shear Behavior of Ultrahigh-Performance Concrete Pretensioned Bridge Girders. *Journal of Structural Engineering* 2022;148. [https://doi.org/10.1061/\(asce\)st.1943-541x.0003279](https://doi.org/10.1061/(asce)st.1943-541x.0003279).
- [53] Graybeal BA. Flexural Behavior of an Ultrahigh-Performance Concrete I-Girder. *J Bridge Eng* 2008;13:602–10. <https://doi.org/10.1061/ASCE1084-0702200813:6602>.
- [54] Kodur VKR, Solhmirzaei R, Agrawal A, Aziz EM, Soroushian P. Analysis of flexural and shear resistance of ultra high performance fiber reinforced concrete beams without stirrups. *Eng Struct* 2018;174:873–84. <https://doi.org/10.1016/j.engstruct.2018.08.010>.
- [55] Voo YL, Foster SJ, Gilbert RI. Shear Strength of Fiber Reinforced Reactive Powder Concrete Prestressed Girders without Stirrups. vol. 4. 2006.
- [56] PCI. Implementation of Ultra-High-Performance Concrete in Long-Span Precast Pretensioned Elements for Concrete Buildings and Bridges Phase I. 2020.
- [57] Chen B, Wu H, An M, Huang Q, Zhao Q. Application of Ultra-High Performance Concrete in Bridge Engineering in China. First International Interactive Symposium on UHPC, Iowa State University Digital Press; 2016. <https://doi.org/10.21838/uhpc.2016.124>.
- [58] Fan D, Zhu J, Fan M, Lu J-X, Chu SH, Dong E, et al. Intelligent design and manufacturing of ultra-high performance concrete (UHPC) – A review. *Constr Build Mater* 2023;385:131495. <https://doi.org/10.1016/j.conbuildmat.2023.131495>.
- [59] U.S. Department of Transportation - Federal Highway Administration. Deployments of UHPC in Highway Bridge Construction 2021. <https://highways.dot.gov/research/structures/ultra-high-performance-concrete/deployments> (accessed August 30, 2023).
- [60] Kodur V, Banerji S. Comparative fire behavior of reinforced concrete beams made of different concrete strengths. *Structures in Fire Conference, University of Queensland Library*; 2020. <https://doi.org/10.14264/bd10594>.
- [61] Banerji S, Kodur V, Solhmirzaei R. Experimental behavior of ultra high performance fiber reinforced concrete beams under fire conditions. *Eng Struct* 2020;208. <https://doi.org/10.1016/j.engstruct.2020.110316>.
- [62] Missemer L, Ouedraogo E, Malecot Y, Clergue C, Rogat D. Fire spalling of ultra-high performance concrete: From a global analysis to microstructure investigations. *Cem Concr Res* 2019;115:207–19. <https://doi.org/10.1016/j.cemconres.2018.10.005>.
- [63] Lo Monte F, Felicetti R, Meda A, Bortolussi A. Assessment of concrete sensitivity to fire spalling: A multi-scale experimental approach. *Constr Build Mater* 2019;212:476–85.

- [64] Dwaikat MB, Kodur VKR. Hydrothermal model for predicting fire-induced spalling in concrete structural systems. *Fire Saf J* 2009;44:425–34. <https://doi.org/10.1016/j.firesaf.2008.09.001>.
- [65] Kalifa P, Menneteau È-D, Quenard D. Spalling and pore pressure in HPC at high temperatures. *Cem Concr Res* 2000;30:1915–27.
- [66] Gil A, Banerji S, Kodur V. Factors influencing pore pressure measurements in concrete during heating and its influence on fire-induced spalling. *Cem Concr Compos* 2023;142. <https://doi.org/10.1016/j.cemconcomp.2023.105228>.
- [67] Moore WL. Performance of fire-damaged prestressed concrete bridges. *Missouri S&T*, 2008.
- [68] Ma J, Low S-G. Precast-Pretensioned Concrete Girder Bridges. In: Chen W-F, Duan L, editors. *Bridge Engineering Handbook - Superstructure Design*. 2nd ed., Boca Raton, FL: Taylor & Francis Group; 2014, p. 1–50.
- [69] Meir J V., Ciccirelli MR, Ramirez JA, Lee RH. Alternatives to the Current AASHTO Standard Bridge Sections. *PCI Journal* 1997;42:56–66.
- [70] Geren KL, Tadros MK. The NU Precast/Prestressed Concrete Bridge I-Girder Series. *PCI Journal* 1994;39:26–39.
- [71] El-Helou RG, Graybeal B. The Ultra Girder: A Design Concept for a 300-foot Single Span Prestressed UHPC Bridge Girder. *Proceedings of the Second International Interactive Symposium on Ultra High-Performance Concrete*, 2019.
- [72] Tadros MK, Lawler J, El-Khier MA, Gee D, Kurt A, Lucier G, et al. *Implementation of Ultra-High Performance Concrete in Long-Span Precast Pretensioned Elements for Concrete Buildings and Bridges*. Chicago, IL: 2021.
- [73] Barron R, Jaber F, Tadros MK, Morcous G. Development of Standardized Nebraska Family of UHPC Decked I-Beams. *Proceedings of the Third International Interactive Symposium on Ultra High Performance Concrete*, Wilmington, DE: Iowa State University; 2023.
- [74] Graybeal B, El-Helou R. Development of an AASHTO Guide Specification for Ultra-High Performance Concrete. *Proceedings of the Second International Interactive Symposium on Ultra High Performance Concrete*, 2019.
- [75] AFNOR - French standard institute. NF P 18-710 - National addition to Eurocode 2-Design of concrete structures: specific rules for Ultra-High Performance Fibre-Reinforced Concrete (UHPRFC). 2016.
- [76] CSA (Canadian Standards Association). *Canadian highway bridge design code*. Canada: 2019.

- [77] American Concrete Institute (ACI). ACI 544.4R-18 Guide to Design with Fiber-Reinforced Concrete. Farmington Hills, MI: 2018.
- [78] Shafieifar M, Farzad M, Azizinamini A. A comparison of existing analytical methods to predict the flexural capacity of Ultra High Performance Concrete (UHPC) beams. *Constr Build Mater* 2018;172:10–8. <https://doi.org/10.1016/j.conbuildmat.2018.03.229>.
- [79] El-Helou RG, Graybeal BA. Flexural Behavior and Design of Ultrahigh-Performance Concrete Beams. *Journal of Structural Engineering* 2022;148. [https://doi.org/10.1061/\(ASCE\)ST.1943-541X.0003246](https://doi.org/10.1061/(ASCE)ST.1943-541X.0003246).
- [80] Aaleti S, Petersen B, Sritharan S. FHW A-HIF-13-032 - Design Guide for Precast UHPC Waffle Deck Panel System, Including Connections. Washington, DC: 2013.
- [81] Bentz EC, Vecchio FJ, Collins MP. Simplified Modified Compression Field Theory for Calculating Shear Strength of Reinforced Concrete Elements. *ACI Struct J* 2006;103:614–24.
- [82] Bierwagen D, Abu-Hawash A. Ultra high performance concrete highway bridge. *Proceedings of the 2005 Mid-Continent Transportation Research Symposium*, Ames, IO: Iowa State University; 2015.
- [83] Hajar Z, Simon A, Lecointre D, Petitjean J. Construction of the first road bridges made of ultra-high-performance concrete. *Proceedings of International Symposium on High Performance Concrete-ISHPC*, Orlando, FL: 2003.
- [84] Graybeal BA. *Ultra-High Performance Concrete: A State-of-the-Art Report for the Bridge Community*. McLean, VA: 2013.
- [85] Endicott WA. Iowa Bridge Gives Glimpse Into The Future. *ASCENT - Summer* 2006:41–6.
- [86] Ozyildirim C. *Evaluation of Fiber-Reinforced Concrete Ultra-High-Performance*. 2011.
- [87] Keierleber B, Bierwagen D, Wipf T, Abu-Hawash A. FHWA, Iowa Optimize Pi Girder. *ASPIRE - Winter* 2010:24–9.
- [88] Kim H. Design and field construction of Hawkeye Bridge using ultra high performance concrete for accelerated bridge construction. University of Iowa, 2016. <https://doi.org/10.17077/etd.4b9futmh>.
- [89] Castellote M, Alonso C, Andrade C, Turrillas X, Campo J. Composition and microstructural changes of cement pastes upon heating, as studied by neutron diffraction. *Cem Concr Res* 2004;34:1633–44. [https://doi.org/10.1016/S0008-8846\(03\)00229-1](https://doi.org/10.1016/S0008-8846(03)00229-1).

- [90] Vandamme M. The Nanogranular Origin of Concrete Creep: A Nanoindentation Investigation of Microstructure and Fundamental Properties of Calcium-Silicate-Hydrates. Doctorate. Massachusetts Institute of Technology, 2008.
- [91] Zanni H, Cheyrezy M, Maret V, Philippot S, Nieto P. Investigation of hydration and pozzolanic reaction in Reactive Powder Concrete (RPC) using ^{29}Si NMR. *Cem Concr Res* 1996;26:93–100. [https://doi.org/10.1016/0008-8846\(95\)00197-2](https://doi.org/10.1016/0008-8846(95)00197-2).
- [92] Shaw S, Clark SM, Henderson CMB. Hydrothermal formation of the calcium silicate hydrates, tobermorite ($\text{Ca}_5\text{Si}_6\text{O}_{16}(\text{OH})_2 \cdot 4\text{H}_2\text{O}$) and xonotlite ($\text{Ca}_6\text{Si}_6\text{O}_{17}(\text{OH})_2$): an in situ synchrotron study. *Chem Geol* 2000;167:129–40. [https://doi.org/10.1016/S0009-2541\(99\)00205-3](https://doi.org/10.1016/S0009-2541(99)00205-3).
- [93] Way RT, Wille K. Effect of Heat-Induced Chemical Degradation on the Residual Mechanical Properties of Ultrahigh-Performance Fiber-Reinforced Concrete. *Journal of Materials in Civil Engineering* 2016;28. [https://doi.org/10.1061/\(ASCE\)MT.1943-5533.0001402](https://doi.org/10.1061/(ASCE)MT.1943-5533.0001402).
- [94] Hager I. Behaviour of cement concrete at high temperature. *Bulletin of the Polish Academy of Sciences: Technical Sciences* 2013;61:145–54. <https://doi.org/10.2478/bpasts-2013-0013>.
- [95] Fédération Internationale du Béton (FIB). *fib Bulletin 38: Fire design of concrete structures - materials, structures and modelling*. Lausanne, Switzerland: 2007.
- [96] Eurocode 2. EN 1992-1-2: Design of concrete structures - Part 1-2: General rules - Structural fire design. Brussels, Belgium: 2004.
- [97] ASCE 29. *Standard Calculation Methods for Structural Fire Protection*. Reston, Virginia, USA: 2005.
- [98] Chen Y, Zhang Y, Zhang S, Guo Q, Gao Y, Zhang T, et al. Experimental study on the thermal properties of a novel ultra-high performance concrete reinforced with multi-scale fibers at elevated temperatures. *Constr Build Mater* 2023;366:130229. <https://doi.org/10.1016/j.conbuildmat.2022.130229>.
- [99] Xue C, Yu M, Xu H, Xu L, Saafi M, Ye J. Experimental study on thermal performance of ultra-high performance concrete with coarse aggregates at high temperature. *Constr Build Mater* 2022;314:125585. <https://doi.org/10.1016/j.conbuildmat.2021.125585>.
- [100] Li H, Hao X, Qiao Q, Zhang B, Li H. Thermal Properties of Hybrid Fiber-Reinforced Reactive Powder Concrete at High Temperature. *Journal of Materials in Civil Engineering* 2020;32. [https://doi.org/10.1061/\(ASCE\)MT.1943-5533.0003053](https://doi.org/10.1061/(ASCE)MT.1943-5533.0003053).

- [101] Yang I-H, Park J. Mechanical and Thermal Properties of UHPC Exposed to High-Temperature Thermal Cycling. *Advances in Materials Science and Engineering* 2019;2019:1–12. <https://doi.org/10.1155/2019/9723693>.
- [102] Zheng W, Luo B, Wang Y. Compressive and tensile properties of reactive powder concrete with steel fibres at elevated temperatures. *Constr Build Mater* 2013;41:844–51. <https://doi.org/10.1016/j.conbuildmat.2012.12.066>.
- [103] Ju Y, Liu H, Liu J, Tian K, Wei S, Hao S. Investigation on thermophysical properties of reactive powder concrete. *Sci China Technol Sci* 2011;54:3382–403. <https://doi.org/10.1007/s11431-011-4536-4>.
- [104] Kodur V, Banerji S, Solhmirzaei R. Effect of Temperature on Thermal Properties of Ultrahigh-Performance Concrete. *Journal of Materials in Civil Engineering* 2020;32. [https://doi.org/10.1061/\(ASCE\)MT.1943-5533.0003286](https://doi.org/10.1061/(ASCE)MT.1943-5533.0003286).
- [105] Kodur VKR, Banerji S, Solhmirzaei R. Test methods for characterizing concrete properties at elevated temperature. *Fire Mater*, vol. 44, John Wiley and Sons Ltd; 2020, p. 381–95. <https://doi.org/10.1002/fam.2777>.
- [106] Zheng W, Luo B, Wang Y. Stress–strain relationship of steel-fibre reinforced reactive powder concrete at elevated temperatures. *Mater Struct* 2015;48:2299–314. <https://doi.org/10.1617/s11527-014-0312-9>.
- [107] Tai Y-S, Pan H-H, Kung Y-N. Mechanical properties of steel fiber reinforced reactive powder concrete following exposure to high temperature reaching 800°C. *Nuclear Engineering and Design* 2011;241:2416–24. <https://doi.org/10.1016/j.nucengdes.2011.04.008>.
- [108] Zheng W, Li H, Wang Y. Compressive behaviour of hybrid fiber-reinforced reactive powder concrete after high temperature. *Mater Des* 2012;41:403–9. <https://doi.org/10.1016/j.matdes.2012.05.026>.
- [109] Sanchayan S, Foster SJ. High temperature behaviour of hybrid steel–PVA fibre reinforced reactive powder concrete. *Mater Struct* 2016;49:769–82. <https://doi.org/10.1617/s11527-015-0537-2>.
- [110] Xiong MX, Liew JYR. Mechanical behaviour of ultra-high strength concrete at elevated temperatures and fire resistance of ultra-high strength concrete filled steel tubes. *Mater Des* 2016;104:414–27. <https://doi.org/10.1016/j.matdes.2016.05.050>.
- [111] Abid M, Hou X, Zheng W, Hussain R. Effect of Fibers on High-Temperature Mechanical Behavior and Microstructure of Reactive Powder Concrete. *Materials* 2019;12:329. <https://doi.org/10.3390/ma12020329>.

- [112] Banerji S, Kodur V. Effect of temperature on mechanical properties of ultra-high performance concrete. *Fire Mater* 2022;46:287–301.
- [113] Bošnjak J, Ožbolt J, Hahn R. Permeability measurement on high strength concrete without and with polypropylene fibers at elevated temperatures using a new test setup. *Cem Concr Res* 2013;53:104–11. <https://doi.org/10.1016/j.cemconres.2013.06.005>.
- [114] Li Y, Tan KH, Yang E-H. Influence of aggregate size and inclusion of polypropylene and steel fibers on the hot permeability of ultra-high performance concrete (UHPC) at elevated temperature. *Constr Build Mater* 2018;169:629–37. <https://doi.org/10.1016/j.conbuildmat.2018.01.105>.
- [115] Li Y, Zhang Y, Yang E-H, Hai Tan K. Effects of geometry and fraction of polypropylene fibers on permeability of ultra-high performance concrete after heat exposure 2018. <https://doi.org/10.1016/j.cemconres.2018.11.009>.
- [116] Lyu X, Elchalakani M, Ahmed T, Sadakkathulla MA, Youssf O. Residual strength of steel fibre reinforced rubberised UHPC under elevated temperatures. *Journal of Building Engineering* 2023;76:107173. <https://doi.org/10.1016/j.jobe.2023.107173>.
- [117] Li Y, Yang E-H, Zhou A, Liu T. Pore pressure build-up and explosive spalling in concrete at elevated temperature: A review 2021. <https://doi.org/10.1016/j.conbuildmat.2021.122818>.
- [118] Phan LT. Pore pressure and explosive spalling in concrete. *Materials and Structures/Materiaux et Constructions* 2008;41:1623–32. <https://doi.org/10.1617/s11527-008-9353-2>.
- [119] Mindeguia JC, Carré H, Pimienta P, La Borderie C. Experimental discussion on the mechanisms behind the fire spalling of concrete. *Fire Mater* 2015;39:619–35. <https://doi.org/10.1002/fam.2254>.
- [120] Kodur VKR. Properties of concrete at elevated temperatures. *ISRN Civil Engineering* 2014;2014. <https://doi.org/10.1155/2014/468510>.
- [121] Jansson R, Boström L. The influence of pressure in the pore system on fire spalling of concrete. *Fire Technol* 2010;46:217–30. <https://doi.org/10.1007/s10694-009-0093-9>.
- [122] Ju Y, Liu J, Liu H, Tian K, Ge Z. On the thermal spalling mechanism of reactive powder concrete exposed to high temperature: Numerical and experimental studies 2016. <https://doi.org/10.1016/j.ijheatmasstransfer.2016.03.033>.
- [123] Peng GF, Huang ZS. Change in microstructure of hardened cement paste subjected to elevated temperatures. *Constr Build Mater* 2008;22:593–9. <https://doi.org/10.1016/j.conbuildmat.2006.11.002>.

- [124] Fernandes B, Gil AM, Bolina FL, Tutikian BF. Microstructure of concrete subjected to elevated temperatures: physico-chemical changes and analysis techniques. *Revista IBRACON de Estruturas e Materiais* 2017;10:838–63. <https://doi.org/10.1590/s1983-41952017000400004>.
- [125] Consolazio GR, McVay MC, Rish JW. Measurement and Prediction of Pore Pressure in Cement Mortar Subjected to Elevated Temperature. In: Phan LT, Carino D, Duthiuh E, Garboczi, editors. *Proceedings of the International Workshop on Fire Performance of High-Strength Concrete*, Gaithersburg, MD: NIST; 1997, p. 69–73. <https://doi.org/10.6028/NIST.SP.919>.
- [126] Harmathy TZ. *Effect of Moisture on the Fire Endurance of Building Elements*. vol. 385. Ottawa, Canada: 1965. <https://doi.org/10.4224/40001466>.
- [127] Kannangara T, Joseph P, Fragomeni S, Guerrieri M. Existing theories of concrete spalling and test methods relating to moisture migration patterns upon exposure to elevated temperatures – A review. *Case Studies in Construction Materials* 2022;16. <https://doi.org/10.1016/j.cscm.2022.e01111>.
- [128] Maier M, Zeiml M, Lackner R. On the effect of pore-space properties and water saturation on explosive spalling of fire-loaded concrete. *Constr Build Mater* 2020;231. <https://doi.org/10.1016/j.conbuildmat.2019.117150>.
- [129] Liu JC, Tan KH, Yao Y. A new perspective on nature of fire-induced spalling in concrete. *Constr Build Mater* 2018;184:581–90. <https://doi.org/10.1016/j.conbuildmat.2018.06.204>.
- [130] Dal Pont S, Colina H, Dupas A, Ehrlacher A. An experimental relationship between complete liquid saturation and violent damage in concrete submitted to high temperature. *Magazine of Concrete Research* 2005;57:455–61.
- [131] Ollivier JP, Massat M. Permeability and microstructure of concrete: A review of modelling. *Cem Concr Res* 1992;22:503–14.
- [132] Ko J, Ryu D, Noguchi T. The spalling mechanism of high-strength concrete under fire. *Magazine of Concrete Research* 2011;63:357–70. <https://doi.org/10.1680/macr.10.00002>.
- [133] Debicki G, Haniche R, Delhomme F. An experimental method for assessing the spalling sensitivity of concrete mixture submitted to high temperature. *Cem Concr Compos* 2012;34:958–63. <https://doi.org/10.1016/j.cemconcomp.2012.04.002>.
- [134] Mendes A, Sanjayan JG, Gates WP, Collins F. The influence of water absorption and porosity on the deterioration of cement paste and concrete exposed to elevated temperatures, as in a fire event. *Cem Concr Compos* 2012;34:1067–74. <https://doi.org/10.1016/j.cemconcomp.2012.06.007>.

- [135] Khoury GA. Compressive strength of concrete at high temperatures: a reassessment. *Magazine of Concrete Research* 1992;44. <https://doi.org/10.1680/mac.1992.44.161.291>.
- [136] Zhang D, Liu Y, Hai Tan K. Spalling resistance and mechanical properties of strain-hardening ultra-high performance concrete at elevated temperature 2020. <https://doi.org/10.1016/j.conbuildmat.2020.120961>.
- [137] Ren P, Hou X, Kodur VKR, Ge C, Zhao Y, Zhou W. Modeling the fire response of reactive powder concrete beams with due consideration to explosive spalling. *Constr Build Mater* 2021;301. <https://doi.org/10.1016/j.conbuildmat.2021.124094>.
- [138] Du Y, Qi H-H, Huang S-S, Liew JYR. Experimental study on the spalling behaviour of ultra-high strength concrete in fire n.d. <https://doi.org/10.1016/j.conbuildmat.2020.120334>.
- [139] Kahanji C, Ali F, Nadjai A. Explosive spalling of ultra-high performance fibre reinforced concrete beams under fire. *Journal of Structural Fire Engineering* 2016;7:328–48. <https://doi.org/10.1108/JSFE-12-2016-023>.
- [140] Yang J, Peng GF, Zhao J, Shui GS. On the explosive spalling behavior of ultra-high performance concrete with and without coarse aggregate exposed to high temperature. *Constr Build Mater* 2019;226:932–44. <https://doi.org/10.1016/j.conbuildmat.2019.07.299>.
- [141] Dwaikat MB, Kodur VKR. Response of Restrained Concrete Beams under Design Fire Exposure. *Journal of Structural Engineering* 2009;135:1408–17. <https://doi.org/10.1061/ASCEST.1943-541X.0000058>.
- [142] Kodur VKR, Wang TC, Cheng FP. Predicting the fire resistance behaviour of high strength concrete columns. *Cem Concr Compos* 2004;26:141–53. [https://doi.org/10.1016/S0958-9465\(03\)00089-1](https://doi.org/10.1016/S0958-9465(03)00089-1).
- [143] Lee JH, Sohn YS, Lee SH. Fire resistance of hybrid fibre-reinforced, ultra-high-strength concrete columns with compressive strength from 120 to 200MPa. *Magazine of Concrete Research* 2012;64:539–50. <https://doi.org/10.1680/mac.11.00034>.
- [144] Kalifa P, Chéné G, Gallé C. High-temperature behaviour of HPC with polypropylene fibres From spalling to microstructure. n.d.
- [145] Khaliq W, Kodur V. Effectiveness of Polypropylene and Steel Fibers in Enhancing Fire Resistance of High-Strength Concrete Columns. *Journal of Structural Engineering* 2018;144. [https://doi.org/10.1061/\(asce\)st.1943-541x.0001981](https://doi.org/10.1061/(asce)st.1943-541x.0001981).
- [146] Ozawa M, Subedi Parajuli S, Uchida Y, Zhou B. Preventive effects of polypropylene and jute fibers on spalling of UHPC at high temperatures in combination with waste porous ceramic fine aggregate as an internal curing material. *Constr Build Mater* 2019;206:219–25. <https://doi.org/10.1016/j.conbuildmat.2019.02.056>.

- [147] Li Y, Zhang D. Effect of lateral restraint and inclusion of polypropylene and steel fibers on spalling behavior, pore pressure, and thermal stress in ultra-high-performance concrete (UHPC) at elevated temperature. *Constr Build Mater* 2021;271. <https://doi.org/10.1016/j.conbuildmat.2020.121879>.
- [148] Bangi MR, Horiguchi T. Effect of fibre type and geometry on maximum pore pressures in fibre-reinforced high strength concrete at elevated temperatures. *Cem Concr Res* 2012;42:459–66. <https://doi.org/10.1016/j.cemconres.2011.11.014>.
- [149] Li Y, Pimienta P, Pinoteau N, Tan KH. Effect of aggregate size and inclusion of polypropylene and steel fibers on explosive spalling and pore pressure in ultra-high-performance concrete (UHPC) at elevated temperature. *Cem Concr Compos* 2019;99:62–71. <https://doi.org/10.1016/j.cemconcomp.2019.02.016>.
- [150] Ding Y, Zhang C, Cao M, Zhang Y, Azevedo C. Influence of different fibers on the change of pore pressure of self-consolidating concrete exposed to fire. *Constr Build Mater* 2016;113:456–69. <https://doi.org/10.1016/j.conbuildmat.2016.03.070>.
- [151] Zhang D, Chen B, Wu X, Weng Y, Li Y. Effect of polymer fibers on pore pressure development and explosive spalling of ultra-high performance concrete at elevated temperature. *Archives of Civil and Mechanical Engineering* 2022;22. <https://doi.org/10.1007/s43452-022-00520-7>.
- [152] Ozawa M, Morimoto H. Effects of various fibres on high-temperature spalling in high-performance concrete. *Constr Build Mater* 2014;71:83–92. <https://doi.org/10.1016/j.conbuildmat.2014.07.068>.
- [153] Schneider U, Herbst HJ. Pressure development in heated concrete members. 10th International Conference on Structural Mechanics in Reactor Technology, 1989, p. 113–8.
- [154] Felicetti R, Lo Monte F, Pimienta P. A new test method to study the influence of pore pressure on fracture behaviour of concrete during heating. *Cem Concr Res* 2017;94:13–23. <https://doi.org/10.1016/j.cemconres.2017.01.002>.
- [155] LI Y, ZHANG D, TAN KH. On measuring techniques of pore pressure in concrete at elevated temperature. *Cem Concr Compos* 2020;114. <https://doi.org/10.1016/j.cemconcomp.2020.103737>.
- [156] Banerji S, Gil A, Kodur V. Application of structural health monitoring techniques for tracing fire-induced spalling in concrete structures. SHMII-11: 11th International Conference on Structural Health Monitoring of Intelligent Infrastructure. Paper ID# SHMII-11_T03-13, Montreal, Canada: 2022.
- [157] Choe G, Kim G, Yoon M, Hwang E, Nam J, Guncunski N. Effect of moisture migration and water vapor pressure build-up with the heating rate on concrete spalling type. *Cem Concr Res* 2019;116:1–10. <https://doi.org/10.1016/j.cemconres.2018.10.021>.

- [158] Hou X, Ren P, Rong Q, Zheng W, Zhan Y. Comparative fire behavior of reinforced RPC and NSC simply supported beams. *Eng Struct* 2019;185:122–40. <https://doi.org/10.1016/j.engstruct.2019.01.097>.
- [159] Hou X, Ren P, Rong Q, Zheng W, Zhan Y. Effect of fire insulation on fire resistance of hybrid-fiber reinforced reactive powder concrete beams. *Compos Struct* 2019;209:219–32. <https://doi.org/10.1016/j.compstruct.2018.10.073>.
- [160] Yan K, Qin H, Hu Y, Yang J, Doh J-H, Zhang X. Experimental and numerical studies on the fire resistance of prestressed reactive powder concrete beams. *Structures* 2022;45:1814–32. <https://doi.org/10.1016/j.istruc.2022.10.006>.
- [161] Yang J, Yan K, Doh J-H, Zhang X. Experimental study on shear performance of ultra-high-performance concrete beams at elevated temperatures. *Eng Struct* 2023;291:116304. <https://doi.org/10.1016/j.engstruct.2023.116304>.
- [162] Simwanda L, Kahanji C, Ali F. Numerical modelling, parametric analysis and design of UHPFRC beams exposed to fire. *Structures* 2023;52:1–16. <https://doi.org/10.1016/j.istruc.2023.03.155>.
- [163] Ren P, Hou X, Rong Q, Zheng W. Quantifying Fire Insulation Effects on the Fire Response of Hybrid-Fiber Reinforced Reactive Powder Concrete Beams. *Fire Technol* 2020;56:1487–525. <https://doi.org/10.1007/s10694-019-00937-2>.
- [164] Kodur VKR, Dwaikat M. A numerical model for predicting the fire resistance of reinforced concrete beams. *Cem Concr Compos* 2008;30:431–43. <https://doi.org/10.1016/j.cemconcomp.2007.08.012>.
- [165] Banerji S, Kodur V. Numerical model for tracing the response of Ultra-High performance concrete beams exposed to fire. *Fire Mater* 2023;47:322–40. <https://doi.org/10.1002/fam.3099>.
- [166] Ren P, Hou X, Cui Z, Xie H, Abid M. Fire resistance evaluation and minimum reinforcement ratio for hybrid fibre-reinforced RPC beams under fire exposure. *Journal of Building Engineering* 2021;44:103216. <https://doi.org/10.1016/j.jobbe.2021.103216>.
- [167] Gales J, Chorlton B, Jeanneret C. The Historical Narrative of the Standard Temperature–Time Heating Curve for Structures. *Fire Technol* 2021;57:529–58. <https://doi.org/10.1007/s10694-020-01040-7>.
- [168] ISO 834. Fire resistance tests - Elements of building construction. Geneva, Switzerland, Switzerland: 2014.
- [169] ASTM E119. Standard Test Methods for Fire Tests of Building Construction and Materials. West Conshohocken, PA, USA: 2018. <https://doi.org/10.1520/E0119-18CE01>.

- [170] Eurocode 1. EN 1991-1-2: Actions on structures - Part 1-2: General actions - Actions on structures exposed to fire. Brussels, Belgium: 2002.
- [171] Maraveas C, Vrakas AA. Design of Concrete Tunnel Linings for Fire Safety. *Structural Engineering International* 2014;24:319–29. <https://doi.org/10.2749/101686614X13830790993041>.
- [172] ASTM E1529. Standard Test Methods for Determining Effects of Large Hydrocarbon Pool Fires on Structural Members and Assemblies. West Conshohocken, PA, USA, USA: 2004.
- [173] Babrauskas V, Peacock R. Heat Release Rate: The Single Most Important Variable in Fire Hazard. *Fire Saf J* 1992;18:255–72. [https://doi.org/https://doi.org/10.1016/0379-7112\(92\)90019-9](https://doi.org/10.1016/0379-7112(92)90019-9).
- [174] NFPA. NFPA 502: Standard fo Road Tunnels, Bridges, and Other Limited Access Highways. 2017.
- [175] Wickström U, Duthinh D, Mcgrattan K. Adiabatic surface temperature for calculating heat transfer to fire exposed structures. 2007.
- [176] Takehara K, Imagawa Y, Ohyama O, Kurita A. An actual test and FE analysis of a steel and concrete composite girder bridge exposed to fire. *Steel Construction* 2009;2:72–7. <https://doi.org/10.1002/stco.200910010>.
- [177] Alos-Moya J, Paya-Zaforteza I, Hospitaler A, Rinaudo P. Valencia bridge fire tests: Experimental study of a composite bridge under fire. *J Constr Steel Res* 2017;138:538–54. <https://doi.org/10.1016/j.jcsr.2017.08.008>.
- [178] Beneberu E, Yazdani N. Performance of CFRP-Strengthened Concrete Bridge Girders under Combined Live Load and Hydrocarbon Fire. *Journal of Bridge Engineering* 2018;23. [https://doi.org/10.1061/\(ASCE\)BE.1943-5592.0001244](https://doi.org/10.1061/(ASCE)BE.1943-5592.0001244).
- [179] Liu Z, Li G-Q, Paya-Zaforteza I, Cai CS, Huang Q. Fire Hazards in Bridges: State of the Art, Recent Progress, and Current Research Gaps. *Journal of Bridge Engineering* 2023;28. <https://doi.org/10.1061/JBENF2.BEENG-5790>.
- [180] Hu J, Usmani A, Sanad A, Carvel R. Fire resistance of composite steel & concrete highway bridges. *J Constr Steel Res* 2018;148:707–19. <https://doi.org/10.1016/j.jcsr.2018.06.021>.
- [181] Song C, Zhang G, Li X, Kodur VKR. Experimental and numerical study on failure mechanism of steel-concrete composite bridge girders under fuel fire exposure. *Eng Struct* 2021;247:113230. <https://doi.org/10.1016/j.engstruct.2021.113230>.
- [182] Alos-Moya J, Paya-Zaforteza I, Garlock MEM, Loma-Ossorio E, Schiffner D, Hospitaler A. Analysis of a bridge failure due to fire using computational fluid dynamics and finite element models 2014. <https://doi.org/10.1016/j.engstruct.2014.02.022>.

- [183] Nariman NA. Thermal fluid-structure interaction and coupled thermal-stress analysis in a cable stayed bridge exposed to fire. *Frontiers of Structural and Civil Engineering* 2018;12:609–28. <https://doi.org/10.1007/s11709-018-0452-z>.
- [184] Liu Z, Silva JCG, Huang Q, Hasemi Y, Huang Y, Guo Z. Coupled CFD–FEM Simulation Methodology for Fire-Exposed Bridges. *Journal of Bridge Engineering* 2021;26. [https://doi.org/10.1061/\(ASCE\)BE.1943-5592.0001770](https://doi.org/10.1061/(ASCE)BE.1943-5592.0001770).
- [185] Cui C, Chen A, Ma R. Stability assessment of a suspension bridge considering the tanker fire nearby steel-pylon. *J Constr Steel Res* 2020;172:106186. <https://doi.org/10.1016/j.jcsr.2020.106186>.
- [186] Ma R, Cui C, Ma M, Chen A. Numerical simulation and simplified model of vehicle-induced bridge deck fire in the full-open environment considering wind effect. *Structure and Infrastructure Engineering* 2021;17:1698–709. <https://doi.org/10.1080/15732479.2020.1832535>.
- [187] Choi J, Haj-Ali R, Kim HS. Integrated fire dynamic and thermomechanical modeling of a bridge under fire. *Structural Engineering and Mechanics* 2012;42:815–29. <https://doi.org/10.12989/sem.2012.42.6.815>.
- [188] Gong X, Agrawal AK. Safety of Cable-Supported Bridges during Fire Hazards. *Journal of Bridge Engineering* 2016;21. [https://doi.org/10.1061/\(ASCE\)BE.1943-5592.0000870](https://doi.org/10.1061/(ASCE)BE.1943-5592.0000870).
- [189] Gong X, Agrawal AK. Numerical Simulation of Fire Damage to a Long-Span Truss Bridge. *Journal of Bridge Engineering* 2015;20. [https://doi.org/10.1061/\(ASCE\)BE.1943-5592.0000707](https://doi.org/10.1061/(ASCE)BE.1943-5592.0000707).
- [190] Inoue M, Takai Y, Yanagihara M, Durmaz M, Kara A, Kroon IB. Active protection system for Main cable of suspension bridge against HGV or Hazardous material fires. *IABSE Symposium: Towards a Resilient Built Environment Risk and Asset Management, Guimarães, Portugal: Towards a Resilient Built Environment Risk and Asset Management; 2019, p. 131–7. <https://doi.org/10.2749/guimaraes.2019.0131>*.
- [191] Cerema. *Résistance à l'incendie des ponts routiers*. Sourdun, France: 2018.
- [192] Liu F, Wu B, Wei D. Failure modes of reinforced concrete beams strengthened with carbon fiber sheet in fire. *Fire Saf J* 2009;44:941–50. <https://doi.org/10.1016/j.firesaf.2009.05.006>.
- [193] British Standards. *BS EN 1363-1:2020 - TC Fire resistance tests - General requirements*. Brussels, Belgium: 2020.
- [194] British Standard (BS). *BS476-20 - Fire tests on building materials and structures – Part 20: Method from determination of the fire resistance of elements of construction (general principles)*. London, UK: 1987.

- [195] Beneberu E, Yazdani N. Residual strength of CFRP strengthened prestressed concrete bridge girders after hydrocarbon fire exposure. *Eng Struct* 2019;184:1–14. <https://doi.org/10.1016/j.engstruct.2019.01.057>.
- [196] Wu X-Q, Huang T, Au F, Li J. Posttensioned Concrete Bridge Beams Exposed to Hydrocarbon Fire. *J Struct Eng* 2020;146. [https://doi.org/10.1061/\(ASCE\)ST.1943](https://doi.org/10.1061/(ASCE)ST.1943).
- [197] Song C, Zhang G, Lu Z, Li X, Zhao X. Fire resistance tests on polypropylene-fiber-reinforced prestressed concrete box bridge girders. *Eng Struct* 2023;282:115800. <https://doi.org/10.1016/j.engstruct.2023.115800>.
- [198] Zhang G, Kodur VKR, Xie J, He S, Hou W. Behavior of prestressed concrete box bridge girders under hydrocarbon fire condition. *Procedia Eng*, vol. 210, Elsevier Ltd; 2017, p. 449–55. <https://doi.org/10.1016/j.proeng.2017.11.100>.
- [199] Zhang G, Kodur VKR, Hou W, He S. Evaluating fire resistance of prestressed concrete bridge girders. *Structural Engineering and Mechanics* 2017;62:663–74. <https://doi.org/10.12989/sem.2017.62.6.663>.
- [200] Song C, Zhang G, Hou W, He S. Performance of prestressed concrete box bridge girders under hydrocarbon fire exposure. *Advances in Structural Engineering* 2020;23:1521–33. <https://doi.org/10.1177/1369433219898102>.
- [201] Wu X, Huang T, Au FTK, Li J. A Localized Fire Model for Predicting the Surface Temperature of Box Girder Bridges Subjected to Tanker Truck Fire. *Fire Technol* 2020;56:2059–87. <https://doi.org/10.1007/s10694-020-00966-2>.
- [202] Timilsina S, Yazdani N, Beneberu E. Post-fire analysis and numerical modeling of a fire-damaged concrete bridge. *Eng Struct* 2021;244:112764. <https://doi.org/10.1016/j.engstruct.2021.112764>.
- [203] Bhatt PP. Fire performance of FRP-strengthened concrete flexural members. Doctoral Dissertation. Michigan State University, 2021.
- [204] Banerji S. Behavior of ultra-high performance concrete beams under fire conditions. Doctoral Dissertation. Michigan State University, 2021.
- [205] JSCE. JSCE-SF6-1990 - Method of test for shear strength of steel fiber reinforced concrete. Yotsuya, Shinjuku, Tokyo: 1990.
- [206] Mirsayah AA, Banthia N. Shear Strength of Steel Fiber-Reinforced Concrete. *ACI Mater J* 2002;99:473–9.
- [207] Zhang D, Zhang Y, Dasari A, Tan KH, Weng Y. Effect of spatial distribution of polymer fibers on preventing spalling of UHPC at high temperatures. *Cem Concr Res* 2021;140. <https://doi.org/10.1016/j.cemconres.2020.106281>.

- [208] Gil A, Kodur V. Effect of Temperature on the Shear Strength of Ultra-High Performance Concrete. Third International Interactive Symposium on Ultra-High Performance Concrete, Iowa State University Digital Press; 2023. <https://doi.org/10.21838/uhpc.16639>.
- [209] Kodur VKR, Phan L. Critical factors governing the fire performance of high strength concrete systems. *Fire Saf J* 2007;42:482–8. <https://doi.org/10.1016/j.firesaf.2006.10.006>.
- [210] Payá-Zaforteza I, Garlock MEM. A numerical investigation on the fire response of a steel girder bridge 2012. <https://doi.org/10.1016/j.jcsr.2012.03.012>.
- [211] Aziz EM. Response of fire exposed steel bridge girders. Doctoral dissertation. Michigan State University, 2015.
- [212] Simulia. Abaqus/CAE User's Guide 2023.
- [213] Gil A, Kodur V. Evaluating Shear Response of UHPC Bridge Girders Exposed to Fire. *Fire Technol* 2023. <https://doi.org/10.1007/s10694-023-01506-4>.
- [214] Eurocode 3. EN 1993-1-2: Design of steel structures - Part 1-2: General rules - Structural fire design. Brussels, Belgium: 2005.
- [215] McGrattan KB, Hostikka S, Floyd J, McDermott R, Vanella M, Mueller E. Fire Dynamics Simulator User's Guide. Gaithersburg, MD: 2024. <https://doi.org/10.6028/NIST.SP.1019>.
- [216] Kmieciak P, Kamiński M. Modelling of reinforced concrete structures and composite structures with concrete strength degradation taken into consideration. vol. XI. 2011.
- [217] Nasrin S, Ibrahim A. Finite-element modeling of UHPC hybrid bridge deck connections. *International Journal of Advanced Structural Engineering* 2018;10:199–210. <https://doi.org/10.1007/s40091-018-0192-2>.
- [218] Liang X, Wu C, Su Y, Chen Z, Li Z. Development of ultra-high performance concrete with high fire resistance. *Constr Build Mater* 2018;179:400–12. <https://doi.org/10.1016/j.conbuildmat.2018.05.241>.
- [219] Liu J-C, Du L-P, Yao Y, Beaucour A-L, Wang J-Q, Zhao X-Y. A close look at fire-induced explosive spalling of ultra-high performance concrete: from materials to structures. *Archives of Civil and Mechanical Engineering* 2024;24:124. <https://doi.org/10.1007/s43452-024-00942-5>.
- [220] Kodur VKR, Gil AM, Naser MZ. Fire-induced collapse of an I-95 overpass in Philadelphia: Causes, collapse mechanism, and mitigation strategies. *Eng Struct* 2024;303:117578. <https://doi.org/10.1016/j.engstruct.2024.117578>.
- [221] Fox 29 Philadelphia. I-95 collapse: Surveillance video captures tanker crash, fire in Northeast Philadelphia. Fox 29 Philadelphia 2023.

- [222] Mitman H. Surveillance video shows crash, explosion that triggered I-95 collapse. NBR Philadelphia 2023.
- [223] Arancio V, Jacobo J, Margolin J, Foster M. I-95 collapse updates: 1 vehicle trapped under the highway, no one injured, governor says. Abc News 2023.
- [224] Jackson S. “I have no idea what is on fire”: Dispatch audio reveals moments before I-95 collapse in Philly. 6 Abc 2023.
- [225] Aziz EM. Response of fire exposed steel bridge girders. Doctoral Dissertation. Michigan State University, 2015.
- [226] Kodur VKR, Naser MZ. Designing steel bridges for fire safety. *J Constr Steel Res* 2019;156:46–53. <https://doi.org/10.1016/j.jcsr.2019.01.020>.
- [227] Kodur VKR, Gil A. Enhancing fire resistance of steel bridges through composite action. *Steel and Composite Structures* 2022;43:353–62. <https://doi.org/https://doi.org/10.12989/scs.2022.43.3.353>.
- [228] Lie TT. *Structural Fire Protection: Manual of Practice*. American Society of Civil Engineers; 1992.
- [229] Astaneh-Asl A, Noble CR, Son J, Wemhoff AP, Thomas MP, McMichael LD. *Fire Protection of Steel Bridges and the Case of the MacArthur Maze Fire Collapse*. TCLEE 2009, Reston, VA: American Society of Civil Engineers; 2009, p. 1–12. [https://doi.org/10.1061/41050\(357\)69](https://doi.org/10.1061/41050(357)69).
- [230] Kodur VKR, Shakya AM. Effect of temperature on thermal properties of spray applied fire resistive materials. *Fire Saf J* 2013;61:314–23. <https://doi.org/10.1016/j.firesaf.2013.09.011>.
- [231] Faber TE. *Fluid Dynamics for Physicists*. Cambridge University Press; 1995. <https://doi.org/10.1017/CBO9780511806735>.
- [232] Dwaikat MB, Kodur VKR. Fire Induced Spalling in High Strength Concrete Beams. *Fire Technol* 2010;46:251–74. <https://doi.org/10.1007/s10694-009-0088-6>.
- [233] Jeyashree TM, Kannan Rajkumar PR, Satyanarayanan KS. Developments and research on fire response behaviour of prestressed concrete members – A review. *Journal of Building Engineering* 2022;57:104797. <https://doi.org/10.1016/j.job.2022.104797>.
- [234] Kodur V, Mcgrath R. Fire Endurance of High Strength Concrete Columns. *Fire Technol* 2003;39:73–87. <https://doi.org/10.1023/A:1021731327822>.

- [235] Kodur VKR, Cheng F-P, Wang T-C, Sultan MA. Effect of Strength and Fiber Reinforcement on Fire Resistance of High-Strength Concrete Columns. *Journal of Structural Engineering* 2003;129:253–9. <https://doi.org/10.1061/ASCE0733-94452003129:2253>.
- [236] Zhang D, Dasari A, Tan KH. On the mechanism of prevention of explosive spalling in ultra-high performance concrete with polymer fibers. *Cem Concr Res* 2018;113:169–77. <https://doi.org/10.1016/j.cemconres.2018.08.012>.
- [237] Zhu Y, Hussein H, Kumar A, Chen G. A review: Material and structural properties of UHPC at elevated temperatures or fire conditions. *Cem Concr Compos* 2021;123:104212. <https://doi.org/10.1016/j.cemconcomp.2021.104212>.
- [238] Ridha MMS. Combined effect of natural fibre and steel fibre on the thermal-mechanical properties of UHPC subjected to high temperature. *Cem Concr Res* 2024;180:107510. <https://doi.org/10.1016/j.cemconres.2024.107510>.
- [239] Khan M, Lao J, Ahmad MR, Dai J-G. Influence of high temperatures on the mechanical and microstructural properties of hybrid steel-basalt fibers based ultra-high-performance concrete (UHPC). *Constr Build Mater* 2024;411:134387. <https://doi.org/10.1016/j.conbuildmat.2023.134387>.
- [240] Kodur VKR, McGrath R. Effect of silica fume and lateral confinement on fire endurance of high strength concrete columns. *Canadian Journal of Civil Engineering* 2006;33:93–102. <https://doi.org/10.1139/105-089>.
- [241] Kodur VR, Sultan MA. Thermal properties of high strength concrete at elevated temperatures. 1998.
- [242] Babrauskas V. Heat Release Rates. *SFPE Handbook of Fire Protection Engineering*, New York, NY: Springer New York; 2016, p. 799–904. https://doi.org/10.1007/978-1-4939-2565-0_26.

APPENDIX A – TEMPERATURE-DEPENDENT MATERIAL MODELS

This appendix presents details on the material models adopted to account for temperature-induced degradation of thermal and mechanical properties of steel and concrete. Thermal properties include thermal conductivity, specific heat, and thermal expansion, while mechanical properties include elastic modulus, tensile and compressive strength. These properties have been determined for reinforcing and prestressing steel, as well as for normal-strength concrete (NSC), high-strength concrete (HSC), and ultra-high performance concrete (UHPC), based on design codes and experimental studies available in the literature as presented herein.

A.1. Reinforcing Steel

Thermal properties of reinforcing steel have been derived from Eurocode 3 [214] relations. Equations (A.1), (A.2), and (A.3) are used to determine thermal conductivity (λ_s , in W/mK), specific heat (c_s , in J/kgK), and thermal strain (ε_s) of steel as a function of temperature (T , in °C).

$$\lambda_s = \begin{cases} 54 - 3.33 \times 10^{-2}T, & 20^\circ\text{C} \leq T < 800^\circ\text{C} \\ 27.3, & 800^\circ\text{C} \leq T < 1200^\circ\text{C} \end{cases} \quad (\text{A.1})$$

$$c_s = \begin{cases} 425 - 7.73 \times 10^{-1}T - 1.69 \times 10^{-3}T^2 + 2.22 \times 10^{-6}T^3, & 20^\circ\text{C} \leq T < 600^\circ\text{C} \\ 666 + \frac{13002}{738 - T}, & 600^\circ\text{C} \leq T < 735^\circ\text{C} \\ 545 + \frac{17820}{T - 731}, & 735^\circ\text{C} \leq T < 900^\circ\text{C} \\ 650, & 900^\circ\text{C} \leq T \leq 1200^\circ\text{C} \end{cases} \quad (\text{A.2})$$

$$\varepsilon_s = \begin{cases} -2.416 \times 10^{-4} + 1.2 \times 10^{-5}T + 0.4 \times 10^{-8}T^2, & 20^\circ\text{C} \leq T \leq 750^\circ\text{C} \\ 11 \times 10^{-3}, & 750^\circ\text{C} < T \leq 860^\circ\text{C} \\ -6.2 \times 10^{-3} + 2 \times 10^{-5}T, & 860^\circ\text{C} < T \leq 1200^\circ\text{C} \end{cases} \quad (\text{A.3})$$

Stress-strain curves of reinforcing steel have been derived from Eurocode 2 [96] relations. The stress for each strain range in Figure A.1 can be calculated through Equation (A.4), using the

parameters in Equations (A.5), (A.6), and (A.7). The code prescribes the strain levels for all levels of temperature: $\varepsilon_{sy,T} = 0.02$, $\varepsilon_{st,T} = 0.15$, and $\varepsilon_{su,T} = 0.20$. The effect of temperature is accounted through a stress reduction parameter prescribed for steel yielding stress (f_y), ultimate stress (f_u), and elastic modulus (E_s), as shown in Table A.1.

$$\sigma_{s,T} = \begin{cases} \varepsilon E_{s,T}, & \varepsilon_{sp,T} = f_{sp,T}/E_{s,T} \\ f_{sp,T} - c + (b/a) \left[a^2 - (\varepsilon_{sy,T} - \varepsilon)^2 \right]^{0.5}, & \varepsilon_{sp,T} < \varepsilon \leq \varepsilon_{sy,T} \\ f_{sy,T}, & \varepsilon_{sy,T} < \varepsilon \leq \varepsilon_{st,T} \\ f_{sy,T} \left[1 - (\varepsilon - \varepsilon_{st,T}) / (\varepsilon_{su,T} - \varepsilon_{st,T}) \right], & \varepsilon_{st,T} < \varepsilon \leq \varepsilon_{su,T} \\ 0, & \varepsilon = \varepsilon_{su,T} \end{cases} \quad (\text{A.4})$$

$$a^2 = (\varepsilon_{sy,T} - \varepsilon_{sp,T})(\varepsilon_{sy,T} - \varepsilon_{sp,T} + c/E_{s,T}) \quad (\text{A.5})$$

$$b^2 = c(\varepsilon_{sy,T} - \varepsilon_{sp,T})E_{s,T} + c^2 \quad (\text{A.6})$$

$$c = \frac{(f_{sy,T} - f_{sp,T})^2}{(\varepsilon_{sy,T} - \varepsilon_{sp,T})E_{s,T} - 2(f_{sy,T} - f_{sp,T})} \quad (\text{A.7})$$

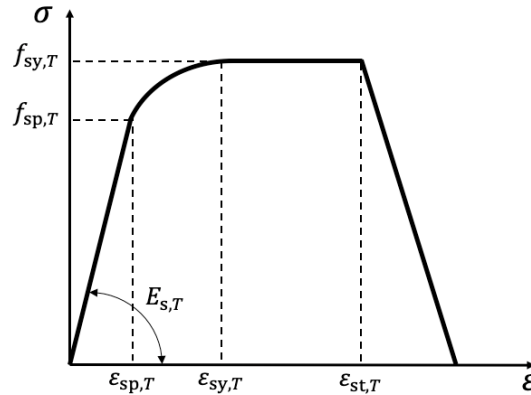


Figure A.1: Stress-strain relation for reinforcing and prestressing steel at elevated temperatures

Table A.1: Strength reduction parameters for reinforcing steel bars based on Eurocode 2 [96]

Temperature (°C)	$f_{y,T}/f_y$	$f_{u,T}/f_u$	$E_{s,T}/E_s$
20	1.00	1.00	1.00
100	1.00	1.00	1.00
200	1.00	0.81	0.90
300	1.00	0.61	0.80
400	1.00	0.42	0.70
500	0.78	0.36	0.60
600	0.47	0.18	0.31
700	0.23	0.08	0.13
800	0.11	0.05	0.09
900	0.06	0.04	0.07
1000	0.04	0.03	0.05
1100	0.02	0.01	0.02

A.2. Prestressing Steel

According to Eurocode 3 [214], the relations from equations (A.1) and (A.2) for thermal conductivity (λ_s , in W/mK) and specific heat (c_s , in J/kgK) can be also be applied for prestressing steel. The code, however, proposes the relation in Equation (A.8) for thermal strain (ε_s) of prestressing steel as a function of temperature (T , in °C).

$$\varepsilon_s = \{-2.016 \times 10^{-4} + 10^{-5}T + 0.4 \times 10^{-8}T^2, \quad 20^\circ\text{C} \leq T \leq 1200^\circ\text{C} \quad (\text{A.8})$$

As for the mechanical properties, Eurocode 2 [96] states that the same formulations used for reinforcing steel can be applied to determine the stress-strain response of prestressing steel. However, the strength reduction parameters for prestressing steel presented in Table A.2 have been adopted for developing the stress-strain curves.

Table A.2: Strength reduction parameters for prestressing steel wires based on Eurocode 2 [96]

Temperature (°C)	$f_{py,T}/f_{py}$	$f_{pp,T}/f_{pp}$	$E_{p,T}/E_p$	$\epsilon_{p,T}$	$\epsilon_{pu,T}$
20	1.00	1.00	1.00	0.050	0.100
100	1.00	0.68	0.98	0.050	0.100
200	0.87	0.51	0.95	0.050	0.100
300	0.70	0.32	0.88	0.055	0.105
400	0.50	0.13	0.81	0.060	0.110
500	0.30	0.07	0.54	0.065	0.115
600	0.14	0.05	0.41	0.070	0.120
700	0.06	0.03	0.10	0.075	0.125
800	0.04	0.02	0.07	0.080	0.130
900	0.02	0.01	0.03	0.085	0.135
1000	0.00	0.00	0.00	0.090	0.140

A.3. Normal-Strength Concrete

Thermal properties of NSC have been derived from Eurocode 2 [96] relations. Equations (A.9), (A.10), and (A.11) are used to determine thermal conductivity (λ_{NSC} , in W/mK), specific heat (c_{NSC} , in J/kgK), and thermal strain (ϵ_{NSC}) of NSC as a function of temperature (T , in °C), considering calcareous aggregates and the lower limit specified in the code.

$$\lambda_{NSC} = \{1.36 - 0.136(T/100) + 0.0057(T/100)^2, \quad 20^\circ C \leq T < 1200^\circ C \quad (A.9)$$

$$c_{NSC} = \begin{cases} 900, & 20^\circ C \leq T \leq 100^\circ C \\ 900 + (T - 100), & 100^\circ C < T \leq 200^\circ C \\ 1000 + (T - 200)/2, & 200^\circ C < T \leq 400^\circ C \\ 1100, & 400^\circ C < T \leq 1200^\circ C \end{cases} \quad (A.10)$$

$$\epsilon_{NSC} = \begin{cases} -1.2 \times 10^{-4} + 6 \times 10^{-6}T + 1.4 \times 10^{-11}T^3, & 20^\circ C \leq T \leq 805^\circ C \\ 12 \times 10^{-3}, & 805^\circ C \leq T \leq 1200^\circ C \end{cases} \quad (A.11)$$

The stress-strain formulation prescribed by Eurocode 2 [96] has been adopted to describe the compression behavior of NSC at elevated temperatures through Equation (A.12), as illustrated

in Figure A.2. Table A.3 presents the strength reduction parameters adopted in the model, considering carbonate aggregate.

$$\sigma_{c,T} = \begin{cases} \frac{3\varepsilon f_{c,T}}{\varepsilon_{c1,T} \left(2 + (\varepsilon/\varepsilon_{c1,T})^3\right)}, & \varepsilon < \varepsilon_{c1,T} \\ \text{Linear descending branch,} & \varepsilon_{c1,T} < \varepsilon \leq \varepsilon_{cu1,T} \end{cases} \quad (\text{A.12})$$

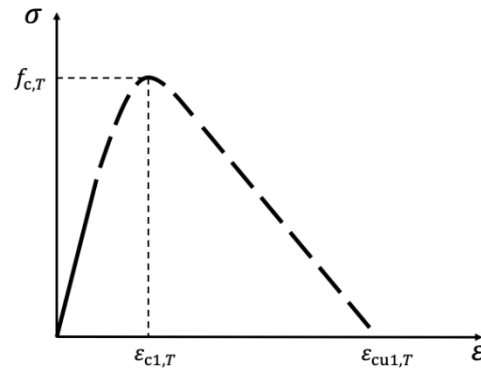


Figure A.2: Stress-strain relation for NSC and HSC at elevated temperatures

Table A.3: Strength reduction parameters for NSC based on Eurocode 2 [96]

Temperature (°C)	$f_{c,T}/f_c$	$\varepsilon_{c1,T}$	$\varepsilon_{cu1,T}$
20	1.00	0.0025	0.0200
100	1.00	0.0040	0.0225
200	0.97	0.0055	0.0250
300	0.91	0.0070	0.0275
400	0.85	0.0100	0.0300
500	0.74	0.0150	0.0325
600	0.60	0.0250	0.0350
700	0.43	0.0250	0.0375
800	0.27	0.0250	0.0400
900	0.15	0.0250	0.0425
1000	0.06	0.0250	0.0450
1100	0.02	0.0250	0.0475

A.4. High-Strength Concrete

Thermal properties of HSC have been derived from the relations established by Kodur and Sultan [241] based on experimental tests conducted by the authors. Equations (A.13), (A.14), and (A.15) are used to determine thermal conductivity (λ_{HSC} , in W/mK), specific heat (c_{HSC} , in J/kgK), and thermal strain (ε_{HSC}) of HSC as a function of temperature (T , in °C) and density (ρ , in kg/m³), considering the concrete is made with calcareous aggregates.

$$\lambda_{HSC} = \begin{cases} 2.00 - 0.0013T, & 20^\circ\text{C} \leq T \leq 300^\circ\text{C} \\ 2.21 - 0.0020T, & 300^\circ\text{C} < T \leq 1000^\circ\text{C} \end{cases} \quad (\text{A.13})$$

$$c_{HSC} = \begin{cases} 2.45 \times 10^{-6}/\rho, & 20^\circ\text{C} \leq T \leq 400^\circ\text{C} \\ (0.0260T - 12.850) \times 10^{-6}/\rho, & 400^\circ\text{C} < T \leq 475^\circ\text{C} \\ (0.0143T - 6.295) \times 10^{-6}/\rho, & 475^\circ\text{C} < T \leq 650^\circ\text{C} \\ (0.1894T - 120.11) \times 10^{-6}/\rho, & 650^\circ\text{C} < T \leq 735^\circ\text{C} \\ (-0.2630T + 212.40) \times 10^{-6}/\rho, & 735^\circ\text{C} < T \leq 800^\circ\text{C} \\ 2.00 \times 10^{-6}/\rho, & 800^\circ\text{C} < T \leq 1000^\circ\text{C} \end{cases} \quad (\text{A.14})$$

$$\varepsilon_{HSC} = \begin{cases} -0.0002 + 0.000008T, & 20^\circ\text{C} \leq T \leq 450^\circ\text{C} \\ -0.0061 + 0.000021T, & 450^\circ\text{C} < T \leq 920^\circ\text{C} \\ 0.0242 - 0.000012T, & 920^\circ\text{C} < T \leq 1000^\circ\text{C} \end{cases} \quad (\text{A.15})$$

As for the mechanical properties, the same formulations used for NSC were applied to determine the stress-strain response of HSC. This is based on the fact that both materials present similar levels of strain when exposed to elevated temperatures.

A.5. Ultra-High Performance Concrete

Since thermal and mechanical properties of UHPC at elevated temperatures have not been incorporated to any design codes yet, relations derived from experimental tests have been adopted. Relations for UHPC thermal properties derived by Kodur et al. [104] are presented in (A.16),

(A.17), and (A.18) for thermal conductivity (λ_{UHPC} , in W/m°C), specific heat (c_{UHPC} , in MJ/m³°C), and thermal strain (ε_{UHPC}) of UHPC, respectively, as a function of temperature (T , in °C).

$$\lambda_{UHPC} = \begin{cases} -0.0092T + 3.1136, & 20^\circ C \leq T \leq 100^\circ C \\ -0.0035T + 2.5802, & 100^\circ C < T \leq 400^\circ C \\ 0.0021T - 0.3481, & 400^\circ C < T \leq 500^\circ C \\ -10^{-5}T^2 + 0.0111T - 1.6565, & 500^\circ C < T \leq 700^\circ C \end{cases} \quad (A.16)$$

$$c_{UHPC} = \begin{cases} 2 \times 10^{-6}T^2 + 0.0013T + 1.6918, & 20^\circ C \leq T \leq 300^\circ C \\ -0.0046T + 3.6677, & 300^\circ C < T \leq 400^\circ C \\ 0.0054T - 0.3217, & 400^\circ C < T \leq 600^\circ C \\ 0.0006T + 2.5588, & 600^\circ C < T \leq 700^\circ C \end{cases} \quad (A.17)$$

$$\varepsilon_{UHPC} = \begin{cases} 2 \times 10^{-6}T^2 + 0.0002T + 0.0014, & 20^\circ C \leq T \leq 600^\circ C \\ -1.443 \times 10^{-5}T^2 + 0.0188T - 5.2031, & 600^\circ C \leq T \leq 800^\circ C \\ 0.0037T - 2.342, & 800^\circ C \leq T \leq 900^\circ C \end{cases} \quad (A.18)$$

For the mechanical properties of UHPC, the relations proposed by Banerji and Kodur [112] based on their experimental tests have been adopted.

APPENDIX B – MESH SENSITIVITY ANALYSIS

Mesh sensitivity analysis in finite element models is important to ensure the accuracy and reliability of simulation results. This analysis involves refining the mesh to observe how changes in mesh size impact the model's outcomes, such as temperature or deflection. As the mesh becomes finer, the numerical approximation of the solution should converge towards a stable value, allowing the identification of an optimal mesh density that balances computational efficiency with solution accuracy. In this study, mesh sensitivity analysis was made with consideration to both thermal and structural response.

B.1. Thermal Response

In the thermal analysis, temperatures are usually constant through a certain length of the member and for that reason the mesh sensitivity analysis for the thermal response can be simplified to the girder cross-section. In concrete bridge girders, prestressing strands are spaced at 50 mm from each other and from the girder contour. Thus, this value is taken as the minimum mesh size in the girder cross-section. A second mesh size of 25 mm was implemented to refine the mesh and verify its effect on the thermal response of girders with different cross-sectional sizes.

Figure B.1 presents the temperatures at the concrete cover region of the bottom flange of AASHTO Types I through IV cross-sections, considering a mesh size of 25 and 50 mm. It can be seen that the temperatures predicted by the model are very similar in both situations for a fire exposure time up to 240 min. Table B.1 presents the temperatures measured in different locations within the girder considering the two mesh sizes, including at two strand locations, at the center of both flanges and in the middle of the web. Overall, it can be seen that there is very little variation in the temperatures predicted with these two mesh sizes (less than 1% for most situations).

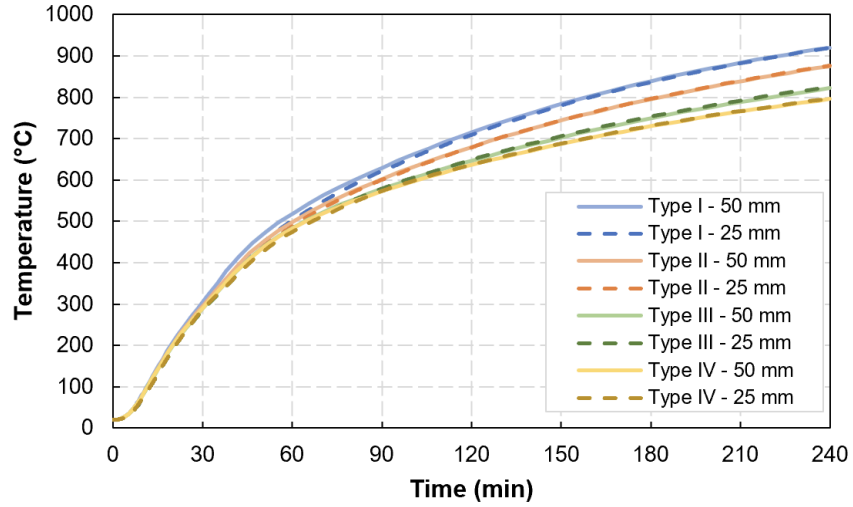


Figure B.1: Concrete cover temperature for different girder sizes considering two mesh sizes

Table B.1: Variation of temperature in different locations within girders' cross-section

Girder section	Mesh size (mm)	Temperature (°C)				
		Corner strand	Center strand	Bottom flange	Web	Top flange
Type I	50	1037.7	920.2	792.8	1018.9	749.7
	25	1033.9	919.6	791.3	1016.6	744.5
	Variation	0.368%	0.070%	0.188%	0.227%	0.707%
Type II	50	1014.9	875.2	683.4	1028.1	768.4
	25	1020.2	876.2	679.1	1027.1	763.2
	Variation	-0.515%	-0.116%	0.629%	0.097%	0.690%
Type III	50	1011.1	822.0	535.8	962.4	579.5
	25	1008.5	825.4	535.5	964.0	580.3
	Variation	0.258%	-0.421%	0.044%	-0.174%	-0.129%
Type IV	50	997.1	795.5	422.7	881.8	438.1
	25	1001.8	796.9	416.3	883.1	433.7
	Variation	-0.476%	-0.172%	1.524%	-0.151%	1.028%

B.1. Structural Response

The mesh sensitivity analysis on the structural response of the member was evaluated by comparing the progression of midspan deflections during fire exposure of four girder types (AASHTO Types I through IV). The analysis was conducted on the longitudinal side of the girder, considering a cross-sectional mesh size of 50 mm, as defined through the thermal analysis. To maintain an appropriate element aspect ratio, the maximum mesh size for the girder in the longitudinal direction was set at 125 mm. A more refined mesh was created by reducing the mesh size to 62.5 mm.

Figure B.2 shows the progression of midspan deflections as a function of fire exposure time for the UHPC girders with four cross-sectional types exposed to the hydrocarbon fire curve, using a mesh size of 50 mm in the transverse direction and two mesh sizes (125 mm and 62.5 mm) in the longitudinal direction. Table B.2 presents the variation of measured deflections at different fire exposure times (30, 60, 90, 120, and 150 minutes). Overall, there is very little variation in midspan deflections with mesh refinement. Therefore, to save computational time, the coarser mesh size was selected for all analyses carried out in this research.

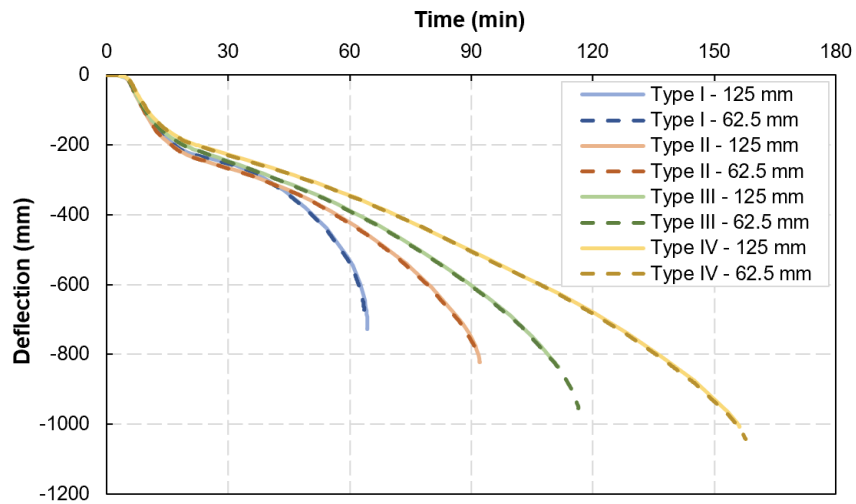


Figure B.2: Midspan deflections for different girder sizes considering two mesh sizes

Table B.2: Variation in midspan deflections at different fire exposure times based on mesh size

Girder section	Mesh size (mm)	Midspan deflection (mm)				
		30 min	60 min	90 min	120 min	150 min
Type I	125	-252.6	-530.7	-	-	-
	62.5	-253.8	-537.4	-	-	-
	<i>Variation</i>	<i>-0.452%</i>	<i>-1.247%</i>	<i>-</i>	<i>-</i>	<i>-</i>
Type II	125	-266.6	-422.9	-751.2	-	-
	62.5	-267.8	-425.4	-761.5	-	-
	<i>Variation</i>	<i>-0.438%</i>	<i>-0.584%</i>	<i>-1.343%</i>	<i>-</i>	<i>-</i>
Type III	125	-246.4	-388.3	-602.8	-	-
	62.5	-247.7	-388.9	-599.1	-	-
	<i>Variation</i>	<i>-0.543%</i>	<i>-0.154%</i>	<i>0.615%</i>	<i>-</i>	<i>-</i>
Type IV	125	-228.3	-345.3	-503.3	-679.6	-928.5
	62.5	-229.2	-345.9	-504.7	-682.9	-934.0
	<i>Variation</i>	<i>-0.414%</i>	<i>-0.170%</i>	<i>-0.275%</i>	<i>-0.484%</i>	<i>-0.590%</i>

APPENDIX C – FIRE DYNAMICS SIMULATIONS RESULTS

This appendix presents all the results obtained in the Fire Dynamics Simulator (FDS) modeled using the commercial software PyroSim. In total, eight simulations were performed to evaluate the influence of three main parameters: bridge span (which is related to the girder size and spacing), clearance height and fire intensity (in terms of burning area). Table C.1 presents the varying parameters evaluated in each simulation. The adiabatic surface temperatures (AST) measured in different points throughout the model during 60 minutes of fire exposure, as described in Section 4.3.4, are presented in Figures C.1 to C.8.

Table C.1: Varying parameters evaluated in each simulation

Simulation	Girder depth (mm)	Girder spacing (m)	Bridge length (m)	Bridge height (m)	Spillage area (m ²)
1	700	1.5	12	5	30
2	700	1.5	12	5	80
3	1,400	3.0	24	5	30
4	1,400	3.0	24	5	80
5	700	1.5	12	8	30
6	700	1.5	12	8	80
7	1,400	3.0	24	8	30
8	1,400	3.0	24	8	80

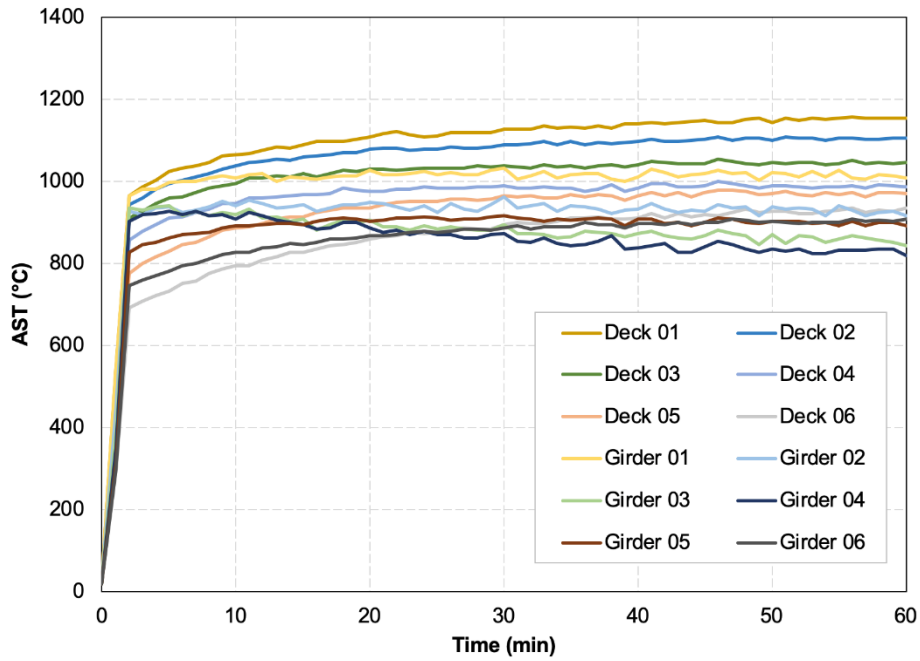


Figure C.1: Adiabatic surface temperature as a function of fire exposure time in Simulation 1

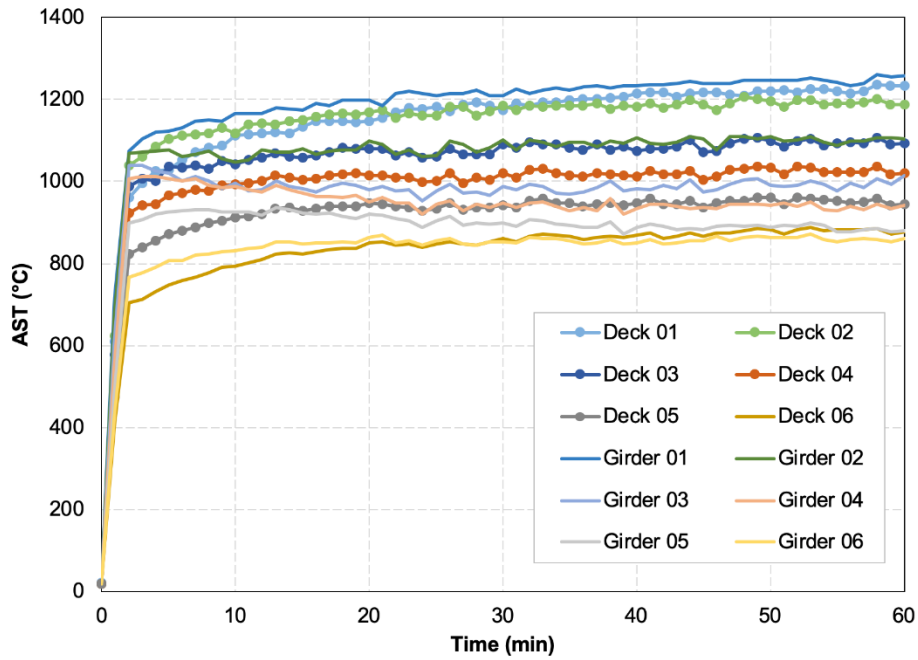


Figure C.2: Adiabatic surface temperature as a function of fire exposure time in Simulation 2

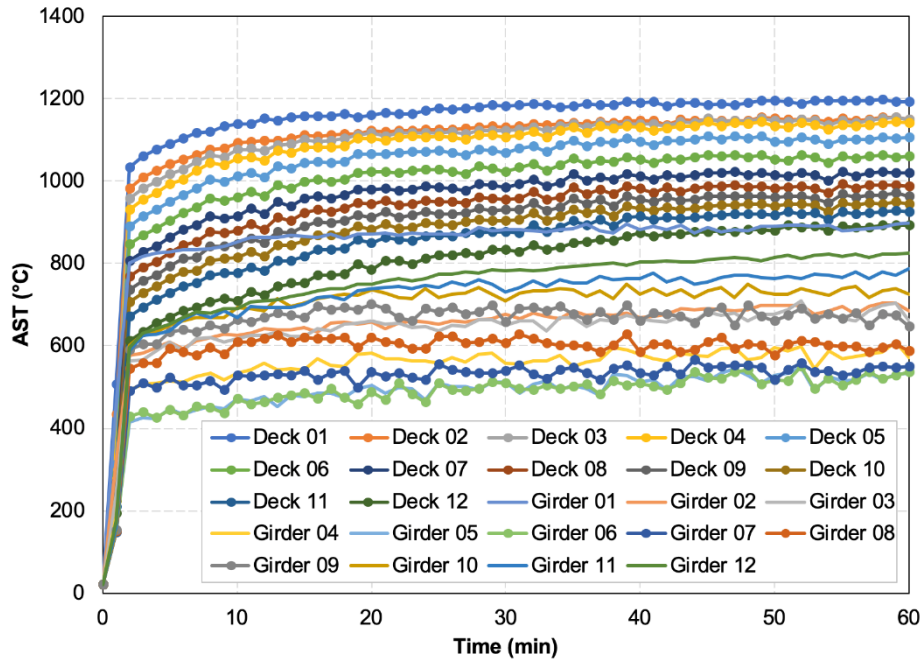


Figure C.3: Adiabatic surface temperature as a function of fire exposure time in Simulation 3

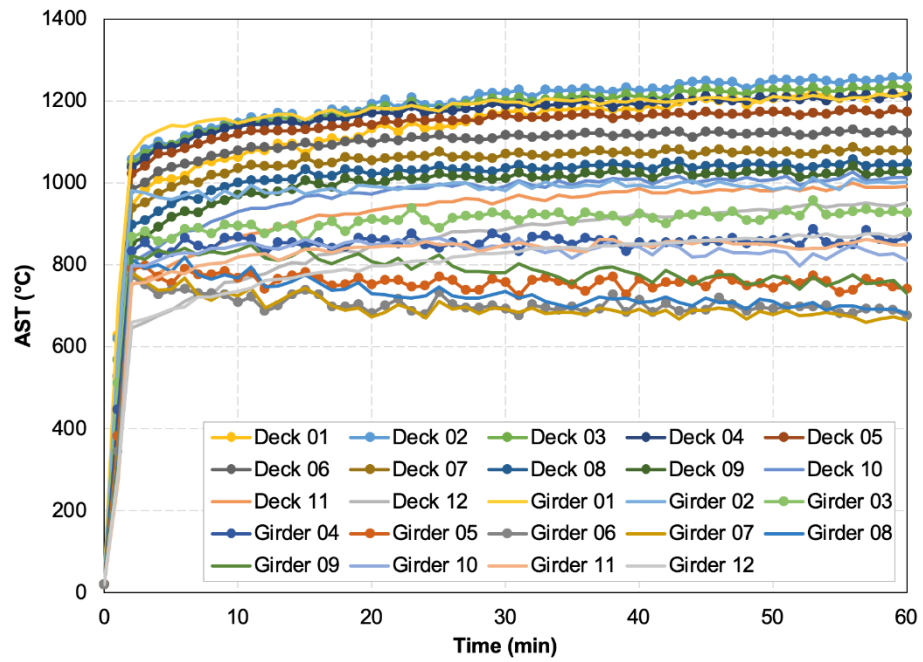


Figure C.4: Adiabatic surface temperature as a function of fire exposure time in Simulation 4

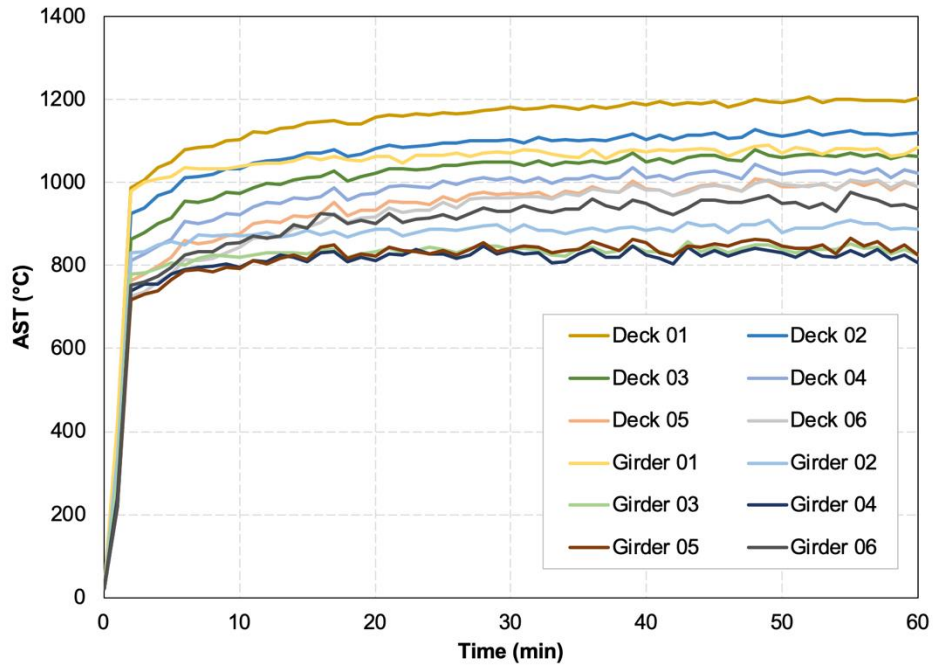


Figure C.5: Adiabatic surface temperature as a function of fire exposure time in Simulation 5

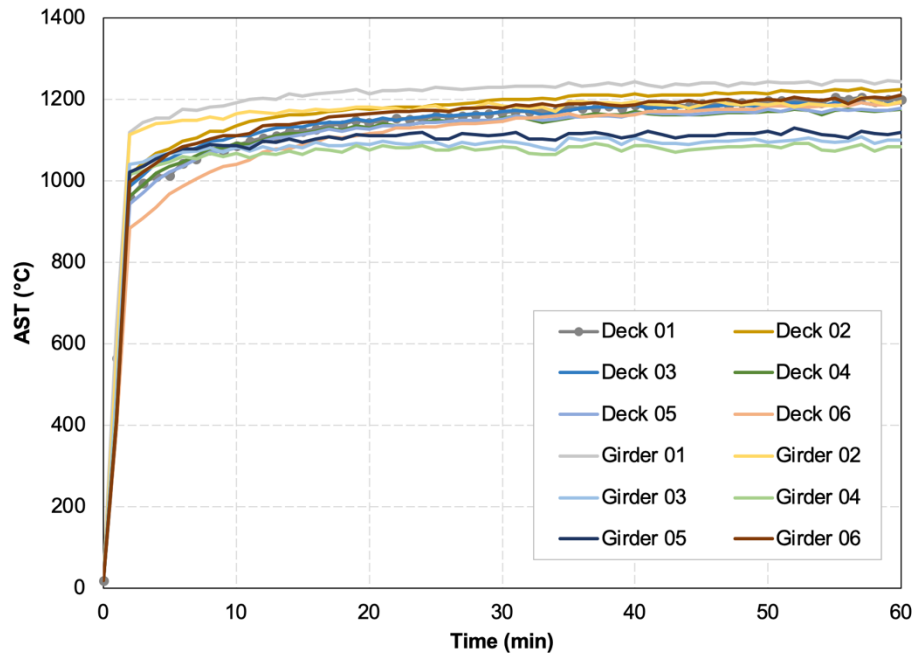


Figure C.6: Adiabatic surface temperature as a function of fire exposure time in Simulation 6

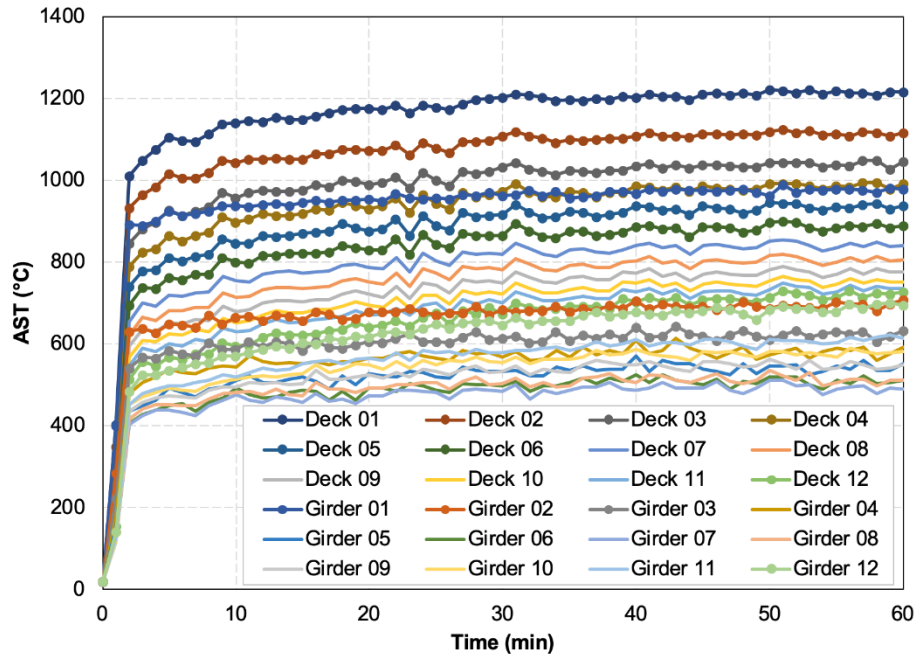


Figure C.7: Adiabatic surface temperature as a function of fire exposure time in Simulation 7

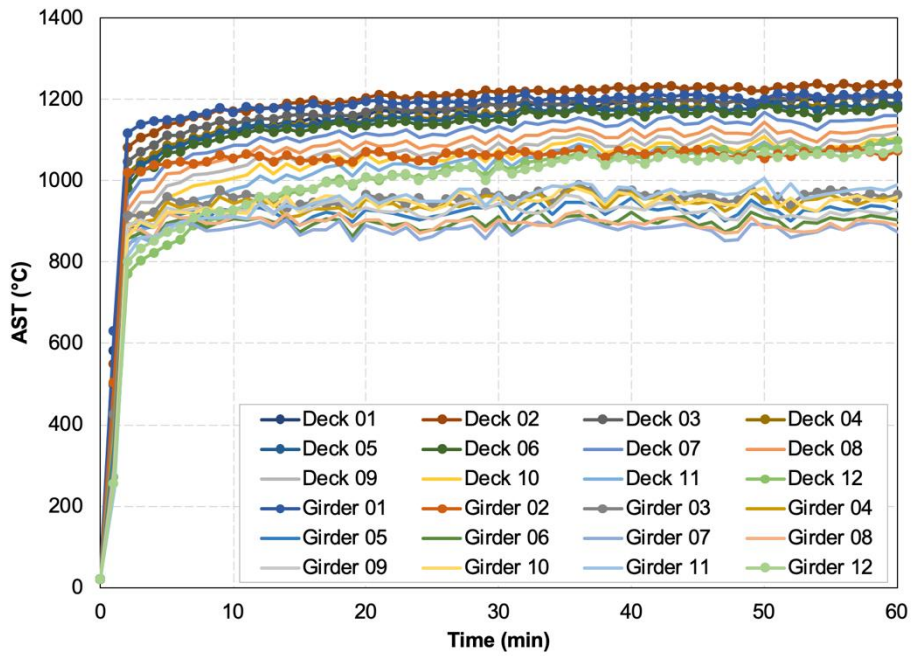


Figure C.8: Adiabatic surface temperature as a function of fire exposure time in Simulation 8

APPENDIX D – THERMO-STRUCTURAL ANALYSIS RESULTS

This appendix presents the results obtained in eight thermo-mechanical analysis carried out in ABAQUS using the field temperatures obtained in the fire model in FDS-PyroSim.

D.1. Thermal Analysis Results

Figures D.1-D.8 present temperatures measured at different points within the girder exposed to each fire simulation (Table C.1) at midspan and support locations.

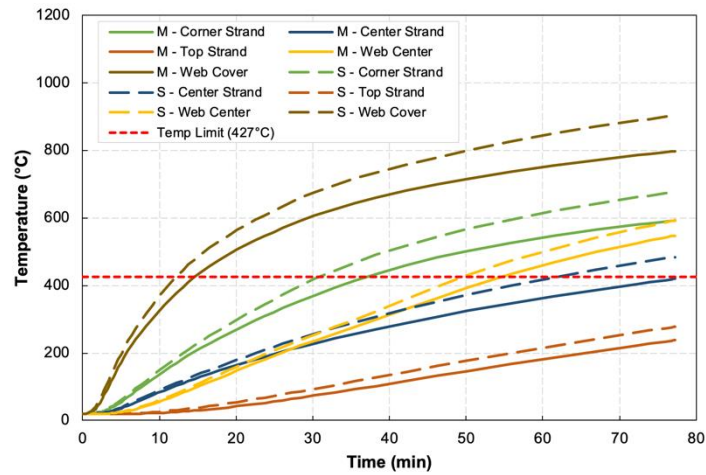


Figure D.1: Temperatures within the girder subjected to fire simulation 1

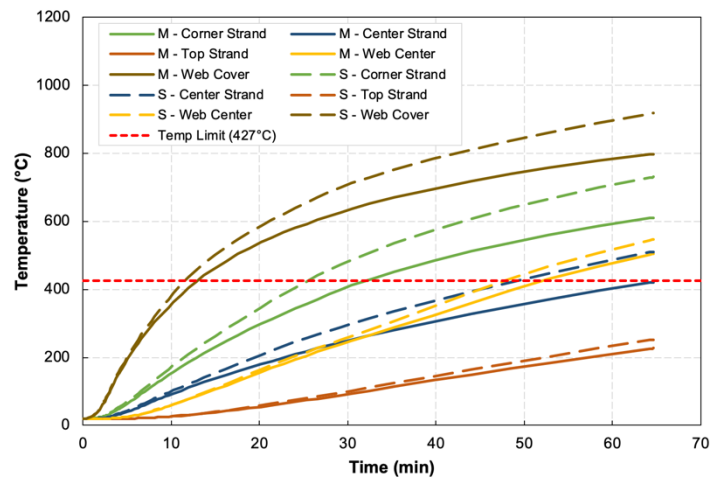


Figure D.2: Temperatures within the girder subjected to fire simulation 2

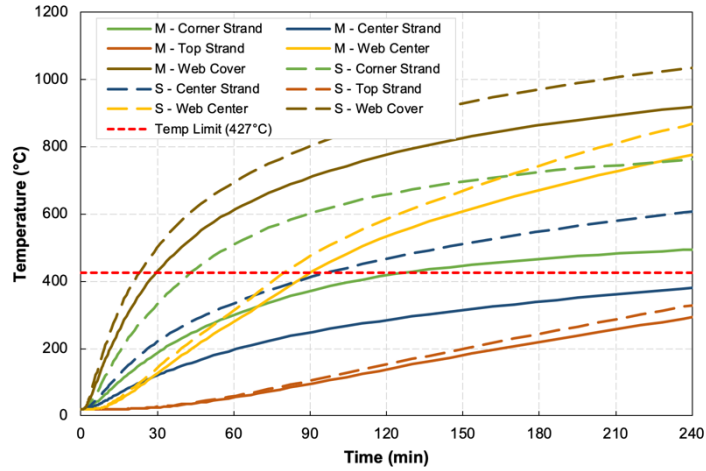


Figure D.3: Temperatures within the girder subjected to fire simulation 3

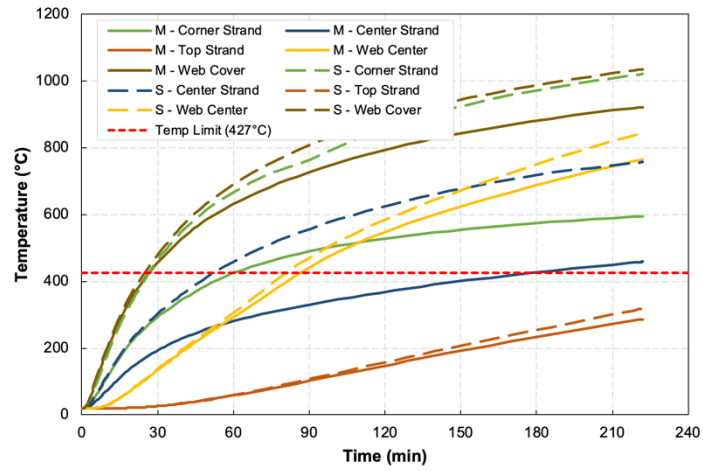


Figure D.4: Temperatures within the girder subjected to fire simulation 4

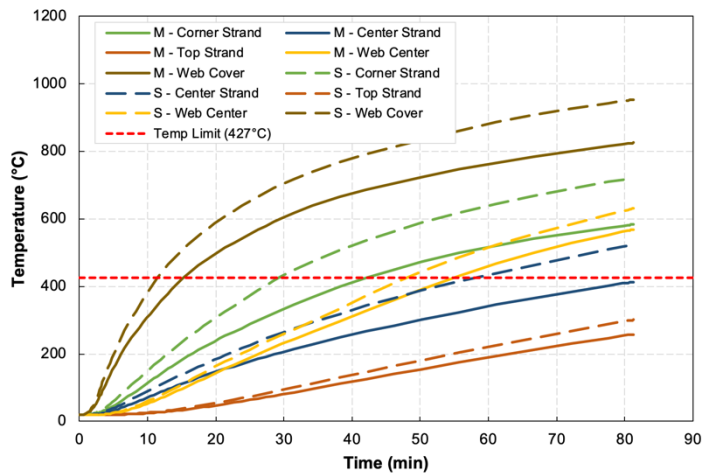


Figure D.5: Temperatures within the girder subjected to fire simulation 5

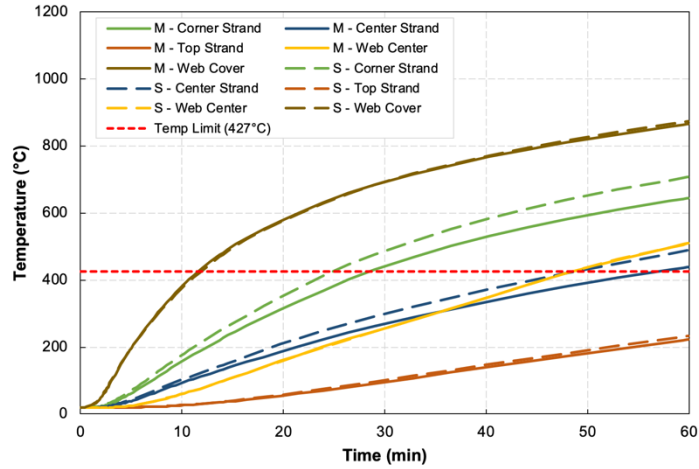


Figure D.6: Temperatures within the girder subjected to fire simulation 6

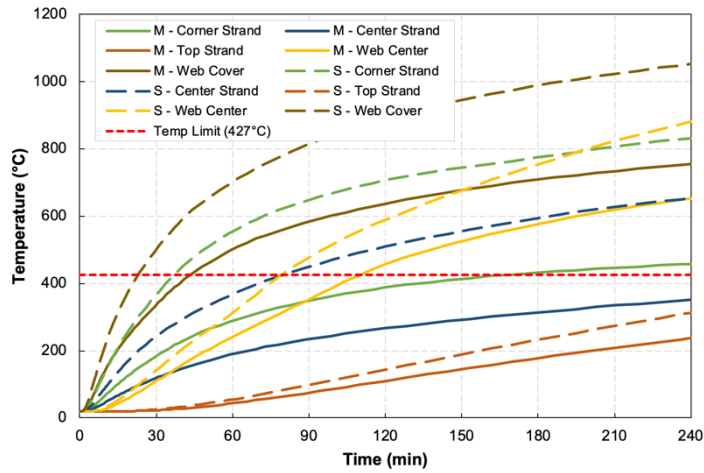


Figure D.7: Temperatures within the girder subjected to fire simulation 7

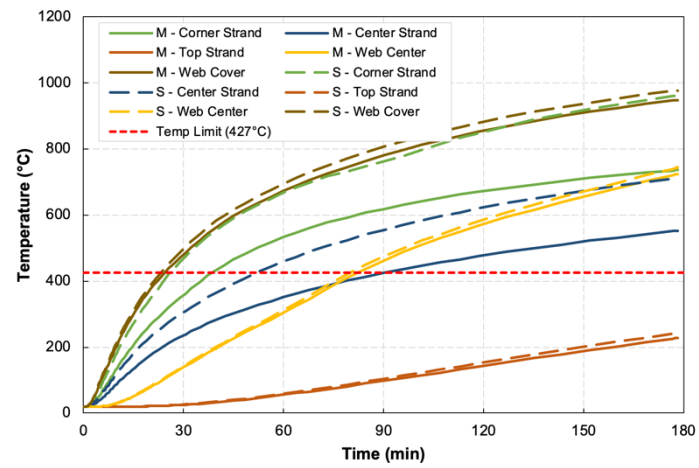


Figure D.8: Temperatures within the girder subjected to fire simulation 8

D.2. Structural Analysis Results

Figures D.9 and D.10 present the deflection response of the girder exposed to each of the eight fire simulations (Table C.1) based on their span lengths.

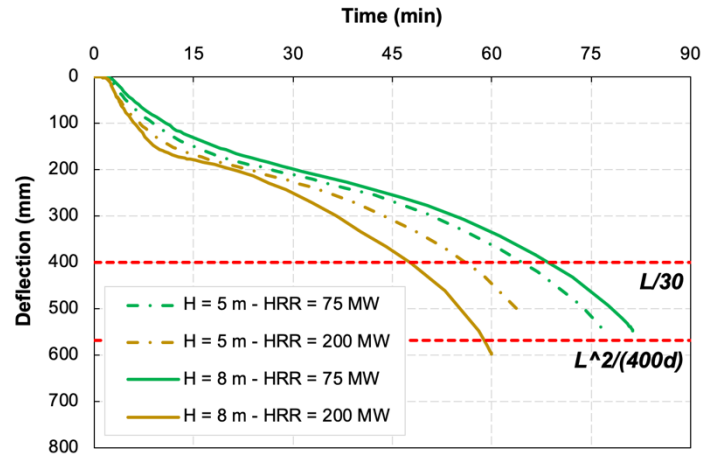


Figure D.9: Deflection response for the girders with a 12 m span length

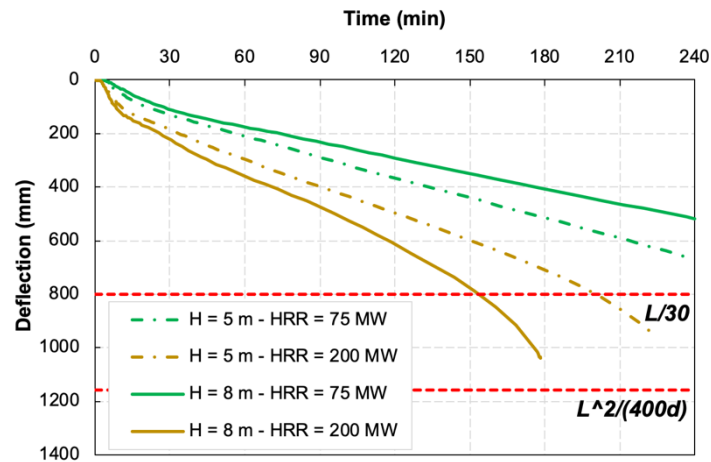


Figure D.10: Deflection response for the girders with a 24 m span length

Figures D.11 and D.12 present flexural capacity degradation as a function of fire exposure time for the girders with a span length of 12 and 24 m, respectively, while Figures D.13 and D.14 present the shear capacity degradation as a function of fire exposure time for the girders with a span length of 12 and 24 m, respectively.

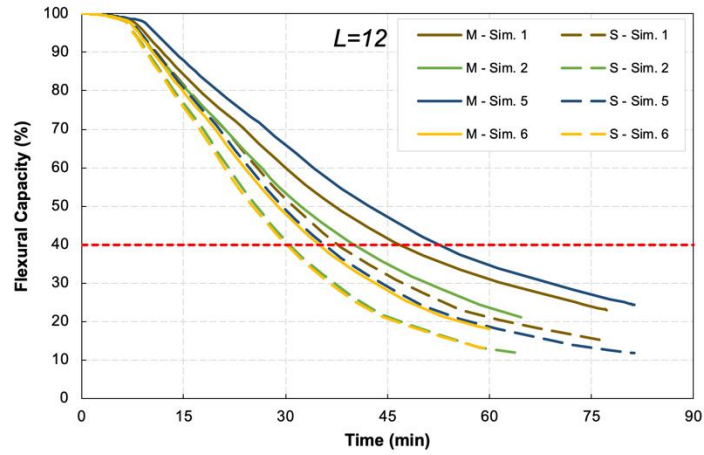


Figure D.11: Flexural capacity degradation for the girders with a 12 m span length

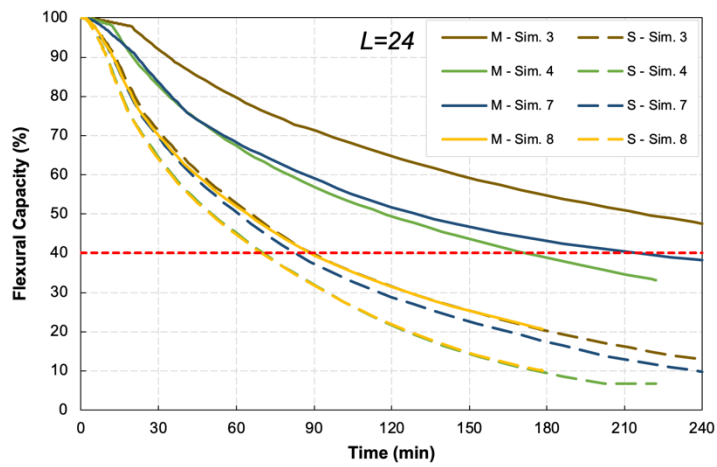


Figure D.12: Flexural capacity degradation for the girders with a 24 m span length

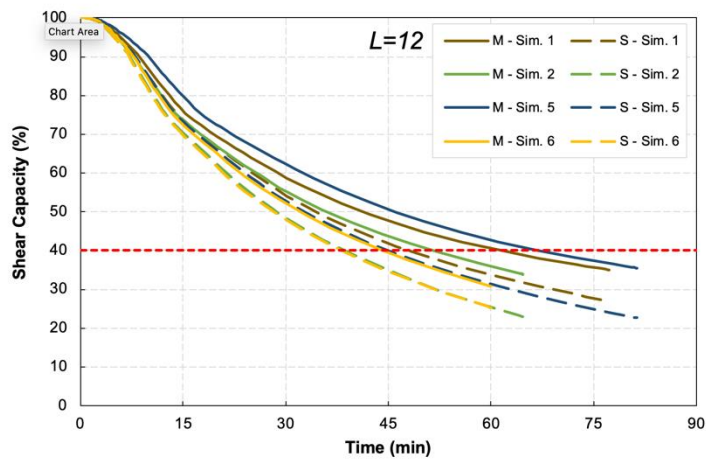


Figure D.13: Shear capacity degradation for the girders with a 12 m span length

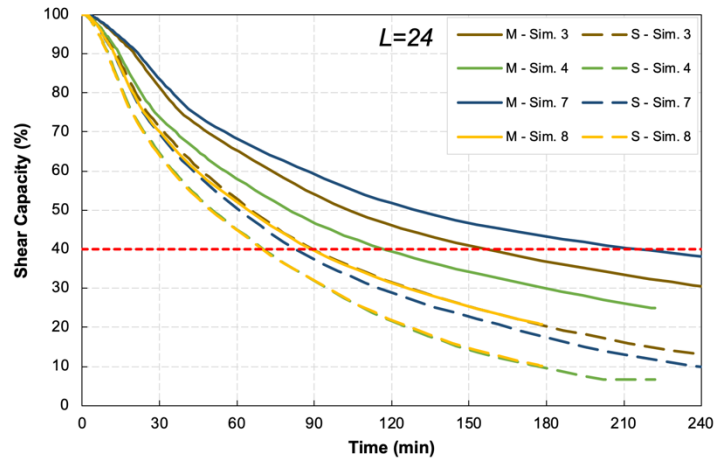


Figure D.14: Shear capacity degradation for the girders with a 24 m span length

APPENDIX E – FIRE LOAD CALCULATION

This appendix presents calculations made to define the fire load used in the fire dynamics model. In order to simulate bridge fires accurately, the fire load has been calculated considering the worst case scenario, which has been defined as an incident involving a gasoline tanker. The properties of gasoline were adopted from the SFPE handbook [242].

Typically, gasoline tankers carry around 8,500 gallons of gasoline, or 32 m³. Based on the density of gasoline (740 kg/m³), the total mass of gasoline in the tanker is calculated as:

$$m_g = V \times \rho = 32 \text{ m}^3 \times 740 \text{ kg/m}^3 = 23,680 \text{ kg} \quad (\text{E.1})$$

Considering the mass loss rate per unit area of gasoline is (0.055 kg/m²/s) and the truck area (30 m²), the time needed to consume the gasoline content in a tanker is:

$$t = \frac{m_g}{\dot{m}'' \times A} = \frac{23,680}{0.055 \times 30} = 13,352 \text{ s} = 239.2 \text{ min} \approx 4 \text{ hrs} \quad (\text{E.2})$$

Based on these results, the time needed for this fire to start cooling down naturally is approximately four hours. Based on these results, it can be observed that the duration of the fire incident is long enough to exclude the necessity of a decay (cooling) phase in both the fire model and in the proposed fire curve. This is because this duration allows firefighters enough time to extinguish the fire and most bridge structures will not be designed to withstand higher levels of fire resistance. Therefore, a decay phase is not introduced in the model.

Considering the heat of combustion of gasoline (43.7 MJ/kg), the total energy released during this bridge fire can be calculated as:

$$E = \Delta h_c \times m_g = 43.7 \text{ MJ/kg} \times 23,680 \text{ kg} = 1,034,816 \text{ MJ} \quad (\text{E.3})$$

Considering the fire duration estimated in Equation E.2, the heat release rate (HRR) of this bridge fire is calculated as:

$$HRR = \frac{1,034,816 \text{ MJ}}{13,352 \text{ s}} = 77.5 \text{ MW} \quad (\text{E.4})$$

Finally, based on the burning area (30 m^2), the heat release rate per unit area (HRRPUA) to input into the fire model is calculated as:

$$HRRPUA = \frac{77.5 \text{ MW}}{30 \text{ m}^2} = 2.583 \text{ MW/m}^2 \approx 2,500 \text{ kW/m}^2 \quad (\text{E.5})$$

These parameters are in accordance with other similar studies presented in the literature, as shown in the literature review presented in 2.4.1.

APPENDIX F – PUBLICATIONS

This dissertation includes material previously published in the following conference and journal publications. This work is made available for academic purposes only and may not be used for commercial purposes without explicit permission from the copyright holders.

- V. Kodur, A.M. Gil, (2022) “Fire hazard in concrete bridges: review, assessment and mitigation strategies,” *Structure and Infrastructure Engineering Journal*.
<https://doi.org/10.1080/15732479.2022.2152465>
- A.M. Gil, S. Banerji, V. Kodur, (2023) “Factors influencing pore pressure measurements in concrete during heating and its influence on fire-induced spalling,” *Cement and Concrete Composites*, 142, 105228.
<https://doi.org/10.1016/j.cemconcomp.2023.105228>
- A.M. Gil, V. Kodur, (2023) “Effect of temperature on the shear strength of ultra-high performance concrete,” *Proceedings of the 3rd International Interactive Symposium on Ultra-High Performance Concrete*, Paper No. 5, Wilmington, DE.
- A.M. Gil., V. Kodur, (2023) “Evaluating shear response of UHPC bridge girders exposed to fire”, *Fire Technology*. <https://doi.org/10.1007/s10694-023-01506-4>
- V.K.R. Kodur, A.M. Gil, M.Z. Naser. (2024) “Fire-induced collapse of an I-95 overpass in Philadelphia: Causes, collapse mechanism, and mitigation strategies,” *Engineering Structures*, 303, 117578. <https://doi.org/10.1016/j.engstruct.2024.117578>